THE EFFECT OF MINERALOGY AND MICROSTRUCTURE ON SINTER SOLID-STATE REDUCTION

MAGDALINI NTOUMA – 4743229

Master thesis submitted to Delft University of Technology
in partial fulfilment of the requirements for the degree of

MASTER OF SCIENCE

in

Geo-Resources Engineering
Faculty of Civil Engineering and Geosciences

To be defended on 14 April 2020

Supervisors TU Delft

Dr. Yongxiang Yang
Dr. Mike Buxton

Supervisors Tata Steel Ijmuiden

Dr. Yanping Xiao
Dr. James Small

Delft, the Netherlands
2020

Summary

Ironmaking in the blast furnace is a rather complex process, governed by the generation of multi-phases and fluid-flow conditions. It includes the reduction of iron ore pellet or sinter material towards producing metallic iron.

The metallurgical behaviour of sinter and its reduction rate are controlled by its initial physical and chemical properties, as well as the blast furnace gaseous conditions. To improve and optimize the metallurgical performance of sinter for ironmaking, it is necessary to understand the fundamental mechanisms of phase equilibria, microstructural transformations and reaction kinetics of different sinter in the upper shaft down to the reserve zone of the blast furnace. The objective of the present MSc research is to study the sinter solid state reduction reactions that take place in terms of thermodynamics and metallurgical kinetics when varying the initial material composition under certain temperature and gas atmosphere conditions.

Six pilot scale sinter materials with strongly variable bulk mineralogical and chemical composition were sized down to fractions of 250-500μm, being a grain range adequately fine to isolate microstructural effects, while excluding the impact of meso-porosity and mechanical fractures (>1 mm), as practically as possible. A industrial sinter sample, obtained from the production line of Tata Steel Ijmuiden was included in order to verify potential differences in reduction. The starting materials were characterized with XRD, XRF, size distribution and BET measurements.

Thirty six (36) isothermal reduction experiments were performed in the TGA and GERO furnace under two set of conditions; i) T=750°C/XCO=0.55/N_2=0.5, ii) T=950°C/XCO=0.65/N_2=0.5 simulating point-conditions of the BRASS test, as relevant to the stability field of Wüstite and solid state reduction. The reduction experiments were interrupted at different reduction times. The 36 reduced samples were further analysed with XRD for phase quantification to then be placed in polished sections for microscopical analysis. The materials were examined under Reflected Light Optical (LOM) and Scanning Electron (SEM) microscopes in order to verify microstructural changes, visualize phase transitions and identify existing stable and meta-stable phases. In total 396 microscopical images were produced. The results of the experiments were compared with thermodynamic models, which show which phases and reduction degree are theoretically expected at equilibrium.

Hereby, based on research results, the study attempted to give answers to the initial reseach questions in order to confirm or deny the research hypothesis. The main findings of the study were mostly qualitative, referring to the mineralogical changes observed during reduction and their impact on reduction kinetics. Results verified that starting composition and mineralogy influences reducibility kinetics, while the way minerals impact reducibility is depended on the imposed conditions. It was observed that at T= 950°C/XCO=0.65/N_2=0.5, the differences between the reduction rates of low and high basicity samples become smaller, due to enhancement of the relative reduction progress of minerals like precipitated Magnetite. At T=750°C/XCO=0.55/N_2=0.5, the transition of Magnetite to Wüstite occurred in different stages of reduction progress, amongst samples. In addition, the effect of mineralogy and microstructure could not be distinguished of that of open particle porosity.

Findings obtained from the XRD analysis and microscopy verified that Hematite is the most prone mineral to reduction followed by SFCA, while Magnetite stays stable for longer. Even within the same microstructure, Hematite is clearly reduced to a greater distance from the particle exterior than the Ca-ferrites surrounding it, and its normalized decrease in the XRD analyses from its initial concentration is clearly faster than that for any of the Ca-ferrites (SFCA, CF2). Moreover, the relative reduction of Hematite and SFCA differs between the two sets of conditions; more reducing conditions converge the reduction progress of the two phases, due to SFCA's greater reduction. The reduction fronts of Hematite and SFCA converge in a single sinter particle with higher temperature conditions.

Two types of unreacted SFCA were identified under the microscope, one Fe-rich SFCA and one Ca-Al-rich SFCA. SFCA 1 starts reducing into a multiphase intergrowth, comprised by a Fe-rich path and a Ca-Si-Al -rich path, while the high Ca type SFCA demonstrates one -to-one phase transition.

The reduction experiments in the GERO showed that longer-time experiments always give the same sample sequence based on reduction progress; WCS108 is the most reduced, followed by WCS90, WCS86, the industrial sinter MH1785, WCS62 and WCS94, whilst no particular differences were observed in reduction behavior of the industrial sinter MH1785/21 compared to pilot-pot sinter samples. In addition, the comparisons between the reduction experiments and the thermodynamic predictions showed that there is mostly qualitative agreement, but results differ quantitatively.

Finally, based on the total of findings of the research work conducted, the study hypothesis was confirmed; S*inter microstructure and mineralogy influences sinter solid state reduction.*

Table of Content

List of Figures

List of Tables

List of Symbols

bC_2SA	Larnite
BET	Brunauer-Emmet-Teller technique
BF	Blast Furnace
BRASS	Blast Furnace Reduction and Softening Simulation
C_2AF	Brownmillerite
C2F	Brownmillerite
C2S	Larnite
Ca_2SiO_4	Larnite
CF	$CaFe_2O_4$
CFs	Calcium- Ferrites
CRC	Ceramic Research Centre
CW3F	$CaFe_5O_7$
CWF	$CaFe_3O_5$
CxFx	Calcium Ferrite
D50	Median Diameter
DR	Intensity of Disintegration per gram of O_2 removed
EDS	Energy Dispersive Spectrometry
GERO	Vertical Gas Mixing Tube Furnace
Hem	Hematite
HOSIM	Hoogoven Simulation Model
KPI	Key Performance Indicator
LER	Lime Excess Ratio
MeO	Wüstite
MeO_#1	Wüstite
Mt_1	Precipitated/Ore Magnetite
Mt_2	Newly formed Magnetite due to reduction
R	Reduction Degree
R&D	Research and Development
SEM	Scanning Electron Microscope
SFCA	Silico-ferrites of Calcium and aluminium
SSA	Specific Surface Area
TGA	Thermo-Gravimetric Analysis
WCS	World- Class- Sinters
WD	Working Distance
Wt%	Weight Percentage
XCO	$CO/[CO+CO_2]$
XRD	X-ray Powder Diffraction
XRF	X-ray Fluorescence

1. Introduction

1.1. General

Ironmaking is a multifaceted process, controlled by the generation of various phases and fluid-flow conditions. It includes the reduction of iron ore pellet or sinter material in the blast furnace towards producing metallic iron. Understanding all the reactions that take place in the blast furnace plays a vital role for operation and quality control. How the loaded ferrous material reacts in the furnace, depends on its initial characteristics, both in micro and macroscale, but also on the reaction driving force, corresponding to the conditions in the blast furnace, both in terms of gas composition and temperature at different time intervals.

This means that the blast furnace provides a very dynamic environment in terms of temperature, composition, oxygen partial pressure, time and atmosphere, it causes the characteristics of sinters to alter. Whether these can change in favourable way towards facilitating blast furnace reducibility is based on sinter's properties, initial compositional and physical characteristics and formation mode (Umadevi, et al., 2011). Based on scale, these characteristics can be classified into (Small, 2010);

1) Mineralogical and chemical composition, i.e. phase proportions and phase chemistry, and bulk chemical composition of the material

2) Microstructure, i.e. how the phases are intergrown on the sub-mm scale - crystallite sizes, morphology, intergrowth style (e.g. preferentially or randomly oriented crystallites) – plus how the void structure is on the micro-scale (pores and cracks < 1 mm)

3) Meso-structure i.e. features on the > 1 mm length-scale such as larger cracks and porosity, the sinter fragment size and shape distribution, specific surface area of the sinter fragments, plus also the distribution of different microstructural 'domains' when 'stitched' together on the > 1 mm scale.

It is rather difficult to separate mineralogy and microstructure in practice. When one of these features changes the other one inevitably changes too (Jursova, et al., 2018; Jursová, et al., 2017).

Hence, there are multiple variables controlling the performance of sinters in the blast furnace, making the optimization of sinter metallurgical quality an important challenge. A plethora of factors contributes to higher metallurgical quality, making the mechanisms that drive phenomena in the ironmaking process even harder to understand and regulate. The current body of knowledge struggles to accountably justify the behaviour in the blast furnace and to explain the exact consecutive reactions that take place, or the rates at which the latter occur (Jursova, et al., 2018). Sinter reducibility, reduction kinetics and raw material consumption in different thermal zones of the blast furnace need to be more deeply comprehended.

Metallurgical quality control is also rather essential for the industry. Understanding and controlling the factors governing sinter reducibility and disintegration can help optimize the blast furnace operation and facilitate developing new quality control testing methods (Konstanciak, 2012). Optimizing operations also involves limiting costs endured for raw material usage and confining environmental implications. Reducing raw material purchase is nowadays necessary for the steel industry due to increased prices (Moffat, 2008). Therefore, it can make a great economic difference if the process becomes more efficient, cost effective and environmentally sound.

The blast furnace shaft can be divided in different thermal zones. The stack is in the upper- middle shaft, where the preliminary reduction and thermal reserve zone take place starting from around 400°C and reaching temperatures up to 1000°C (Woollacott & Eric, 1994). Further down in the shaft, there is the cohesive zone reaching up to 1800°C, where fusion and further reduction occur and slag and metal reach equilibrium.

Considering the above, improving solid state reduction of sinter in the upper shaft thermal zone is important for limiting coke consumption later in the process; when the material reaches the cohesive zone and reduces further. Therefore, if most of the sinter reduction takes place under lower thermal regimes, less reduction will occur in the lower shaft of the blast

furnace, and less coke raw material will be consumed (Song, 2013). To achieve a greater direct reduction, it is necessary to understand how the initial sinter composition and microstructure can affect sinter behaviour in the respective zone in the blast furnace.

1.2. Introduction to the project

The current research aims to understand the effect of sinter microstructure on the solid-state reduction reactions that take place in the BF primary reduction zone, starting from the upper shaft down to the reserve zone, while excluding the influence of macrostructural characteristics. Reduction is studied in terms of thermodynamics and metallurgical kinetics when varying the initial material composition, under realistic gas atmosphere conditions, in order to determine reaction starting and finishing points, as well as the timeline in between.

The project was partly inspired by an initial statistical analysis on historical BRASS tests performed during the past 10 years at Tata Steel Ijmuiden, which show the performance variability of sinters (and pellets) of different origin during their exposure to the reducing conditions of the simulation test. The BRASS test stands for blast furnace reduction and softening simulation and it is a metallurgical test that simulates the real blast furnace process and it is used for quality control. Some interesting findings of this historical data analysis were taken as a base case for the following research and helped formulate the research scope and objectives as they are presented within the next section.

The historical data analysis has shown that sinters of various composition behave differently when reduced, as a result of conditions and starting material characteristics. As mentioned above, both micro and macro characteristics of sinter control its performance, also during the test. Therefore, this project aims to separate their effect by focusing solely on microscale, by taking 5 different sinter samples of controlled composition and one operation sample and sizing them down to a level where macroscale effects are excluded. It is also of interest to establish if there are any differences between the effect of mineralogy and microstructure on the reduction behaviour of production sinter and controlled sinters.

In addition, having the complete curves of reduction of every material tested the past 10 years in the BRASS test also helped to determine the set of conditions that are mostly suitable for investigating the effect of sinter microstructure and mineralogy on solid state reducibility.

The set of experiments is also performed under these conditions. The experiments aim to show the reduction performance of the 6 different sample materials in terms of kinetics and thermodynamics. Kinetics are considered in order to show whether different composition in sinters can affect reduction rate (& reduction degree) and how, while thermodynamics present which phases tend to stabilize in the samples. Thermodynamic calculations are also conducted in order to determine which phases are theoretically expected to occur when the reactions reach equilibrium, demonstrating the potential end products of the reduction experiments under adequate reduction times. The predictions are then compared with the real experimental outcomes. Finally, microscopy is used with the aim to capture unreacted cores and enable the observation of microstructural changes along phase transitions.

The next section presents the research scope and research questions. A state-of-art literature review is presented within the next chapter, addressing relevant research areas and the current understanding on sinter reducibility. Then, the methodology approach and experimental set up are established. These sections give an indication of the scientific gaps this study aims to cover and present the research methods used to do so. The analysis techniques and how the results will be presented are then addressed, followed by a realistic schedule of the project, which sets the expected deliverables and milestones. Finally, a discussion section follows examining potential research outcomes, correlating them to the initial research questions.

1.3. Scope and research questions

The objective of the present MSc research is to understand the phase equilibria, microstructural transformations and ultimately reaction kinetics as relevant for finely grounded

sinter material being reduced in the upper shaft down to the reserve zone of the blast furnace. To achieve this, the study uses the BRASS test analysis as its base case and aims to subtract and isolate certain conditions given at certain stages of the test, in order to clear out the effect of co-variables and enable a more fundamental understanding of the reduction key mechanisms. Melting and softening behaviour of sinter under the cohesive zone conditions of the blast furnace is out of scope for this research, since the study only focuses on the primary reduction zone mechanisms.

In addition, reduction behaviour of sinter is controlled by physical properties on one hand and its compositional properties on the other. The hypothesis of this study is that mineralogy and microstructure have an impact on sinter reducibility rate and reduction degree, when deliberately excluding meso-structure. The main research objective is to verify this impact on reduction behaviour of different sinter materials with strongly variable bulk mineralogical and chemical composition (CaO and Fe2+/[Fe3+ Fe2+] in most immediate terms). On the contrast, macrostructural effects on reduction are deliberately excluded from the research scope. Table 1 presents the research activities as mentioned above, which are considered parts of scope, as well as the respective research areas which are eliminated.

Table 1. Research activities in scope and out of scope

Scope
Research the influence of microstructure and mineralogy on primary reducibility, excluding the effect of primary and secondary porosity (meso-structure) on solid state reducibility
Focusing on reducibility kinetics & thermodynamics as relevant to the conditions of the upper shaft reduction zone, instead of cohesive zone conditions.
The solid-state conditions are subtracted from specific points of the everchanging conditions of the blast furnace simulation test (BRASS TEST); Isothermal experiments.

The conditions of interest were selected based on the prior BRASS test analysis. A plethora of sinter data and their reducibility performance in the test aspired the research objectives as mentioned below.

More specifically, isothermal experiments were established as part of scope, with the aim to isolate and monitor specific reduction reactions at known points of conditions and time on the BRASS test curves, generating more interpretable results. The BRASS test is a simulation of the real process in the blast furnace, where the sample gradually reacts with the rise of temperature and the simultaneous change of atmosphere. When the reducing process escalates, several phases are formed as the conditions constantly change, while different stability fields are circumstantially favoured. Therefore, in order to reproduce and control certain reactions of interest at certain time intervals, the current experiments consist abstractions from the complete BRASS test. If these experiments were performed otherwise, taking the ever-changing conditions of the BRASS test as a basis, there would be several competing driving forces that would cancel out each other's effect, making it very difficult to take reliable measurements and to control the intermediate processes. Therefore, in order to capture and study specific critical reactions that take place during reduction, it is essential to isolate the conditions under which they can occur.

These points of conditions are taken from a range within the primary reduction thermal zone. The upper shaft conditions were firstly selected due to the relatively low temperatures in

this zone that cause the material to reduce without melting. In addition, the upper shaft reduction degree is considered a key performance indicator especially sensitive for sinter, hence the respective conditions can provide a good indication of sinter reduction performance, even at stages further down in the process, as verified by the results of the initial BRASS test analysis.

Therefore, the research hypothesis is that microstructure and mineralogy do influence upper shaft sinter reducibility. To confirm this relationship but also understand the microstructural transformations and phase transitions that take place during sinter primary reduction under the specified conditions, the current study aims to answer following research questions (Table 2);

Table 2. Research objective and research questions

Research hypothesis
Sinter microstructure and mineralogy influence sinter reducibility
Main objective;
Confirm that the effect of microstructure and mineralogy do influence sinter solid state reducibility
Research questions;
• Do different starting composition and mineralogy influence reducibility kinetics?
• Can the effect of open porosity on reducibility kinetics be separated from the effects of composition and mineralogy?
• How do different starting composition and mineralogy influence kinetics (reduction rate and reduction degree)?
• Which sample composition is more prone to reduction?
• What microstructural changes are observed under the microscope due to reduction?
• Do the production sinter and controlled sinter with similar composition reduce differently in practice?
• How does different initial composition and mineralogy impact phase equilibria in practice? Is there agreement with the thermodynamic predictions about the expected reduction and mineral phase assemblage at equilibrium?

2. Literature Review

2.1. Project background

2.1.1. Introduction to Blast furnace ironmaking

Ironmaking is an important step in a typical processing route towards steelmaking. Iron- bearing material is combined with limestone and coke breeze in order to be introduced in the blast furnace and produce hot metal. Then the steel refining process follows, where the hot metal is purified, while its chemical properties and its temperature get adjusted and homogenized (Song, 2013). The final step of refining involves the steel adjustment to the required specifications, in order to be proceed with the next step of continuous casting into slabs, blooms or billets. Finally, these products will be further processed in the rolling mills (Song, 2013; Odenthal, 2017). A scheme of the ironmaking and steelmaking process is given in Figure 1.

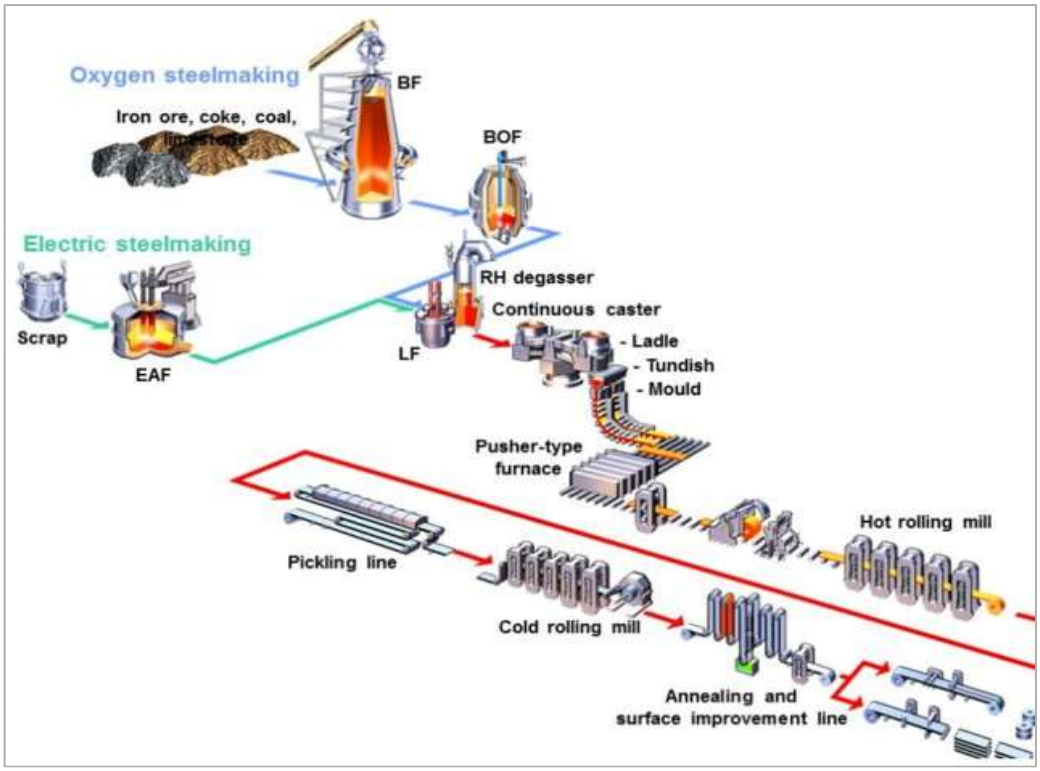

Figure 1. Ironmaking and steelmaking process chain. (Odenthal, 2017)

2.1.2. Blast furnace ferrous burden preparation: Pelletizing & Sintering

The iron-bearing components of the raw material used in the blast furnace are iron ores. These are used in the form of pellets, lump ores or sinters. Some iron ore concentrates, or fines cannot be directly placed into the blast furnace, since their very fine sizes can have a detrimental effect to the BF permeability (Zhang & Andrade, 2016). Therefore, they are first introduced to a process of agglomeration, so that they can be charged into the furnace as larger components (Strassburger, 1969; Ball, et al., 1973). Pelletizing is used for the agglomeration of iron ore and iron ore concentrates in order to remove silica and gangue minerals from the ore matrix through a mineral beneficiation technique (Cameron, et al., 2019). In the ironmaking industry, this technique most frequently corresponds to the combination of fine grinding and certain separating methods, based on the ore type. Magnetic separation is used for Magnetite ores, while spirals or dense media separation is chosen for Hematite ores. The pelletizing process

flow sheets vary regarding the pellet induration technology that is applied (Cameron, et al., 2019). Whether the iron ore is dry or slurry, and whether it is collected on size or in coarser forms play a role on the pelletizing process to be followed, along with the plant availability in processing water. Pellets are uniformly sized and generally within a range of 9-16 mm, with purity of 63%- 68% contributing to faster reduction and high metallization rates.

Sintering is the most common and cost-effective agglomeration method that also prepares the iron ore fines for blast furnace (Loo, et al., 2011; Dawson, 1993; Torre de Palacios, 2011; Cores, et al., 2010). This agglomeration process turns fine ore into a porous and lumpy mass by incipient fusion caused by heat produced by combustion of solid fuel within the mass itself. Sinters differ from pellets, since they are not informally sized. Sintering takes place in the sinter plant, where sinters are produced at high temperatures by mixing the iron ore fines with limestone and coke (Zhang & Andrade, 2017). The initial mix of raw material used for sinter making, as well as the sintering process govern the resulting sinter mineralogy and microstructure, and thus sinter metallurgical behaviour (Jursova, et al., 2018). During this process, the micro pelletized sinter mix is heated up to temperatures until partial fusion is achieved, and a molten phase is produced (Zhang & Andrade, 2017). This phase then crystallizes and solidifies upon cooling towards forming the sinter's minerals and overall structure (Fernandez-González, et al., 2017). The final sinter product is microscopically comprised by relict ore particles, bonding phases, glassy phases and small irregular pores and fractures. Different minerals consist the bonding phases of sinter structure. Apart from iron ore constituents, also flux material, coke and recycled material are used for sinter making. Basic flux materials like dolomite and other MgO bearing additions are included, as well as Al_2O_3 bearing material, being the recycled sinters are being used in order to reduce the cost of raw materials usage (Zhang & Andrade, 2017).Therefore, it is plausible that these additions affect the composition of the mix and the resulting mineralogy.

Hence, which phases are formed, depends on the initial raw material blend composition and sintering process parameters and conditions. The most common minerals observed in iron ore sinter are Hematite (Fe2O3), Magnetite (Fe3O4), Magnesioferrite (MgFe2O4), Silicoferrite of Calcium and Alumina (SFCA), with stoichiometry M14O20 (M= Ca, Fe, Al, Si), Anorthite (CaAl2Si2O8), Calcium Di-ferrite (CaFe4O7), Di-calcium Ferrite (Ca2Fe2O5), Di-calcium Silicate (Ca2SiO4), SiO2-rich glass, free lime, Periclase (MgO) and Olivine (Mg, Fe)2SiO4 (Webster, et al., 2012; Wang, et al., 2011). Therefore, the main types of mineral phases typically correspond to iron oxides, calcium ferrites and crystalline or glassy silicates. The way these mineral phases develop and in which proportions, reflect the mode of formation and formulate sinter microstructure and their dispersal in the sinter, as well as their crystal size and structure have a significant impact on the physical and chemical characteristics of the sinter product (Phillips & Muan, 2006; Umadevi, et al., 2011).

Sinter materials are also characterized by their meso-structure. This refers to their porosity, cracks and other physical characteristics, which also have a significant effect on sinter performance in the blast furnace. On a macroscopic scale, iron ore sinters present an irregular structure with large non-uniform pores, and their sizes can range from 5 to 40mm (Buytendijk, 2019).

2.1.3. Ironmaking

Once pellets and sinters are produced, they are charged as a burden into the blast furnace, where they start to descend from the top through manifold temperature stages. In a simplified scheme, during this process, the ferrous materials undergo heating, reduction, softening and melting, resulting to the production of hot metal. This happens in a range of temperatures, starting from 500°C in the furnace upper-shaft up to 2300°C, as approaching the raceway flames (Geerdes, et al., 2015). The blast furnace can be characterized as a counter-current heat and mass exchanger, since heat is transformed from the gas phase to burden and oxygen from burden to gas (Geerdes, et al., 2015). The gas is provided from the bottom and ascends to the furnace, while the burden and coke material descends.

The material in the blast furnace is placed as alternating layers of coke and burden (iron bearing component). Pre-heated air (1200°C), enriched in pure oxygen and moisture, is blown

into the furnace through the tuyere pipes. The oxygen triggers the exothermic combustion of coke and coal, and carbon is gasified by air into CO and heat (Ghost & Chatterjee, 2008). The gaseous carbon monoxide then ascends through the burden, removing its oxygen, and leading to pellet or sinter reduction in the upper shaft of the furnace. The very hot gas also consumes the coke in front of the tuyeres, creating void. When reaching temperatures of 1100°C and above, the CO2 destabilizes and transforms into CO (Ghost & Chatterjee, 2008). The gaseous reduction of sinter takes place within the heating range of 500°C and 1200-1250°C, causing it to soften and eventually melt. Upon melting, hot metal is produced, as well as slag, which precipitate via the coke zone to the hearth, from where they are removed though casting from the tap-hole (Geerdes, et al., 2009).

2.1.4. Blast furnace thermal zones

The blast furnace shaft can be divided in different thermal/reduction zones. The stack is in the upper- middle shaft, where the preliminary reduction and thermal reserve zone take place starting from around 400°C and reaching temperatures up to 1000°C (Woollacott & Eric, 1994). Further down in the shaft, there is the bosh zone reaching up to 1800°C, where fusion and further reduction occur and slag and metal reach equilibrium. The hearth is placed in at the point where temperature is as high as 1400°C, and this is where the slag is separated from metal (Woollacott & Eric, 1994). Sinters charged in the upper shaft of the BF and they descent through different thermal regimes. First, they undergo the preliminary reduction until they reach a reaction plateau, which is referred to as the reserve zone. The reserve zone corresponds to a time interval with relatively very slow temperature increase between two faster heating intervals or, in chemical terms, it is a zone where the gas composition changes very slowly (Geerdes, et al., 2015). The different reduction zones are illustrated in Figure 2 and Figure 3.

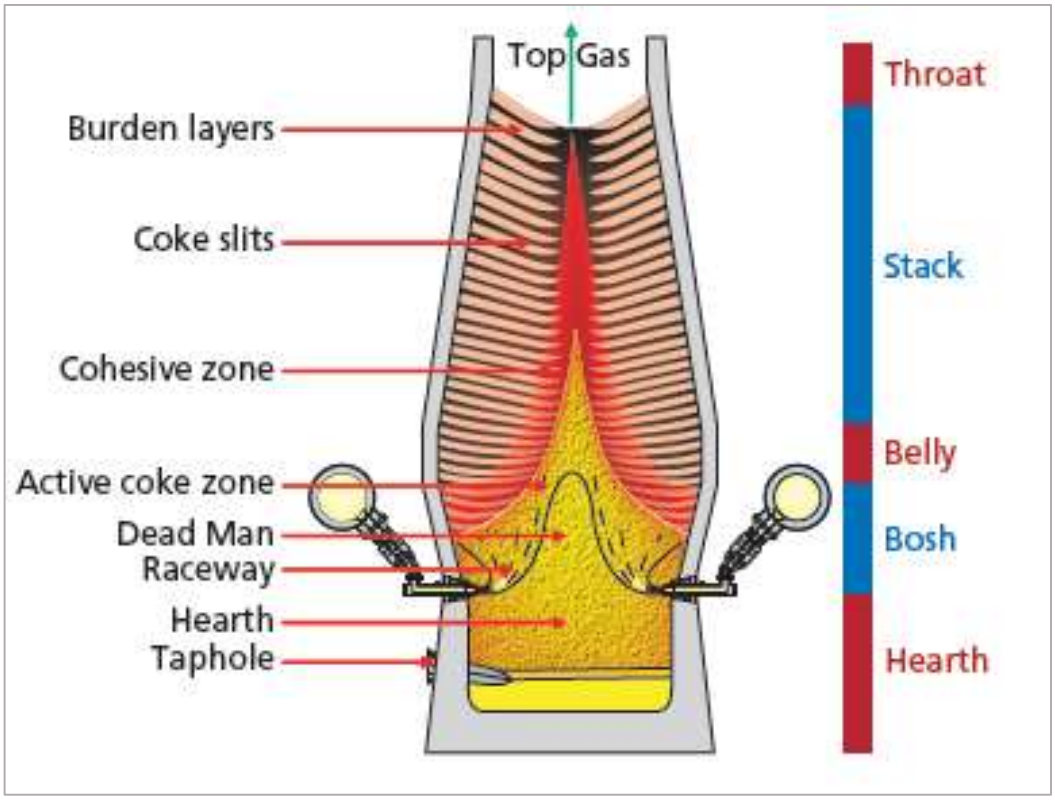

Figure 2. Schematic figure of the Blast furnace (Geerdes, et al., 2009)

2.1.5. Metallurgical quality of ferrous burden

For a balanced blast furnace operation, it is essential to ensure good quality feedstock material. When referring to metallurgical quality, reducibility and disintegration of sinter or pellets are key properties towards achieving optimal blast furnace properties and operation (Konstanciak, 2012). This means that these iron ore agglomerates will be able to sufficiently limit the consumption of the reducing agent, being the coke, while increasing the productivity of the blast furnace (Song, 2013). In addition, advancing the reduction speed, apart for being economically essential for reducing the consumption of costly raw material such as coke, benefits the mechanical strength of the sinters and limits their disintegration in a desirable degree.

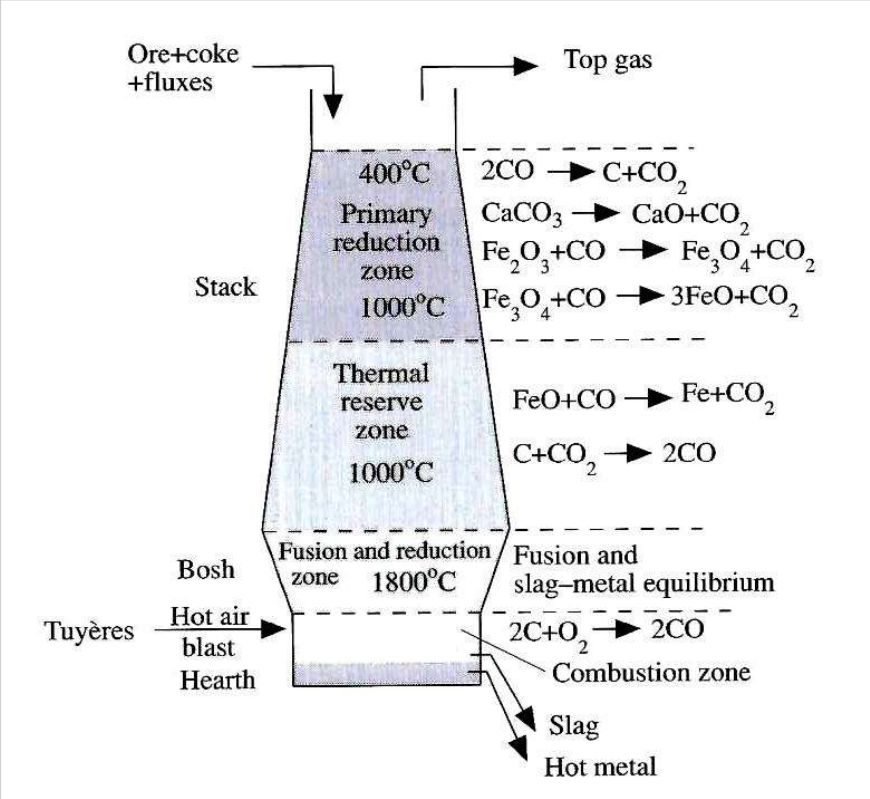

Figure 3. Metallurgical model of the blast furnace: Blast furnace thermal zones (Woollacott & Eric, 1994).

2.1.6. Iron oxides reactions

The key chemical components in sinter in the process of ironmaking are iron oxides. The basic idea behind the reduction in the blast furnace is the subtraction of oxygen from iron oxides, after exposing them to certain atmosphere and temperature conditions. The reduction reactions occur in different temperatures, as every iron phase is stable under different conditions. This means that, temperature is one of the key factors controlling which phase transition will occur. More specifically, at temperatures below 570 °C, Hematite reduces to Magnetite and then directly to iron. On the other hand, when reduced in temperatures above, Hematite eventually turns into metallic iron, but with Magnetite and Wüstite as intermediate phases. The respective chemical reactions taking place during these phase transitions are given below (Song, 2013).

If T < 570 °C,

$$3Fe_2O_3 + CO(H_2) = 2Fe_3O_4 + CO_2\,(H_2O) \qquad \text{eq.1}$$

$$0.25Fe_3O_4 + CO(H_2) = 0.75Fe + CO_2\,(H_2O) \qquad \text{eq.2}$$

If T > 570 °C,

$$3Fe_2O_3 + CO(H_2) = 2Fe_3O_4 + CO_2\,(H_2O) \quad \text{eq.3}$$

$$\frac{w}{4w-3}\,Fe_3O_4 + CO(H_2) = \frac{3}{4w-3}Fe_wO + CO_2\,(H_2O) \quad \text{eq.4}$$

$$Fe_wO + CO(H_2) = wFe + CO_2(H_2O) \quad \text{eq.5}$$

The Fe-O diagram of Figure 4 shows which iron phases can form in respect to the temperature regime and oxygen percentage (Biswas, 1981). It consists a theoretical basis for the reduction of iron oxides. According to the diagram, at temperatures below 570 °C and with gradual decrease of oxygen percentage, the phase transition follows this reduction order; Hematite (**Fe_2O_3**) → Magnetite (**Fe_3O_4**) → iron (**Fe**), while in temperatures greater that 570 °C, the phase transformation follows a different route; Hematite (**Fe_2O_3**) → Magnetite (**Fe_3O_4**) → Wüstite (**FeO**) →iron (**Fe**) (Biswas, 1981). This implies that the stability field of Wüstite is only met at temperatures above 570 °C, while at temperatures below that threshold, Wüstite destabilizes into Fe and Fe_3O_4 according to the following chemical reaction;

$$4FeO(s) = Fe_3O_4 + Fe \quad \text{eq.6}$$

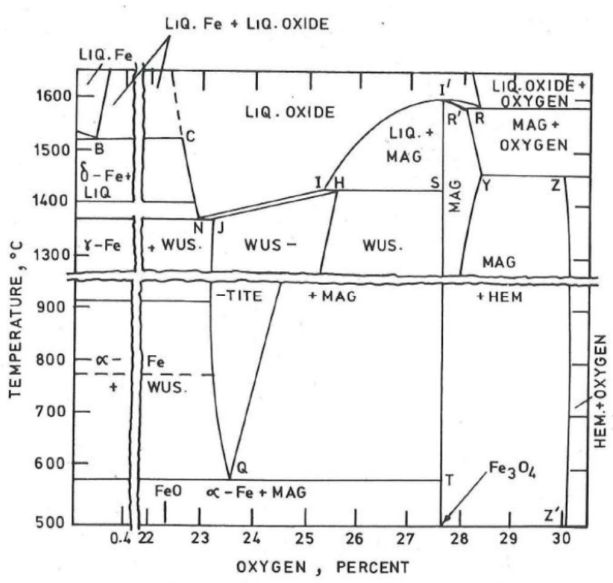

g

Figure 4. Fe-O phase diagram (Biswas, 1981)

The reducing gas used for the reduction of iron oxides in the ironmaking process, is predominately consisted of CO and varying amounts of H_2. The phase Fe-O-CO (or -H_2) equilibrium diagram is shown in Figure 5 (Biswas, 1981). The diagram presents which reactions and phases are favored in respect to the everchanging conditions of gas atmosphere and temperature. On the vertical axis where the gas composition is shown, CO or H_2 are expressed as functions of CO and CO_2 and H_2 and H_2O, respectively. As shown in the equilibrium graph, three different stability areas can be distinguished from top to bottom; the one of iron (Fe), Wüstite (FeO) and Magnetite (Fe_3O_4). When CO is greater to the sum of CO+CO_2 at a certain temperature, reactions occur as shown in the right side from the diagram, stepping from Hematite, Magnetite and Wüstite to the iron stability field with increasing temperatures from 570°C and above (Biswas, 1981).

The diagram also shows the impact of using H_2 as a reducing agent, as opposed to CO. It is observed that when hydrogen is used the reaction curves follow a different route. The curves first intersect with the ones of CO at 821°C, but after that point they go further down in relation to CO, indicating that H_2 consists a much more powerful reducing agent, especially when temperatures are higher than 821°C (Biswas, 1981).

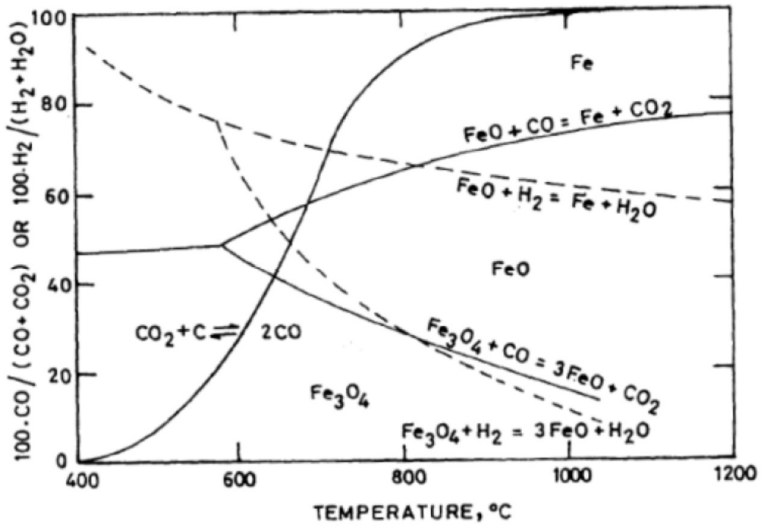

Figure 5. Fe-O-CO (Fe-O-H_2) equilibrium diagram (Biswas, 1981)

The reduction of iron oxides is majorly influenced by the Boudouard reaction, which is the chemical reaction of C(s) with CO_2 towards forming CO, as shown in the formula below (eq.7)

$$C(s) + CO_2(g) = CO(g) \quad \text{eq.7}$$

The reaction presents its maximum instability within the temperature range of 600°C to 800°C, as presented in the Boudouard reaction stability diagram in Figure 6. The boudouard reaction is also highly endothermic and energy consuming, with an enthalpia equal to $\Delta H^{\theta}_{298} = 165390\, J/mol$ (Biswas, 1981). As shown in the diagram, at high temperatures the CO_2 destabilizes and decomposes to CO and C. This reaction in the reverse direction is called carbon deposition. The CO produced by this reaction acts as the reducing agent for iron oxides. When the boudouard reaction is combined with the iron oxide reduction by CO, then it is characterized as direct reduction. The direct reduction consumes less carbon than an indirect one for every mole of oxygen (Biswas, 1981).

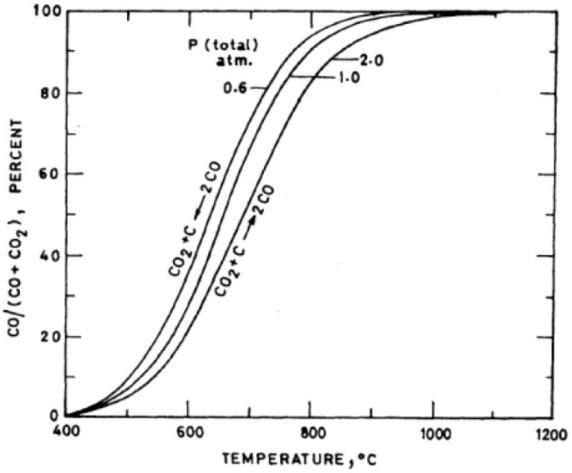

Figure 6. The stability diagram of the Boudouard at various temperatures and the influence of total pressure (Biswas, 1981)

2.1.7. Dynamics of reduction reactions in the Blast furnace

The conditions of the blast furnace are very dynamic and complex, resulting to the formation of multiple phases under various fluid flow conditions. The reactions occurring during reduction in the BF can be studied in terms of thermodynamics and kinetics. The thermodynamics show the possibility of one reaction occurring, at which direction and within which limits. It only considers the starting and finish points of a thermodynamic reaction. On

the other hand, kinetics not only focuses on the starting and ending status, but also in the timeline in between. This means that, when looking at a reaction based on its kinetics, the reduction rate and reaction steps and mechanisms are the main factors considered. During ironmaking, most metallurgical reactions are governed by diffusion, momentum transfer and mass transfer. The fluid flow and heat transferred in the blast furnace open the chemical system of sinter components causing phase transformations, favoring different thermodynamic directions based on the imposed conditions.

2.1.8. Iron oxides reactions mechanisms

The key chemical components in sinter in the process of ironmaking are iron oxides. The basic idea behind the reduction in the blast furnace is the subtraction of oxygen from iron oxides, after exposing them to certain atmosphere and temperature conditions. It is widely known, that regardless of the reducing agent used, the higher oxides fundamentally reduce to lower oxides (Song, 2013). The higher iron oxide is Hematite Fe_2O_3. When it reacts with CO or H_2, it starts forming Magnetite Fe_3O_4 at first, and then Wüstite FeO, which will eventually turn into metallic iron. In a dense granule of Hematite this reduction will start from the edges of the crystal progressing gradually to the core. Therefore, when the Hematite will be reduced with CO or H_2, it will start forming a layer or a zone on its outer part comprised by Magnetite, then by Wüstite and finally from Fe, resulting to a structure of consecutive zones surrounding a Hematite core, as shown in Figure 7.

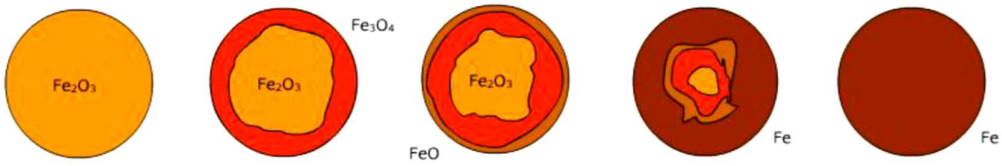

Figure 7. Phase transition of reduced Hematite (Song, 2013).

2.2. Research on sinter reducibility

Sinter reducibility plays an essential role for an efficient blast furnace performance, as it is a measure of metallurgical quality that influences the cost of iron production. Hence, many researchers have shown interest on how to control sinter reducibility behavior, by varying its starting composition and mineralogy, in order to improve blast furnace productivity. This chapter will demonstrate a review of the work that has been carried out by other academics, along with the current understanding on sinter reducibility and sinter mineralogy. The section ends with an explicit state-of-the-art link to the work addressed in the proposal, including the value added to the current the body of knowledge.

Bölükbaşi, et al. 2013 studied the influence of raw material composition on the mineralogy and quality of sinter, focusing on the effect of iron ore composition on sinter and its properties (Bölükbaşi, et al., 2013). Different industrial iron ores were separately used for generating 3 individual sinters with constant basicity, coke dust and flux, but also for the generation of a forth sinter, in which they were mixed in equal proportions. The presence of ferrites was highly present in all the structures, and it was found to favor sinter properties like cold strength and reducibility. The image of Hematite nucleus surrounded acicular ferrite lattice was associated with higher basicity in samples, while higher MgO content was found to facilitate Magnetite stabilization over Hematite, which can have implications in terms of lower stress caused by Hematite's reduction to Magnetite in the blast furnace (Umadevi, et al., 2014; Zhou, et al., 2015; Zhang & Andrade, 2016).

This is also in line with the findings of Umadevi et al. (2012), who studied the changes in sinter structure and properties having FeO content in the range 6.20 – 14.75% versus the coke breeze variation from 55 to 85 kg/t of sinter (Umadevi, et al., 2012). FeO is a measure of Magnetite and increasing the coke breeze and mill scale contents of green mix increases the

sinter FeO content. When increasing FeO as a result of coke breeze rate, the reducibility decreases, which could be related to decreased Hematite and acicular Ca-ferrite contents and increased Magnetite and columnar SFCA (Silico-ferrite of Calcium and Aluminium) amounts. In addition, the quantity of open fine pores in Hematite and SFCA could increase the reducibility. Knepper (1962) reported that Ca^{2+} affects the Fe redox equilibria in the melt, increases the Fe^{3+}/Fe^{2+} ratio and subsequently increases the formation of SFCA where the oxidation state of Fe is Fe^{3+}. Small particles assimilate it faster than large particles leading to early melt formation low in CaO and high in SiO_2 and Fe resulting in lower Fe^{3+}/Fe^{2+} ratio and subsequent crystallization of Magnetite (Knepper, 1962).

According to the results of Umavedi et al. 2012, sinters with FeO content below 8.6% showed porous structure and low strength, and contained reduced Magnetite, dendritic SFCAs and more unreacted ore particles with bigger pores (Umadevi, et al., 2012). Sinters with FeO content between 8.60 and 9.88% showed high strength due to the formation of more acicular ferrites stabilizing the sinter porosity and uniformly distributed among other phases such as Magnetite, Hematite and glass in the structure. Fine acicular SFCAs reduce the cracks and large pores improving strength. Large amount of acicular SFCAs could be obtained by optimizing the sintering temperature and time. For FeO contents above 9.88%, maximum amount of columnar SFCAs formed containing small pores internally linked to form thin cracks. Small secondary pores were observed on the columnar SFCA surface. Due to the formation of large columnar SFCAs and Magnetite, the strength is reduced (Umadevi, et al., 2012; Zhu, et al., 2019). Phase forming at high temperatures are more susceptible to internal stress and crack formation due to shrinkage difference in phases during cooling. At high temperatures, less porosity forms due to greater melt formation. In the absence of large pores in sinter, the sinter strength is controlled by the size and morphology of Hematite, Magnetite and SFCAs distributed in the glassy matrix (Hida, et al., 1982).

Zhang & Andrade (2016) have studied the effect of MgO and basicity on the microstructure and metallurgical properties of iron ore sinter (Zhang & Andrade, 2016). Sinter pot experiments were conducted for the quantitative analysis of the mineralogy of the sinters, during which MgO contents were varied from 2.2 to 4.5 for both low basicity (2.1), and high basicity (3.5) sinter mixes. It was found that high basicity with medium range of MgO sinter is the most favorable composition for a balanced sinter quality adequate to meet blast furnace specifications.

More explicitly, it was shown that increased sinter basicity with stable MgO content, consists a stronger bonding phase for sinter, because it increases its cold strength (Zhang, et al., 2015); (Zhang & Andrade, 2016). In terms of mineralogy, in sinters with higher CaO/SiO_2 ratio, reducibility is governed by the presence of more easily reducible calcium ferrites, less reducible magnesium ferrites and hardly reducible fayalites. When CaO is increased, the phases of calcium ferrites take the place of magnesium ferrites and they are more abundant in the structures, while lesser amounts of fayalites and glassy silicates slag are observed. However, even though sinters of higher basicity present a stronger bonding phase in low temperatures and non-reducing conditions, characterized by needle-shaped calcium ferrites, when reduction starts in the BF and the volume of the oxidized ferrites changes, micro-fracturing is observed while strength degrades rapidly (Zhang & Andrade, 2016; Jursova & Honus, 2016). In consonance to this, it is shown that higher basicity in sinters facilitates reduction.

This conclusion is also in line with the study of Cores et al. (2010), which suggests that the integration of porous ores and high basicity in sinters, can improve reducibility. Based on their experiments, increasing basicity in sinter from 1.6 to 1.9 leads to an increase in the amount of sinter Ca-ferrite, as well as to an increase of sinter reducibility (Cores, et al., 2010).

On the other hand, adding MgO content in the sinter mix, as noted by Zhang & Andrade (2016), can have the opposite effects. The study confirms that magnesio-ferrites and Magnetite increase accordingly to MgO additions in the sinter blend, while their nature makes the structure less reducible (Zhang & Andrade, 2016; Umadevi, et al., 2009; Zhu, et al., 2019). In addition, albeit they are characterized as weaker binders under room conditions and reduce sinter's cold strength (Shi, et al., 2019; Zhu, et al., 2019), their resistance to reduction in the BF makes the samples more resilient when reducing at temperatures of 500ºC (Zhang & Andrade, 2016).This

can be attributed to the lesser Hematite content in their structures, which is displaced by Magnetite (Umadevi, et al., 2014; Zhou, et al., 2015). The transition of Hematite to Magnetite can generate stresses in the sinter's structure during reduction, therefore sinters with greater relative Magnetite content present lower or no stresses when reduced (Pimenta & Seshadri, 2002; Zhang & Andrade, 2016);.

The above studies can be associated with past researches, such as the one from Panigrahy et al. (1984), which had issued the influence of MgO addition on the mineralogy of sinter with different basicity ($CaO+MgO/Al_2O3+SiO_2$), ranging between 0.7 and 1.9 (Panigrahy, et al., 1984). The addition of MgO, also in this case, prevented the formation of Hematite and Ca-ferrite and favored the formation of Magnetite and glass, as well as CaFeMg olivines and pyroxenes by suppressing the dicalcium silicate precipitation (Panigrahy, et al., 1984; Umadevi, et al., 2014). Most of MgO was incorporated into the Magnetite structure to form spinel $(Fe,Mg)O{\cdot}Fe_2O_3$. Increasing the replacement of CaO by MgO leads to an increase in the FeO contents of slag and sinter in overall (Dwarapudi, et al., 2011).

In a similar context, the study conducted by Sato (1982), presents corresponding findings as the ones mentioned previously. Sato (1982) had examined the impact of different Al_2O_3 and MgO sinter contents with varying sinter basicity on sinter mineralogy and reducibility. Nine different sinter samples with changing basicity (CaO/SiO_2 ratio) between 1.6 – 2.0 were considered. In addition, the Al_2O_3 and MgO contents ranged between 1.75 – 2.0 and 0.9 – 1.8, respectively (Sato, 1982). Increasing basicity from 1.6 to 2.0, rises the number of Ca-ferrites from 20 to 50%. The amount of slag initially grows with increasing basicity to 1.7, then decreases with further increasing the basicity to 1.75, followed by other peaks with further increase of sinter basicity. Greater amount of Ca-ferrites and higher porosity, results to a higher reduction degree (Sato, 1982; Jursová, et al., 2017);. The reduction disintegration index (RDI) decreases with the presence of Magnetite and Wüstite in sinters, while it increases in accordance to the number of 100~300 μm Hematite grains (mm^2). The pressure drop during softening test under load is affected by the slag and total porosity quantities, since it increases with an increase in the slag quantity and a decrease in the total porosity. Temperature at the beginning of melt down is predicted by the quantity of Ca-ferrites and total porosity.

The SFCA phases are also observed to increase in higher MgO content sinter samples. These phases are beneficial for sinter cold strength and reducibility According to Zhang et al. (2016) and Cores et al. (2010), SCFAs are formed when Fe2O3 CaO melt reacts with Hematite with subsequent assimilation of SiO2 and Al2O3. On the contrast with MgO, the SFCA phase is found to decrease with higher basicity, while the acicular/columnar SFCA ratio increases along with the glassy phase content. According to Cores et al. (2010) and Clout & Manuel (2003), the formation of fine acicular SFCA (< 10 μm) increases sinter strength and reducibility and the optimal structure for reducibility is proposed to be primary Hematite nuclei enclosed by acicular ferrites (Clout & Manuel, 2003; Cores, et al., 2010).

Similar results to their previous study were demonstrated by Zhang & Andrade (2017), issuing the effect of MgO and Al_2O_3 on sinter mineralogy and microstructure (Zhang & Andrade, 2017). The MgO and Al_2O_3 contents in sinter were varied through fluxes additions and recycled materials respectively. Also, sinter basicity was altered (CaO/SiO_2), with values ranging from 2.1 to 3.5. It was found that higher magnesia content results in higher SFCA phase in sinter, especially in needle-like forms, in both low and high basicity sinter. In accordance, higher MgO levels are associated with greater Magnetite and magnesiospinel presence in the resulting sinter, combined with lower porosity and an increase in slag phase, which is contradictory to other studies that have demonstrated that MgO increase, and the presence of Magnetite results to lower SFCA content (Oluwadare, 2007; Umadevi, et al., 2014; Shi, et al., 2019; Zhu, et al., 2019). The study of Zhang & Andrade (2017) also showed the impact of basicity variations. It was found that lower basicity sinters present higher porosity and higher content in Hematite, magnesiospinel and slag phases while having lesser SFCA amount. On the other hand, increasing basicity favors the formation of mainly acicular SFCAs, due to higher alumina content. According to the findings of Sasaki et al. acicular ferrites are more reducible than columnar SFCAs, due to their very porous microstructure, which provides pathways for

reducing gases to reach the reaction surface (Hida, et al., 1982). As the SFCA density increases from acicular to columnar the reducibility decreases (Bristow & Waters, 1991). .

Costa et al. (1995) investigated the relation between the formation of SFCAs in sinter microstructure and temperature. Their findings argued that more acicular SFCAs would be present in sinter under low temperatures, while intermediate temperatures would rise the amount of SFCAs in overall (Costa, et al., 1995). However, further increase in temperature would cause the content in SFCA to decrease and form big ferrite crystals instead. Sinters with Hematite ore nuclei would react less to the liquid phase during sintering and the obtained sinter structure was dominated by primary Hematite encircled by mostly acicular SFCA and fine porosity, resulting in increased cold and hot strengths and good reducibility (Costa, et al., 1995; Clout & Manuel, 2003).

Yamaguchi et al. (1994) investigated the effect of sinter Al_2O_3 content on sinter properties. Lowering the sinter Al_2O_3 content to 1.5% (in comparison to 1.85% normal Al_2O_3 content) resulted in the improved reducibility from normal 60% to 68% in JIS-RI (Yamaguchi, et al., 1994). This was related to an increase in Hematite, a decrease in slag and Magnetite formation and the formation of fine needle-like Ca-ferrite. According to off-line model experiments, the shaft efficiency raised 2.5% with increasing the JIS-RI of 5% in the blast furnace lumpy zone. At the cohesive zone (where the melt forms above 1150 ^oC), the amount of FeO-containing melt decreased reducing the pore blockage by the melt (improving the sinter total porosity) due to increase in reduction efficiency and decrease in Al_2O_3 and SiO_2 contents of sinter, resulting in better permeability at the cohesive zone. Therefore, the heat transfer to the lower parts of the blast furnace was more efficient due to decreased smelting reduction of dropping material through the coke layer (Yamaguchi, et al., 1994). They suggested that for an improved reduction-meltdown behavior of sinter in BF, the sinter matrix strength at the lumpy region should be enough, while highly reducible minerals considering chemistry and microstructure should form, achieved by lowering the sinter Al_2O_3 content. Furthermore, they mentioned that it is also important to reduce the amount of FeO-containing melt in the sinter in addition to increasing the sinter porosity by decreasing the sinter Al_2O_3 and SiO_2 contents.

The findings are similar to the work of Higuchi et al. (2004), who investigated the reduction properties of sinters with a wide range of composition using reduction test under load to improve reducibility. For advancement reasons, they tried lowering the molten Fe dripping temperature in sintering by increasing the sinter basicity content (Higuch, et al., 2004). Hence, this ranged between 1.0-1.5, while low Al_2O_3 and high MgO amounts were also considered. Their results indeed showed basicity's strong influence on the dripping temperature, therefore it is suggested that the prior should be within the range 1.0 and 1.5. The dripping temperature could be further decreased by decreasing Al_2O_3 amount and increasing the MgO content of sinter. Decreasing Al_2O_3 led to an increase in softening-melting temperature, which indicates an increase in fine pores that enhances reducibility (Higuch, et al., 2004). Sinter constituent minerals affect the reducibility at high temperatures depending on the assimilation extent and grain size of Hematite and distribution of gangue materials. Therefore, at constant chemical composition, different mineralogy could also affect the reducibility and softening-melting behavior.

Pimenta & Seshadri (2002) studied the effect of sinter coke content on sinter properties including microstructure and disintegration under low temperature reducing conditions. Sinter's content in fuel (coke) controls its thermal profile and the maximum possible temperature achieved (Pimenta & Seshadri, 2002). At low temperature, produced sinter consisted of fine acicular Ca-ferrite while at high temperatures, columnar and dendritic Ca-ferrites formed. Higher Al_2O_3 and TiO_2 contents stabilized the Ca-ferrite and Hematite, respectively, and sinters showed high disintegration and DR (intensity of disintegration per gram of oxygen removed) values, especially in the early stage of reduction. Also, it was noted that the reduction reaction of Hematite to Magnetite leads to the sinter disintegration, whereas no disintegration was found for the Magnetite and Wüstite reduction. Sinters produced at high temperatures and with greater coke content, showed large DR values (Pimenta & Seshadri, 2002). These values were higher in the early stages, due to the reduction secondary Hematite forming on the sample surface close to large pores leading to the disintegration of sinter.

Maeda & Ono (1985, 1986) focused on the factors governing sinter reducibility in a series of studies. Their research revealed that both chemical compositions, as well as microstructures of constituent minerals and pores affect sinter reducibility. They investigated the behavior of constituent minerals on the reduction of sinter at 900°C in the gas mixture 90%CO-10% CO_2 using optical microscopy (Maeda & Ono, 1985).They observed that the reduction of Hematite and Magnetite to Wüstite happens rather rapidly in both cases, however, their reduction rates to pure iron differ. Wüstite originating from Hematite reduction is reduced much faster to iron than the one formed from reduced Magnetite. The Hematite reduced Wüstite is reduced homogeneously to iron and the entire reduction period is accelerated, and it is only at the end that Wüstite is surrounded by dense iron and gets no further reduced. On the other hand, the Magnetite reduced Wüstite grains are surrounded by dense iron from an earlier stage in the reduction, resulting to a lower reduction rate (Maeda & Ono, 1985). The reduction speed of Ca-ferrite is much higher than that of Wüstite. This is attributed to the topochemical reduction of Calcium-ferrites which occurs at the boundary of solid phases, producing iron that is very porous and unconsolidated, and hence more reductive.

In their following research, Maeda & Ono (1986) studied the effect of sinter microstructure (mineralogy and porosity) on reducibility using six sinter mixtures with different basicity (Maeda & Ono, 1986). The microstructure of constituent minerals, micropores and macropores (pathways of reducing gas to mineral grains) are factors affecting sinter reducibility. Fine and coarse sinters showed different reducibility characteristics. For fine sinters (Ø = 0.8 mm) containing a few macropores, the reduction rate (%/min) increased from 3.5 to 7.0 with increasing the basicity from 1.1 to 2.0. Sinters containing Hematite and Ca-ferrite were reduced much faster than sinters containing slag and Magnetite (Maeda & Ono, 1986). On the other hand, coarse sinters (Ø = 12 mm) did not demonstrate any direct relation between reducibility and basicity, but their macropores and porosity were shown to affect reducibility. Figure 8 illustrates the effect of basicity on the reduction rate of fine and coarse sinters and the total porosity of the system, increasing with higher basicity.

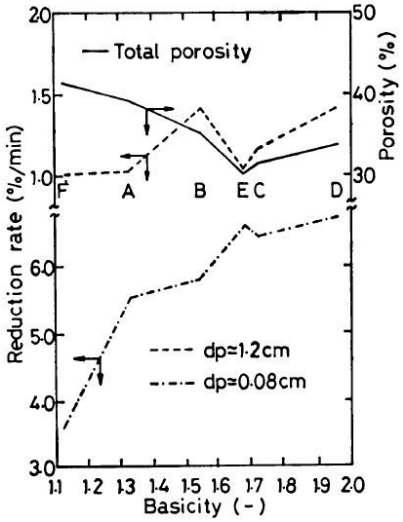

Figure 8. Reduction rates of coarse sinter (broken line) and fine sinter (dot dash line) and total porosity (full line) vs. basicity (Maeda & Ono, 1986).

Ono et al. (2009) also synthesized a composite iron ore sinter, consisting of dense pre-granulated pellets and porous induction bed to study the effect of mineralogy and pore structure on reducibility. The reduction experiment using $H_{2(g)}$ was performed at 900°C. They reported the reduction rate of the composite iron ore sinter is better than that of a pellet with uniform chemistry (Ono, et al., 2009). In addition, the reduction rate increases if there is a compositional gradient between the porous induction bed and dense pellets. The inclusion of CaO and SiO_2 and increasing Ca-ferrite in the porous induction bed is desired to improve reducibility. The accumulation of pore volume > 10 µm was reported to enhance the reduction rate.

Bhagat et al. (2006) argue in their study that sinter reducibility is mostly related to the ration of micro-pores to macro-pores in sinter. This classification was made with the threshold of 10mm, thus pores with radius between 0.001 – 10 μm are categorized as micro-pores, and ranges within -100+10 are characterized as macropores. The decrease in particle size of coke breeze led to increased micro-porosity and sinter reducibility (100%, -3.3 mm sized coke breeze). Decreasing the ore particle size from 8.0 to 6.3 mm increases the microporosity, pore average radius and density of sinter followed by sinter increased reducibility (Bhagat, et al., 2006). The micro-porosity and reducibility of sinter slightly increase with the replacement of pyroxenite by dolomite. Sakomoto et al. investigated the correlation of sinter structure and mineralogy to reducibility. The reducibility of a single mineral phase was studied, using a one-interface unreacted core model to predict the sinter blend reducibility by knowing ratios of individual minerals in a synthesized sinter mixture. They reported that the reducibility of diffusion bonded sinter is better than the melted one due to good diffusivity of reducing gas through the reduced layer (Sakamoto, et al., 1984). The reduction test on single mineral phase showed that the reducibility decreases in the order: fine Hematite and fine Ca-ferrite, secondary Hematite (skeletal type), Ca-ferrite (needle type) and Ca-ferrite (prismatic, crystallizing upon the melt cooling).

As it can be implied from above, a plethora of studies has addressed sinter reducibility. However, it is observed that most of the existing literature studies, if not all, are investigating reducibility at much less controlled starting materials or at more complicated experimental conditions (metallurgical simulations). To elaborate, although the composition and mineralogy of sinters is often controlled by variating the initial raw materials used for its formation in order to control reducibility in the blast furnace, the effect of mineralogy and microstructure is never separated from the effect of physical properties, such as porosity. This means that these very important characteristics of sinter covariate during reduction, obscuring each other's influence on reducibility. Other studies address the reduction behavior of completely pilot scale starting materials, such as single phases of SFCA or Hematite, Magnetite and Wüstite, instead of examining the behavior of sinter samples under more controlled conditions.

As such, the following research presented in this study can be considered as unique, since the body of knowlegde so far has focused on either investigating the behavior of single phases much more fundamentally (i.e. single mineral phases), or on looking at much less controlled starting materials and complex testing conditions where the interpretation of results is severely hampered. Therefore, the aim of this study is to fill the gap in between, and be able to monitor the transitions of as many phases as possible, under much more controlled conditions, which do not co-variate, and thus do not obscure potential correlations. Therefore, by controlling the effect of material characteristics, and simplifying testing conditions, phase equilibria, microstructural transformations and ultimately reaction kinetics as relevant for sinter material being reduced, can be comprehended on a more fundamental level.

3. Analysis of historical BRASS test data and affiliation to the project

The current research was partly motivated by the need to understand the underlying physical-chemical explanations of the findings of an initial statistical analysis of historical simulation test data. More specifically, the BRASS test was selected in order to verify the performance variability of sinters (and pellets) of different origin, during their exposure to ever-changing reducing conditions. The BRASS test accounts for Blast furnace Reduction and Softening Simulation. It is a metallurgical test used at Tata Steel Ijmuiden for quality control of ferrous burden material. The realization and operation of this simulation test was initiated by the results of vertical probing at a real blast furnace at Tata Steel's plant in Ijmuiden (Song, 2013). The BRASS test monitors the reduction process of the ferrous burden material, while the latter is exposed to increasing temperatures and a gas mixture of CO-CO_2-H_2-H_2O versus time. Therefore, the BRASS test can simulate the performance of sinters (and pellets) in the blast furnace, while it can demonstrate reduction rate and reduction degree at any time and temperature interval.

Such tests have been largely conducted at Tata Steel Ijmuiden for the past ten years. Hence, it was considered insightful to collect all this historical information, accumulated throughout the years, with the aim to examine the extent at which different sinters and pellets of various initial compositions behave differently during the test. The purpose of this would be to find potential correlation of material starting chemistry and reduction performance in the BRASS test. In addition, this would be instructive to determine whether the BRASS test could be used as the main test for production metallurgical quality control; The behavior of sinters during reduction is expressed with several "Key Performance Indicators". Besides finding which initial sinter chemistries result to better KPIs, determining which indicators are more sensitive regarding variating composition was considered important for production metallurgical quality control and the selection of BRASS test as the main quality test (i.e. as oppose to HOSIM test).

In order to curry out this analysis, the entire test database of the last 10 years was collected from the MLY laboratories, at Tata Steel Ijmuiden. All the complete BRASS tests were then separated from this database and were classified further to BRASS 1 & 2, pellets and sinters and according to their test profile (center, middle and wall). Then, different diagrams were generated plotting reduction degree and reduction rate with time and temperature, in order to determine the KPIs of interest and give them respective values. In addition, the initial chemical compositions of all the samples tested were collected and combined with the respective test performance (KPIs). Finally, correlations between different chemistries and KPIs were performed in order to find trends and sensitivities.

3.1. Historical data collection and analysis

All the tests carried out for the past 10 years in MLY laboratories, at Tata Steel Ijmuiden were collected. These corresponded to 1.300 tests in total, with most of them being HOSIM tests, while the rest 355 tests would be BRASS tests. Then from this bunch, all interrupted BRASS tests were separated, leaving 83 complete ones to be used for the analysis. Further classification was performed separating BRASS 1 and BRASS 2 tests. These were separated to sinters and pellets, and then to wall, middle and center profile tests as shown in the scheme of Figure 9. Each test file contained all sorts of information for the test, presented in different columns, such as; time, respective concentration of gasses (N_2, H_2, CO, CO_2), temperature, the actual O/Fe ratio and other. The "reduction rate" d[O/Fe]/dt, was also calculated for each test, for every time/temperature interval using the rate of change of O/Fe to time change.

The reduction of ferrous materials during the BRASS test is expressed as a function of the initial Fe content of each sample (O/Fe). Hence, the mass loss reported during the test is assumed to solely correspond to oxygen loss, which was initially bound to Fe. In addition, the

results are documented in graphs displaying the O/Fe change versus time, temperature and other parameters. The O/Fe ratio is selected because it is an absolute coordinate system of the redox state of the Fe in a bulk sample. It can be associated with mineral stability fields progressing from Hematite (O/Fe = 1.5) to metallic Fe (O/Fe = 0), where Magnetite and Wüstite can also be used as reference compositions in between.

It is important to note that since it refers to the redox state of the sample, it should not be confused with the "reduction degree R" or the reaction progress. These are relative parameters defined based on a reference start and end point. The reduction degree scales the values between their different starting points per sample and the final reference when O_2 bound to Fe is zero, meaning complete metallization is reached.

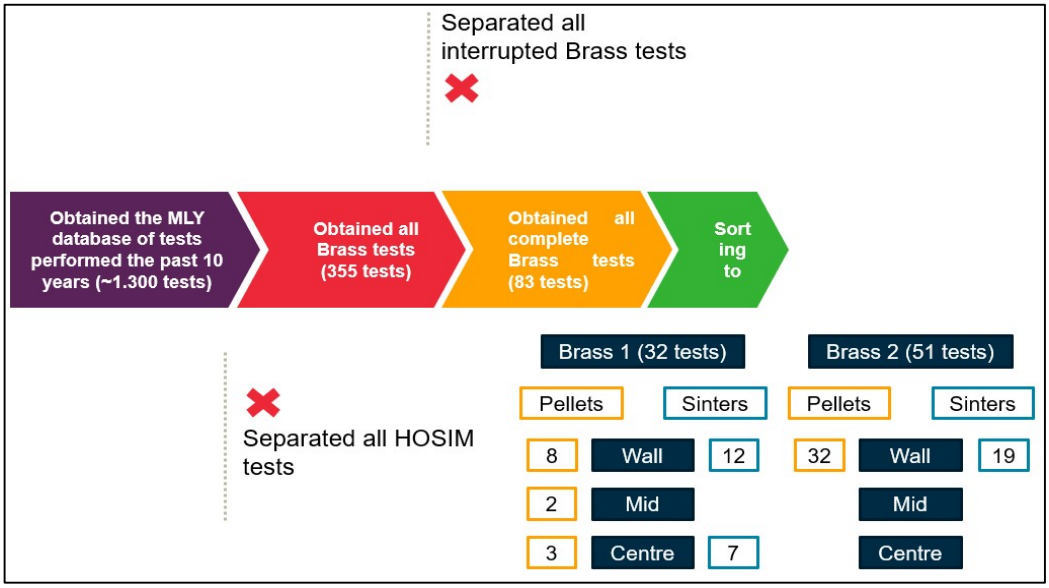

Figure 9. Selection procedure and classification of BRASS tests performed in the last decade in MLY, Tata Steel Ijmuiden.

This data was then used to plot 9 different diagrams corresponding to each test, in order to show reduction behavior in terms of time and temperature. More specifically, the following graphs were considered;

- O/Fe ratio vs. temperature
- O/Fe ratio vs. time
- Temperature vs. time
- d[O/Fe]/dt vs. time
- d[O/Fe]/dt vs. temperature x2
- d[O/Fe]/dt vs. O/Fe ratio x2
- Gas flow vs. time

Temperature was plotted with time to show the temperature profile being middle, center or wall, while the regulated gas flow was also plotted with time to verify that all tests have matching gas profiles. In addition, O/Fe was plotted with temperature and time in order to present how much oxygen is subtracted at any given time and temperature value, hence, to show how the O/Fe changes throughout the test's-controlled conditions for a specific ferrous burden material. Also, it is important to demonstrate at which O/Fe the material reaches the reserve zone and its reduction stagnates. The d[O/Fe]/dt was schemed with temperature, time and O/Fe ratio to display how the reduction rate changes over time, temperature and O/Fe changes.

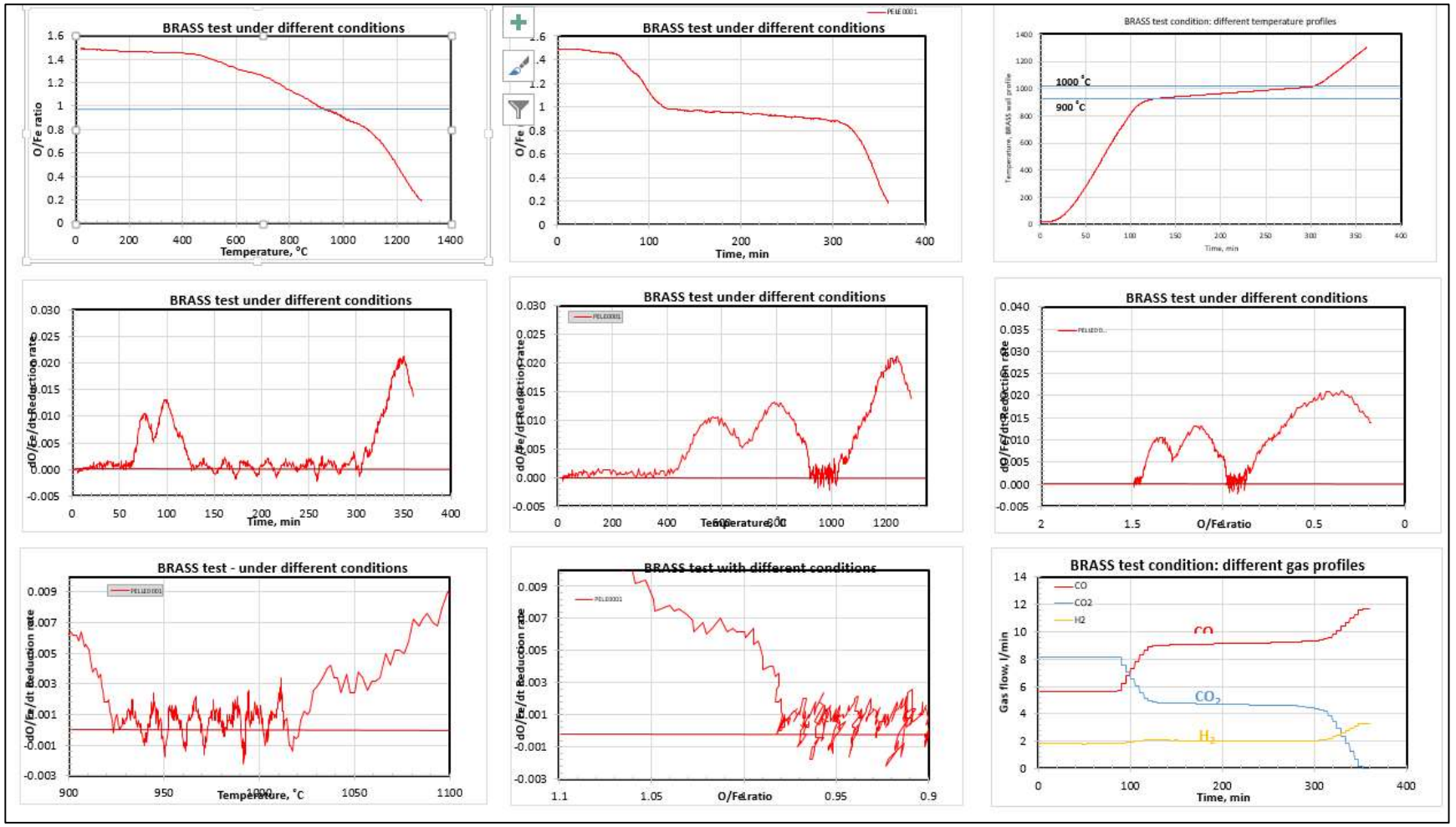

Figure 10. BRASS test; Example of performance diagrams for pellets

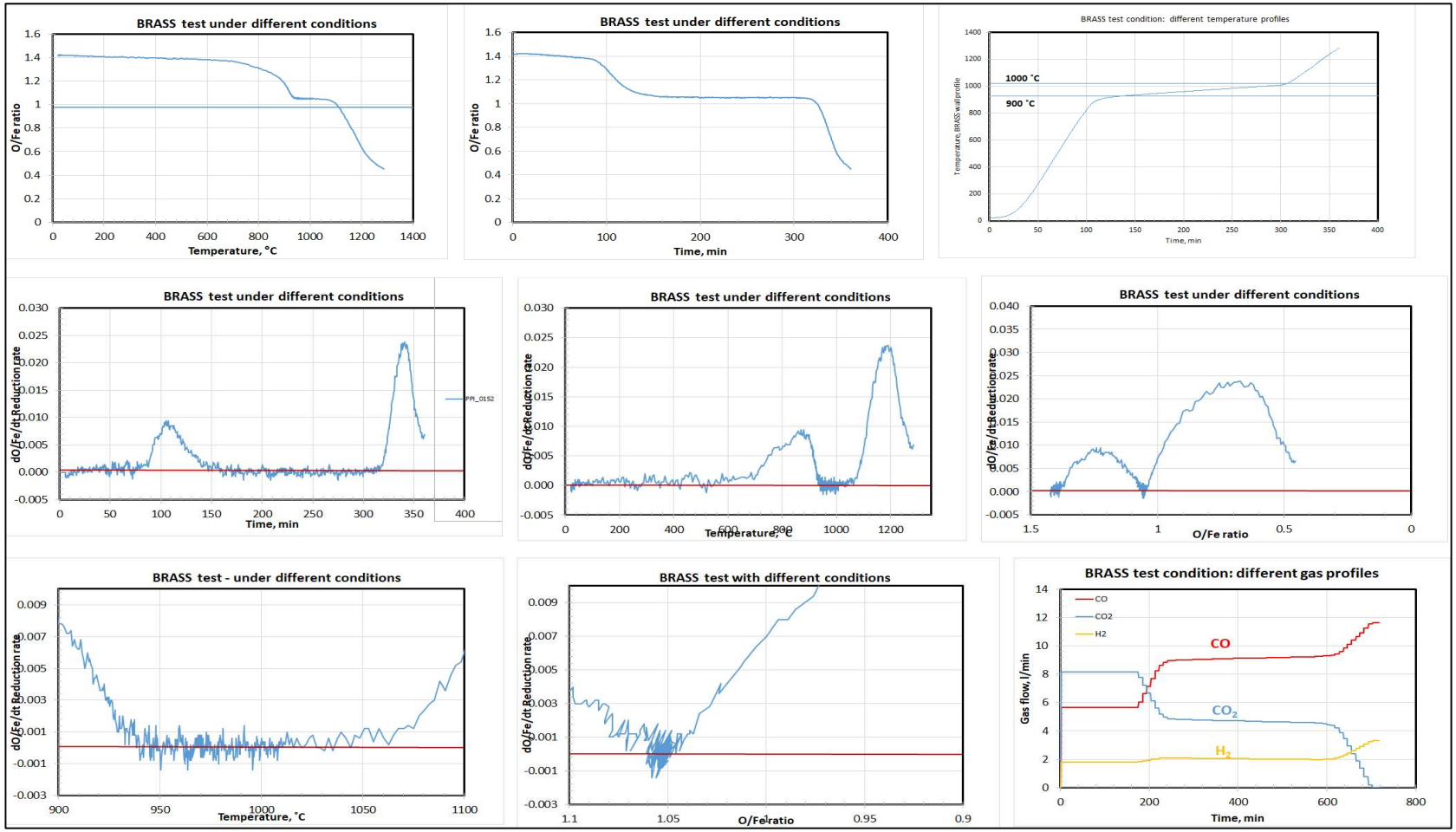

Figure 11. BRASS test; Example of performance diagrams for sinters.

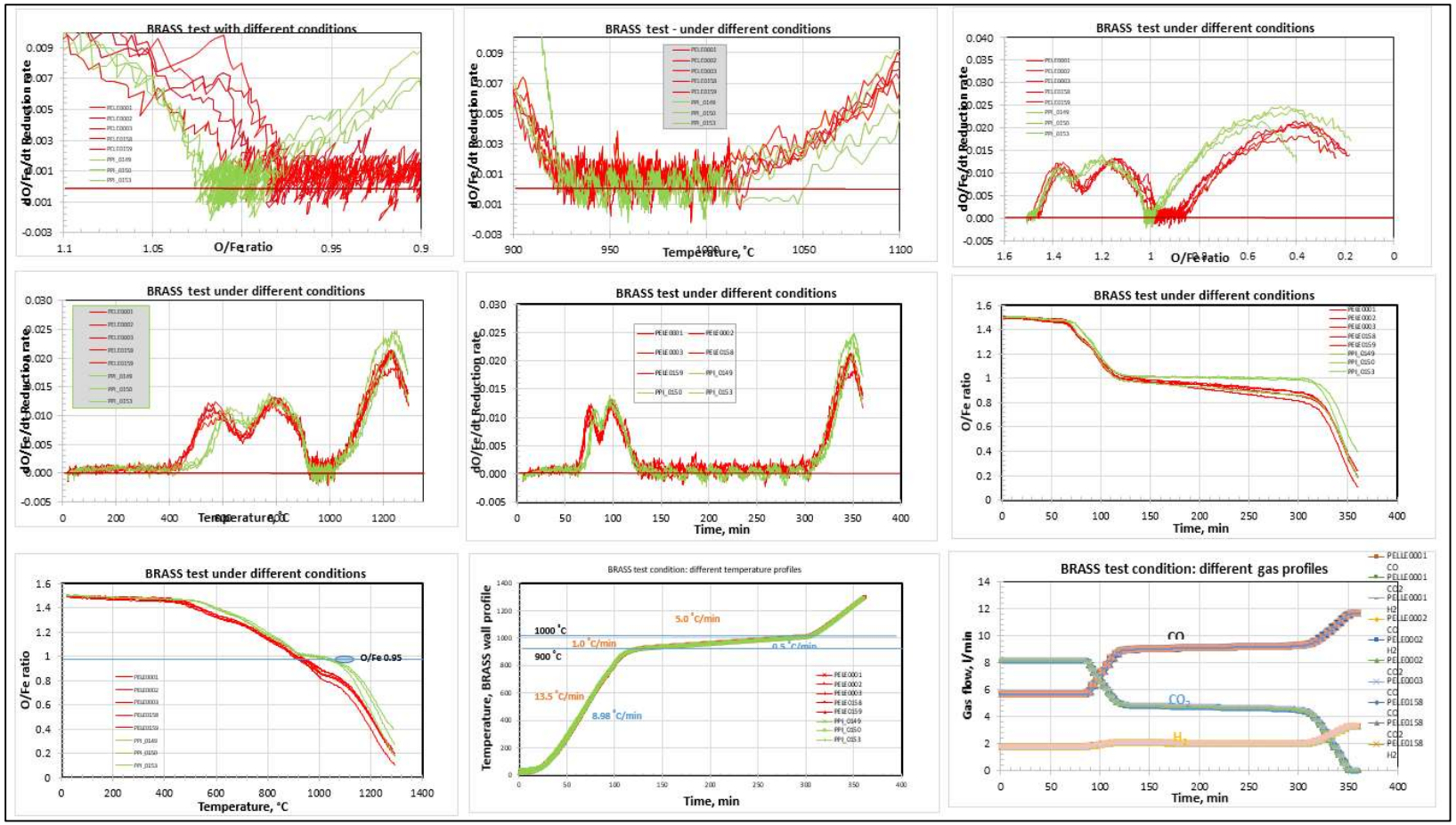

Figure 12. All complete, wall profile, pellet BRASS tests performed the past test 10 years in Tata Steel, Ijmuiden. Two different clusters are observed based on reduction behavior; the red cluster corresponds to pellets with earlier direct reduction and lower indirect reduction, as relevant for the second reduction peak. The green one corresponds to pellets with slightly slower direct reduction, earlier and narrower reserve zone, and higher indirect reduction.

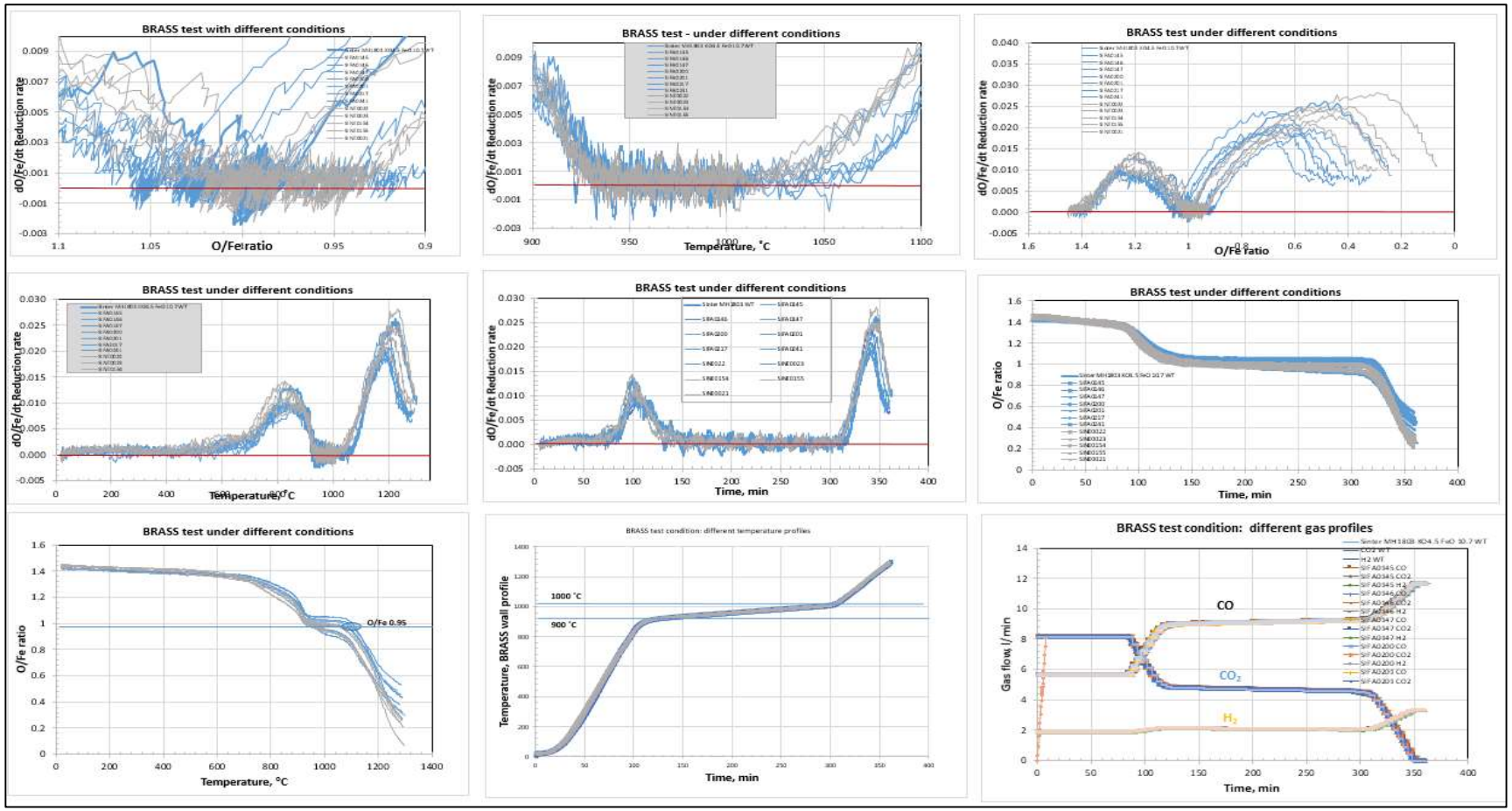

Figure 13. All complete, wall profile, sinter BRASS tests performed the past test 10 years in Tata Steel, Ijmuiden. Two different clusters are observed based on reduction behavior; the gray cluster corresponds to sinters with higher indirect reduction.

When reduction rate is greater, reduction occurs more rapidly, therefore it is an important factor showing the speed and altitude of one sample's reduction during the test, due to the regulated alteration of conditions. An example of each test's graphs is given in Figure 10 and Figure 11. Figure 10 presents the performance plots of a pellet and Figure 11 shows the respective performance of a sinter.

In addition, all individual tests of pellets and sinters were plotted all together to compare their reduction behavior under the continuously changing conditions of the test. Hence, 9- all test inclusive- plots were generated for each temperature profile, so that trends could be more clearly sketched and visualized. Since most of the tests were performed with a wall temperature profile, their "cumulative" graphs were the most informative due greater abundance of tests. The resulting graphs, which include the performance of all the pellets and sinter tests, conducted under the wall profile, are presented in Figure 12 and Figure 13.

As observed from the graphs, there is a behavioral pattern in all the tests, as reduction shows two peaks, one at the beginning of the test and one at the end. The first peak can be referred to as direct reduction and the second peak as indirect. In terms of conditions, the area of the direct reduction correlates to the *upper shaft zone* in the blast furnace, while the indirect reduction occurs in the *cohesive zone* of the blast furnace. There is an area in between, within the range of temperatures of 900°C and 1150°C, where the reduction stagnates and reaches a plateau. This area corresponds to the Wüstite to iron transition and according to the BRASS test, at this range of temperatures, the samples are introduced in the *reserve zone* of the blast furnace. The reserve zone is reached as the reaction rate gradually slows down.

There are some clear differences observed in the reduction behavior of pellets and sinters. During direct reduction, pellets start to reduce earlier than sinters, while they demonstrate two clear peaks of direct reduction, whereas sinters show only one. This can be attributed to the sketched differences in their composition. Pellets contain a relatively excessive amount of Hematite when compared to sinters, hence this can influence their solid-state reduction behavior, which is assumed to be a result of the subtraction of oxygen solely from iron oxides, such as Hematite and Magnetite. Therefore, the first peak in pellets possibly corresponds to the reduction of Hematite, which is followed by the reduction of Magnetite. On the other hand, sinters present their first reduction peak when conditions are more progressed due to the abundance of Magnetite, which is stable over a wider range of lower temperatures, until the conditions allow, and its reduction starts as well. The second peak of the pellets and the sole sinter direct reduction peak nearly fall into the same range of time and temperature.

Apart from the apparent behavioral differences of sinters and pellets in the BRASS test, as types of ferrous material they do present different performance also among them. Therefore, ferrous material of different composition and origin display different O/Fe at specified times, different times of reaching the reserve zone, different residence times in the reserve zone, as well as different indirect reductions. This is an indicator that material properties play an important role to the test outcome, since starting chemical composition, mineralogy and porosity all seem to potentially have a clear influence on reducibility and BRASS test performance.

In addition to the plots, a table containing all the KPIs (Key Performance Indicators) for each test was tailored. An example of such a table is given in Table 3.

Table 3. Example of KPI table of a sinter sample illustrating reduction rate, time, temperature and O/Fe at start and at the end of each reduction zone of the BRASS test.

	dOFe/dt				Time(min)			Temperature			O/Fe	
Ranges	start	finish	**max**	average	start	finish	**Δt=duration**	**start**	finish	ΔT	start	finish
1st reduction	0.003	0.002	**0.0132**	**0.0080**	66	124	**58**	**450**	921	471	1.440	0.980
Reserve zone	0.002	0.0022	**0.0026**	**0.0005**	124	295	**171**	**921**	1010	89	**0.98**	**0.882**
2nd reduction	0.0022	0.131	**0.0212**	**0.0104**	295	364.5	**69.5**	**1010**	1309	299	0.882	0.131

The entire range of reduction during the test is divided into clusters, being the direct reduction (1st pulse of reduction), the reserve zone and a second, indirect pulse of reduction. The O/Fe and O/Fe rate could be documented at the start and at the end of each test condition

"zone", hence several performance factors could be estimated for every test. The resulting KPIs based on the table are the following;

1. O/Fe just before the reserve zone
2. Maximum O/Fe rate (max d[O/Fe]/dt) at the upper shaft
3. Time reaching reserve zone (min)
4. Time in the reserve zone (dt)
5. Average O/Fe in the reserve zone
6. Final O/Fe

The resulting KPIs were subtracted from the raw data, in order to verify whether they can be correlated with different starting sample chemistry. Therefore, if there are performance patterns between starting material with similar composition, this would indicate how strong of a factor starting chemical composition can be for sinter or pellet reducibility. In addition, how strong a correlation is between certain KPIs and starting chemistry, can demonstrate which performance indicator is more sensitive to compositional changes. This way multiple input (material chemistry) and output (BRASS curve characteristics) parameters can be matched, in order to find the ones, have the best mutual statistical correlation.

In accordance, the chemistry of each ferrous material tested was collected from the Tata Steel databases, and the content in certain important chemical figures was separated (Fe, FeO, and two kinds of basicity; B2= (CaO +MgO)/SiO2 and B3= CaO/SiO2). An example table of a pellet's chemistry is given in Table 4; such tables were made for each sample.

Table 4. Example of pellet chemistry. Content in Fe (%), FeO (%), B2 and B3 were correlated with all 6 specified KPIs.

Fe [%]	FeO [%]	CaO [%]	MgO [%]	SiO2 [%]	CaO/SiO2	(CaO+MgO)/SiO2	P2O5 [%]	Al2O3 [%]	TiO2 [%]	MnO [%]
64.72	2.17	0.91	1.47	2.49	0.37	0.96	0.06	0.44	0.19	0.1

After correlating the respective chemical figures with each sample's KPIs for BRASS 1, the most sensitive key performance indicators for pellets were found to be:

- O/Fe before Res. zone (O/Fe)
- Average O/Fe in the reserve zone

, while for sinters the most influential indicators were;

- Upper shaft Max d[O/Fe]/dt
- Final O/Fe

In addition, the results of BRASS 1 and BRASS 2 were combined to see their coinciding results. According to the cumulative outcome, for pellets "average O/Fe in the reserve zone" and "O/Fe before Res. zone" are the most sensitive performance indicators, while for sinters "Time reaching reserve zone" and "average O/Fe in the reserve zone" present a better association with compositional changes.

3.2. Relevance to the current project

The statistical analysis of the historical tests performed in the BRASS test has helped to determine the scope of the current project. Based on the BRASS test, sinters of various composition demonstrate different O/Fe values and kinetics under identical condition profiles.

The BRASS curves of each sinter sample are a result of sinter's physical properties that differ between samples; that is mineralogy, microstructure and meso-structure. Which mineralogical phases are present, at which proportions and how they are intergrown comprise sinter features, as relevant to the micro-scale. Sinter features on the > 1 mm length-scale such as larger cracks and porosity, the sinter fragment size and shape distribution, specific surface area of the sinter fragments set sinter meso-scale properties. All these characteristics coincide to have an effect on sinter reducibility and underlie the observed variation seen in the behaviour of sinter samples.

From the analysis, it is indicated that, for sinters, one of the most sensitive performance indicators is the time a sinter material takes to reach the reserve zone. This aided to define the conditions of interest for the project. Hence, the current research aims to understand why there is a difference in the kinetics of the reduction reactions of sinters of different composition, when the latter tend to reach the reserve zone, and how much different starting chemistry influences this important performance factor.

In accordance, the project focuses on the processes that take place in the BF direct reduction zone, starting from the upper shaft down to the reserve zone. Apart from terms of thermodynamics, reduction is studied also based on metallurgical kinetics when varying the initial material composition, under specific gas atmosphere conditions, in order to determine reaction starting and finishing points when direct reduction begins and reserve zone is reached, as well as the timeline in between.

The experimental work of this study is based on this range, while it uses the same static conditions at the beginning and endpoint of the specified direct reduction zone in the BRASS test. This means that experiments subtract specific conditions equivalent to certain points at the BRASS test and reproduce them. This range was specifically defined based on the resulting graphs where the performance of all the sinters is displayed. The graph that shows the reduction rate of all the sinters, plotted with temperature indicates that the range of temperatures of 750^{o}C and 950^{o}C is best for studying performance in the upper shaft zone conditions. This is because most reduction reactions start to happen at 750^{o}C, while at 950^{o}C most reactions start to reach the reserve zone. A more thorough description of the conditions and their relation to the BRASS test is given in the following section.

4. Research methodology and experimental setup

To achieve the research scope and to verify the impact of microstructure and mineralogy on sinter primary reduction, it is essential to build a methodology focusing on isolating the microstructural effects of controlled sinter samples and to set the conditions for their relative reduction. The next section presents the origin and characteristics of the materials used for the experiments, followed by an argumentation for the conditions used. The following parts demonstrate the set of experiments and activities that were performed in order to cover the reduction of the sinter samples in terms of kinetics and thermodynamics, as well as the methods used for interpretation and visual capture of phase transitions. Finally, the scheme of the entire research methodology is presented, along with a correlation of each activity to a research question.

4.1. Starting materials

4.1.1. Chemical composition and mineralogy of starting materials

Six sinters with strongly different bulk mineralogical and chemical composition (basicity and Fe^{2+}/ [Fe^{3+} +Fe^{2+}] were used as starting materials. Five of them were produced in a pilot pot for the purposes of a previous research project conducted in the Ceramic Research Centre at Tata Steel, Ijmuiden, along with a wider bunch of sinter samples (Small, et al., 2017). This group of sinters is characterized by the same composition with only two parameters strictly variating, being the lime excess ratio and FeO (%) content, while the rest of raw chemical inputs remained constant.

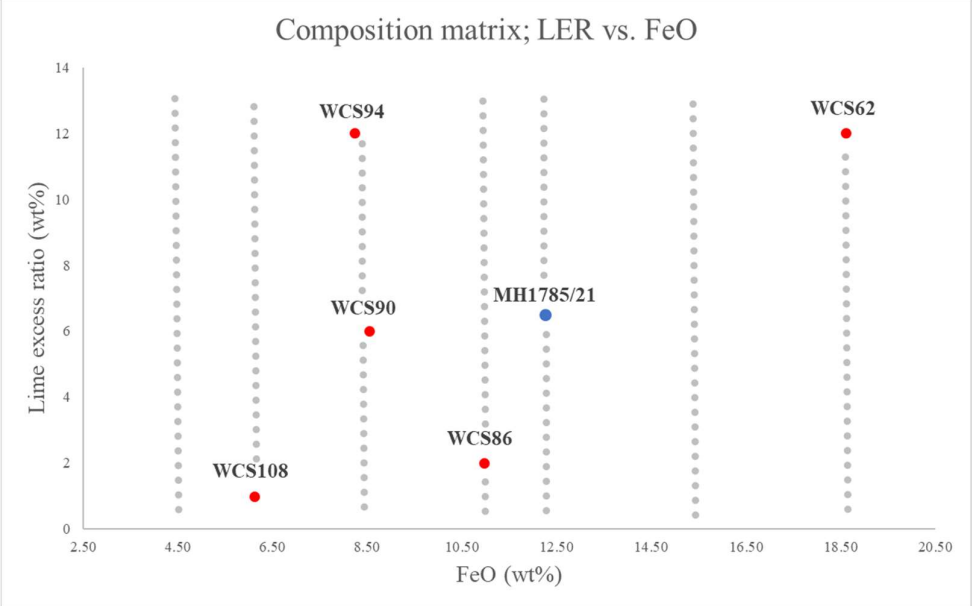

Figure 14. Composition matrix of the six sinters studied, with varying FeO (%) and nominal LER (lime excess ratio) (%) contents.

Lime excess ratio is linearly linked to the addition of lime flux and correlates to the basicity of the samples. The samples selected for this study are the pilot-scale WCS108, WCS86, WCS90, WCS94 WCS62 and an industrial sinter (MH1785/21). The composition of the 5 pot samples is controlled, and each sample is characterized by a different pair of FeO and lime excess ratio, as shown in Figure 14.

The sample WCS108 plots at the low left corner of the graph and corresponds to an extreme composition of low lime excess ratio and low FeO, while its opposite, WCS62, is a sample with high values in both two composition parameters. The rest of the samples demonstrate moderate FeO, and variating LER (lime excess ratio) content from low, to moderate and higher values. This context was selected with the aim to examine the effect of different basicity in samples with similar FeO input, as well as the FeO variation impact at similar basicity levels. The FeO content also shows some variation between the middle samples, as WCS86 and MH1785/21 demonstrate greater amounts than WCS90 and WCS94. The industrial sinter MH1785/21 has moderate lime excess ratio, similar to WCS90, but it much more enriched in FeO, more even than WCS86.

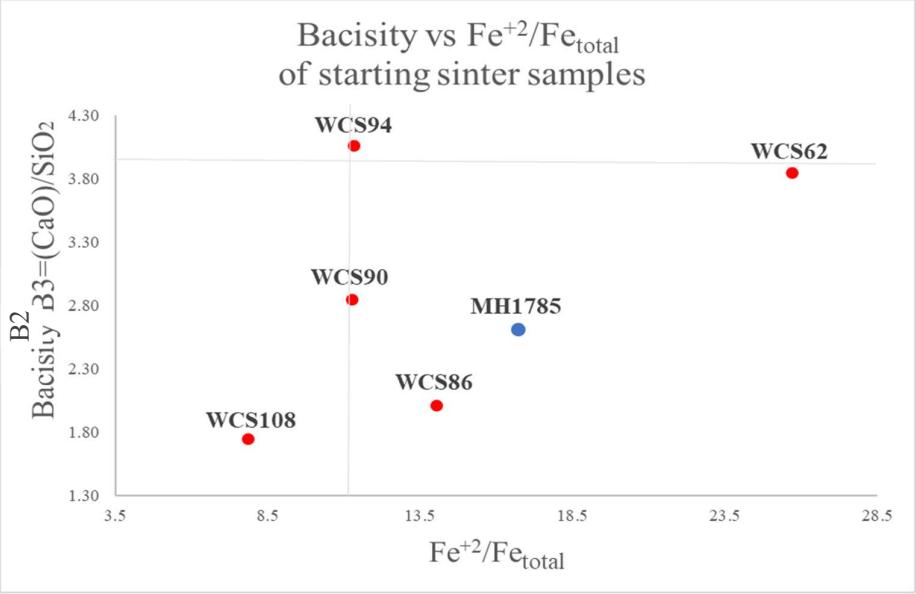

Figure 15. Varying chemical factors of sinter samples; Basicity vs. FeO

Figure 15 displays the actual basicity of the samples as a function of CaO/SiO2 versus their Fe+2/Fetotal ratios. Again, sample WCS86 and MH1785 are shown to be richer in Fe+2 than the rest of middle samples, being WCS90 and WCS94. A higher Fe+2/ Fetotal ratio corresponds to more reduced samples due to a more reduced FeOx component after sintering. The industrial sinter's basicity is slightly lower than the respective WCS90 basicity, in contrast to their LER contents which are in reverse order. Table 5 shows the normalised bulk chemical analysis of all sinter samples.

Table 5. Chemical analyses of starting sinter materials.

Bulk chemistry START		WCS108	WCS86	WCS90	WCS94	WCS62	MH1785
Fe	%	0.30	0.30	0.30	0.30	0.30	0.30
FeO	%	6.12	10.96	8.53	8.23	18.60	12.25
MgO	%	1.28	1.27	1.21	1.18	1.23	1.42
Al2O3	%	1.73	1.65	1.55	1.51	1.65	1.11
SiO2	%	3.54	3.48	3.36	3.26	3.68	4.48
P2O5	%	0.07	0.07	0.07	0.06	0.06	0.04
CaO	%	6.19	7.00	9.58	13.25	14.17	11.80
TiO2	%	0.17	0.16	0.16	0.15	0.15	0.11
MnO	%	0.36	0.35	0.38	0.31	0.34	0.19
Zn	%	0.02	0.01	0.01	0.01	0.01	0.02
V	%	0.02	0.02	0.02	0.02	0.02	0.02
Fe2O3	%	80.20	74.73	74.83	71.72	59.80	67.85
Total	%	100	100	100	100	100	100

As far as sinter mineralogy is concerned, there are specific patterns identified in the samples. The varying mineralogy of the samples is presented in Figure 16. Each sinter is characterized by certain dominant phases in the phase assemblage. All the samples with low basicity, including WCS108 and WCS86 present high content in iron oxides and less content in SFCA and Ca-ferrite phases. More specifically, WCS108 which is a low excess ratio - low basicity sample presents a high Hematite content, while WCS86 has the highest Magnetite contents amongst all samples.

The middle samples WCS86, MH1785, WCS90 and WCS94 show mineralogical variations due to their varying basicity content, corresponding to different amounts of iron oxides, SFCA and CF phases. The moderate bacisity -moderate FeO sample WCS90 demonstratess the highest Hematite and SFCA amount amongst the four samples. MH1785 and WCS94 have similar amounts of Hematite, but differ in Magnetite contents since MH1785 is richer in the mineral. On the other hand, WCS94 is more enriched in calcium ferrites and SFCA. The C_xF_x phases are considered beneficial for an advanced blast furnace operation. They consist strong binders for sinter material, while also being highly reducible with high low temperature degradation (Webster, et al., 2012).

The phases Larnite (C2S=Ca_2SiO_4) and Wüstite 1 also increase with higher basicity. WCS62 has low Hematite and the greatest contents in Magnetite/Ca-Magnetite and Wüstite1. Finally, WCS62, which is an extreme high LER – high coke breeze sample, is characterized by increased content in Wüstite and calcium ferrites. The presence of Wüstite is also high in WCS90 (2,12%), but still less than WCS62. The difference in Wüstite content is attributed to the reduction state of the samples. The higher Fe^{+2}/Fe^{+3} ratio in WCS62 indicates that its reduction state is already more reduced in composition than some of the other sinters before any reduction treatment in the experiments

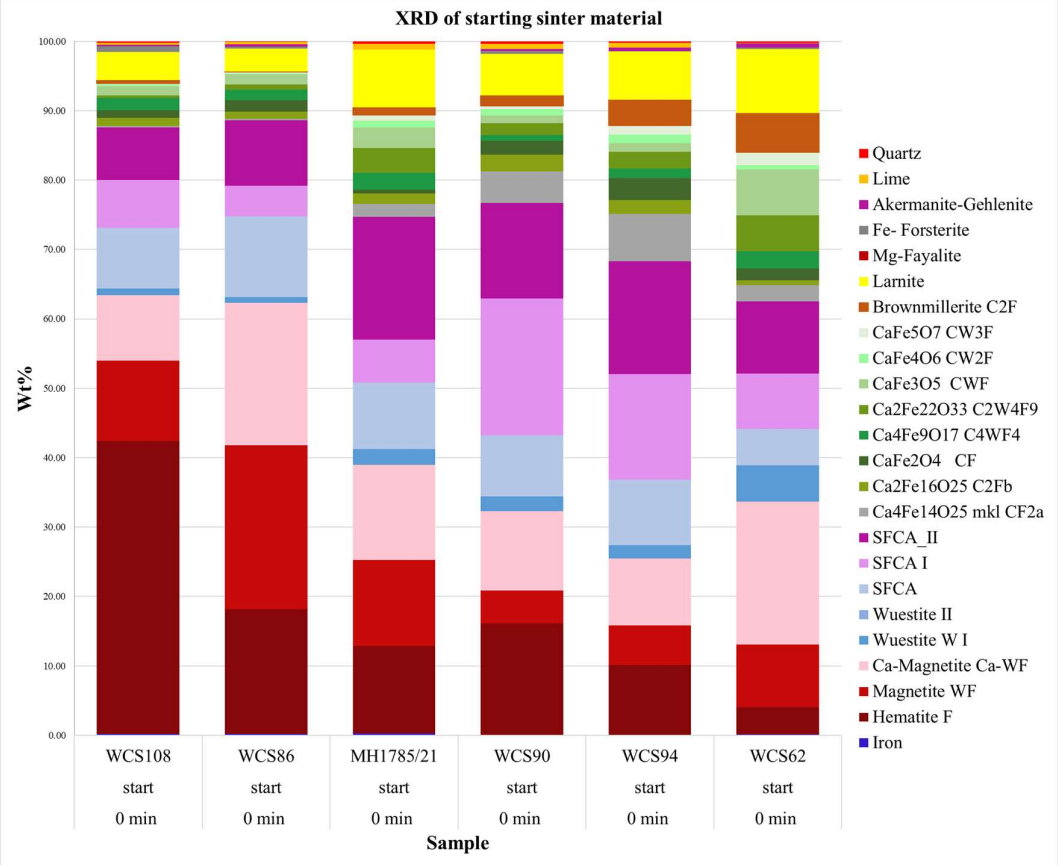

Figure 16. Mineralogy of starting sinter material.

Some of the pilot-pot sinters, including duplicate batches of the ones used in this study were tested in the BRASS test (Xiao, 2018). Their performance in the test is shown in two graphs, plotting O/Fe and d[O/Fe]/dt with time. It is observed that these sinters behave differently to industrial sinters (MH samples). They appear to be more reducible on the whole, as shown in Figure 17. They start reaching the reserve zone quicker than the MH samples, while demonstrating higher reduction rates. Aspired from this performance difference, apart from these 5 pilot-pot sinter samples, the additional production sinter was considered in the current study. This sinter was taken directly from production and it was selected based on its chemical composition, as it is broadly similar to the one of WCS90. This way a comparison could be made between the 2 samples, by limiting compositional effects in order to see whether microstructure and mineralogy are factors that contribute to the different reduction behavior of the sinters.

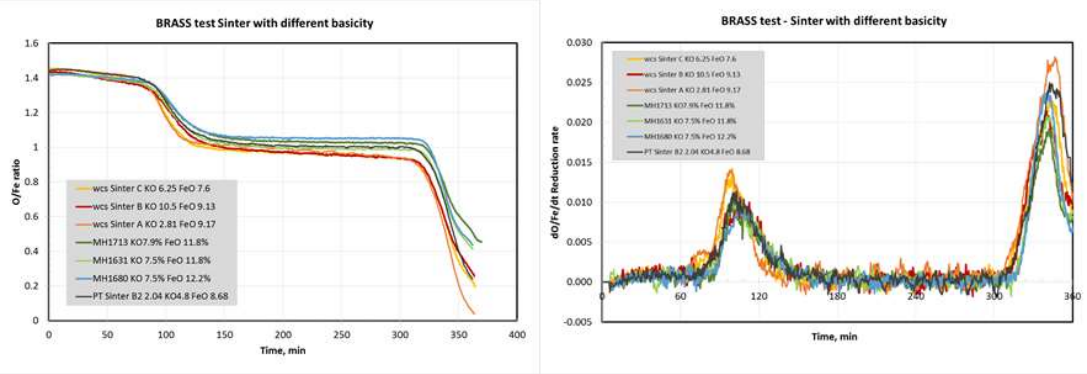

Figure 17. Performance of WCS (controlled sinter) and MH (production sinter) samples (Xiao, 2018).

4.1.2. Size and specific surface are of starting materials

In order to study the effect of mineralogy and microstructure on sinter reducibility, all the effects of meso-structure should be excluded. For that purpose, the samples were sized down to fractions of 250-500μm, being a grain range adequately fine to isolate microstructural effects, while excluding the impact of macro-porosity and mechanical fractures (Krajňák, et al., 2014; Janeček, et al., 2014). In addition, this size range still remains coarse enough to preserve sinter microstructure, and allow the observation of mineralogical phases.

The WCS samples were already grounded down at the CRC and were taken at size for this study (Buytendijk, 2019). The industrial sample had to be milled down from its initial size, as taken from production. The rest of the samples had a starting size of 10 to 15mm. The jaw crusher was used to coarsely break them down to the size of 2-8mm. All WCS samples and the MH sample were repeatedly grounded down in a tungsten carbide mill, until no coarse material was left during sieving. Only the material within the 250-500μm was collected from the sieves. The resulting material was then tested for its size distribution and micro-porosity, in order to verify the scale of the effect of these two physical characteristics on sinter reduction behaviour during the experiments. For that cause, size distribution and BET measurements were performed.

The particle size distribution of all the samples was measured using a particle fitting model, where all the particles are assumed to be dense spherical bodies. A Malvern Mastersizer instrument was used to characterize the starting materials based on their agglomarates behavior, along with a particle fitting model abinding to the principle of laser diffraction. The sample particles are energized using ultrasonic energy, which is increased gradually as the particles complete route cycles in the equipment. During this route, particles pass through a zone where lazer is introduced and scattered once it hits a grain. The signal of the scatter diffraction is then captured by the obscuration detector, so that it can be processed. The processing includes translating the real particle shape using a fitted methematical model.This calculated model

measures the specific surface area assuming that all particles are dense spherical spheres with no open porosity.

The specific surface areas and median diameters of all the samples are given in Table 6. Based on the assumption that all the particles are dense spherical balls, the specific surface areas of the sample shows limited variation, being nearly 15% between the most different samples. The diameters of generally more than half of the model spherical particles in the modelled distribution are greater than the nominal 500-micron sieve size that was intended for screening the material. This small size deviation is attributed to the presence of elongated particles in the sieved samples, which eventually fall through the sieve parallel to their long axis. Hence, their maximum dimension can be larger than the sieve dimension used. When the particles get modelled as spherical bodies in the distributions shown, then this can give larger particle sizes than those expected. More specifically, the D50 (median) diameter of the particles' ranges from about 444 microns for WCS108 to 537 microns for WCS90. Therefore, the largest D50 (corresponding to WCS90) is about 20% relative larger than the smallest (WCS108).

Table 6. Median diameter of the particles' ranges of each sinter sample

Size distribution results	WCS108	WCS86	MH1785	WCS90	WCS94	WCS62
SSA (m2/g) dense spheres	0.014	0.013	0.013	0.012	0.013	0.012
Diameter (µm): d(0.5)	444	493	501	537	502	514

The size distribution curves of the samples are shown in Figure 18. The calculated model specific surface area (m^2/g) also comes out of the size distribution curves. This is not a true measurement of the specific surface area of the samples, which would include all the surface irregularities and open pores, but rather the equivalent surface area of the modelled spheres in the size distribution. According to the graph, variations between the size distributions of the different samples are not too distinct, and all of them appear to have rather similar sizes. As mentioned, the greatest value corresponds to WCS 108, and it is about 20% relative greater than the lowest value, given by WCS90.

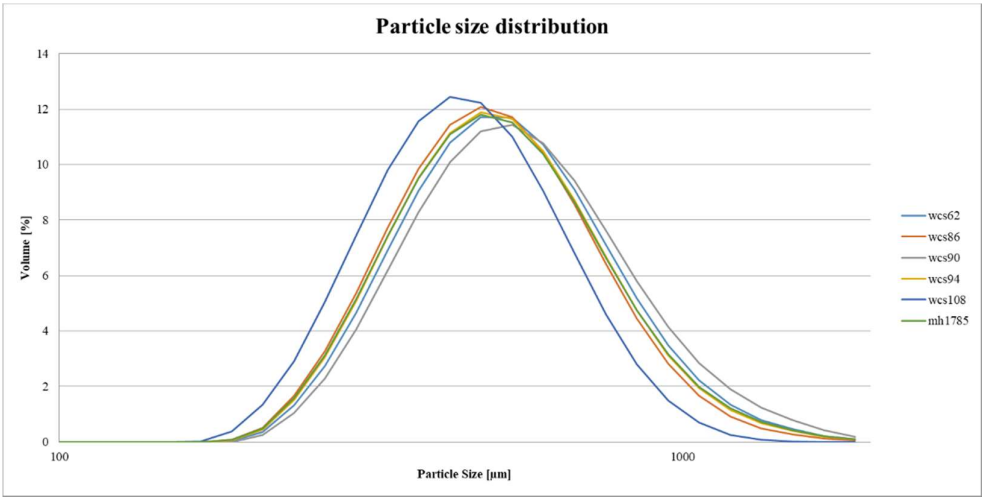

Figure 18. Size distributions of sinter samples

The BET (Brunauer-Emmett-Teller) technique was used to measure the specific surface area of the samples, translating to intraparticle porosity and pore size distribution ((Brunauer, et al., 1938). During this process, the 5 grams of each of the sinter samples are put in small sealed tubes with no gas, no pressure and high vacuum. These tubes are positioned in a bigger container filled with cold liquid nitrogen. Then, a small amount of N_2 gas is introduced in the sample-containing tubes, with a pressure of 150 milibars. The gas forms layers around the sample, and whenever it cofronts some accessive surface area for reaction, it changes its

state to liquid. The open specific surface area corresponds to the reactive area of all porous structures that adsorb the small gas molecules. According to the technique, wet nitrogen is used for the measurements of the sinters in the BET. The boiling point of nitrogen (-196°C) is used in order to measure the volume of the absorbed gas to the surface of the particles. Gas adsorption also enables the determination of size and volume distribution of micropores.

The BET results are presented in Figure 19. The measurement of similar particle size distribution between the samples, ensures that the BET result is not attibuted to differences due to grinding of the materials and their outer surface, rather than in internal microstructure and intra-particle porosity. Based on the result, intraparticle porosity and particle size tends to vary between the different samples. Different internal porosity is important, since it can be a contributing factor on sample reduction behavior. Sinter sample WC108 has the greatest specific surface area (SSA of approximatelly 0.06 m^2/g). WCS94 and WCS90 have quite similar SSA approaching 0.04 m^2/g, WCS62 has a lower SSA=0.028 m^2/g, followed by the industrial sinter MH1785/21 with SSA=0.025 m^2/g, while WCS86 has the lowest specific surface area of 0.022m^2/g.

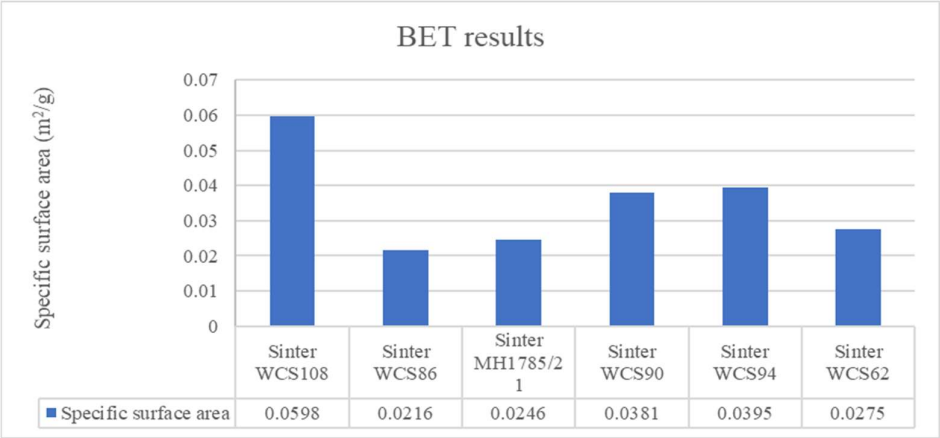

Figure 19. BET measurement on sinter samples; Sample reactive specific area.

4.2. Reducing conditions

In order to research sinter reducibility, the grounded starting materials were exposed to reducing conditions in two types of experiments, which are explained thoroughly in the following subsections. For the realization of these experiments, two important parameters had to be determined, being the temperature and the gas atmosphere. These were established based on the BRASS test, as they consist abstractions from it.

The complete BRASS test gives different curves when plotted with temperature, time and reduction degree. The curves correspond to sinter behavior under the everchanging conditions in the test, as the temperature rises and the gas composition changes. In order to isolate and study the reduction mechanisms, specific conditions equivalent to certain points at the BRASS test were reproduced during experiments. The points of conditions selected for this study are shown in Figure 20. The graph shows the reduction rate of all the sinters, that were analyzed in the historical BRASS test analysis, plotted with temperature. The sinters are divided in two clusters marked with different color based on reducibility. The two points of conditions used in the experiments were selected from this curve, and they correspond to temperatures of 750oC and 950oC. Isothermal experiments at these temperatures were considered, because they are well positioned within the range limits of primary reduction zone. More specifically, at 750oC most reduction reactions start to happen, while at 950oC most reactions reach the reserve zone and slow down. The present focus is on the 'first pulse' of reduction, because it reduces the sinter material from its initial composition towards a mineralogy dominated by Wüstite, i.e. the reserve zone, where net reduction degree stagnates close to the Fe-Wüstite boundary. Hence, it would be instructive to examine which mineralogical phases form in the sinters under

these conditions, as well as to establish the reduction degree and relative reduction rate of the samples.

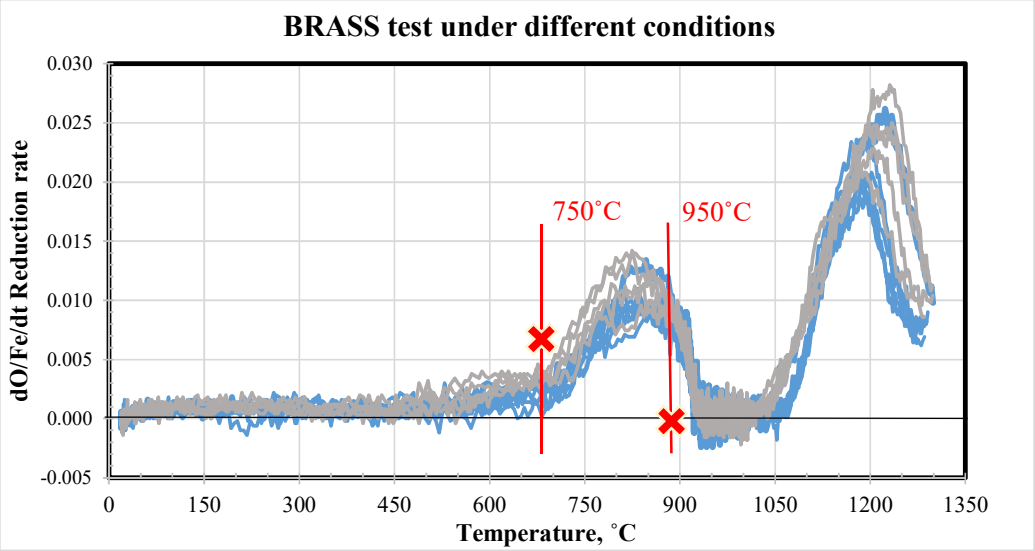

Figure 20. The condition points selected for the performance of experiments. These are subtractions from the resulting graph of all the sinter BRASS tests performed the past 10 years at MLY, Tata Steel Ijmuiden.

As far as the gas regime of the experiments is concerned, the relative kinetics of the different starting materials were studied under a CO-CO_2-N_2 gas atmosphere. The initial intention was to try and reproduce the exact atmosphere conditions of the BRASS metallurgical test, corresponding to an atmosphere of CO-CO_2-H_2-H_2O-N_2. However, this case was considered problematic due to condensation issues in the lower part of the tube of the furnaces related to the usage of hydrogen. The available equipment used for the following experiments is not equipped with a heating system that resolves this problem, unlike the BRASS test furnaces.

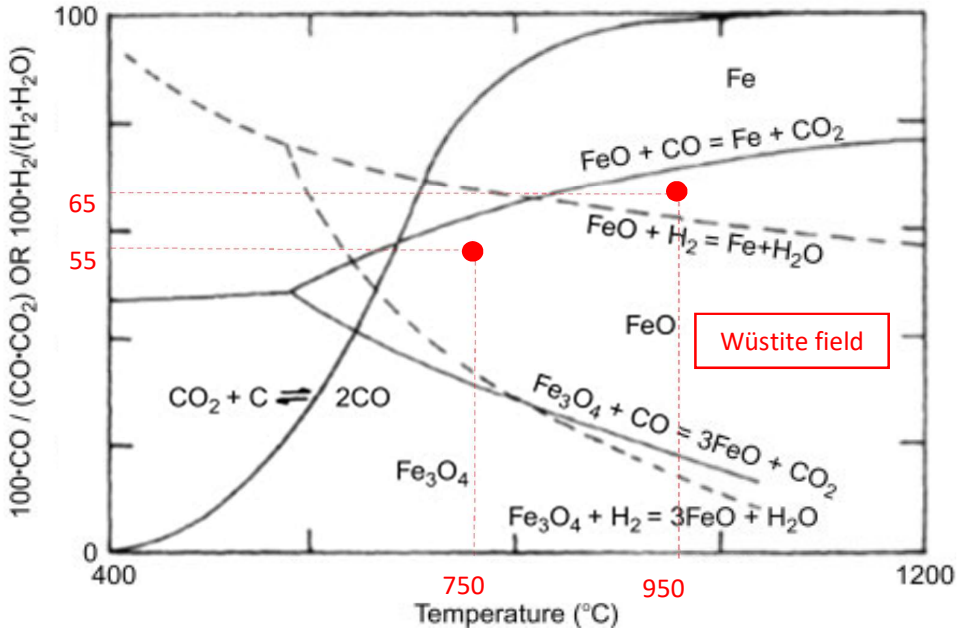

Figure 21. Equilibrium diagram of iron oxide reduction with CO and H2; Set of experimental conditions: XCO=55, T=750ºC / XCO=0.65, T=950ºC. (Modified by (Biswas, 1981)).

Therefore, CO-CO_2 atmosphere diluted with N2 was used, as it is still a more realistic condition than the ones used in most metallurgical tests, since the latter do not precisely follow the exact reaction routes and stability fields. In accordance, the CO-CO_2-N_2 was used in order to ensure a well-controlled and verified gas composition, corresponding accurately to the gas amounts which are intended. Based on the equilibrium diagram of iron oxide reduction with CO and H2 diagram shown in Figure 21, in order to place the conditions well within the Wüstite stability field at the two specified temperatures of 750°C and 950°C, atmospheres with XCO=0.55 and XCO=0.65 are used, respectively. The $CO/[CO+CO_2]$ = 0.65 is considered useful since it is securely within the Wüstite + C_2(A,F) field but relatively close to the boundary with Wüstite-metal transition.

4.3. Experiments

4.3.1. Thermo-Gravimetric Analysis (TGA)

The Thermo-Grevimetric analysis (TGA) was used in order to study the reduction kinetics of the sieved pilot scale sinters. The TGA is an analytical technique that gradually heats up a sample at a constant rate in order to establish its thermal stability and the percentage of volatile components by monitoring weight change (Rajisha, et al., 2011). The current experiments were performed on a Seteram Setys Evolution 1700 TGA-7^{TM}, which measures mass loss in wt%, due to the reduction of the samples during heating. The difference in weight is considered to occur due to the subtraction of oxygen during reduction, assumed to be solely sourced from iron oxides.

As mentioned above, two sets of conditions were applied. The first one was at a higher temperature with T = 950°C, and a gas atmosphere of 32.5 % CO, 17.5% CO_2 and 50% dilution (N_2 or He) corresponding to a gas atmosphere of $XCO=CO/[CO+CO_2]$ = 0.65, and the second at a lower temperature T = 750°C with $XCO=CO/[CO+CO_2]$ = 0.55 and a 50% dilution (N_2 or He). These conditions with a diluted CO-CO_2 gas mixture are placed inside the Wüstite stability field, comfortably underneath the metal-Wüstite transition, which would help identify the kinetics of reduction towards Wüstite stability.

In accordance, a small amount of loosely spaced material was put into the TGA crucible and was heated up under He (inert gas) to the isothermal dwell temperature for the reduction treatment. The reducing gas atmosphere of CO-CO_2-N_2 was then switched on and the mass change with time at constant temperature was monitored until a plateau was reached in reaction progress.

The two extreme samples were both tested at 750°C and 950°C. However, it was shown that at 950°C the reaction progressed too quickly, thus the results delivered were not very instructive, and the rest of the samples were only tested for 750°C. Another reason for doing experiments at 750°C was that the effect of gradually increasing driving force as the gas approaches its target composition on the total reaction progress. This was more significant on the TGA curves taken for 950°C, while 750°C may give liable results, since the lower temperature would slow down the overall kinetics. An overview of the samples tested and the respective experimental conditions in the TGA is given in Table 7.

Table 7. Series of experiments with the TGA.

TGA			
Sample	Temperature (°C)	Gas Atm. (%)	Time (hours)
WCS108	950°C	XCO=0.65	1
	750°C	XCO=0.55	1
WCS62	950°C	XCO=0.65	1
	750°C	XCO=0.55	1
WCS86	750°C	XCO=0.55	1
WCS90	750°C	XCO=0.55	1

An alternative experiment would be to keep one constant gas composition and heat the sample under that specific gas mixture. The problem with this case was that the reactions would follow a straight line through the phase diagram, deviating from the real BF profile or BRASS profile not only quantitatively, but also qualitatively (in terms of which stability fields are passed through). Therefore, it was excluded due to the difficulty of relating the outcome to the BRASS test results, which is the study's base-case.

4.3.2. GERO (vertical gas mixing tube furnace) experiments

Reduction experiments were also performed using a CarboliteTM GERO Hogh tempera tureturofen GmbH & Co furnace. This a vertical gas mixing corundum tube furnace which heats up the samples at a specified temperature triggering heated reduction. The samples are weighed in a crucible before and after experiments in order to monitor weight loss due to oxygen subtraction. In addition, the end products, being the reduced samples, are kept for further analysis of microstructure and mineralogy. A scheme of the GERO furnace equipment is presented in Figure 22.

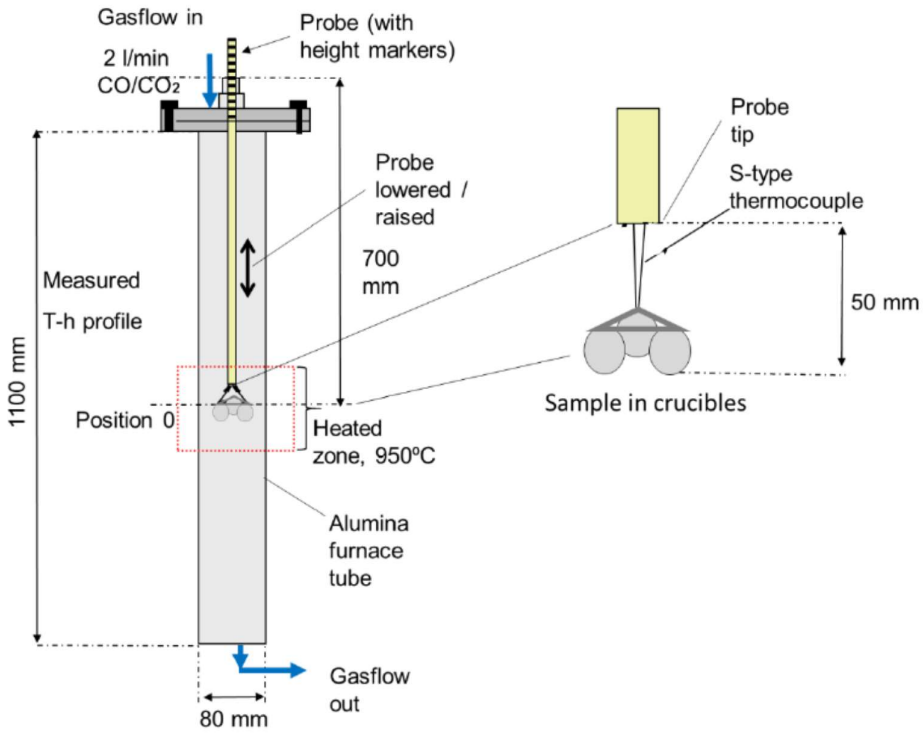

Figure 22. Schematic overview of the GERO (Carbolite^{TM} GERO Hogh tempera tureturofen GmbH & Co) furnace, displaying the setup of the GERO experiments (Buytendijk, 2019).

For the current research, 0.5 grams of powdered sinters (250-500µm) were put into small ceramic crucibles, as shown in Figure 23. This limited quantity was selected due to focus on reaction kinetics. A greater quantity of material would cause a bed-scale effect, meaning that the packing of grains and bed dimensions would have an influence on the overall sample reaction progress. For studying the kinetics, it is aimed to maximise gas access to the individual particles and exclude other effects, therefore a small portion of material was selected to form a slice of grains at the bottom of the crucibles.

Figure 23. The three ceramic crucibles containing the sinter material (top= 2 cm, bottom = 1cm, height= 3.5cm).

The three ceramic crucibles, containing the 0.5 grams of fine sinter material were hanged from a thermocouple probe via platina wires, before the probe was positioned into the GERO furnace tube. The GERO furnace would already be at constant temperature when flashed with Ar for 15 minutes. Then, the crucibles would be introduced to the heated zone, where the temperature corresponds to the specified experiment temperature (950ºC or 750ºC regarding the experiment) and the reducing gas would be applied. After reduction at the time duration of interest the crucibles containing the samples were rapidly pulled up at 50cm and cooled down, as the temperature at the top of the furnace would be much lower (200ºC) than the one in the heated zone.

Different time-series experiments were performed in the GERO furnace likewise, with varying dwell times under reducing gas atmosphere and stable temperature prior to rapid cooling. The dwell times in the experiments were based on the TGA results, which indicated the reduction progress at different time intervals (Figure 24). Therefore, some pre-chosen times were selected to fill in a range of the reaction progress. However, it is important to emphasise that the measured reduction behaviour in the GERO experiments differs from the TGA experiments, and they are not literally interrupted experiments at the same reduction progress as in the TGA, due to differences in diffusion and airflows between the two.

Post-experimental measurements were taken for determining overall reduction degree by compering mass difference before and after the GERO experiment, mineralogical phase proportions and microstructure.

Based on residence time, two types of experiments were performed overall;

- Isothermal experiments with long residence time at T=950ºC and T=750ºC. The long rounds at 950ºC were kept in the furnace for 5 hours, while the prolonged 750ºC experiments, where reactions progress much slower and equilibrium requires more time, had a residence time of 4.5 days. These were conducted in order to determine the reaction starting and finishing points, as well as the initial and final reduction degree and phase equilibrium.

- Shorter experiments in a time-series in order to focus on reduction kinetics. According to the TGA results, at T=950ºC and XCO=0.65 the reaction escalates rapidly, hence the residence times selected for the samples were t=2min and t=4min. On the other hand, samples reduced at 750ºC were cooled down after t=5min and t=20min residence time into the GERO furnace. These times enabled comparison of the reduction rates of different sinters along the way of reaching the reaction equilibrium (/plateau). With interrupted experiments and rapid cooling of the samples at different times, it was also meant to capture changes in the proportions of mineralogical phases as the reduction progresses, but also generate samples that capture frozen reduction

fronts as those are passing through the individual sinter particles. This would make it possible to capture unreacted cores of the initial microstructure before reduction, along with the reduced front within only one particle and avoid having to do educated guess-work to relate fully-reduced particles with initial microstructures.

The time-series experiments resemble specific progress points on the reduction reaction curve, which correspond to a certain reduction degree, mineralogy and microstructure at the ever-specified time. The long experiments were performed with the aim to show the "end-destination" of the reaction. Schematic examples for each of the reduction curves at 750ºC and 950ºC are shown in Figure 24.

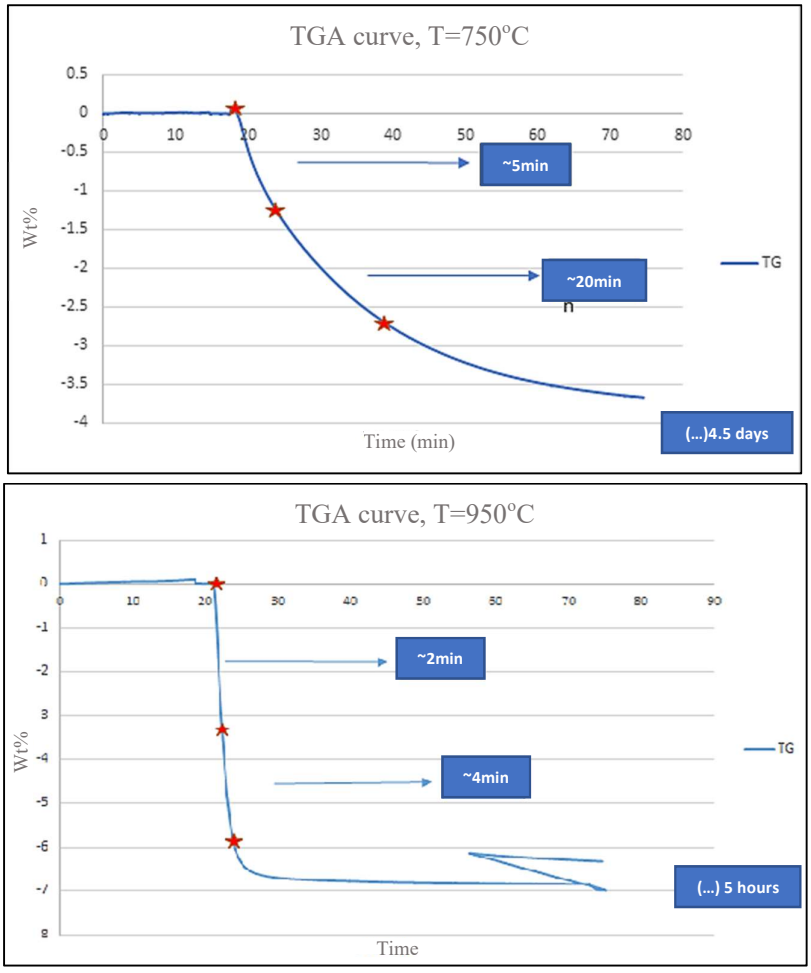

Figure 24. Reduction curves at 750ºC and 950ºC from TGA. The dwell times in the GERO experiments were based on these TGA results, in order to capture reduction progress at different times.

An overview of the samples tested and the respective experimental conditions in the GERO is given at the following table (Table 8).

Table 8. Experiment series in the GERO furnace.

	GERO		
Sample	Temperature (ºC)	Gas Atm. (%)	Time
WCS108	950ºC	XCO=0.65	2 min
	950ºC	XCO=0.65	4 min

	950°C	XCO=0.65	5 hours
	750°C	XCO=0.55	5 min
	750°C	XCO=0.55	20 min
	750°C	XCO=0.55	4.5 days
WCS62	950°C	XCO=0.65	2 min
	950°C	XCO=0.65	4 min
	950°C	XCO=0.65	5 hours
	750°C	XCO=0.55	5 min
	750°C	XCO=0.55	20 min
	750°C	XCO=0.55	4.5 days
WCS86	950°C	XCO=0.65	2 min
	950°C	XCO=0.65	4 min
	950°C	XCO=0.65	5 hours
	750°C	XCO=0.55	5 min
	750°C	XCO=0.55	20 min
	750°C	XCO=0.55	4.5 days
WCS90	950°C	XCO=0.65	2 min
	950°C	XCO=0.65	4 min
	950°C	XCO=0.65	5 hours
	750°C	XCO=0.55	5 min
	750°C	XCO=0.55	20 min
	750°C	XCO=0.55	4.5 days
WCS94	950°C	XCO=0.65	2 min
	950°C	XCO=0.65	4 min
	950°C	XCO=0.65	5 hours
	750°C	XCO=0.55	5 min
	750°C	XCO=0.55	20 min
	750°C	XCO=0.55	4.5 days
MH1785/21	950°C	XCO=0.65	2 min
	950°C	XCO=0.65	4 min
	950°C	XCO=0.65	5 hours
	750°C	XCO=0.55	5 min
	750°C	XCO=0.55	20 min
	750°C	XCO=0.55	4.5 days

4.3.2.1. The GERO calibration

In order to control and verify that the temperature and gas composition in the GERO furnace corresponds accurately with what is intended, additional calibrating experiments took place before the ones mentioned above.

The temperature was verified by placing a gold wire between the platina wires of the thermocouple probe, and then introducing it into the furnace. The temperature of the furnace was gradually increased until it was equal to 1.064°C in the heated zone, which is the melting temperature of gold. If the gold decomposed at this temperature, this would mean that the thermocouple displays the right indication, which was indeed the case in the test.

For control of the gas atmosphere in the GERO furnace, the mass-flow-controllers were calibrated for all gas species (CO, CO_2, N_2) and experiments were performed to verify the furnace gas composition with respect to the reference transition: Fe – Wüstite. The idea was to establish where the Fe-Wüstite transition is at the specified temperatures in terms of target gas composition in the GERO. Since, it a very well-known reaction line, it could be easily used as a reference. In accordance, a metallic Fe-wire was suspended in the furnace at equilibrium with a CO-CO_2 gas mixture at 950°C. As the gas mixture was meant to be within the Fe-metal

stability, the gas composition of XCO=0.8 ($CO/[CO+CO_2]$ = 0.8) was selected as a starting point. Then, this composition was modified in small steps towards the expected composition of the Fe-Wüstite transition, which should be at XCO = 0.71 according to thermodynamic calculations performed at FactSage software. In principle it should be possible to detect the first oxidation of the metal wire by the change in electrical resistance. In case deviation was shown between the Fe-Wüstite transition and the expected gas composition when using CO-CO_2-N_2 gas atmosphere, then this would imply an issue with the mass-flow-controller calibration. If the transition was as expected, then the actual experiments could proceed. Also, as an alternative, a pure Fe powder was used to perform experiments at the expected Fe-Wüstite boundary to check whether they give compatible results with what's expected. Finally, it was verified that the gas composition in the blast furnace is rather accurate and results given can be considered valid.

4.4. Analytical Techniques

The initial and reduced sinter samples, which resulted from the GERO furnace experiments, were further analyzed by using analytical techniques such XRD analysis and microscopy.

4.4.1. XRD analysis – Rietveld quantifying analysis for phase identification

The XRD analysis was conducted by powder diffraction analysis and Rietvield refinement in order to identify all the phases present in each sample and their relative proportions. The preparation for this quantitative analysis of the sinter products included grinding a small portion of reduced material using a mortar into powder and then placing the material on a specific zero-background XRD holder, where the powder is grounded with ethanol drops. Then, the XRD dish is transferred into the XRD bucket, in order to take the measurement. Phase proportions are determined by XRD and subsequent Rietveld analysis. The XRD patterns are recorded in the range of 8 to 100 ° (2 Q) in reflection mode using a fully automated Bruker D8 Endeavour (CuKa-radiation) equipped with a position sensitive detector (Lynxeye XE-T. The step size was 0.02 °, time per step is 144 s (total measurement time 60 min). Quantitative determination of phase proportions is also performed by Rietveld analysis. The refinement was done on the assumption of pure phases. Unit cell parameters, background coefficients, preferred orientations, profile parameters and phase proportions were refined using the TOPAS software package for Rietveld refinement.

Most specifically, an internal template was used for the analysis of the sinter materials. This template was developed in TATA Steel Europe based on previous knowledge on any sinter material produced. This prototype was then manually adjusted to the current starting materials used for this study, resulting to a new, more targeted template. Hence, this new template was used to perform automatic fittings to the reduced sinter samples generated after the time-series experiments in the GERO furnace. The only limitation of this method is that, after long-time reduction experiments, there are certain minerals present in the XRD assemblage which have been consumed in reality. This means that, except for Wüstite, Larnite, Brownmillerite and Melilite, the presence of the rest of the minerals corresponds to XRD fitting artefacts. This discrepancy is attributed to the excessive amount of Wüstite observed by the XRD, which ends up also being fitted in other phases outside Wüstite.

4.4.2. Optical Microscopy -Analysis of microstructure

The reduced sinter materials were analysed under a polarized light microscope. The preparation of material for the microscopical analysis included grounding grains of material in an epoxy resin (Struers EpoFix), which was then polished to form cross sections and expose sample particles. A silicon carbide paper with water as a lubricate was used for polishing to a thickness of 1000 grit, and then a diamond paste was applied for further section thinning, starting from 0.3 micron down to 0.1-micron grit. The optical microscope that was used for the reflected light analysis was an automated ZEISS^{TM} Axiomager Z1 microscope coupled with an integrated AxioVision 4.9^{TM} software. The analysis aimed to capture unreacted cores of sinter

material zoned by reduced fronts, where microstructural transformations could be identified within one particle. 110 Images and 36 mosaics of the respective microscopic structures were obtained using a magnification of 50 to 20x.

4.4.3. Scanning Electron Microscopy – Phase identification

Scanning Electron Microscopy (SEM) was also used for the analysis of the embedded grains. The sample sections were carbon coated and they were introduced into the SEM for phase identification. The SEM used is a Field Emission Scanning Electron microscope JEOL JSM-7001F SEM equipped with two 30 mm2 Thermo Fischer Scientific EDS (energy dispersive spectrometry) detectors and NORAN-System7 hardware with NSS.3.3. Software from Thermo Fisher Scientific™. Backscatter and secondary electron imaging was obtained by using a 13nA probe current detector. Finally, counting live times of 10 to 15s was used in order to guarantee analytical precisions, the working distance (WD) was 11.5 mm and the accelerating voltage used for manual analysis was 10 kV.

4.5. Thermodynamic modelling

Thermodynamic modelling was performed using the FactSage software, by the Thermfact™ and GTT-Technologies™ (Bale, et al., 2016). This was used in order to demonstrate which stability fields to expect when reducing a certain sinter composition (expected equilibrium state), as well as to conduct equilibrium calculations. The results would be directly compared to the outcomes of the TGA and GERO furnace experiments. The equilibrium calculations were enabled due the FactSage databases of FactPS, CON_2 and NSTE, which can be found in the Equilib module of the program. The FactPS database is a public one, while the remaining two require a private access, only given to members of the Steelmaking Consortium group, since they are established by the High Temperature Thermochemistry Laboratory at the McGill University, Montreal, Canada. In the thermodynamic modelling for the current study a new version of FactSage was used, including a newly introduced database that considers real sinter composition, taking into account SFCAs, and Ca-ferrites (CWF, CW_3F can be stable to the exclusion of Wüstite at lower temperature).

The reacting components used in the calculations correspond to Fe_2O_3, FeO, MgO, Al_2O_3, SiO_2, CaO, N_2 and CO. These are set regarding to compositions of the starting sinter materials, being the pilot-pot sinters. The composition is normalized to 100 grams in total, and it includes a CO component with varying mass, based on the conditions imposed. Calculations were run for the two sets of conditions correponding to T=750ºC, N2=0.5g and XCO=0.275g or T=950ºC, N2=0.5g and XCO=0.275g. Several trials were conducted by changing the phase selection and suppressing certain phases in the calculations in multiple combinations (mainly breidgite, olivine and C2S polymorphs) in order to establish possible assembanges. The results of each run are exported in both mass and mols. The most realistic FactSage outcomes based on the XRD results are selected in order to make the phase comparison. The resulting phase compositions and their proportions were subtracted from the program as a text file in order to perform mass balance calculations so that the relative mass and bulk redox state of Fe could be determined. This would generate results that can be directly comparable to the results from the GERO and TGA experiments.

4.6. Summary of activities and correlation with research questions

The main research goal is to verify the effect of microstructure and mineralogy on sinter reducibility, and more specifically on the “first pulse” of reduction that occurs at the upper shaft conditions of the blast furnace. This is because sinters of varying composition present different behavior when reducing, and their reduction degree before reaching the reserve zone consists an indication of their performance further in the process, while having economic implications.

The first activity of the current project was to perform a historical BRASS test analysis, which amongst other conclusive results, inspired the conditions used for the following experiments. These had to be also in line with thermodynamic phase diagrams, since it was aimed to place experiments well into the Wüstite stability field, which is reached during primary

reduction. As far as conditions were set, adequate material had to be selected in order to study mineralogy and microstructure. This means that;

1. Sinter material of different controlled composition, and hence, different mineralogy in a control manner so that the latter can be monitored
2. The meso-structural effects would have to be excluded by grinding the materials down to such sizes that only microstructural effects are accountable for reducibility behavior

Hence, controlled sinter materials were collected corresponding to different known compositions, so that mineralogy is regularly varied at first and regularly monitored at latter steps. Also, a production sinter of similar composition with one of the controlled sinters with moderate compositions was obtained, in order to also verify whether these behave the same way under reduction. These were then grounded down to fractions between 250-500μm. Screening the crushed material to 250-500 μm fraction excludes the meso-scale effects such as larger pores, cracks, sinter (fragment) size distribution, shape and specific surface area and exposes exclusively the effect of differences in mineralogy, microstructure and chemical composition on reduction behavior.

Activity	Research goal
1. Base-Case: Brass historical analysis	To determine experiment conditions
2. Selection of sinter materials: Pilot pot sinters	To isolate the effect of varying basicity and coke breeze
2b. Selection of sinter materials: Industrial sinter	To identify the major differences, if any, in sinter microstructure and mineralogy, in comparison to that produced in small sinter pot.
3. Grinding of materials to size fraction 250-500μm	To isolate the effect of microstructure and mineralogy & exclude mesoscale effects
4. Size distribution and BET measurements	To ensure the influence of sizing and micro-porosity
5. TGA- Thermogravimetric analysis	To study relative reduction kinetics if grinded sinter materials
6. GERO furnace reduction experiments	To produce reduced samples at various reduction interruption times for further analysis (XRD, LOM, SEM)
7. Measure mass change before and after every reduction experiment	To obtain reduction degree of sinter materials at certain time intervals
8. XRD analysis	To determine mineralogy and phase proportions at different reduction stages – Quantitative analysis of phases
9. Microscopy – Visualize phase transitions and microstructure	Study of microstructure; To freeze in microstructural transformations in individual sinter particles.
10. Thermodynamic modelling using FactSage software	To compare obtained mineralogy and reduction degree with thermodynamic predictions

Figure 25. Research methodology and goals.

In order to study the effect of the microstructure and mineralogy of these materials on the primary reduction kinetics, TGA experiments were carried out. These would give an indication of the reduction rate, if any, caused by different mineralogy and composition and would give answers regarding which compositions favor the progress of reduction reactions. The reduction degree at different time intervals, under certain conditions of primary reduction is also measured by the GERO experiments. These also provide reduced samples for further analysis, which would cover the thermodynamic part of the study. This means that except for the rate at which the different materials reduce and reach the reserve zone, it is also aimed to see the equilibrium states that these go through, as well as the final phase equilibrium they could reach to, if held under these conditions for prolonged times. Therefore, the reduced samples are taken for XRD analysis in order to determine which phases dominate each sample and at which proportions. Finally, the materials are examined under reflected light optical and

SEM microscopes in order to verify microstructural changes, visualize phase transitions due to reduction and identify different phases.

The results from the experiments are compared with thermodynamic models, which show what phases and reduction degree are theoretically expected at the specified conditions.

A schematic overview of all the activities carried out in the current study is given in Figure 25. Each activity is linked to a certain research goal.

5. Results of reduction experiments and analytical techniques

This chapter presents the research findings resulting from experimental work. The respective analytical tools, functions and methods used for the analysis of the results are also presented and explained, while results are demonstrated in graphs, tables and schematic figures.

5.1. Reduction experiments

5.1.1. TGA & GERO experiments - Calculation of the reduction state of the materials

Both TGA and GERO experiments reduce the sinter materials up to a certain reduction degree according to the run time of each experiment. Both provide results in terms of mass loss due to reduction. More specifically, the TGA provides the real time reduction - weight loss, when the materials are exposed to a certain reducing atmosphere and temperature. The GERO, on the other hand, demonstrates the final reduction degree at the interruption time of the experiment. Therefore, both types of experiments provide the mass loss occurring in the sample due to reduction. It is assumed that this weight loss is caused due to the subtraction of oxygen solely from iron oxides. This is defined as such, since iron oxides are rather unstable components, and in principle they are easier to reduce. Hence, the mass loss results can be expressed as an O/Fe ratio, which shows the percentage of oxygen lost due to reduction in reference to the total iron content.

The O/Fe ratio can be calculated based on the difference between the initial weight of sinter materials and their final masses after reduction. The chemical analysis of the starting materials was already available prior to this study; therefore, the chemical components present in the materials were known. Based on the atomic mass number of elements and/or molar mass of iron components, Fe^{+2} and Fe^{+3} were calculated from the FeO and Fe_2O_3 components of each sinter based on the following formulas;

$$Fe^{2+} = FeO_{wt} \times \frac{Fe_{atomic\ mass}}{FeO_{molar\ mass}} \quad \text{eq.8}$$

$$Fe^{3+} = Fe_2O_{3_{wt}} \times \frac{2 \times Fe_{atomic\ mass}}{Fe_2O_{3_{molar\ mass}}} \quad \text{eq.9}$$

$$O_{2_{FeO}} = FeO_{wt} \times \frac{O_{2\,atomic\ mass}}{FeO_{molar\ mass}} \quad \text{eq.10}$$

$$O_{2_{Fe_2O_3}} = Fe_2O_{3_{wt}} \times \frac{3 \times O_{2\,atomic\ mass}}{Fe_2O_{3_{molar\ mass}}} \quad \text{eq.11}$$

$$Fe_{total} = Fe^{2+} + Fe^{3+} \quad \text{eq.12}$$

$$O_{2_{total}} = O_{2_{FeO}} + O_{2_{Fe_2O_3}} \quad \text{eq.13}$$

$$O_{2_{reduced}} = O_{2\,total} - O_{2mass\ loss} \quad \text{eq.14}$$

$$O/Fe = \frac{O_{2reduced}}{Fe_{total}} \quad \text{eq.15}$$

The total iron content, as well as total oxygen can be obtained from these functions. Given that the apparent weight loss during reduction corresponds to oxygen loss from iron oxides, the new oxygen weight is calculated at any time interval during reduction in the TGA. The mass is then translated to mols, hence the oxygen mols lost during reduction are calculated for each time step. These are then plotted with the total Fe content, which is also expressed in mols ,and provide the O/Fe ration at any time interval of the reduction process. The O/Fe values of each sample during reduction are then plotted with time and the resulting graphs are

presented, demonstrating whether there are significant differences in reduction kinetics to arrive at specified reduction states. Apart from the O/Fe, reduction in the TGA is also expressed as a function of starting oxygen content, a function of weight loss upon complete metallization and a function of weight loss at equilibrium.

For the GERO results, a table with the initial weights from the starting sinter material and the final weights of the partially reduced material from time-series experiments, is formed and the masses from all the samples are plotted on graphs of mass loss relating to conditions (750ºC, XCO=0.55, N_2=0.5 or 950ºC, XCO=0.65, N_2=0.5) and interruption times. The O/Fe ratio is plotted as such, derived with the same calculation process as described above.

The reduction progress of the 6 samples at different times, from both the TGA and the GERO experiments, is then associated with mineralogical and microstructural differences in the starting and reduced materials in order to draw conclusions, assessed in the following chapters of the study. The current section presents the extensive results from the reduction experiments.

5.1.2. Thermo-Gravimetric Analysis (TGA) results

All 6 samples were tested using the TGA under the specified conditions of temperature and gas atmosphere composition. The results were analyzed in extensive Excel sheets in order to clearly demonstrate the differences between their reduction kinetics.

As mentioned above, the two sets of applied conditions correspond to T = 950ºC, 32.5 % CO, 17.5% CO_2 and 50% dilution (N_2 or He), meaning a gas atmosphere of CO/[CO+CO_2] = 0.65, as well as to T = 750ºC with CO/[CO+CO_2] = 0.55 and a 50% dilution (N_2). Only the two extreme samples were both tested for 750ºC and 950ºC. The rest of the samples were only exposed to the lower temperature experiment conditions, since a higher temperature was considered too intense for displaying substantial differences in the reactions between samples. The results are expressed in 2 different formats for both temperatures of 750ºC and 950ºC;

- Graphs displaying reduction degree; the remaining oxygen mols during reduction over the starting mols of oxygen.
- Graphs displaying the O/Fe change, calculated as explained above, versus time. This ratio was selected because it shows the absolute redox state of the samples, making it easier to compare them, as it takes into account their different starting points apart from their relative journeys.

5.1.2.1. Reduction degree vs time

Real-time "Reduction degree (R)" (Taichi, et al., 2015) was used to demonstrate the results from the TGA for both experiment conditions (T=950ºC, XCO=0.65, N_2=0.5 and T=750ºC, XCO=0.55, N_2=0.5) as a function of reduction progress. In accordance, the weight loss due to oxygen removal is expressed as a percentage of the initial oxygen content ("0" to "100%") and reduction is displayed with the form of an increasing curve along time. The formula generating the curve for each sample versus time, corresponds to:

$$R = \left(\frac{O_2\ removed}{O_2\ original}\right) * 100 \qquad \text{eq.15}$$

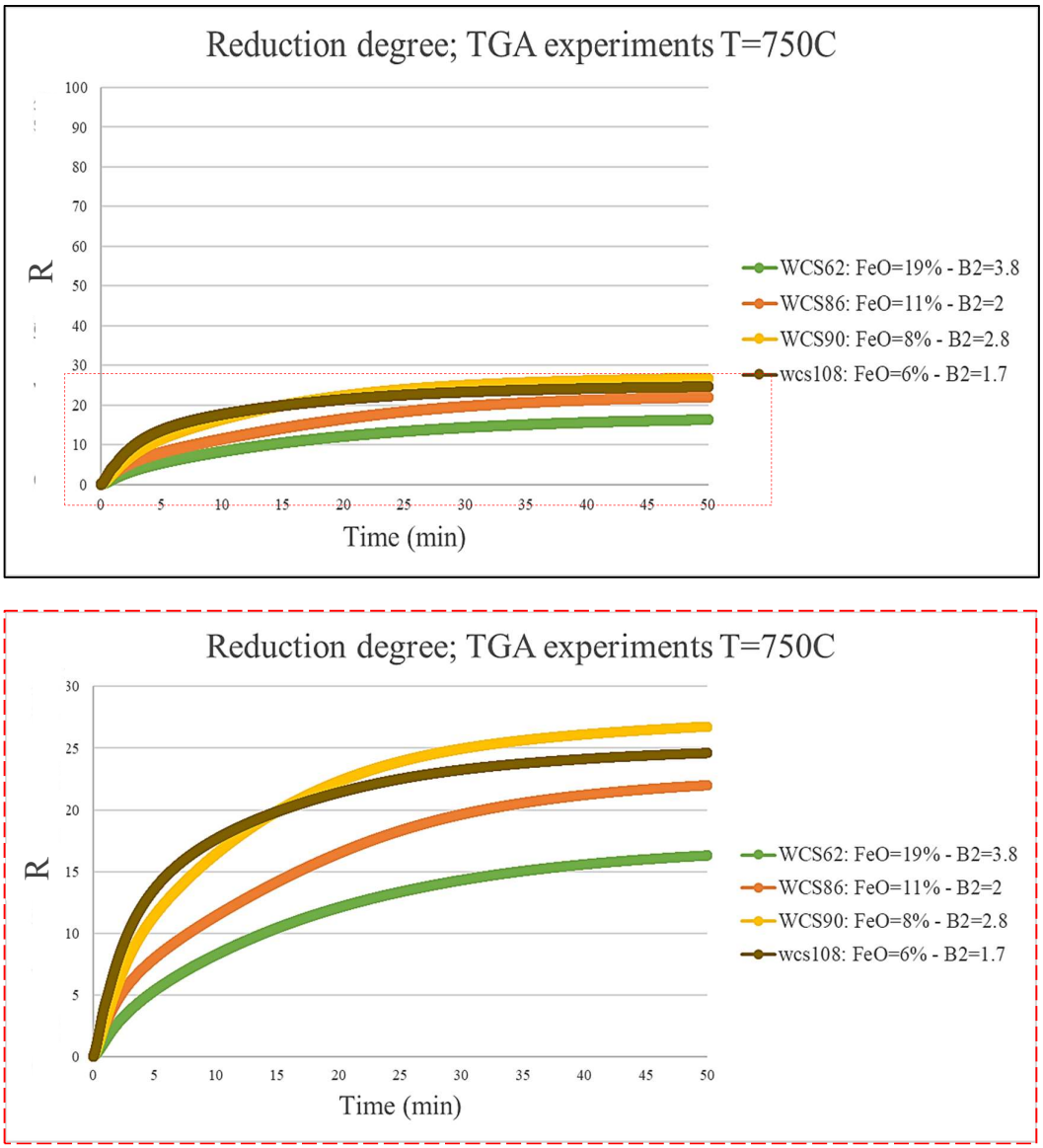

Figure 26. Real-time reduction degree in TGA experiments performed at T=750ºC/XCO=0.55/N_2=0.5. Reduction is expressed as a ratio between weight loss % (due to oxygen subtraction) and starting amount of oxygen.

Figure 26 presents the TGA results from experiments performed under the temperature of T=750ºC and the gas atmosphere of XCO=0.55/N_2=0.5. The weight loss due to the loss of oxygen mass is normalised to the initial amount of oxygen and the ratio is plotted versus time. According to the graph, the moderate basicity - moderate FeO sample WCS90 is the one to perform best in these terms, since its reduction reaches the highest percentages after 15 minutes exposure at the experiment conditions. Its reduction nearly approaches ~30% as time progresses. Very close to WCS90 appears to be WCS108 (reduction reaching up to 25%), which is the lowest basicity - lowest FeO sample, as it starts reducing more than the rest, until it is overpassed by WCS90, approximately after t=15min in the TGA. After WCS108, follows WCS86, reaching a final reduction degree of approximately 20%. WCS86 has greater basicity and FeO than WCS108 and lower basicity, but higher FeO than WCS90. Lastly, poorest reduction is demonstrated by the highest basicity - highest FeO sample WCS62, which only reaches 15% reduction at t=50minutes.

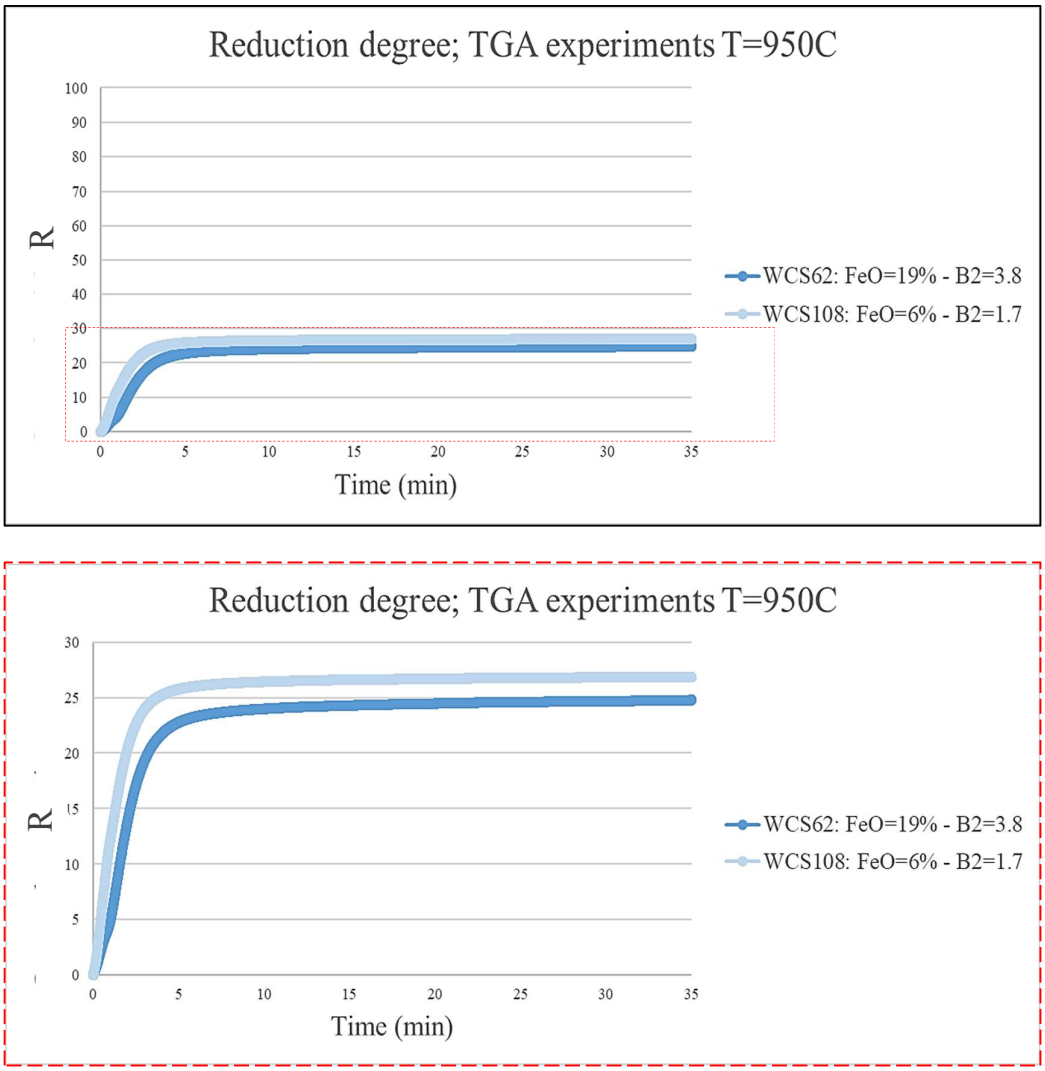

Figure 27. Real-time reduction degree in TGA experiments performed at T=950 C and XCO=0.65/N_2=0.5. Reduction is expressed as a ratio between weight loss due to oxygen subtraction and starting amount of oxygen.

Figure 27 shows the respective reduction curves of the two samples of extreme composition, WCS108 and WCS62, when those are tested for T=950ºC and XCO=0.65/N_2=0.5 in the TGA. The result is relevant to the previous graph; the lowest basicity-lowest FeO WCS108 appears to be more reduced than the highest basicity -highest FeO WCS62. However, the difference between their reduction percentages is smaller in this case, as both plot closer together for the entire duration of the experiment, to finally reach similar levels of reduction at the end (~26%). More specifically, WCS108 reaches a reduction of 27%, while WCS62 reduces up to 25%.

The curves of the two extreme samples are also shown in Figure 28, where they are plotted together for both experiment conditions. It is demonstrated that the sample curves merge closer together under the more reducing conditions. More specifically, the difference in their performance under T=750ºC and XCO=0.55/N_2=0.5 corresponds to 10%, as oppose to 2% at the end of the experiment under the most intense conditions at 950ºC. WCS108 displays nearly the same reduction degree in both experiments, being 25% in the first instance and 27% in the second one. On the other hand, WCS62 shows a clear performance difference under the 2 conditions, since its reduction seems to be severely favoured by higher temperature and higher CO levels in the gas mixture, increasing its reduction from 15% (T=750ºC) to 25% (T=950ºC).

Therefore, this discrepancy is attributed to the performance difference of the sample of highest basicity between the two conditions of varying intensity.

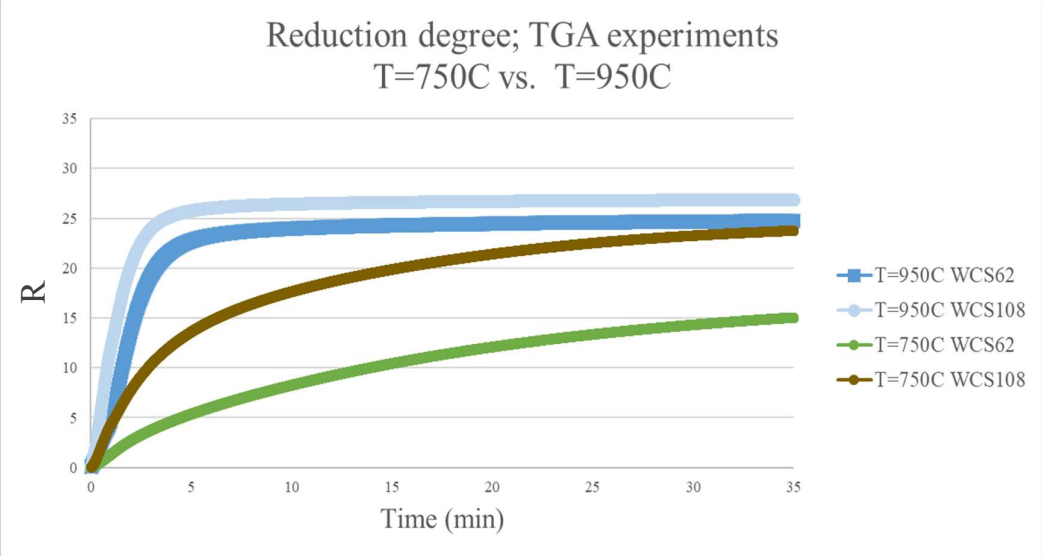

Figure 28. TGA experiments of WCS108 and WCS62 under both conditions of: i) T=950ºC, XCO=0.65, N_2=0.5 and ii) T=750ºC, XCO=0.55, N_2=0.5.

5.1.2.2. O/Fe change vs time

Reduction degree shows the net reduction progress of all the samples under specific conditions and experiment durations. However, the samples start their reduction from different starting points, since some of them are in more reduced states than others. Hence, the different absolute redox of the samples should be considered when expressing reduction. This can be achieved by referring to the oxygen loss as a function of the total amount of iron per sample. Samples approaching O/Fe=1 are considered to be reaching their equilibrium state, as this ration value corresponds theoretically to the transition towards Wüstite stability. Therefore, the lower the value of O/Fe, the more progressed is the reduction.

Figure 29 shows the O/Fe change of all the samples during reduction in the TGA, under the conditions of T=750ºC and XCO=0.65. The O/Fe shows how much oxygen is lost from each sample as reduction progresses, as relevant to iron. The O/Fe curves are also plotted with their respective reduction rates, as presented in Figure 30 in a double-vertical axis graph. The reaction rates of the samples are also displayed in Figure 31, plotted with O/Fe ratio in order to demonstrate how the reaction speed varies as a function of reaction progress, highlighting differences in relative reduction kinetics.

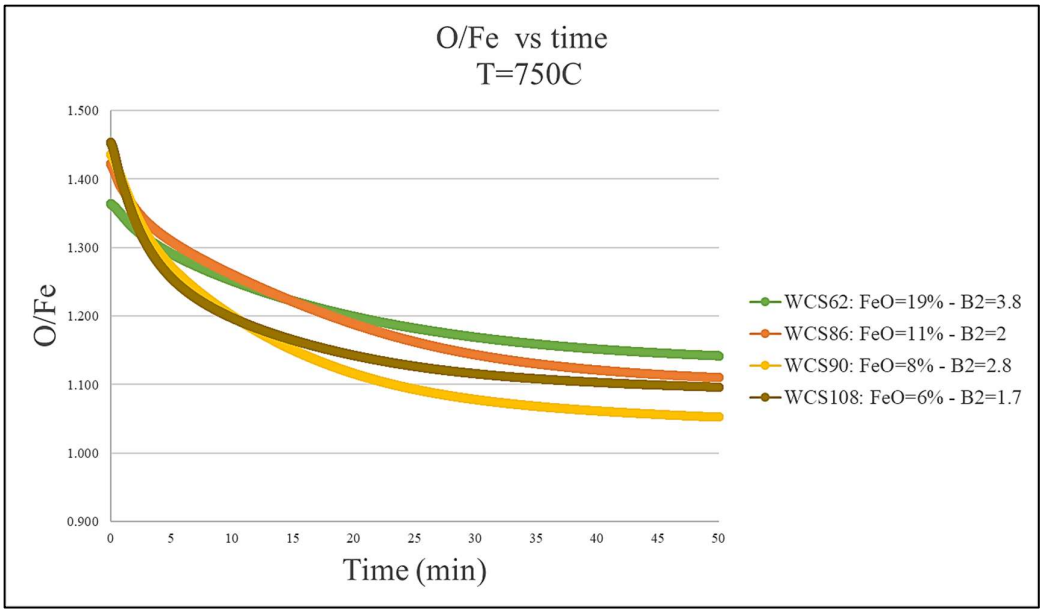

Figure 29. TGA experiments of all the samples; WCS62, WCS86, WCS90, WCS108 at T= 750ºC and CO=0.55/ N_2=0.5. Loss of oxygen to iron content versus time; Reduction expressed as a function of iron content. Each sample starts from a different redox state due to their varying starting composition in terms of FeO content.

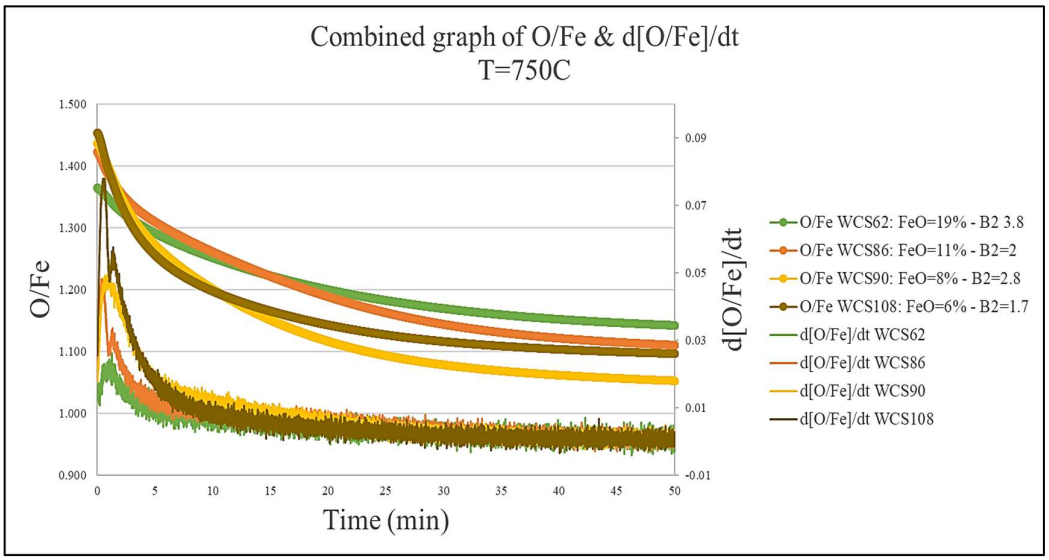

Figure 30. TGA experiments of all the samples; WCS62, WCS86, WCS90, WCS108 and at T= 750ºC and CO=0.55/ N_2=0.5. Graph containing primary and secondary axis; Primary axis displays loss of oxygen to iron content versus time; Reduction expressed as a function of iron content. Secondary axis plots the respective reduction rates versus the times of escalating oxygen loss.

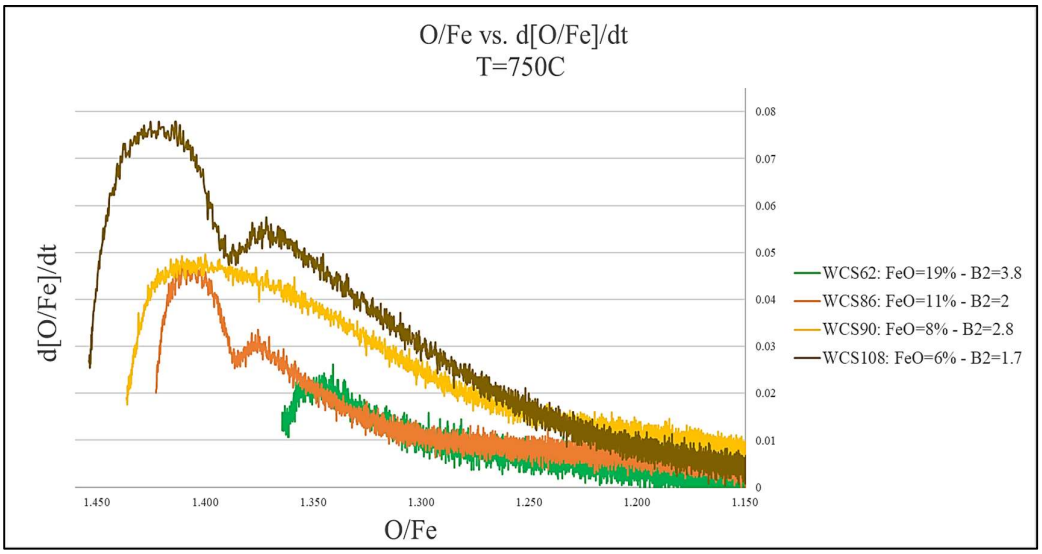

Figure 31. TGA experiments of all the samples; WCS62, WCS86, WCS90, WCS108 at T= 750ºC and CO=0.55/ N_2=0.5. Reduction rates versus O/Fe ratio. Samples start to get reduced from a different starting point in terms of O/Fe, since some are more reduced than other as a result of their different composition.

According to Figure 29, the samples start from a different reduction state, which gets changed as reduction progresses in the TGA. The starting materials are controlled in terms of composition, having a varying redox state as a result of altering their coke breeze content whilst sintering, and consequensily their FeO levels. WCS108 starts from the least reduced position (O/Fe=1.45), while WCS62 starts from the most reduced one (O/Fe=1.36). The samples in between, also start from a slightly different redox ratio; WCS86 (O/Fe= 1.42), WCS90 (O/Fe=1.44), WCS94 (O/Fe=1.43) and MH1785 (O/Fe=1.41). All three graphs in Figure 29**,** Figure 30**,** and Figure 31 take into consideration the starting redox state for each sample, since reduction is expressed as a function of their Fe content, which remains stable during reduction.

Based on the TGA results at T=750ºC and XCO=0.65, WCS90, which is the moderate basicity- moderate FeO sample as shown in the starting composition scheme (Figure 29), arrives to the most reduced state when marking oxygen loss as a function of initial Fe content. After WCS90, the most reduced sample appears to be WCS108, being the low basicity -low FeO sample, followed by the low basicity- higher FeO WCS86 and lastly the highest basicity and highest FeO content WCS62.

The reduction rate of the samples is presented in Figure 30 and Figure 31. In the first one reduction rate is plotted with time, along with the O/Fe curves plotting at a different axis. According to the figure, the reaction speed peaks up at the very first minutes of reduction, while it stabilizes after approximately 25 minutes of exposure at the reducing conditions in the TGA. The highest reduction rate corresponds to the low basicity - low FeO sample WCS108, which has a maximum altitude approaching d[O/Fe]/dt=0.08 mols/0.3sec. WCS90 comes second with a lower and smoother peak than WCS108, with the highest rate point nearly reaching d[O/Fe]/dt=0.05 mols/0.3sec. Finally, WCS86 and WCS62 follow with peaks corresponding to d[O/Fe]/dt=0.045 mols/0.3sec and d[O/Fe]/dt=0.023 mols/0.3sec respectively.

Figure 31 displays the reduction rates plotted with O/Fe. Also, in this graph, samples starting from different O/Fe points get reduced with different speeds and form different signal patterns. The first and most intense pulses of reduction are magnified here by limiting the plot range, so that differences can be more clearly sketched. According to the graph, it can be observed that the samples WCS108 and WCS86 form a different rate curve than the samples of higher basicity, being the WCS90 and WCS62. More specifically, both WCS108 and WCS86 show a characteristic kink in their rate signal, with a high starting peak that slows down only to from a second-rate peak. On the other hand, WCS90 and WCS62 present a smoother rate of reduction with only one wider peak that is not as abrupt as in the case of the other two samples. Therefore, it seems like there is a kinetic barrier for WCS108 and WCS86 that causes their

reduction rates to abruptly slowdown and reach a low peak that is then overpassed, as reduction speed retrieves. It is also worth noticing that this kink occurs at the same O/Fe value for both samples, while the highest peak for WCS86 goes as high as the peak of WCS90.

Figure 32 presents the O/Fe change recorded for the samples of extreme composition, WCS108 and WCS62, during reduction in the TGA under the conditions of T=950ºC and XCO=0.55. Similarly to the results at 750ºC, the TGA reduction curves at 950 C are also plotted along with their respective reduction rates in Figure 33, in a combined graph versus time. Finally, reduction rates are graphed with the O/Fe content of the samples in Figure 34, showing the speed of reduction, as the latter progresses.

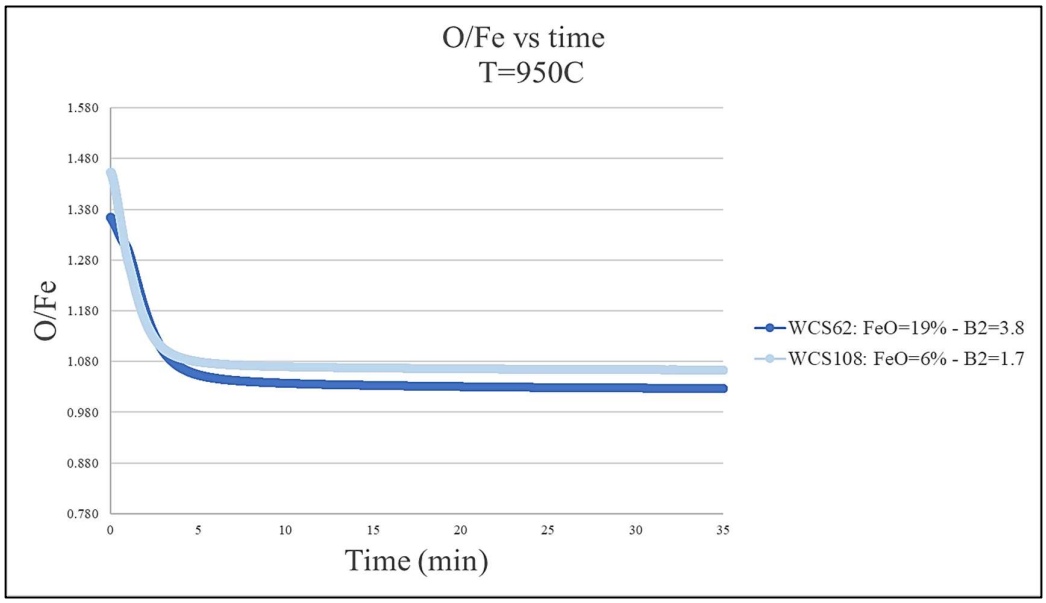

Figure 32. TGA experiments of the extreme composition samples; WCS62 and WCS108 at T= 950ºC and XCO=0.65/ N_2=0.5. Loss of oxygen to iron content versus time; Reduction expressed as a function of iron content. Each sample starts from a different starting redox state.

The reduction of the two samples of extreme composition also initiates from a different starting point, as mentioned above (WCS108 O/Fe_{start}= 1.45, WCS62 O/Fe_{start}=1.36). As reduction progresses, WCS62, starting from a more reduced state, remains more reduced than WCS108 after t=3 min and for rest duration of the experiment.

Figure 33 combines the reduction rate of the samples with their reduction curves versus time in the same graph. Similarly to the moderate conditions at T=750ºC, it is also observed in this case, that the highest reduction rates occur during the first minutes of reduction (dt=5min). WCS108 ($d[O/Fe]/dt_{max}$=0.021) displays a much higher initial rate peak than WCS62 (d[O/Fe]/dt=0.08), while their following reduction rate altitutes (second peaks) nearly coincide (WCS108 d[O/Fe]/dt=0.014 and WCS 62 d[O/Fe]/dt=0.013).

The reduction rates of the two samples are also plotted with O/Fe in order to show the speed of reduction in relation to reduction progress. Both start from a different reduction state and show contrasting patterns. WCS108 starts with a very high speed of reduction, which then suddenly slows down, to ascent back up again forming a second pulse of reduction. On the other hand, WCS62 starts with a much smaller and delayed peak which also forms a much smaller kink, before it forms its maximum reduction rate peak that almost coincides with the second reduction pulse of WCS108.

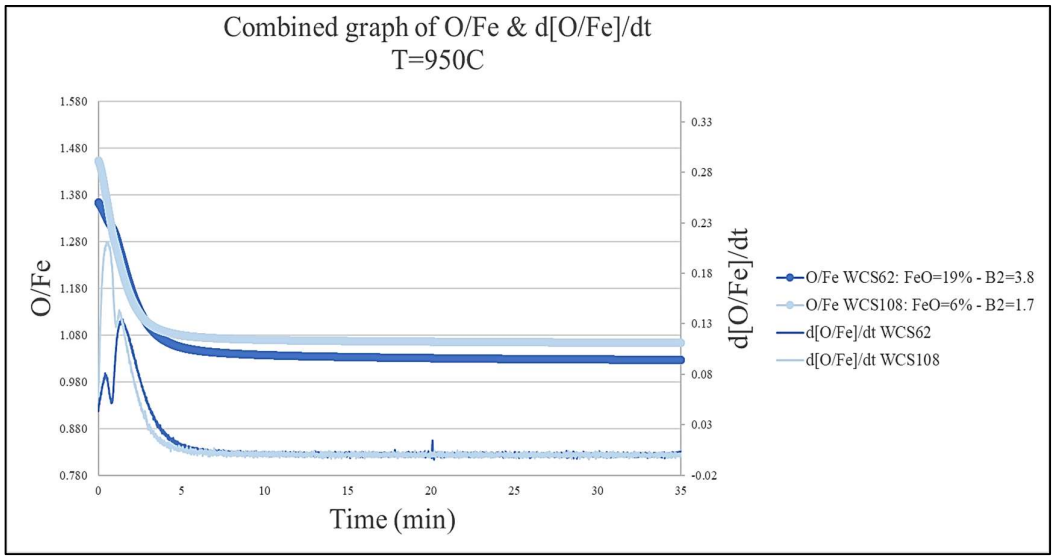

Figure 33. TGA experiments of the extreme composition samples; WCS62 and WCS108 at T= 950°C and XCO=0.65/ N_2=0.5. Graph containing primary and secondary axis; Primary axis displays loss of oxygen to iron content versus time; Reduction expressed as a function of iron content. Secondary axis plots the respective reduction rates versus the times of escalating oxygen loss.

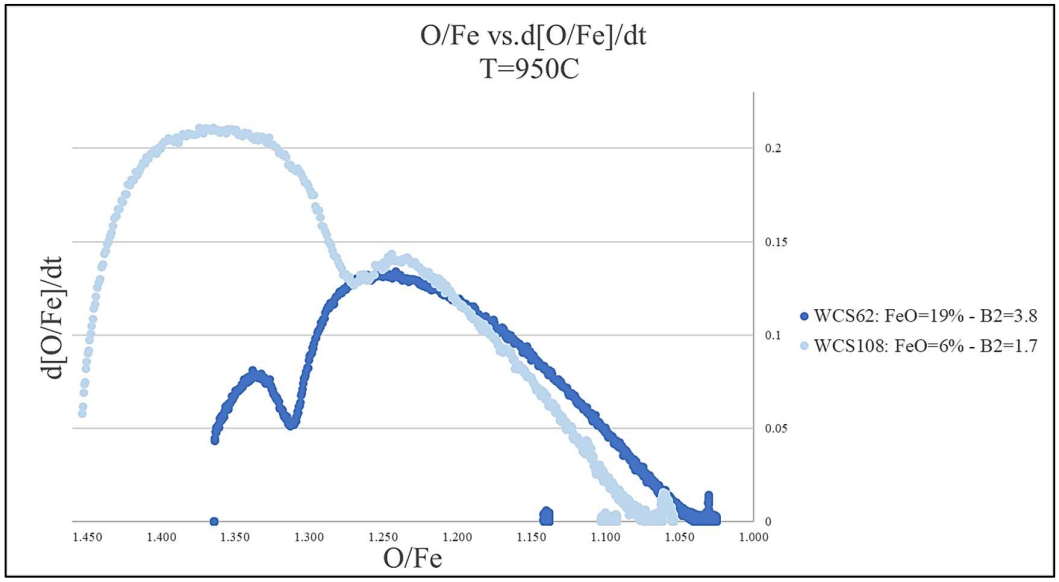

Figure 34. TGA experiments of the extreme composition samples; WCS62 and WCS108 at T= 950°C and XCO=0.65/ N_2=0.5. Reduction rates versus O/Fe ratio. Samples start to get reduced from a different starting point in terms of O/Fe.

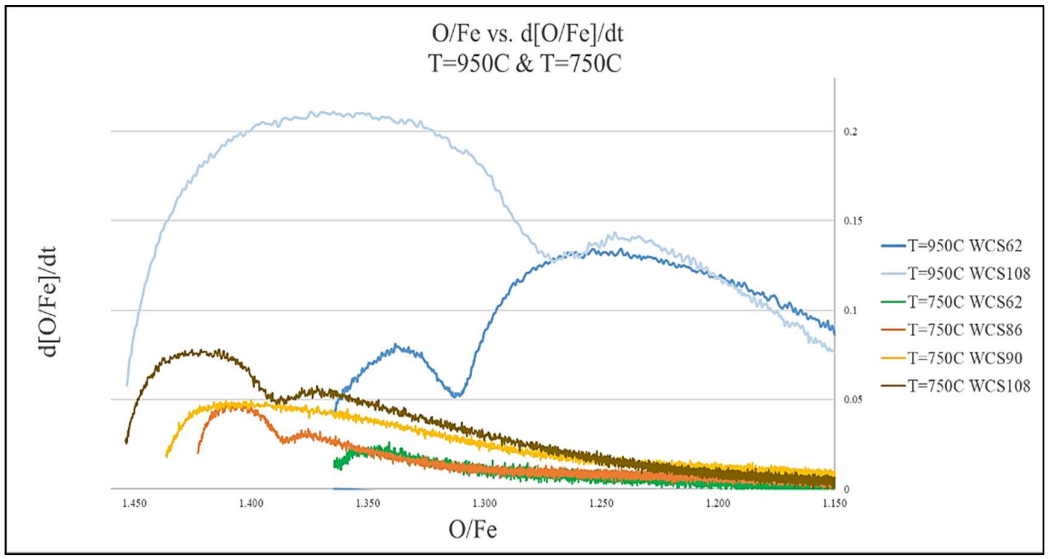

Figure 35. Reduction rates of the two extreme samples WCS108 and WCS62 in the TGA, under both conditions (i. T=950°C, XCO=0.65, N_2=0.5 and ii. T=750°C, XCO=0.55, N_2=0.5) versus O/Fe.

When comparing the behaviour of the sinter samples in the TGA under the two different conditions of temperature and gas composition, it is observed that the reduction rate altitude and reducing range are much greater for T=950°C, XCO=0.65, N2=0.5. The TGA reduction curves of WCS108 and WCS62 are presented in Figure 35 for both experiment conditions. Based on this plot, at 750°C WCS108 displays an initial reducing range between O/Fe=1.450 and O/Fe=1.370, while at 950°C the first pulse of reduction perseveres until O/Fe=1.270.

5.1.2.3. Fractional reduction progress; at equilibrium

The fractional reduction progress corresponds to the normalised reduction progress based on each samples' theoretical mass loss at equilibrium. The expected weight loss at equilibrium is measured through FactSage software. The thermodynamic calculations performed in the software give the expected phase assemblage and final reduction degree at equilibrium for any given sinter composition, for a specified set of experiment conditions, such as temperature and gas composition. The final chemical phases present at each sample are also exported in grams, as well as in mols, after each calculation with FactSage. Adding up the masses of all the existent solid phases, excluding all gas phases, gives the total final mass of each sample at equilibrium.

The expected weight loss expected at equilibrium is then used to calculate the fractional reduction progress of the samples. The ratio plotted with time in this case corresponds to:

Fractional reduction progress = [current mass – initial mass] / [equilibrium mass – initial mass] = [%mass loss measured] / [%mass loss at predicted equilibrium].

This gives the relative progress from the starting point to the expected equilibrium point for each sample, and so it focuses only on how quickly the reaction proceeds in normalised terms. It also conceals the differences where the samples start and finish their journey and shows only how quickly they progress from the starting reduction point to their expected end destination. Equilibrium is reached when the O/Fe ratio value equals to 1.

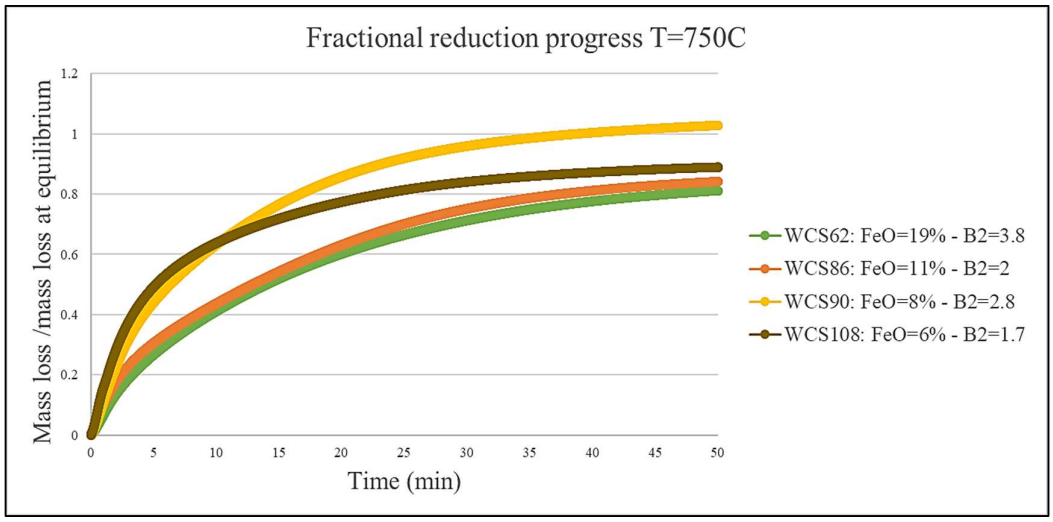

Figure 36. TGA experiments at T=750ºC and XCO=0.55/ N_2=0.5; Fractional reduction progress in terms of sample equilibrium versus time.

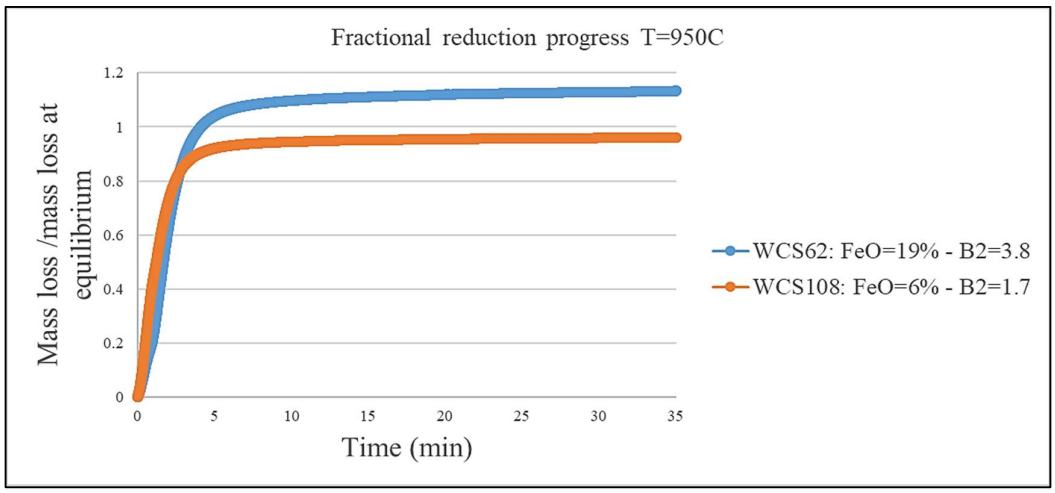

Figure 37. TGA experiments at T=950ºC and XCO=0.65/ N_2=0.5; Fractional reduction progress in terms of sample equilibrium versus time.

According to Figure 36, WCS108 starts to reduce more intensively than the rest of the samples for the first 8 minutes in the TGA, under T=750ºC. However, after that point its reduction seems to fall behind, while WCS90 starts to reduce further, appearing to even reach its equilibrium state after t=30 min. As mentioned, WCS108 starts to reduce relatively quickly but its reduction rate seems to slow down after a while, causing it to eventually plot closer to the curves of WCS86 and WCS62, which are the samples that begin to reduce at much lower rates. In terms of reduction performance, WCS86 follows WCS108, while WCS62 comes last also in this case, reaching a ratio of fractional reduction progress equal to 0.8.

Figure 37 shows the reduction of WCS62 and WCS108 under the high temperature experiment conditions. In this case of conditions, the performance of the two samples is reversed. WCS62 is the one sample that reduces further, reaching and surpassing its theoretical equilibrium even, at the very first minutes of reduction in the TGA. On the other hand, WCS108 reaches 96% of reduction, as relevant to its expected equilibrium for the same given time of exposure in the TGA.

5.1.3. GERO experiments- results

5.1.3.1. Sample weight loss wt% after reduction in the GERO for t_i

The results from the experiments performed in the GERO furnace are shown in the following graphs. Figure 38 and Figure 39 display the weight loss occurring in the samples after the specified run times in the furnace. The percentages of the initial mass that has been lost after reduction for a specific amount of time for each sample is presented in Table 9 and Table 10, corresponding to the two different sets of reduction conditions respectively.

Figure 38 shows the weight loss when the sinters of different composition are tested under the conditions of T=950°C, XCO=0.65, N_2=0.5. All six samples were applied in the GERO under these conditions for short time experiments of t=2 minutes and t=4minutes, as well as for long-time experiments of t=5 hours. The mass losses in relation to the starting mass of each sinter are displayed in Table 9.

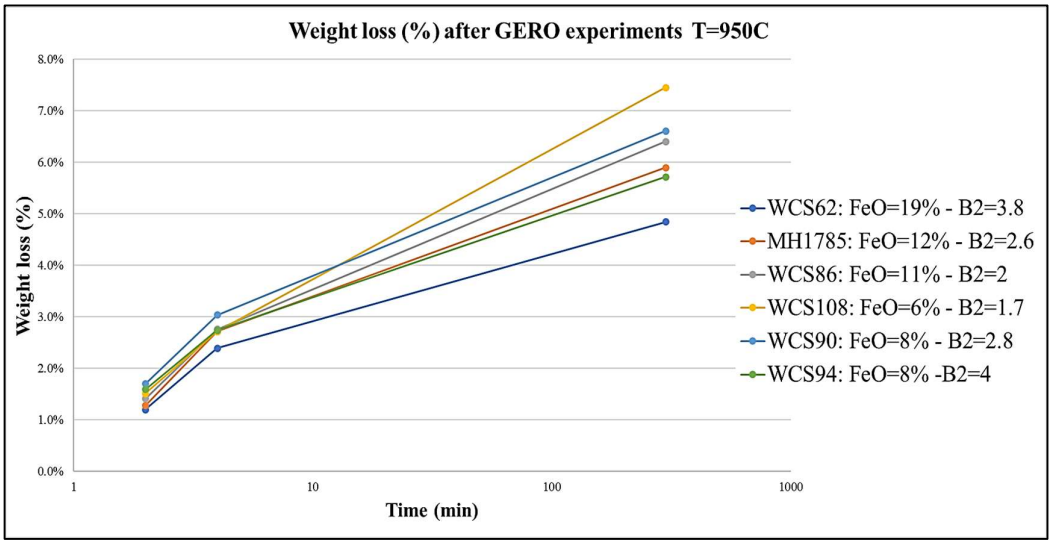

Figure 38. GERO experiments; under T=950°C/XCO=0.65/ N_2 dilution=0.5; Weight loss versus experiment run times.

Table 9. GERO experiments; under T=950°C/XCO=0.65/ N_2 dilution=0.5; Weight loss per sample time-series experiment.

Weight loss	**GERO: T=950°C/ XCO=0.65/ N2=0.5**		
Sample	**2 minutes**	**4 minutes**	**5 hours**
WCS62	1.2%	2.4%	4.8%
WCS94	1.6%	2.7%	5.7%
MH1785	1.3%	2.7%	5.9%
WCS90	1.7%	3.0%	6.6%
WCS86	1.4%	2.8%	6.4%
WCS108	1.5%	2.7%	7.5%

All the samples start from a 0% weight loss. According to the graph in Figure 38, the differences between the samples' weight losses become more pronounced, as experiment residence time increases.

At t=2minutes their weight losses are already different, but they do not plot very far apart. According to the sequence, WCS90 appears to be the one sample that has reduced the most (1.7wt%) after 2 minutes exposure at T=950°C/XCO=0.65/N^2=.05, while WCS62 seems to be the one that has reduced the least (1.2wt%). The samples in between plot very close to each other, with MH1785 (1.3wt%) being the least reduced after WCS62, then WCS86

(1.4wt%), WCS108 (1.5wt%) and finally WCS94 (1.6wt%) before the most reduced WCS90 (1.7wt%).

At t=4 minutes, WCS90 and WCS62 remain the most reduced and least reduced samples, with 3wt% and 2.4wt% weight losses respectively. The rest of the samples have lost almost equal masses during reduction, reaching a percentage of 2.7wt%, except for WCS86 that reached 2.8wt%.

Lastly, the timely elongated experiments show most of the samples being positioned differently, with the most reduced being WCS108 (7.5wt%), followed by WCS90 (6.6wt%), WCS86 (6.4wt%), MH1785 (5.9wt%), WCS94 (5.7wt%) and lastly WCS62 (4.8wt%). Therefore, in the long run, the lowest basicity-lowest FeO sample WCS108 is the most reduced, while the highest basicity-lowest FeO WCS62 is the least. In addition, even though WCS90 has greater basicity compared to WCS86 of higher relative FeO, it consistently appears to be more reduced, also in this case. The industrial MH1785 and high basicity - moderate FeO WCS94 are less reduced than WCS86 based on the long-time experiment, but still more reduced than WCS62.

The samples were also applied in the GERO furnace under the more moderate conditions of T=750°C, XCO=0.55, N_2=0.5. Figure 39 shows the weight loss of each sample as relevant to the experiment residence time in the GERO furnace. The time series are slightly different in this case due to the less intensive conditions; thus, the experiment interruption times correspond to t=5 minutes and t=20 minutes for the short runs, and t=4.5 days for the long runs. According to the graph, as residence time increases the weight losses become more distant regarding each other's values, since their differences become greater with longer experiment durations. WCS108 and WCS62 remain the most reduced and least reduced samples respectively, for the entire spectrum of experiment run times. The rest of the samples demonstrate similar levels of weight losses after the short-time experiments, while after 4.5 days in the furnace their ranking becomes more distinct. Based on the long-experiments results, WCS108 has lost most of its initial mass, with 6.8wt%, followed by WCS90 with 6.3wt%, WCS86 with 6.2wt%, MH1785 with 5.5wt%, WCS94 with 5.3wt%, and finally WCS62 with 4.1wt% weight loss. This order agrees perfectly with the respective ranking of the T=950°C long experiments.

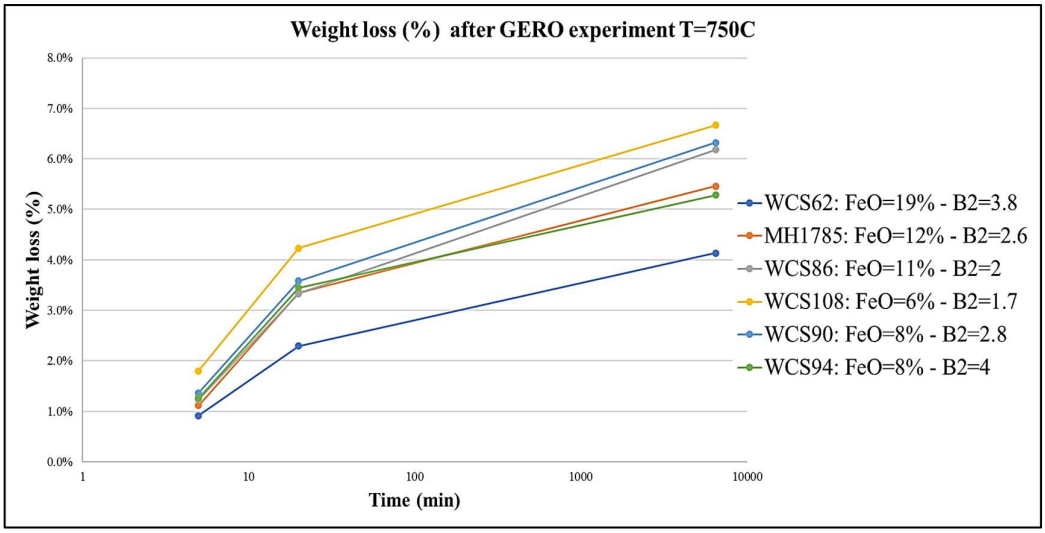

Figure 39. GERO experiment; T=750°C/XCO=0.55/N2 dilution=0.5. Weight loss versus experiment run times.

Similarly to the TGA, the GERO experiments also demonstrate that lower temperature conditions favour greater differences between the weights losses of the samples, compared to the losses observed at more intensive conditions. At higher temperature samples appear to converge, especially at shorter experiment times. In addition, at increasing residence times, samples' weight losses plot more far apart for both conditions.

Table 10. GERO experiments; T=750°C/XCO=0.55/ N_2(dilution)=0.5; Weight loss per sample time-series experiment.

Weight loss	**GERO: T=750°C/ XCO=0.55/ N2=0.5**		
Sample	**5 minutes**	**20 minutes**	**4.5 days**
WCS62	0.9%	2.3%	4.1%
WCS94	1.3%	3.4%	5.3%
MH1785	1.1%	3.3%	5.5%
WCS90	1.4%	3.6%	6.3%
WCS86	1.2%	3.3%	6.2%
WCS108	1.8%	4.2%	6.7%

5.1.3.2. Sample O/Fe after reduction in the GERO for ti

The weight loss of each sample after reduction in the furnace can be expressed as a function of total iron content per sample. That way the oxidation state of iron, from where oxygen is solely removed from each sinter sample, can be monitored in relation to experiment interruption times. Hence, the O/Fe ratio is also used for representation of reduction in the GERO furnace. As such, the weight loss percentage occurring at each sample after reduction is translated into mols, to then be subtracted from the starting oxygen mol content. The remaining oxygen is then divided by the total mols of iron per sample. As a result, the oxidation state of iron (O/Fe) is calculated for each time-series experiment. Expressing reduction in these terms is considered advantageous, since the ratio additionally takes into account the initial oxidation states of the sinter samples, along with their furnace reduction performance.

Figure 40 shows the reduction of the samples at T=950°C and XCO=0.65/N_2=0.5 in the GERO furnace for t=0, t=2min, t=4min and t=300min (5 hours). Figure 41 shows the reduction of the samples for T=750°C and XCO=0.55/N_2=0.5 in the GERO furnace for t=0, t=5min, t=20min and t=6,480min (4.5 days). The tables including the O/Fe values of all the samples after the reduction experiments under the two set of conditions for the specified times are shown below of each respective graph (Table 11 and Table 12).

The samples start reducing from different reduction states, with the basic samples being more reduced at time t=0min, as oppose to the less basic samples which have a lower iron redox state. According to Figure 40, during the short time experiments, the basic samples show resistance to reduction. Especially WCS62 appears to be the less reduced for both t=2min and t=4min, since it also started from the most reduced position. It is then followed by MH1785 and WCS94, although these samples are not very distinct from the rest of intermediate samples between the two extremes, WCS62 and WCS108. The same pattern is followed by WCS108 at t=2min and t=4min, as the sample remains the less reduced even after 4 minutes, before it plots as the most reduced after 5 hours of reduction. At the long experiment times, the samples appear to reverse their positions. This sequence demonstrates the expected ranking of samples. The most basic samples now become the less reduced, while samples of lower basicity have reduced further.

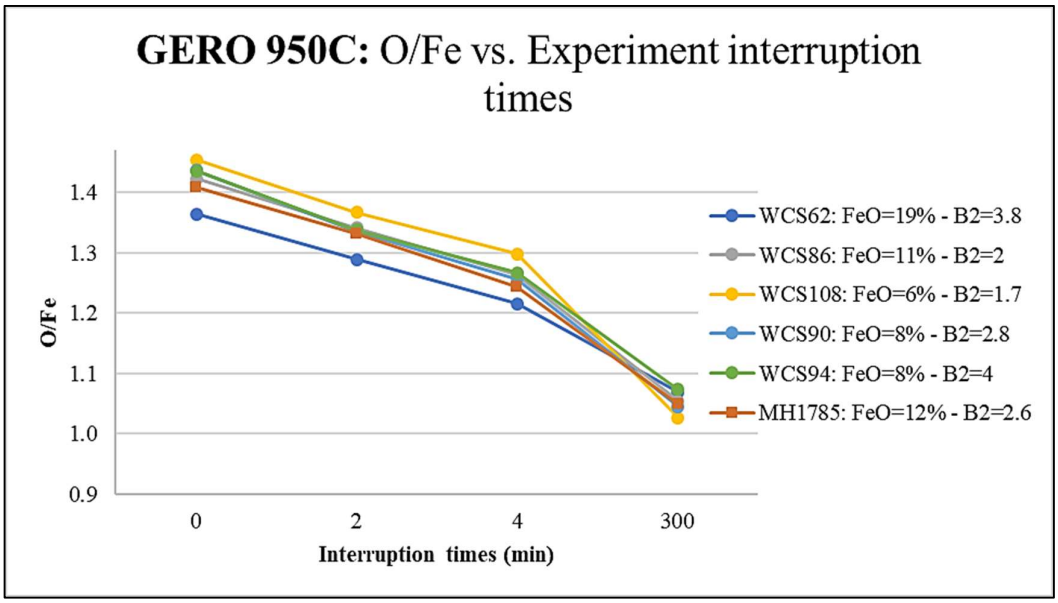

Figure 40. GERO experiment; T=950ºC/XCO=0.65/N_2 dilution=0.5. O/Fe versus experiment run times.

Table 11. GERO experiments; under T=950ºC/XCO=0.65/ N_2 dilution=0.5; O/Fe per sample time-series experiment.

O/Fe	GERO: T=950ºC/ XCO=0.65/ N2=0.5			
Sample	**O/Fe t=0min**	**2 minutes**	**4 minutes**	**5 hours**
WCS62	1.36	1.29	1.22	1.07
WCS94	1.44	1.34	1.27	1.07
MH1785	1.41	1.33	1.24	1.05
WCS90	1.44	1.34	1.26	1.05
WCS86	1.42	1.34	1.26	1.05
WCS108	1.45	1.37	1.30	1.03

Figure 41, which presents the reduction of the samples for T=750ºC and XCO=0.55/N_2=0.5, demonstrates similar results. Also, in this set of conditions the basic samples show resistance to reduction during the shortest experiment times. It is only after 20 minutes that samples begin to be positioned differently and merge close together, to finally show a reverse ranking under the prolonged time experiments. WCS62 starts as the most reduced sample and finishes as one of the less reduced along with the basic WCS94 at reduction after t=4.5 days. The opposite is observed in WCS108 which starts by being one of the less reduced samples to being one of the most reduced ones. In this instance, WCS86, WCS90 and MH1785 also appear to finish relatively moderately reduced after t=4.5 days, plotting in between WCS108 and WCS62/WCS94.

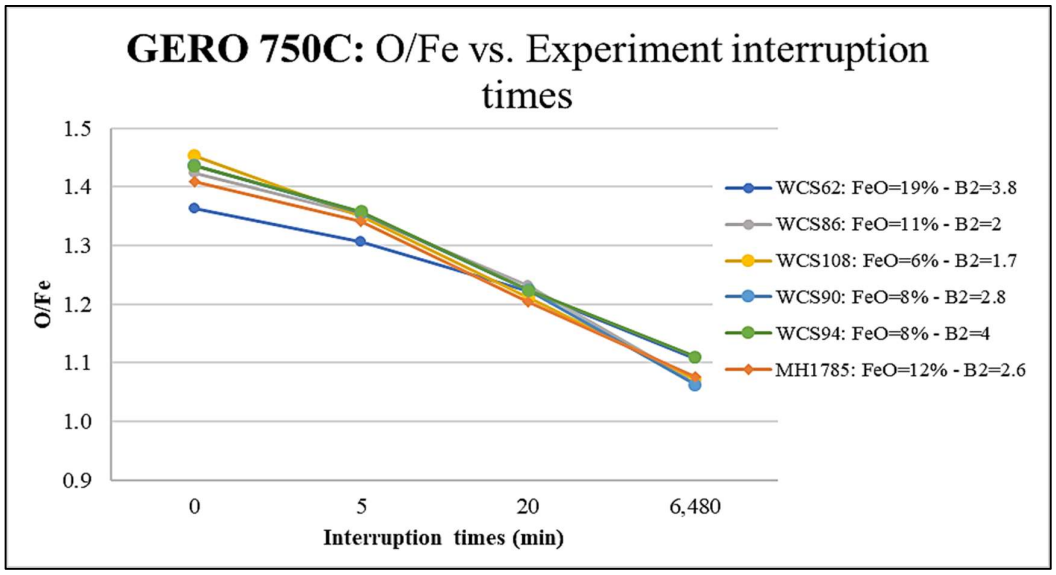

Figure 41. GERO experiment; T=750°C/XCO=0.55/N_2 dilution=0.5. O/Fe versus experiment run times (category x-axis).

Table 12. GERO experiments; under T=950°C/XCO=0.65/ N_2 dilution=0.5; O/Fe per sample time-series experiment.

O/Fe	GERO: T=750°C/ XCO=0.55/ N2=0.5			
Sample	**O/Fe t=0min**	**2 minutes**	**4 minutes**	**5 hours**
WCS62	1.36	1.31	1.22	1.11
WCS94	1.44	1.36	1.22	1.11
MH1785	1.41	1.34	1.20	1.08
WCS90	1.44	1.36	1.22	1.06
WCS86	1.42	1.35	1.23	1.07
WCS108	1.45	1.35	1.21	1.07

5.1.4. TGA – GERO; Comparison of results

In order to verify the differences between the TGA and GERO results, the O/Fe values of the samples vs time for both experiment types were plotted together on one single graph per sample. That shows directly how diverse the GERO and TGA curves are. Figure 42 shows six different graphs that correspond to the performance of each sample. The real -time performance in the TGA is shown with a green curve, and the performance in the GERO is shown as red points for each experiment interruption time.

Based on the graphs, better correlation between the curves and the points is shown for T=750°C, XCO=0.55/N_2=0.5 experiments, while greater deviation is observed in the case of T=950°C, XCO=0.55/N_2=0.5 experiments. In general, reduction appears to be faster in the TGA. This could be attributed to the difference in the amount of material introduced to each of the equipment, as well as to the slightly different environment of the experiment. A few milligrams of material were introduced in the TGA, while the airflow is regulated more frequently than in the GERO furnace, making the TGA environment more reductive. In addition, diffusion effects can differ between the two.

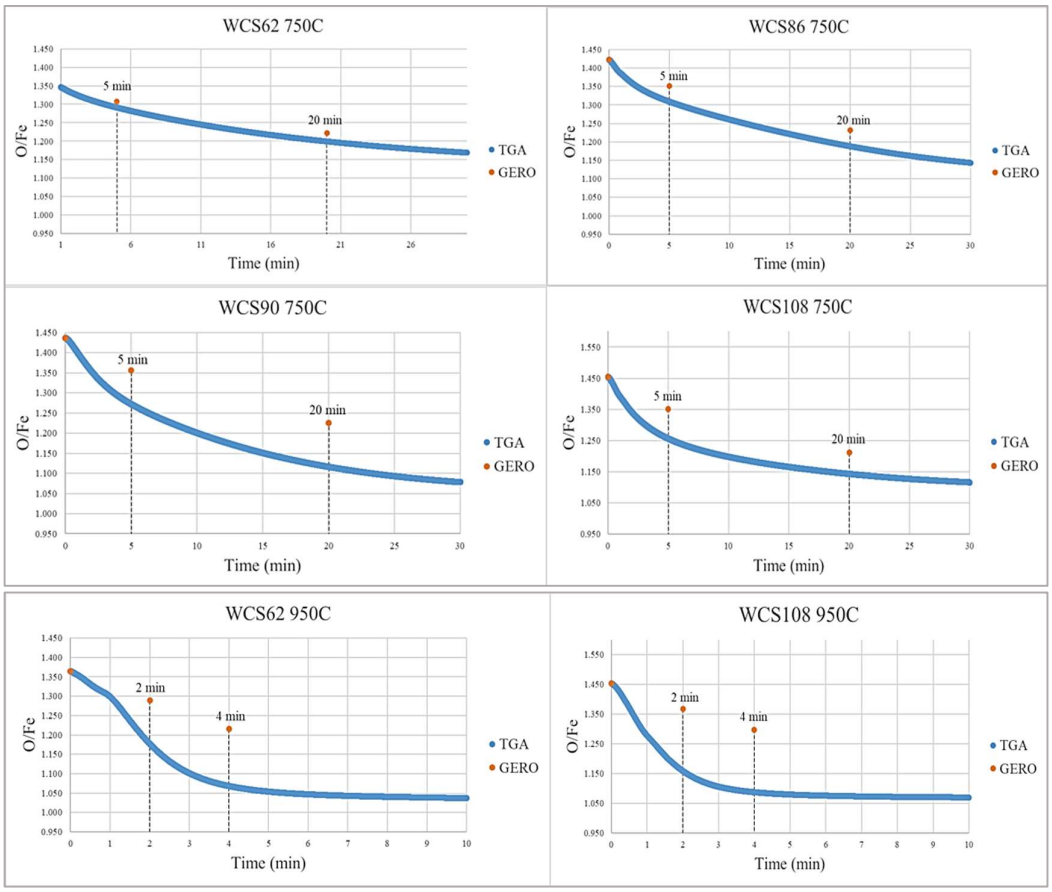

Figure 42. Performance of each sample in the TGA experiments opposed to the GERO experiments.

5.2. Analytical Techniques

5.2.1. XRD analysis

The Eva and BrukerTM Topas softwares were used for the qualitative and quantitative analysis of the XRD results. The outcome included the identification of the phases present in the different sinter materials, as well as their relative proportion in each sample. The resulting phase weight percentages were formulated in tables, showing the relative amounts of mineral phases identified in every sinter sample.

These are visually expressed in histograms, categorized by experiment time, and sample progress. The graphs include mineralogy changes between the different sinters at any given experiment times as well as, changes between starting sinters and their reduced states. Figure 43 shows the mineral phases in the samples at t=0 min, t=2min, t=4 min and t=5hours for the T=950°C, XCO=0.65/N_2=0.5 experiments, while Figure 44 shows the mineral phases in the different samples at t=0 min, t=5min, t=20min and t=4.5days for T=750°C, XCO=0.55/N_2=0.5 experiments. Figure 45 and Figure 46 categorize mineralogical changes per sample progress for the conditions of 950°C and 750°C respectively.

After the long-time reduction experiments, there are certain detected XRD artifacts. These correspond to the false presence of specific phases, which is thoroughly stated in the respective sections.

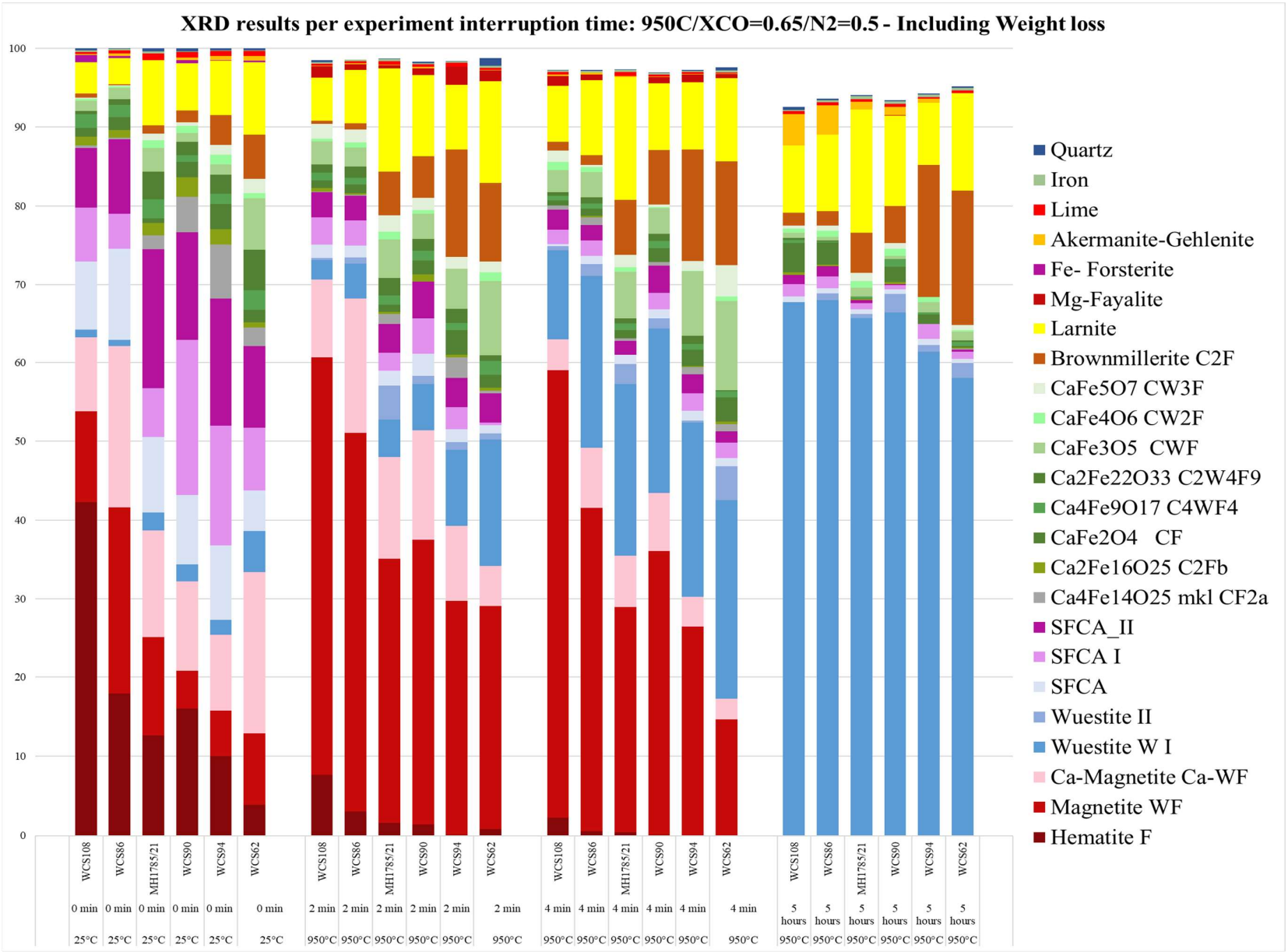

Figure 43. XRD results per experiment interruption time; 950°C/XCO=0.65/N_2=0.5.

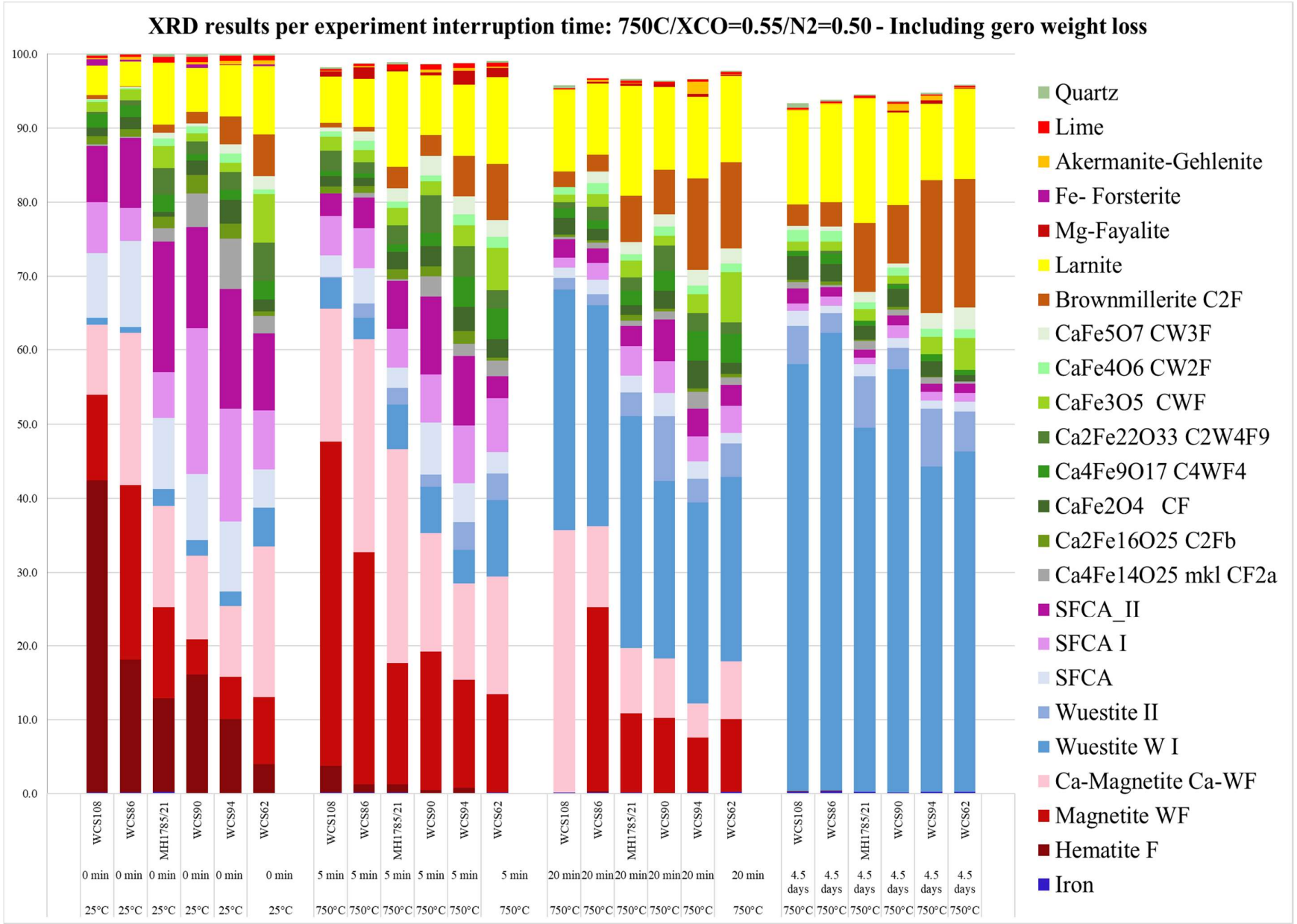

Figure 44. XRD results per experiment interruption time; 750ºC/XCO=0.55/N_2=0.5.

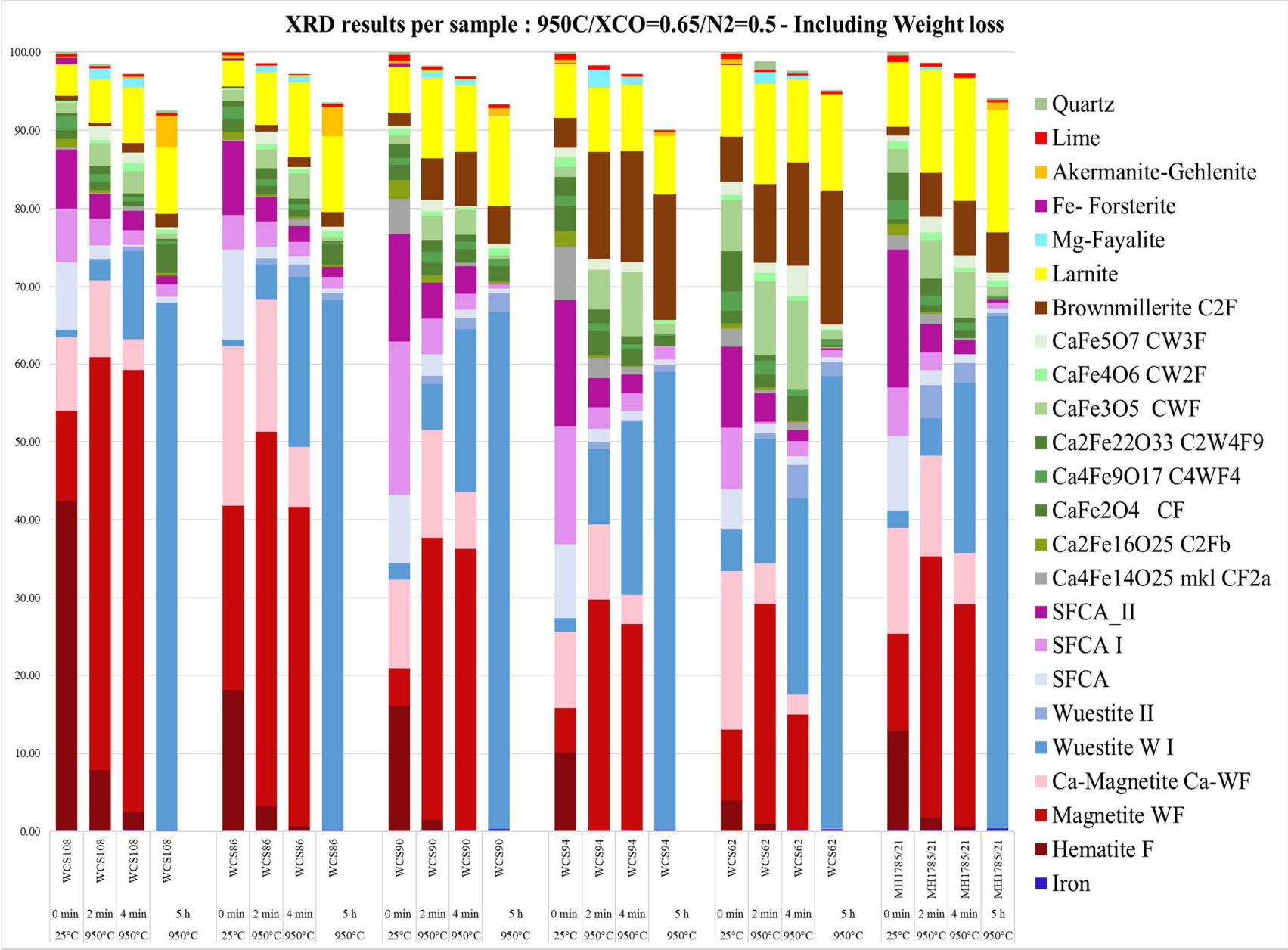

Figure 45. XRD results per sample; 950°C/XCO=0.65/N_2=0.5

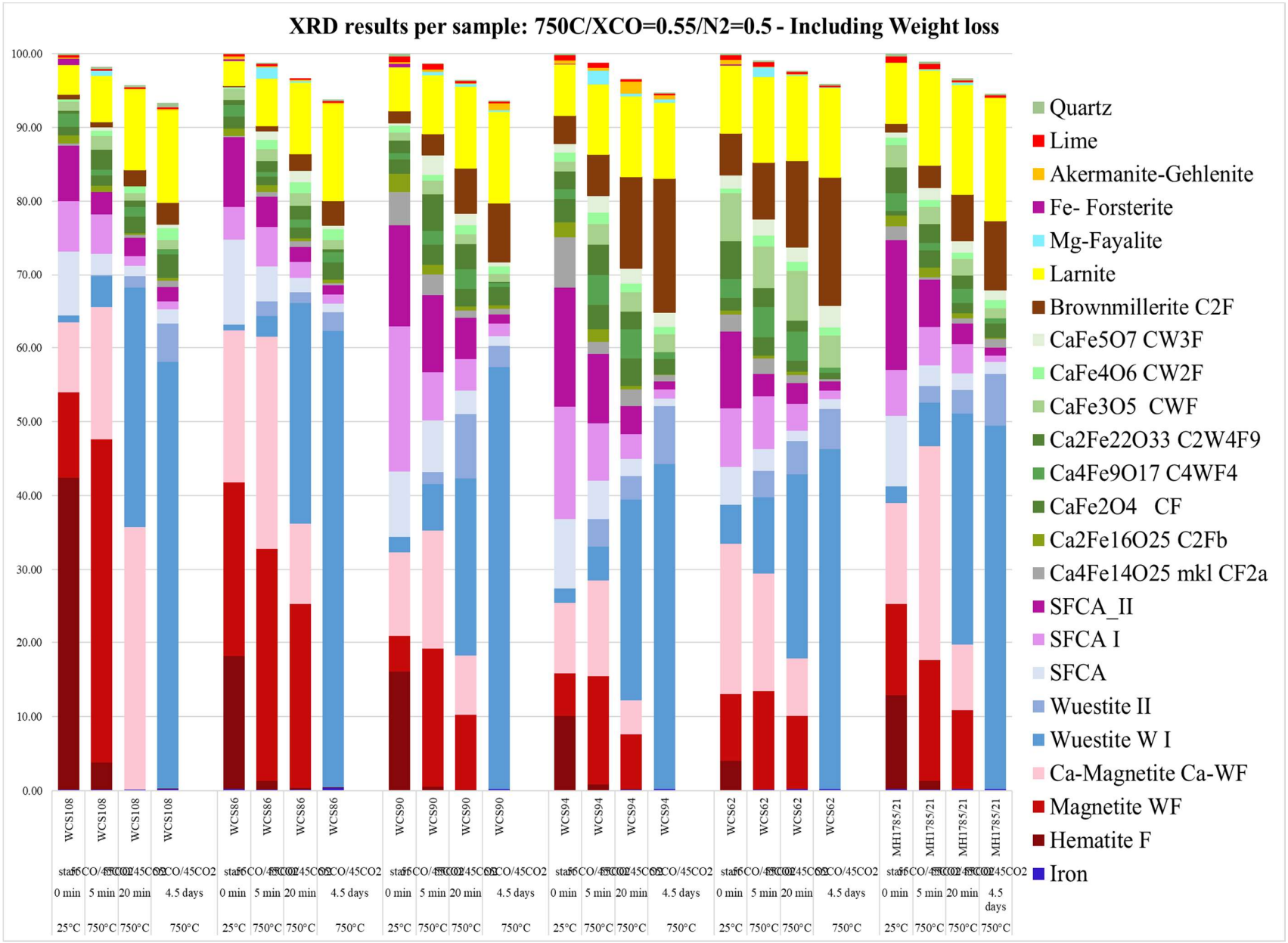

Figure 46. XRD results pre sample; 750°C/XCO=0.55/N_2=0.5

- XRD – T=950°C/XCO=0.65/N_2=0.5

As mentioned in the methodology chapter, the samples start with different initial composition, thus different staring mineralogy. The sample WCS108 starts with the highest content in Hematite, and WCS62 with the lowest. WCS86 and WCS90 have nearly the same amount of Hematite in their structures but they clearly differ in their Magnetite content, since WCS86 is the one sample that demonstrates the greatest Magnetite amounts. WCS62 is also very high in Magnetite, especially the calcium-rich type. MH1785 and WCS94 have similar starting levels of Hematite, but they also differ in Magnetite content, as MH1785 is more enriched in the mineral. As far as SFCAs are concerned, WCS90 is the one sample that presents the greatest amount, followed by WCS94 and MH1785. The greatest amount of Larnite and calcium-ferrites corresponds to the more basic samples WCS62, WCS94 and MH1785. Finally, the WCS62 is the richest in Wüstite, indicating the sample's more reduced starting state.

After reduction for 2 minutes under T=950°C, XCO=0.65/N2=0.5, Magnetite content is clearly increased in all the samples, while Hematite nearly disappears. Only WCS108 demonstrates some substantial amount of remaining Hematite in its whole. The amount of Wüstite also increases in each sample, with the greatest increase observed in WCS62, followed by WCS94, MH1785 and WCS90. The SFCA content greatly shrinks in each sample. The Ca-ferrites in their whole do not present any substantial change, but in particular CF2 seems to be displaced by the increase of CWFs for all the samples. The amount of Brownmillerite is also increased, especially in the most basic samples starting from WCS94 showing the greatest increase, followed by WCS62, MH1785 and WCS94. Larnite also appears to increase, mainly in MH1785, WCS62 and WCS90.

At t=4 minutes, under the high temperature conditions, the samples are further reduced. There is almost no Hematite content left, while the amount of Wüstite shows a great increase in all the samples, in expense of mainly Ca-Magnetite and Magnetite. Small fluctuations are observed in calcium ferrites, Brownmillerite and Larnite. The higher amount of Brownmillerite are contained in the more basic samples WCS62, WCS94, WCS90 and MH1785, also in this instance. The basic samples also show a noticeable increase in CW3F and CWF.

After the long-term reduction for 5 hours at T=950°C, XCO=0.65/N2=0.5, Hematite and both types of Magnetite are absent, as they have been completed replaced by Wüstite. Greater Wüstite content in observed in samples WCS108, WCS86 and WCS90, while WCS62 and WCS94 show relatively less content in the mineral. The basic samples, which at the previous columns of 4 minutes interruption time had showed some substantial content of CW3F, present an increase in Brownmillerite. Larnite appears to mostly remain stable in all the samples after the long hour experiment. The samples of law basicity WCS108 and WCS86 show a clear increase in Akermanite- Gehlenite, which is not the case for the very basic samples WCS62 and WCS94.

Finally, SFCA has almost been removed from the samples, while calcium ferrites have also clearly shrunk in all the samples. Normally, no SFCA is expected at this long reduction time. At long experiment times, except for Wüstite, Larnite, Brownmillerite and Melilite, the presence of the rest of the minerals corresponds to XRD fitting artefacts these are attributed to the excessive amount of Wüstite observed by the XRD, which ends up also being fitted in other phases outside Wüstite.

The different mineral phases are distinguished based on their trends during reduction in Figure 47. The first graph shows the minerals that decrease during reduction under the conditions of T=950°C, being Hematite, SFCA and CF2 types. The middle graph shows meta-stable phases that fluctuate in abundance, whereas the last graph presents increasing mineral phases during reduction. Magnetite, Ca-Magnetite and all types of CWF are meta-stable phases, while Brownmillerite, Larnite and Melilite (Akermanite-Gehlenite) show trends that are bulky increasing.

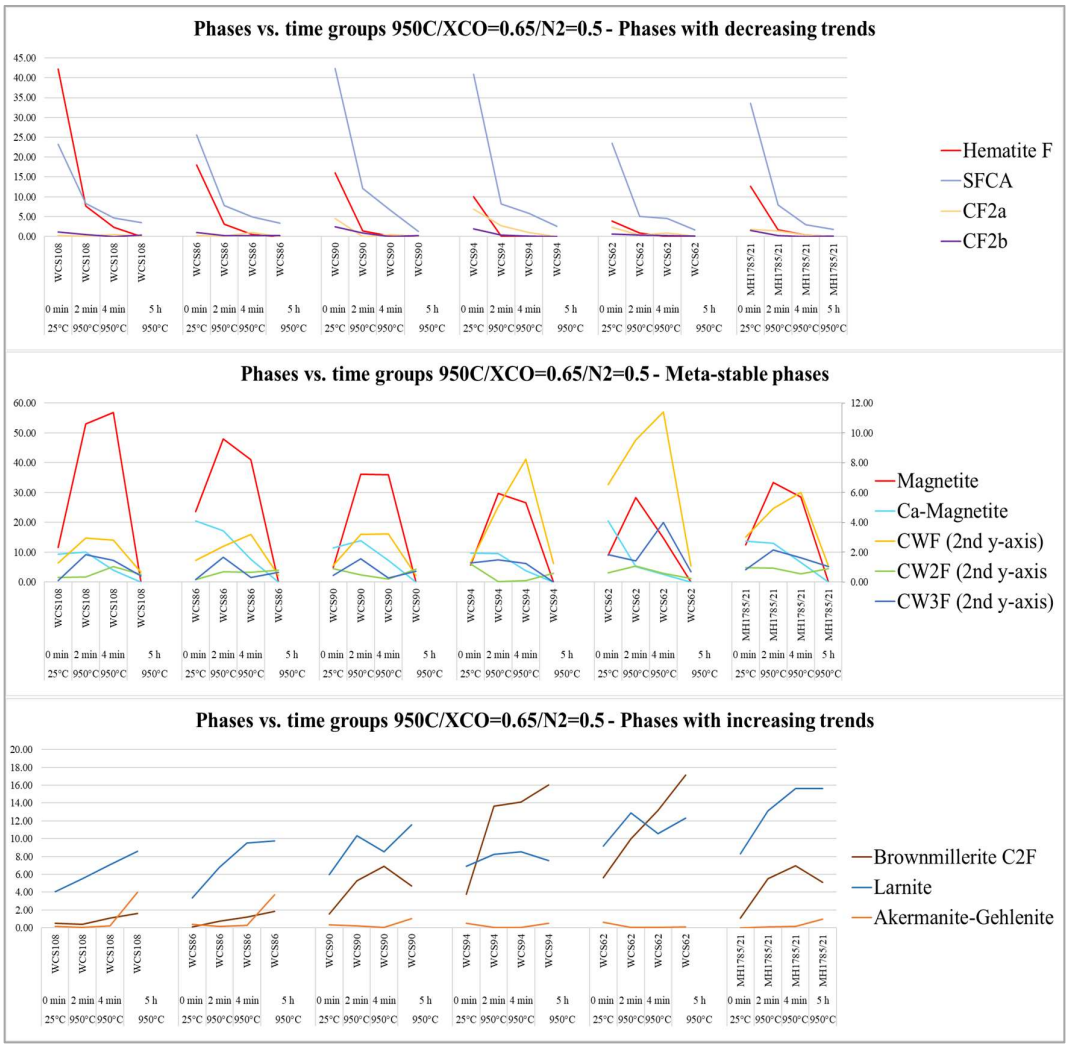

Figure 47. XRD Phase trends vs. Time groups (T=950°C/XCO=0.65/N_2=0.5).

XRD – T=750°C/XCO=0.55/N_2=0.5

After 5 minutes under the moderate experiment conditions of T=750°C, XCO=0.55/N2=0.5, the samples start to get reduced and their Hematite content decreases excessively. WCS108 still has the greatest Hematite content remaining, while it also displays the greatest amount of Magnetite and Ca-Magnetite amongst the samples. The Magnetite and Ca-Magnetite content is also higher in WCS86, followed by MH1785, WCS90, WCS62 and finally WCS94. The experiment seems to have been interrupted during the transition of Magnetite to Ca-Magnetite, as the samples show greater content in Ca-Magnetite obviously in expense of Magnetite. The greatest Wüstite content is again observed in the more basic samples, like WCS62, WCS94, WCS90 and MH1785. SFCAs decrease as reduction progresses. Calcium ferrites present small differences, with the most pronounced being the one of CF2a, which appears to decrease in favour of other calcium ferrites. There is a slight increase in Brownmillerite and Larnite in all the samples.

At t=20 minutes, reduction is more progressed, as Hematite content is completely removed, and Magnetite seems to be decreasing in favour of Wüstite formation. Wüstite content is high, and in similar levels for all the samples. The SFCAs have decreased one step further and calcium ferrites show very small fluctuations, with some increasing after the decrease of others. Brownmillerite content shows a proportional increase in all the samples, while Larnite levels remain stable.

After reduction in the furnace for 4.5 days, under the moderate conditions, the samples only contain Wüstite in their greater extent. Also, in this case, most Wüstite content is observed in samples of relatively lower basicity like WCS86, WCS108 and the moderate basicity WCS90. Brownmillerite content seems to have grown proportionally in all the samples, while content in Larnite remains stable. As mentioned before, the rest of the phases in the assemblage most possibly are XRD fitting artefacts, due to the fitting of Wüstite amounts in different phases.

Figure 48 shows certain mineral phases from the XRD assemblage coupled together based on their trends during reduction under the conditions of T=750°C. The graph at the top of the figure shows the minerals that generally tend to decrease during reduction (Hematite, SFCA and CF2 types). The middle graph shows meta-stable phases, with instable amounts during reduction (Magnetite, Ca-Magnetite and all types of CWF). Finally, the graph at the bottom, depicts mineral phases with overall increasing trends during reduction (Brownmillerite, Larnite and Melilite – displayed as "Akermanite-Gehlenite").

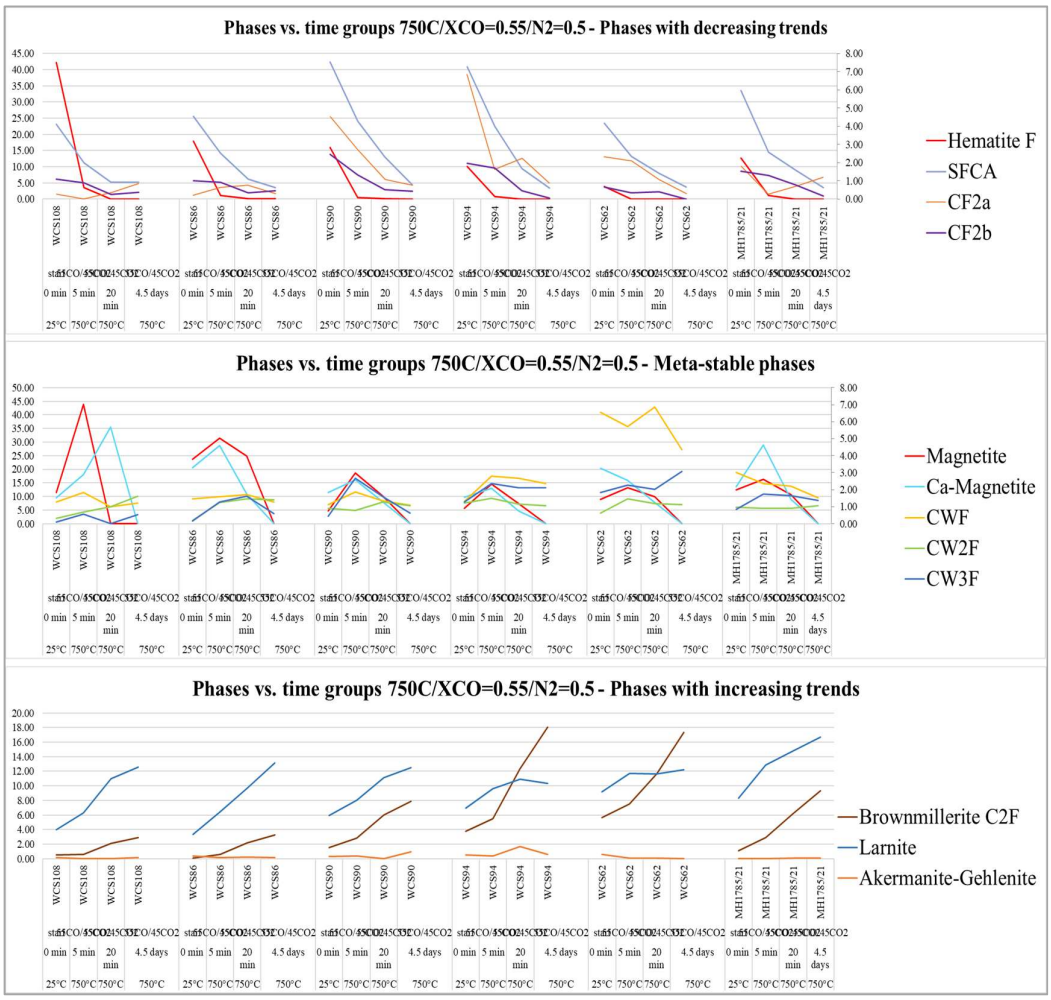

Figure 48. XRD Phase trends vs. Time groups (T=750°C/XCO=0.55/N_2=0.5).

5.3. Thermodynamic modelling

5.3.1. O/Fe at equilibrium

Figure 49 and Figure 50 display the predicted O/Fe values for each sample at equilibrium, as calculated by FactSage software under the conditions of T=950°C/XCO=0.65/N_2=0.5 and T=750°C/XCO=0.55/N_2=0.5 respectively. The FactSage results (blue line) are combined with the O/Fe values of the samples at the end of TGA experiments and the O/Fe values after the long-run reduction experiments in the GERO furnace. Four samples (WCS108, WCS86, WCS90 and WCS62) have TGA values for the conditions of T=750°C, and two samples (WCS108, WCS62) for the conditions of T=950°C.

According to the graph of Figure 49, the majority of GERO results is in good agreement with FactSage predictions. The reduction of samples WCS86, WCS94 and WCS62 is very close to what is projected by the software, with WCS62 to be slightly more reduced. WCS108 and WCS90 reductions are also underestimated by FactSage, with the highest deviation being Δ(O/Fe) =+0.03.

When comparing TGA results with thermodynamic calculations; WCS108 is in close agreement to FactSage prediction after 35 minutes in the TGA (Δ(O/Fe) =-0.008)., while WCS62 is highly underestimated by the theoretical expectation Δ(O/Fe) =+0.05).

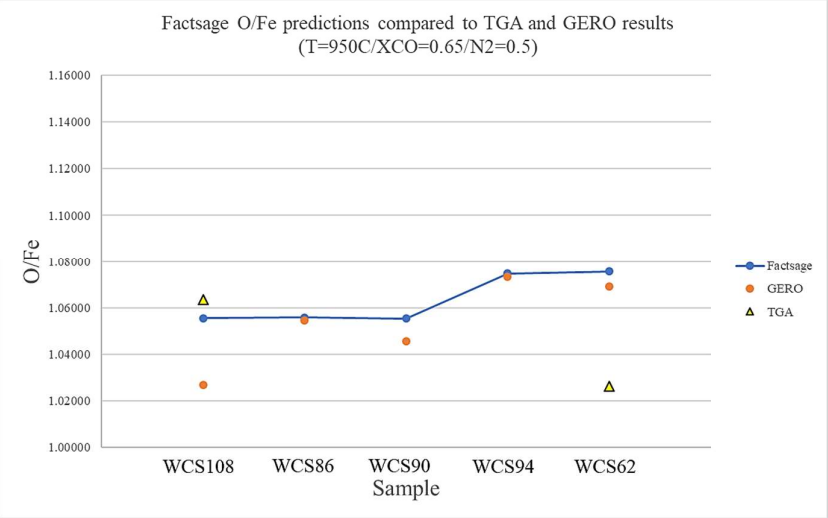

Figure 49. FactSage O/Fe predictions compared to TGA and GERO results (T=950°C/XCO=0.65/N_2=0.5).

Figure 50 shows the FactSage results for the conditions of T=750°C/XCO=0.55/N_2=0.5 compared to the respective GERO and TGA results. According to the graph, most of the samples are not yet at FactSage's predicted equilibrium, with certain exceptions.

The TGA O/Fe results of WCS108, WCS86 and WCS62 fall behind compared to FactSage predicted values, indicating that the samples are not yet at their final assemblage state based on thermodynamic calculations. The only exception is the TGA result of WCS90, which contrastingly underestimated by the software, while the rest of TGA results are overestimated.

The same pattern is observed also regarding the GERO O/Fe values. WCS108, WCS86, WCS94 and WCS62 show similar relative negative distance between their GERO outcomes and FactSage predicted O/Fe values. The only GERO O/Fe result that stands out is the one WCS90, which in fact more reduced after 5 hours in the GERO than what FactSage predicts. All in all, deviations of GERO results from the FactSage line are not that great, with the highest being $\Delta(O/Fe)_{WCS108}$=-0.01. The numbers from the TGA curves also approach the FactSage values, although they do not approach as close as the GERO results.

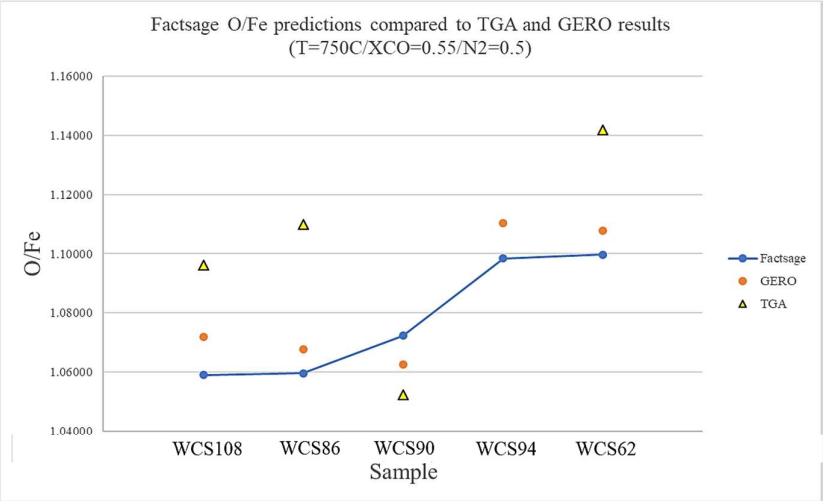

Figure 50. FactSage O/Fe predictions compared to TGA and GERO results (T=750ºC/XCO=0.55/N_2=0.5).

5.3.2. Phase assemblage at equilibrium

The results from the FactSage software include the final equilibrium phase assemblage and the overall redox state of different starting compositions, at the relevant range of temperature and imposed gas composition. The thermodynamic diagrams are presented in Figure 51 and Figure 53, for the two conditions of T=750ºC and 950ºC, respectively. The phases expected at equilibrium are compared with the XRD results to examine whether the thermodynamic predictions are in consent with what was revealed in practice. According to Figure 51, at 950ºC/ XCO=0.65/N2=0.50, only 4 mineral phases are expected to remain present in the sinter samples at equilibrium; these are Wüstite (MeO_#1), Larnite (C2S), Brownmillerite (C2F) and Melilite (C2AS).

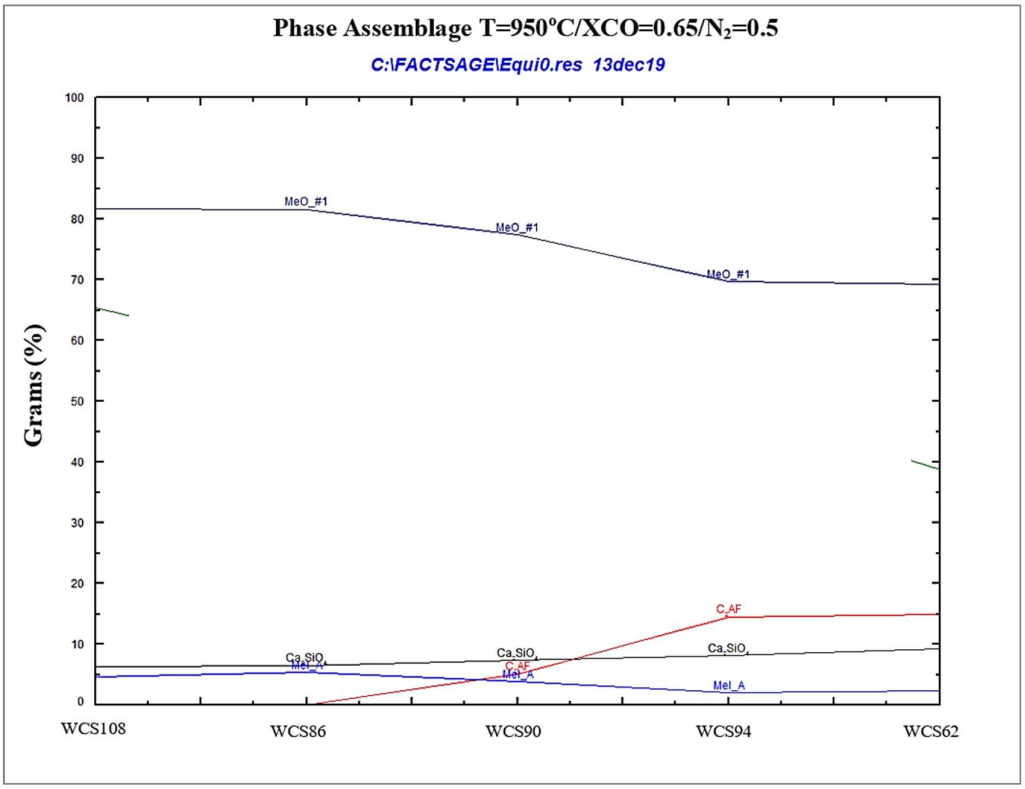

Figure 51. FactSage diagram; Expected phase assemblage at equilibrium per sample, under the conditions of T=950ºC/XCO=0.65/N_2=0.5.

More specifically, Wüstite is expected to be more abundant in the low basicity samples, WCS108 and WCS86, while its amount decreases towards the rest of the samples staring from WCS90, to WCS94 and WCS62. Brownmillerite (C2AF) is only present in WCS90, WCS94 and WCS62. It increases as samples increase in basicity; hence its greater amounts are expected in the most basic samples WCS94 and WCS62. As far as Larnite (C2S) is concerned, it is projected that the phase should be present in all the samples in quite similar levels at equilibrium. Finally, Melilite is also predicted to form in all the samples, with its greater quantities to correspond to samples with lower basicity and breeze content, like WCS108 and WCS86. Its lowest amounts are expected in WCS94 and WCS62.

Comparing this result with the XRD analysis of the actual sinter materials, shows possible correlation with the thermodynamic predictions. The diagram resulting from the XRD analysis is shown in Figure 52. The complete XRD assemblage includes much more phases than the ones presented; hence, FactSage results and XRD differ quantitively. The difference in the phases, is mostly attributed to limitations in the XRD analysis. This means that, except for Wüstite, Larnite, Brownmillerite and Melilite, the presence of the rest of the minerals corresponds to XRD fitting artefacts. This discrepancy is attributed to the excessive amount of Wüstite observed by the XRD, which ends up also being fitted into other phases.

Hence, the current graph includes only the 4 main phases expected at equilibrium, which were obtained from the XRD analysis assemblages and were normalized to the respective GERO weight losses for each sample. In addition, heterogeneity throughout the different grains in the samples also plays a role, since it has a clear effect in the differences observed between the XRD and FactSage assemblages.

In addition, even with the major phases only included in the XRD assemblage, there is a quantitative difference in all the phases compared to FactSage. However, the relative way the main mineral phases fluctuate between the different samples appears to be closely aligned with the predictions of the thermodynamic calculations. After the long-hours experiments, when the phases are relatively the closest to the equilibrium state, Wüstite is indeed more abundant in WCS108 and WCS86, followed by WCS90, WCS94 and finally WCS62.

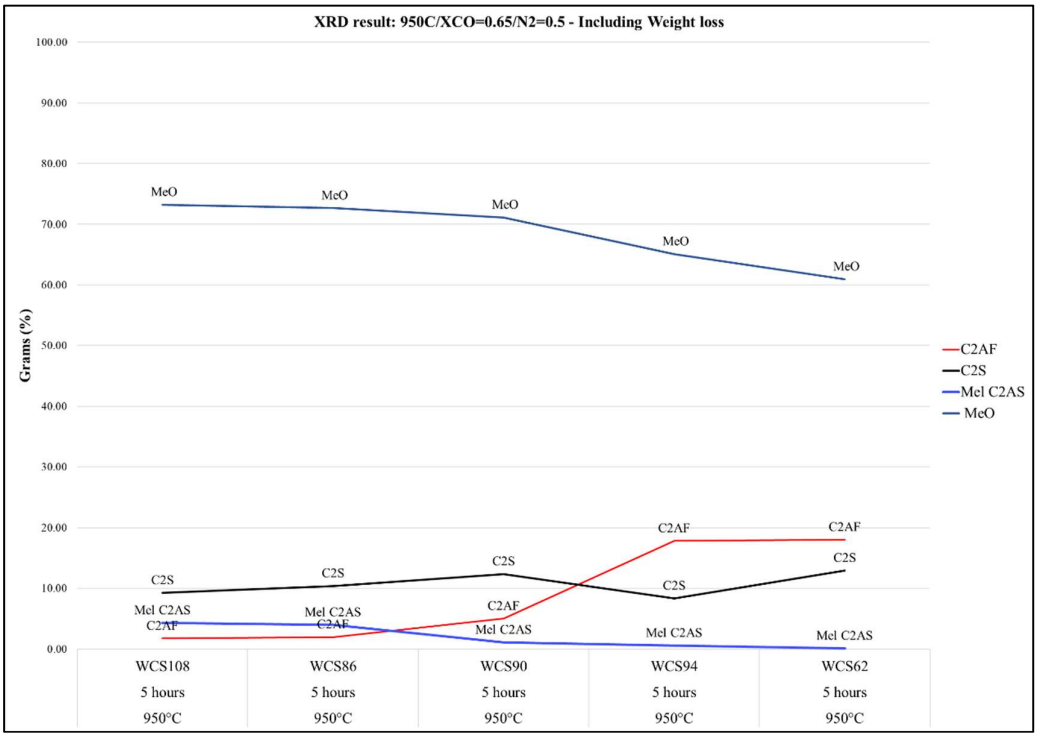

Figure 52. XRD graph; Main phases per sample after long time experiment (t=5hours) at T=950°C/XCO=0.65/N_2=0.5.

In comparison with the FactSage prediction, WCS90 shows a smaller relative difference in Wüstite content with the two samples of lower basicity, WCS86 and WCS108 in the XRD outcome. In addition, a greater difference in Wüstite content is observed between the high basicity samples WCS94 and WCS62, which is not so clearly projected in Figure 51. The general trend is closely in line with the prediction of FactSage, which demonstrates the same relative order in Wüstite relative amounts. Based on Wüstite quantities, FactSage seems to overestimate the minerals content in all the samples by approximately 10%.

The same is observed for Brownmillerite which, based on XRD, is mostly abundant in the samples of higher basicity WCS94 and WCS62, in lesser amounts in WCS90 and low in WCS108 and WCS86, which are of low basicity. In FactSage the low basicity samples appear to have no content in Brownmillerite, showing that if reduction continued transforming these samples, the small amounts of Brownmillerite should gradually tend to disappear. However, the heterogeneity of the sinter samples can also be an attributing factor to these differences. In addition, in the samples where FactSage does show substantial Brownmillerite amounts forming, their abundance is slightly overestimated by nearly 5%.

The presence of Larnite (C2S) in the XRD, shows more fluctuations throughout the different samples when compared with FactSage results. While, the mineral appears to be quite constant throughout the different samples in FactSage, the XRD graph shows its amount to be firmly lower in WCS94, in comparison with the rest of the samples. Quantity wise, the mineral is found in greater amounts in the samples than what FactSage predicts.

Finally, Melilite content per sample is in close agreement with FactSage predictions, as it appears to be more abundant in samples WCS108 and WCS86, while its amount decreases in samples of higher basicity. The difference with the thermodynamic prediction is at sample WCS90, which appears to be slightly overestimated in FactSage.

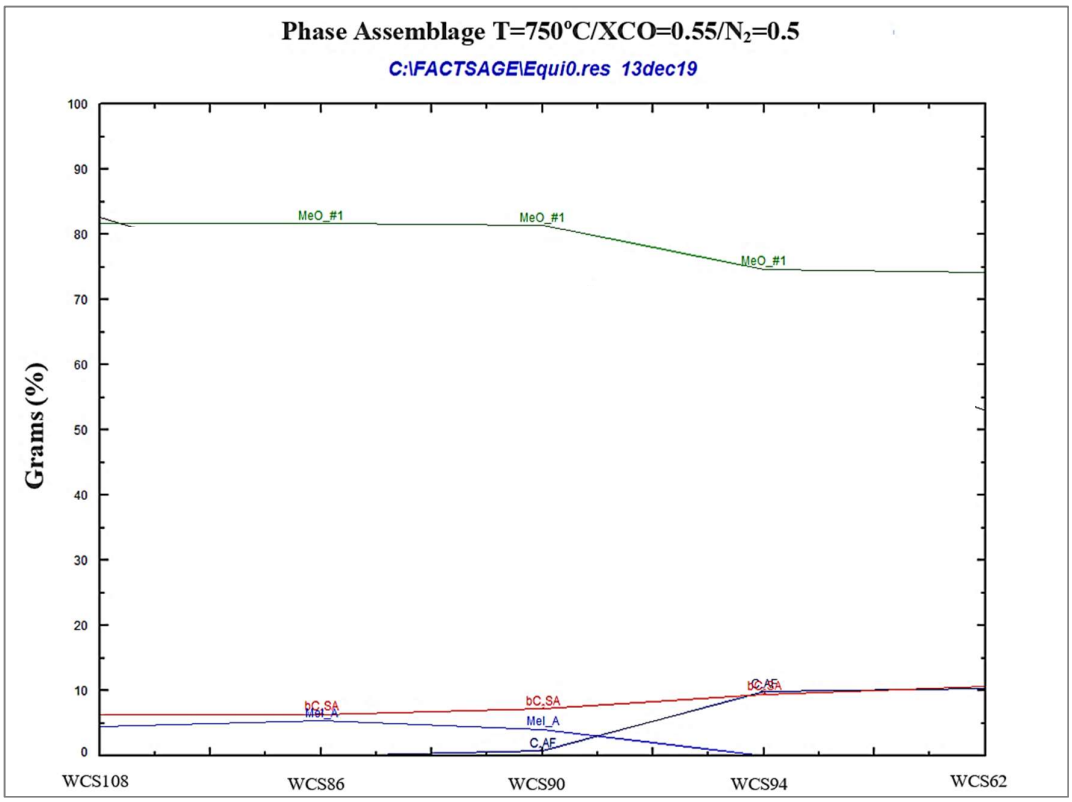

Figure 53. FactSage diagram; Expected phase assemblage at equilibrium per sample, under the conditions of T=750°C/XCO=0.55/N_2=0.5.

At 750°C/ XCO=0.65/N_2=0.50, the phase assemblage proportions are expected to look slightly different in relation to the high temperature conditions. The same minerals appear to

be present also in this instance, being Wüstite, Larnite (bC_2SA), Brownmillerite (C_2AF) and Melilite (C_2AS). Based on FactSage prediction, Wüstite is more abundant in samples with lower basicity. It is also expected to be present in similar levels in sample WCS90, which at 950ºC was shown to contain relatively less amount of Wüstite in comparison to WCS86 and WCS108. Brownmillerite is again solely expected to appear in samples of higher basicity, like WCS90, WCS94 and WCS62, but it is proportionally less than its respective amount appearing in the phase assemblage under T=950ºC. Larnite shows more fluctuations between samples than in 950ºC, since it shows a slight increase with samples of higher basicity. Melilite is only present in samples of lower basicity and WCS90, and no content in the mineral is expected in higher basicity samples.

In the actual XRD results (Figure 54), phase quantities again differ, even though there is a high qualitative correlation with FactSage. More definitely, Wüstite quantities are highly overestimated in FactSage predictions, especially in samples of higher basicity. However, its relative trend regarding the samples is in great agreement with the software result. Samples of lower basicity are indeed richer in Wüstite in comparison to WCS94 and WCS62. A discrepancy is observed regarding WCS90, which shows lower Wüstite content than WCS86 and WCS108, while in Figure 53 (FactSage) it shows similar levels with the two samples.

Brownmillerite is increasing towards samples of higher basicity, but it is present in all the samples in contrast with the FactSage outcome, where it is only present in the high basicity samples. WCS90 demonstrates a greater amount of Brownmillerite than the one predicted. Moreover, Brownmillerite quantities are found to be much greater in all the samples than in the thermodynamic predictions. Finally, Larnite is also highly underestimated by the software. However, quantitatively, it is closely in line with the thermodynamic calculation, only displaying difference regarding WCS94. The sample's content in the mineral is slightly lower than in the rest of the samples. Melilite content is marginal in all the samples according to XRD, with a slight increase in WCS90. This is not in line with the prediction, where Melilite is only expected to be solely present in WCS108, WCS86 and WCS90 in relatively greater amounts.

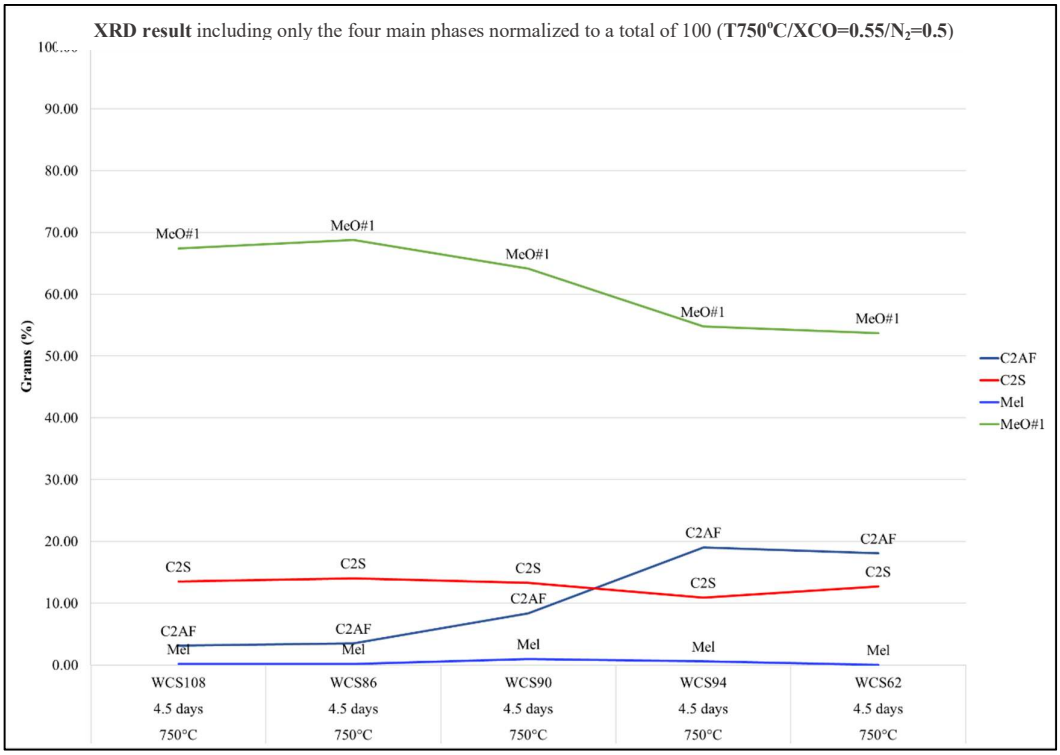

Figure 54. XRD graph; Main phases per sample after long time experiment (t= 4.5days) at T=750ºC/XCO=0.65/N_2=0.5.

5.4. Polarized Reflected light Optical Microscopy and Scanning Electron Microscopy -Analysis of microstructure

This section presents the images taken from the microscopical analysis of the reduced samples after the GERO experiments. The aim is to demonstrate the reduction footprint in specific particles, by freezing active reduction fronts, as these are passing through the individual sinter mineral crystals. This makes it possible to observe starting and reduced microstructures within only one grain and form educative interpretations regarding the impact of reduction on microstructure and different minerals. The following optical micrscope and SEM images were selected with the aim to show an overview of the different structures seen in the reduced different samples of different initial composition, different experiment times and different conditions. Special focus is paid on presenting unreacted cores and reduction fronts of different mineral types.

All six samples were included in a cross section each time, based on their reduction experiment. Six cross sections were made in total in order to capture each sample after t=2minutes, t=4 minutes and t=5hours reduction in the GERO furnace under T=950ºC/XCO=0.65/N_2=0.5, and after t=5minutes, t=20 minutes and t=4.5days reduction under T=750ºC/XCO=0.65/N_2=0.5.

Hence, a total of 36 mosaic pictures were taken in order to seize an overview of the grains of each sample at the specified interruption times and reduction conditions. A mosaic image results from the stitching of numerous individual images taken at 20x time magnification under the microscope. Each picture illustrates dozens of sample grains. Examples of the mosaic pictures are given in Figure 55.

Figure 55. Examples of mosaic images undertaken from optical microscopy; including a close-up of the mosaic of sample WCS90 for T=950ºC, XCO=0.65, N_2=0.5/ t=5hours in the GERO.

5.4.1. Classification of identified microstructures in the sinter samples

- Types of microstructures in starting sinter material

The sinters demonstrate complex microstructures, developing in various forms and patterns, which can differ from grain to grain in a single sample. A plethora of those microstructures is associated with the sintering process, where primary phases may undergo transformation. Therefore, these unique formation patterns consist sinters as highly heterogeneous materials. According to the mineral phases present and their formation mode, microstructures found in different particles can be distinguished, and be fitted into different broad categories. The starting sinter materials in this study are characterized by four main different microstructural types, displayed in Table 13.

Table 13. Types of microstructures identified in initial sinter samples

Types of microstructures identified in initial sinter samples	
Type 1	Precipitated Hematite with acicular Fe-rich SFCA I, precipitated Magnetite, Larnite and other calcium ferrites
Type 2	Precipitated Hematite with tabular (blue) Ca-Si-rich SFCA/SFCA II, precipitated Magnetite, Larnite and other calcium ferrites
Type 3	Ore relict Hematite particle surrounded by Magnetite ore
	Hematite lamella exsolution on Magnetite ore
Type 4	Precipitated Magnetite with calcium ferrites and calcium silicates

These microstructures contain important major phases that can be optically identified, also contained within the broader XRD assemblage. These major minerals are linked to certain microstructure types and formation modes in Table 14.

Table 14. Main mineral phases linked to different types of microstructures and phases is the XRD.

Main phases in microstructures	Formation mechanism	Present in microstructure	Displayed in the XRD as:
Primary Hematite	Ore particle	Ore relict particle	Hematite
Secondary Hematite	sub-solidus oxidation within ore particle (normally an originally Magnetite-rich ore)	Hematite lamella exsolution on Magnetite ore	Hematite
	precipitated from melt – various sub-categories possible based on morphology	Precipitated Hematite with precipitated Magnetite and Ca-ferrites	Hematite
Primary Magnetite	Ore particle	Ore relict particle	Magnetite
Secondary Magnetite	Formed from solid-state reduction of Hematite ore particle	Magnetite rims within otherwise Hematite ore particles	Magnetite
	Precipitated from melt –various sub-categories possible based on morphology	Precipitated Hematite with precipitated Magnetite and Ca-ferrites/ Precipitated Magnetite with precipitated Ca-ferrites	Ca-Magnetite/Magnetite
Ca-ferrite acicular Ca-ferrite columnar Ca-ferrite tabular Ca-ferrite dendritic and others.	Precipitated from melt –various sub-categories possible based on morphology	Precipitated Hematite with precipitated Magnetite and Ca-ferrites/ Precipitated Magnetite with precipitated Ca-ferrites	SFCA, SFCAI, SFCAII, CF2a, CF2b, CF, C4WF4, C2W4F9, CWF, CW2F, CW3F, C2F

- Types of microstructures in reacted sinter material

Generally, four main microstructures were identified in all sinter samples, regardless of their starting composition. The difference in sample mineralogy due to compositional differences is imprinted in the abundance of specific microstructures, and the lack of others. The four different types of microstructures observed are presented in Table 15;

Table 15. Types of microstructures identified in the reduced sinter samples.

Types of microstructures identified in the reduced sinter samples	
Type 1	• Unreacted core; Precipitated Hematite with acicular Fe-rich SFCA I/II, precipitated Magnetite (Mt^1), Larnite and other calcium ferrites • Reacted front; newly formed Magnetite (Mt^2) and porosity from transition from former Hematite, a multiphase intergrowth resulting from SFCA 1 including Wüstite. Unreacted Larnite and other calcium ferrites
Type 2	• Unreacted core; Precipitated Hematite with tabular (blue) Ca-Si-rich SFCA/SFCA II, precipitated Magnetite (Mt^1), Larnite and other calcium ferrites • Reacted front; newly formed Magnetite (Mt^2) from former Hematite, newly formed (brown) SFCA from former (blue) SFCA, Larnite and other calcium ferrites.
Type 3	Ore relict Hematite particle surrounded by Magnetite
Type 4	Precipitated Magnetite with calcium ferrites

5.4.2. Microstructures after short experiments

i. Microstructure Type 1 –conditions of T=950°C/XCO=0.65/N_2=0.5

The microstructure of type 1 was found present in all the samples. It is observed in greater abundance in samples with higher starting Hematite content and short reduction times, where Hematite remains unreacted to a greater extend. Samples with higher basicity demonstrate it often without any Hematite in the structure, including only the rest of the mineral phases. Examples from **microstructure-1** are presented in the following optical and scan electron microscope images taken from various sinter samples.

Low basicity samples - Microstructure 1a

A typical image of this **microstructure 1** is presented in Figure 56. The particle is taken from the lowest basicity sample **WCS108** after reduction for t=2minutes under the intense conditions of **T=950°C** in the GERO furnace.

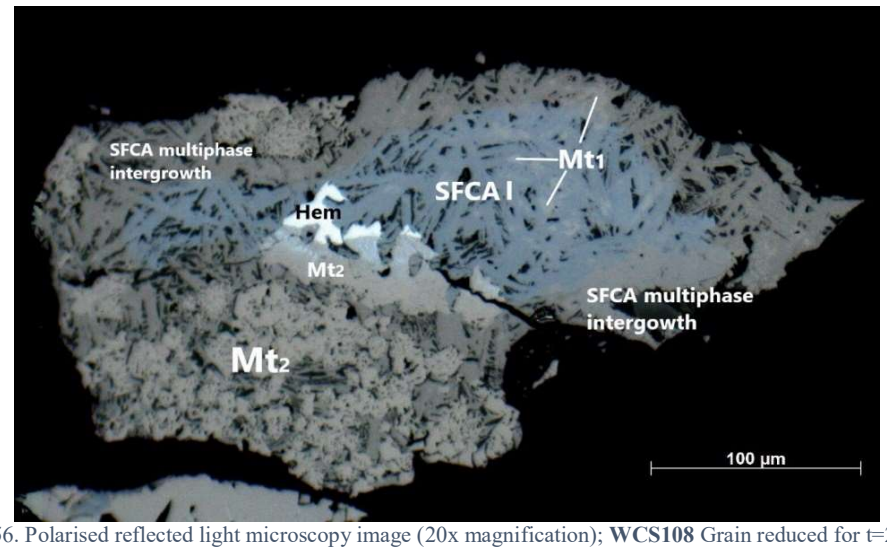

Figure 56. Polarised reflected light microscopy image (20x magnification); **WCS108** Grain reduced for t=2minutes under T=950°C/XCO=0.65/N_2=0.50 in the GERO furnace; **Microstructure type 1.**

The phases identified are labeled on the sinter grain. The sinter particle demonstrates a reduction front, separating the area that has been altered due to reduction and the unreacted core, which preserves the initial sinter microstructure. The main minerals observed in the unreacted part, which is in the core of the particle, are precipitated Hematite, SFCA-I, and precipitated Magnetite; *Precipitated Hematite* is the mineral with the brightest color in the picture due to its higher Fe-content, characterized by light-grey/white idiomorphic crystals. *SFCA-I* has a blue color at the unreacted part and develops in typical acicular structures in this grain. In addition, SFCA-I is intergrown with *precipitated Magnetite (Mt^1)*, which is the grey colored- phase observed between the SFCA crystals, and Larnite C2S. *Larnite C2S* forms very small crystals that are not much visible in the overview image, rather than in SEM imagery. All these minerals were precipitated during the sintering process, which took place prior to the reduction experiments.

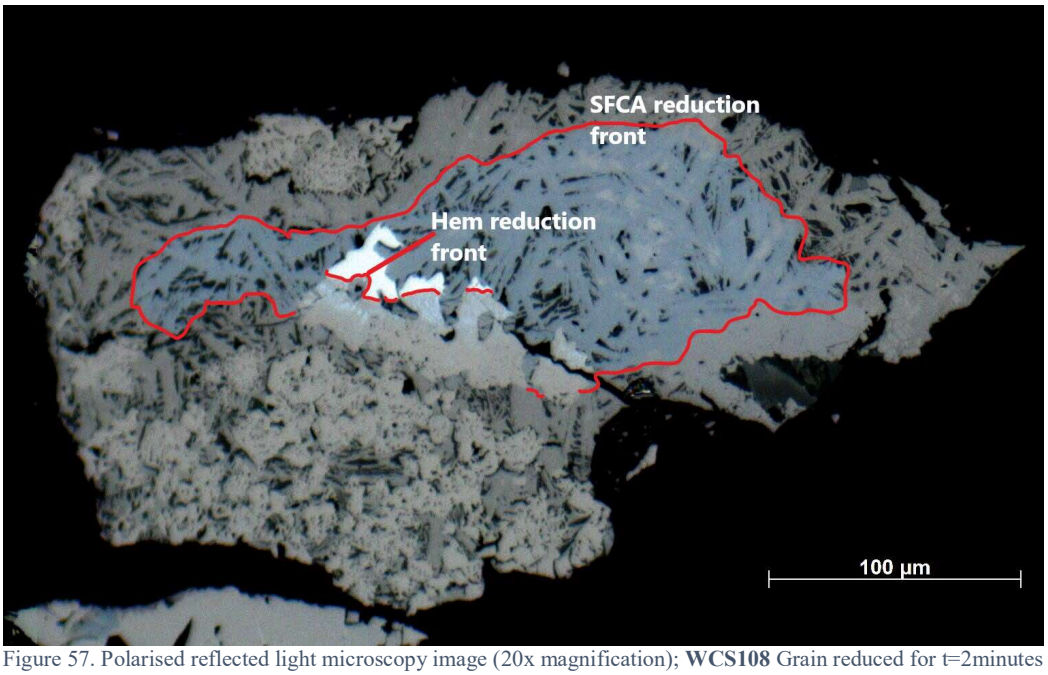

Figure 57. Polarised reflected light microscopy image (20x magnification); **WCS108** Grain reduced for t=2minutes under T=950ºC/XCO=0.65/N_2=0.50 in the GERO furnace; **Reduction fronts of Hematite and SFCA I.**

The boundary of the unreacted core is marked with as red line in Figure 57. It can be seen from the drawing that the Hematite reduction front is deeper in the particle than the respective SFCA reaction front. This indicates that SFCA is more resistant to reduction than Hematite under certain conditions, hence, it can stay stable for longer. Representative SEM chemical analyses of the minerals of the current particle is shown in Table 16, where three representative analysis are given for each mineral. It can be seen from the spot analysis that the SFCA present in this microstructure is the high-Fe type, thus it is referred to as SFCA I.

At the reacted part of the particle, the minerals clearly change their color and/or apparent texture. The reduction products are *newly formed Magnetite (Mt^2)*, developed by the transition of former Hematite, and the *SFCA multiphase intergrowth* which has a brown/grey color in contrast with the initial blue looking SFCA. The newly formed Magnetite appears with numerous dark spots on its structure and shows a different texture compared to the smoother looking precipitated Magnetite. This is because transition from Hematite generates porosity simultaneously to Magnetite's formation. This change in the texture from the phase alteration is more clearly shown in the scatter electron image in Figure 58.

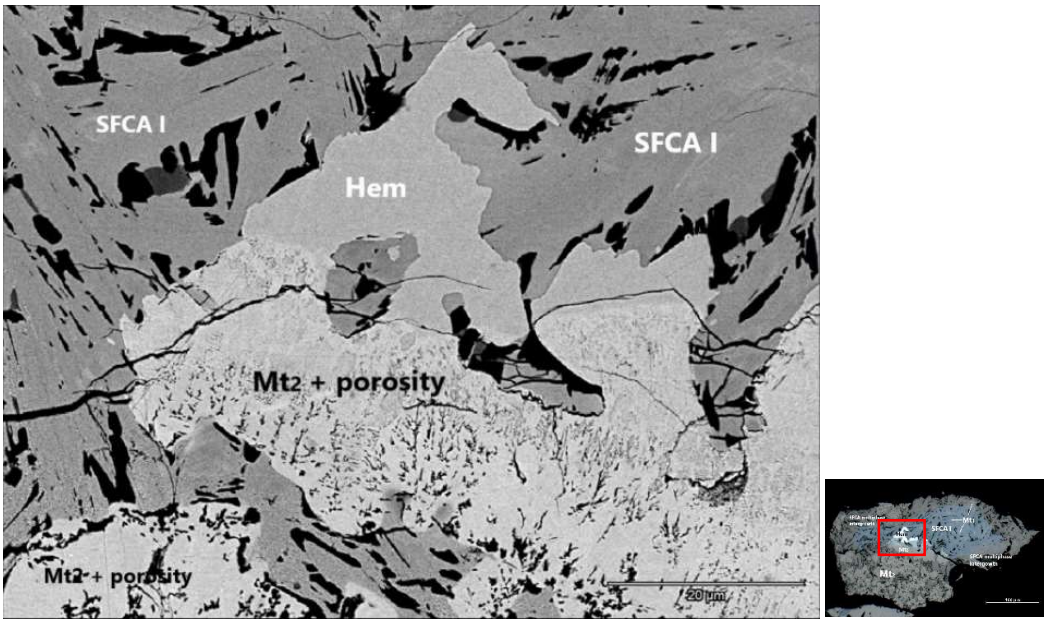

Figure 58. SEM (scanning electron microscope) image. (**WCS108**, t=2min, T=950ºC); Hematite transition to secondary Magnetite and the formation of porosity (**Hem →Mt_2 +porosity**).

Precipitated Hematite has a smooth and clean appearance in its original form, but once it becomes Magnetite, disintegration appears on its surface, escalating to dendritic structures which become coarser and coarser towards the outer areas of the particle. Secondary Magnetite from reduction, is also identified by its different spectrum signal under the SEM. Figure 59 shows the spectrometry of Hematite and Magnetite plotted together at live time.

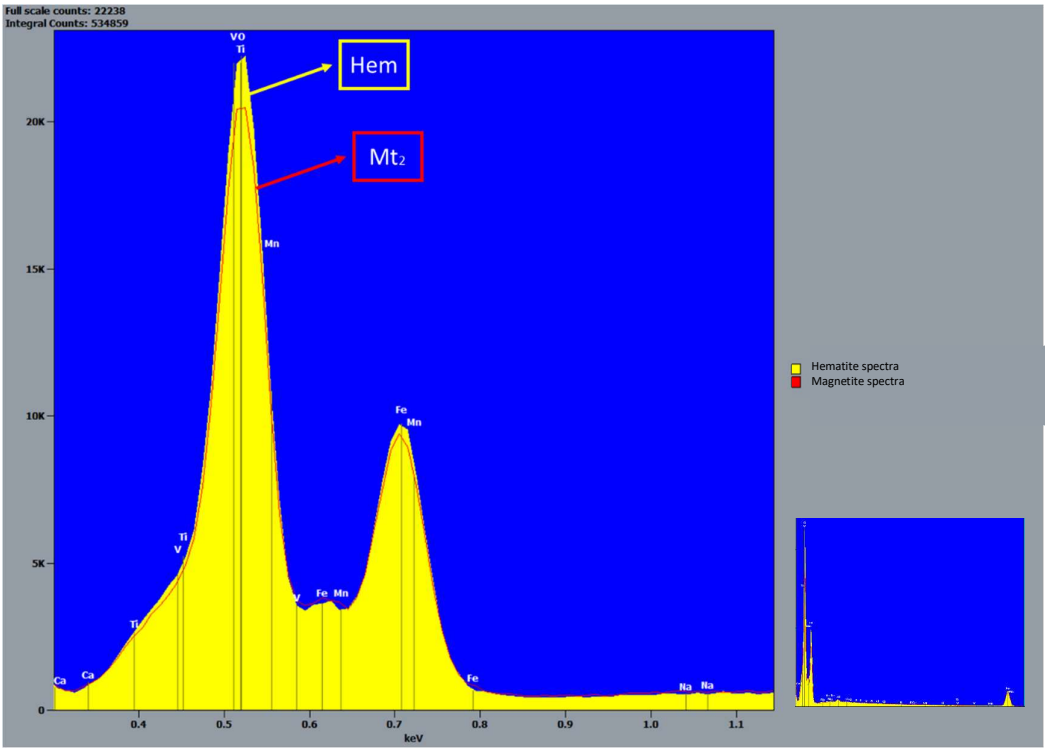

Figure 59. Comparison of Hematite and Secondary Magnetite spectra.

Table 16. Representative SEM chemical analyses, of the main minerals present in microstructure type 1 of sample WCS108 after 2-minute reduction under T=950°C/XCO=0,65/N_2=0.5 in the GERO furnace.

Mineral	Hematite			Secondary Magnetite			Precipitated Magnetite			SFCA-I			C2S			wustite		
Atom %																		
C	0.00	0.00	0.00	0.00	0.00	0.00	0.00	0.00	0.00	0.00	0.00	0.00	0.00	0.00	0.00	0.00	0.00	0.00
O	50.20	50.25	50.27	50.11	50.23	50.15	50.19	50.29	50.19	50.33	50.93	50.90	56.95	56.86	57.04	50.18	50.16	50.20
Na	0.10	0.08	0.07	0.07	0.00	0.03	0.02	0.12	0.10	0.12	0.10	0.13	0.21	0.19	0.20	0.00	0.02	0.01
Mg	0.08	0.13	0.11	0.00	0.10	0.11	2.40	2.85	3.41	1.63	0.86	2.23	0.01	0.01	0.03	0.06	0.10	0.13
Al	0.58	0.68	0.65	0.24	0.31	0.28	0.27	0.69	0.34	0.99	1.20	1.42	0.03	0.02	0.01	0.36	0.29	0.32
Si	0.13	0.11	0.15	0.15	0.28	0.16	0.18	0.16	0.20	0.13	1.30	1.01	13.11	13.01	13.06	0.09	0.15	0.14
P	0.00	0.01	0.02	0.02	0.01	0.01	0.04	0.02	0.02	0.01	0.00	0.01	0.51	0.36	0.68	0.00	0.00	0.00
S	0.00	0.00	0.02	0.00	0.01	0.00	0.00	0.00	0.00	0.01	0.00	0.00	0.03	0.03	0.04	0.00	0.02	0.00
Cl	0.00	0.00	0.01	0.01	0.00	0.00	0.00	0.02	0.00	0.00	0.01	0.00	0.01	0.01	0.00	0.00	0.00	0.00
K	0.00	0.00	0.04	0.06	0.00	0.00	0.00	0.00	0.00	0.00	0.00	0.00	0.04	0.07	0.10	0.00	0.00	0.00
Ca	0.10	0.14	0.12	0.22	0.09	0.16	1.17	1.65	1.92	5.24	6.79	6.54	27.63	27.37	27.31	0.39	0.41	0.33
Ti	0.02	0.04	0.13	0.00	0.01	0.00	0.01	0.00	0.00	0.00	0.00	0.03	0.05	0.23	0.04	0.01	0.00	0.00
V	0.00	0.02	0.00	0.00	0.00	0.00	0.00	0.08	0.02	0.06	0.02	0.08	0.09	0.07	0.10	0.05	0.04	0.07
Mn	0.04	0.04	0.19	0.07	0.00	0.21	0.34	0.40	0.43	0.37	0.07	0.31	0.00	0.00	0.00	0.26	0.27	0.30
Fe	48.75	48.50	48.23	49.05	48.96	48.90	45.39	43.74	43.36	41.13	38.72	37.34	1.33	1.78	1.39	48.61	48.55	48.49
Oxide wt%																		
Na2O	0.09	0.07	0.06	0.06	0.00	0.02	0.02	0.11	0.09	0.11	0.09	0.12	0.26	0.24	0.25	0.00	0.02	0.01
MgO	0.09	0.14	0.12	0.00	0.11	0.12	2.78	3.34	4.01	1.92	1.04	2.72	0.01	0.01	0.05	0.06	0.11	0.15
Al2O3	0.83	0.98	0.93	0.34	0.45	0.40	0.39	1.02	0.51	1.48	1.83	2.18	0.07	0.04	0.02	0.51	0.41	0.46
SiO2	0.22	0.19	0.26	0.26	0.47	0.26	0.31	0.27	0.34	0.23	2.34	1.83	31.60	31.19	31.50	0.15	0.25	0.24
P2O5	0.00	0.01	0.03	0.03	0.02	0.02	0.08	0.04	0.05	0.01	0.00	0.01	1.44	1.03	1.95	0.00	0.01	0.00
S	0.00	0.00	0.01	0.00	0.01	0.00	0.00	0.00	0.00	0.01	0.00	0.00	0.04	0.04	0.05	0.00	0.02	0.00
Cl	0.00	0.00	0.01	0.01	0.00	0.00	0.00	0.02	0.00	0.00	0.01	0.00	0.01	0.01	0.00	0.00	0.00	0.00
K2O	0.00	0.00	0.05	0.07	0.00	0.00	0.00	0.00	0.00	0.00	0.00	0.00	0.08	0.12	0.19	0.00	0.01	0.00
CaO	0.16	0.21	0.19	0.35	0.14	0.25	1.88	2.69	3.14	8.62	11.37	11.09	62.16	61.24	61.49	0.62	0.65	0.52
TiO2	0.04	0.10	0.29	0.00	0.03	0.00	0.01	0.00	0.00	0.00	0.00	0.06	0.15	0.72	0.13	0.03	0.00	0.00
V2O5	0.00	0.05	0.00	0.00	0.00	0.00	0.00	0.21	0.05	0.16	0.05	0.22	0.34	0.26	0.37	0.13	0.09	0.18
MnO	0.08	0.09	0.38	0.15	0.00	0.42	0.70	0.82	0.89	0.77	0.14	0.67	0.00	0.00	0.00	0.51	0.54	0.61
FeO	98.49	98.15	97.66	98.72	98.78	98.50	93.82	91.48	90.91	86.70	83.13	81.09	3.84	5.10	4.01	97.99	97.90	97.83
[Fe+Al]/[Ca+Mg]	274.06	182.15	212.52	224.05	259.32	182.15	12.79	9.87	8.20	6.13	5.22	4.42	0.05	0.07	0.05	108.82	95.76	106.11

The SFCA I on the other hand, when looking at the overview image of Figure 57, appears to only have changed its colour, with no chemical evidence of alteration as shown from the bulk analysis of the reacted and unreacted areas. However, a closer look with the SEM reveals that the SFCA transitions to a multiphase intergrowth of 3 to 4 phases, which in bulk terms coincide to the same chemical composition as SFCA-I.

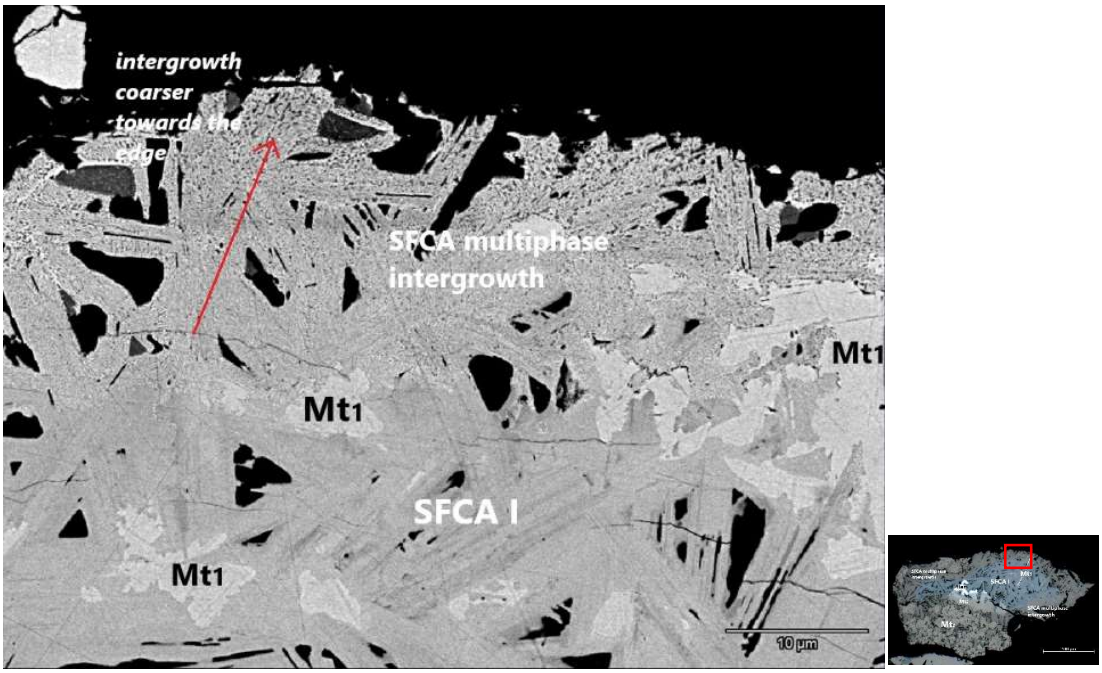

Figure 60. SEM image; SFCA reduction front. SFCA multiphase intergrowth becoming coarser and coarser towards the edge of the particle. Precipitated Magnetite observed with SFCA I and its product phase intergrowth.

The intergrowth is shown in SEM images Figure 60, Figure 61 and Figure 62. Figure 60 presents the gradual change of SFCA and the gradual development of the multiphases, which becomes more distinct towards the edges of the particle. Precipitated Magnetite and Larnite C2S remain unchanged with the same appearance in both reacted and unreacted parts, indicating their stability under these conditions. Figure 61 and Figure 62, show the multiphase intergrowth more closely in order to distinguish between the different phases that comprise it. More specifically, Figure 61 shows the contact of a Magnetite crystal, containing a vein of Wüstite, with Larnite C2S and the intergrowth, while Figure 62 is a back scattered electron image that focuses on the multiphase intergrowth only. The SEM chemical analysis of secondary Magnetite – former Hematite, Larnite C2S and Wüstite are shown in Table 16, along with the rest of the minerals present in the particle.

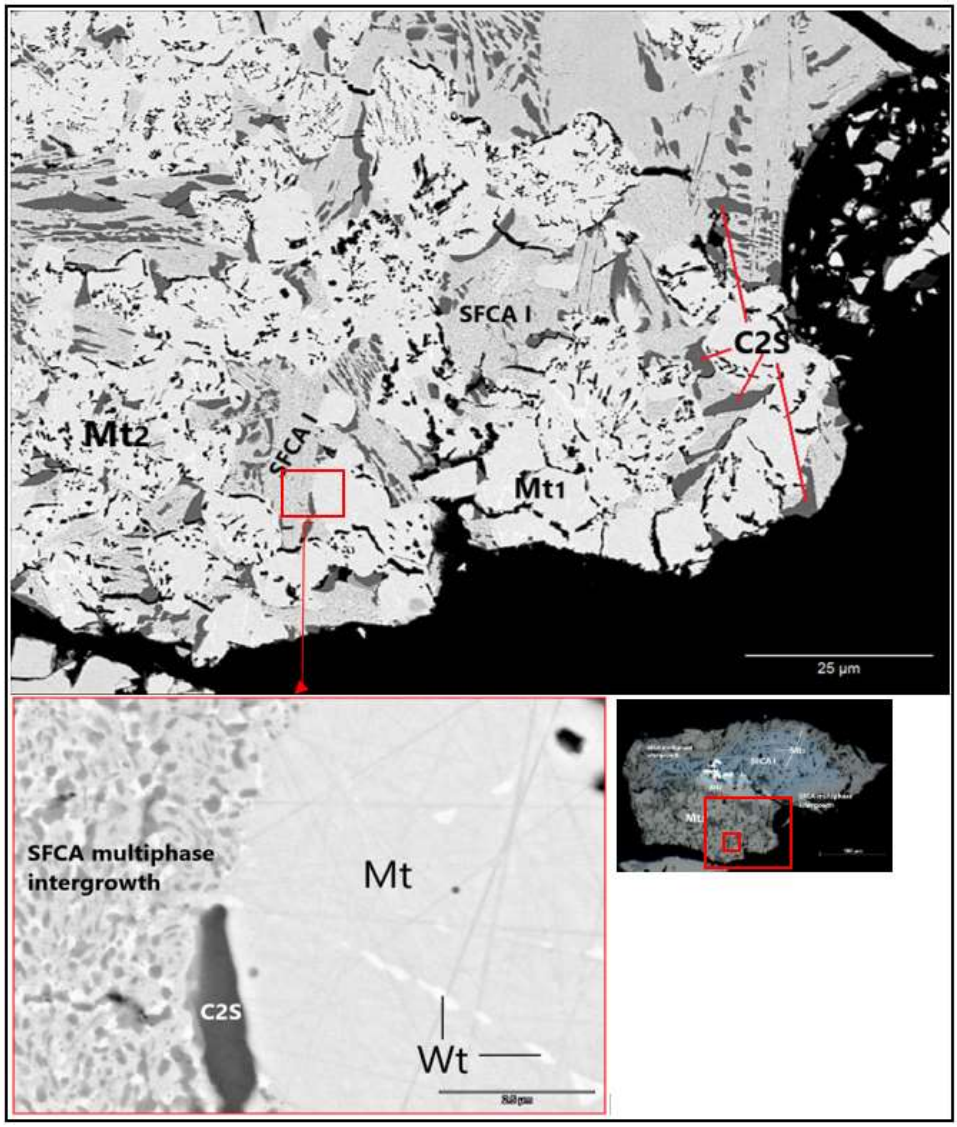

Figure 61. SEM and BSE images. **Top image**; SEM Image of the bottom area of the grain including the microstructure of secondary Magnetite with SFCA multiphase intergrowth and precipitated Magnetite and C2S. **Bottom image**; back scattered image showing the boundary of precipitated Magnetite with C2S and SFCA multiphase intergrowth. Wüstite vein-like exsolution from Magnetite.

SEM chemical analyses from the intergrowth are presented in Table 17, while they are coupled with the back scattered image in Figure 62.

Based on the spectra taken from the different phases of the intergrowth, it is verified that these phases do not exactly meet any stoichiometry of the endmembers of calcium ferrites, while they are not precisely typical SFCAs either. There are three main phases observed, based on their different brightness and color. The *brightest white phase* returns a scattered analysis signal that matches more closely to the one from the high iron SFCA-I. It is a phase enriched in Fe, with similar levels of Ca to the original SFCA I and small amounts of silica and alumina. The *grey phase* on the other hand, appears to be relatively poorer in Fe, while more enriched in calcium. Its composition is in between the composition of unreacted SFCA/SFCAII and Ca-ferrites, but its stoichiometry does not fit precisely neither of them two. The *darkest phase*, appearing as a distinct black spot on the back-scattered image has a stoichiometry that resembles to the one of Brownmillerite (C2F), but its high content in silica does not allow the exact reference structure. Instead, it is more likely to be a pre-existing C2S Larnite crystal, based on its size and excessively high silica contents.

Table 17. SEM point analysis on the SFCA multiphase intergrowth of the back scattered image in figure 58.

Point analysis	**10**	**11**	**13**	**14**	**15**	**16**	**17**	**1**	**2**	**3**	**4**	**5**	**6**	**7**	**8**	**9**	**12**	**18**
Phase	White phase of the intergrowth							Grey phase of the intergrowth										Black spot
Atom %																		
C	0.00	0.00	0.00	0.00	0.00	0.00	0.00	0.00	0.00	0.00	0.00	0.00	0.00	0.00	0.00	0.00	0.00	0.00
O	50.96	51.12	51.35	51.27	51.25	51.46	51.18	51.21	51.01	50.96	51.13	51.01	51.17	51.20	51.55	51.22	51.25	53.67
Na	0.05	0.05	0.06	0.03	0.11	0.07	0.05	0.09	0.10	0.08	0.09	0.10	0.03	0.03	0.04	0.06	0.07	0.11
Mg	0.52	0.52	0.51	0.57	0.50	0.53	0.59	0.41	0.34	0.36	0.28	0.34	0.38	0.35	0.35	0.29	0.53	0.22
Al	1.20	1.10	1.06	1.15	1.06	0.96	1.09	1.36	1.31	1.25	1.39	1.30	1.54	1.44	1.39	1.44	1.10	0.93
Si	1.30	1.63	2.21	1.97	1.86	2.51	1.83	1.84	1.37	1.32	1.54	1.27	1.40	1.67	2.36	1.82	1.91	6.91
P	0.01	0.02	0.00	0.01	0.00	0.00	0.03	0.00	0.04	0.00	0.02	0.00	0.02	0.00	0.03	0.00	0.04	0.01
S	0.01	0.03	0.00	0.01	0.00	0.00	0.03	0.00	0.00	0.02	0.00	0.00	0.02	0.03	0.00	0.00	0.06	0.02
Cl	0.00	0.00	0.01	0.00	0.00	0.00	0.00	0.04	0.04	0.00	0.00	0.00	0.00	0.00	0.00	0.05	0.00	0.04
K	0.00	0.01	0.00	0.02	0.01	0.06	0.03	0.03	0.02	0.01	0.00	0.00	0.00	0.00	0.04	0.04	0.00	0.01
Ca	6.53	5.79	7.74	6.56	6.60	6.27	5.61	11.72	9.36	9.45	13.17	10.75	13.94	11.21	12.41	14.00	8.46	19.04
Ti	0.02	0.01	0.00	0.02	0.10	0.00	0.00	0.00	0.01	0.04	0.00	0.01	0.00	0.00	0.01	0.00	0.00	0.06
V	0.01	0.05	0.00	0.00	0.05	0.00	0.00	0.00	0.02	0.01	0.03	0.08	0.12	0.05	0.02	0.00	0.05	0.00
Mn	0.22	0.30	0.18	0.21	0.32	0.13	0.23	0.15	0.18	0.00	0.19	0.20	0.10	0.20	0.14	0.00	0.24	0.13
Fe	39.18	39.37	36.89	38.19	38.13	38.00	39.33	33.15	36.20	36.50	32.16	34.93	31.29	33.81	31.66	31.08	36.30	18.84
Oxide wt%																		
Na2O	0.04	0.05	0.05	0.03	0.10	0.06	0.04	0.08	0.10	0.08	0.08	0.10	0.03	0.03	0.04	0.05	0.06	0.12
MgO	0.62	0.63	0.62	0.69	0.60	0.65	0.71	0.51	0.42	0.44	0.35	0.42	0.48	0.43	0.44	0.37	0.64	0.30
Al2O3	1.81	1.66	1.63	1.76	1.63	1.48	1.65	2.14	2.01	1.92	2.18	2.01	2.42	2.24	2.21	2.28	1.70	1.63
SiO2	2.32	2.92	4.02	3.55	3.36	4.54	3.28	3.40	2.48	2.39	2.84	2.31	2.60	3.06	4.41	3.40	3.48	14.25
P2O5	0.03	0.04	0.00	0.01	0.00	0.00	0.07	0.00	0.08	0.00	0.04	0.01	0.04	0.00	0.06	0.00	0.08	0.03
S	0.01	0.03	0.00	0.01	0.00	0.00	0.03	0.00	0.00	0.02	0.00	0.00	0.02	0.03	0.00	0.00	0.06	0.02
Cl	0.00	0.00	0.01	0.00	0.00	0.00	0.00	0.04	0.04	0.00	0.00	0.00	0.00	0.00	0.00	0.05	0.00	0.05
K2O	0.00	0.01	0.00	0.02	0.01	0.08	0.05	0.04	0.03	0.01	0.00	0.00	0.00	0.00	0.06	0.06	0.00	0.02
CaO	10.89	9.66	13.13	11.05	11.11	10.60	9.38	20.22	15.85	15.98	22.77	18.30	24.22	19.25	21.64	24.39	14.37	36.64
TiO2	0.04	0.03	0.00	0.06	0.23	0.00	0.00	0.00	0.01	0.09	0.00	0.03	0.00	0.00	0.01	0.00	0.00	0.17
V2O5	0.03	0.12	0.00	0.00	0.14	0.00	0.00	0.00	0.06	0.03	0.08	0.23	0.33	0.14	0.06	0.00	0.15	0.00
MnO	0.47	0.64	0.38	0.45	0.68	0.28	0.49	0.33	0.39	0.00	0.42	0.43	0.21	0.44	0.31	0.00	0.51	0.31
FeO	83.73	84.20	80.16	82.38	82.14	82.30	84.29	73.24	78.53	79.05	71.22	76.16	69.64	74.37	70.75	69.40	78.96	46.45
[Fe+Al]/[Ca+Mg]	5.73	6.41	4.60	5.52	5.52	5.73	6.52	2.85	3.87	3.85	2.49	3.27	2.29	3.05	2.59	2.28	4.16	1.03

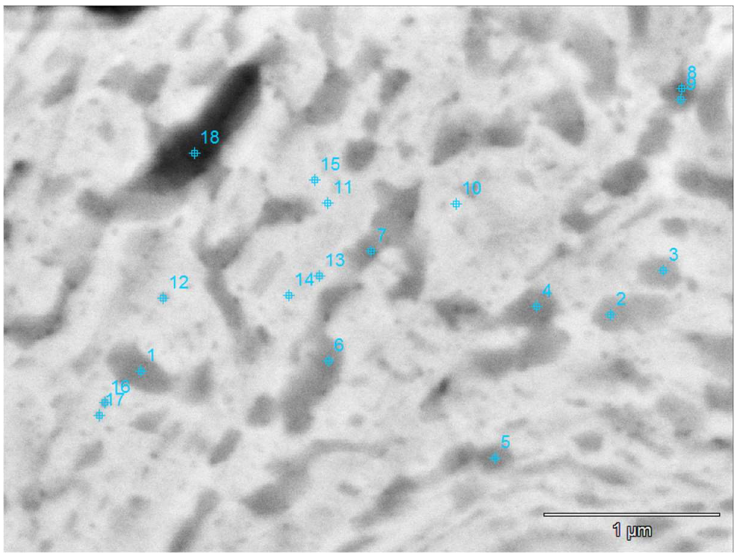

Figure 62. Back – scattered electron image of the SFCA multiphase intergrowth.

The analyses from the multiphase intergrowth were plotted on an Al-Fe-Ca triangular phase diagram (Figure 63 and Figure 64). This includes the end members of calcium ferrites (red) and the compositions of the unreacted SFCAs found in the sinter samples (yellow and blue), in order to demonstrate the positioning of the intergrowth in regard to the reference minerals. According to the graph, the intergrown phases (orange) plot somewhere in between, indicating that they are meta-stable phases.

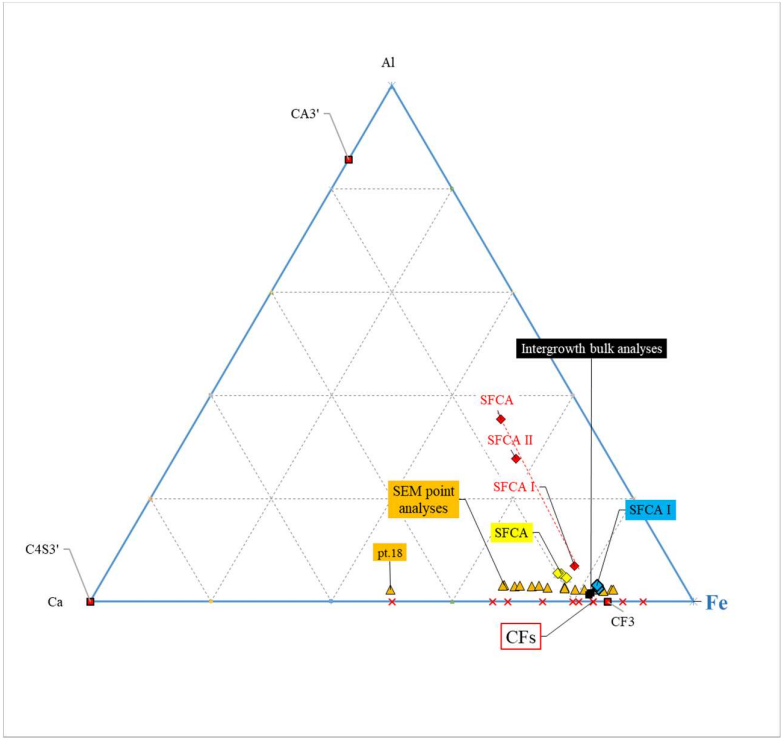

Figure 63. Al-Fe-Ca triangular phase diagram including reference phases and SEM analyses of the SFCA multiphase intergrowth.

The graph also includes the reference compositions of all SFCA types, based on (Mumme, 2003). The starting compositions of both high Fe-SFCA and high Ca-Si SFCA observed in the current sinter samples greatly deviate from the SFCA reference points; hence the same stands for their reduction products. The differences are attributes to the high discrepancy in alumina contents between the SFCAs. The reduction products of the initial SFCAs observed in this study have a range of compositions that do not quite fit at any known stoichiometry.

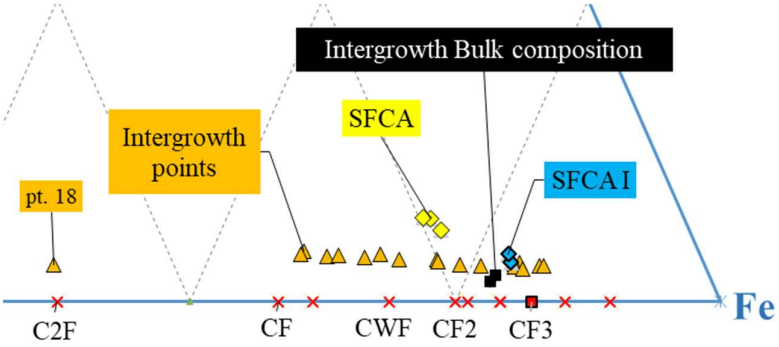

Figure 64. Right corner of triangular diagram. SEM analyses of intergrown phases plot between endmembers of calcium ferrites and reference SFCA compositions. The white phase of the intergrowth plots very close to reference SFCA I.

However, based on the analysis of the multiphase, it seems like there are two paths of chemical separation beginning from the initial SFCA-I, one becoming enriched in Fe, and one becoming more calcic. Knowing the end-products of the reduction being Wüstite FeO, Brownmillerite C2(A)F and Larnite C2S, ±Melilite (FactSage), this intergrowth corresponds to an early stage meta-stable assemblage that tends to transition to one Fe-rich phase, one Ca-rich phase and one Si-rich phase. Separation begins from Fe and Ca, since these current phases have not yet separated their Si and Al contents.

High basicity samples – Microstructure 1b

Microstructure 1 is also present in samples of higher basicity, but often missing Hematite presence in the structure, thus also lacking secondary Magnetite. A typical image of the referred microstructure is given in Figure 65. The grain is taken from sample **WCS62** after the same reduction conditions (t=2minutes under **T=950°C**).

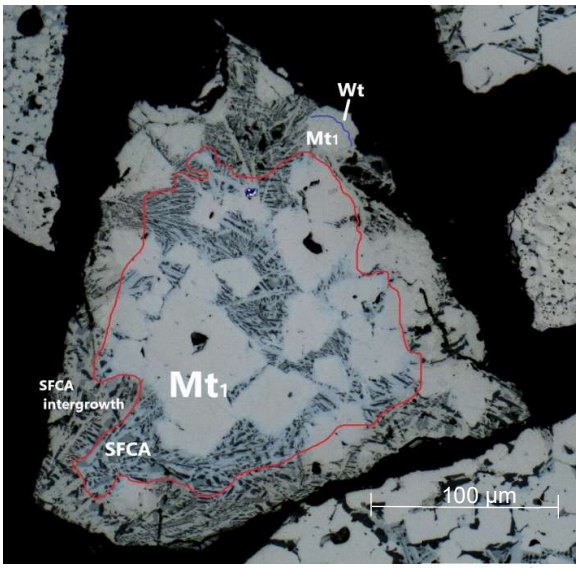

Figure 65 Polarised reflected light microscopy image (20x magnification). **WCS62** Grain reduced for t=2minutes under T=950°C/XCO=0.65/N_2=0.50 in the GERO furnace; **Microstructure Type 1. SFCA reduction front.**

The unreacted part of the particle is composed by *precipitated (blue) SFCA I* and *Larnite C2S* with well-developed *precipitated Magnetite* crystals. The unreacted core is cut by a reduction front visible due to the SFCA I color change from blue to brown. Magnetite also shows a slightly different color tone indicating some compositional change, while the SEM images reveal its transition to Wüstite at the edge of the particle. The two reaction fronts are shown in Figure 65. Representative SEM analyses of all the minerals are presented in Table 18.

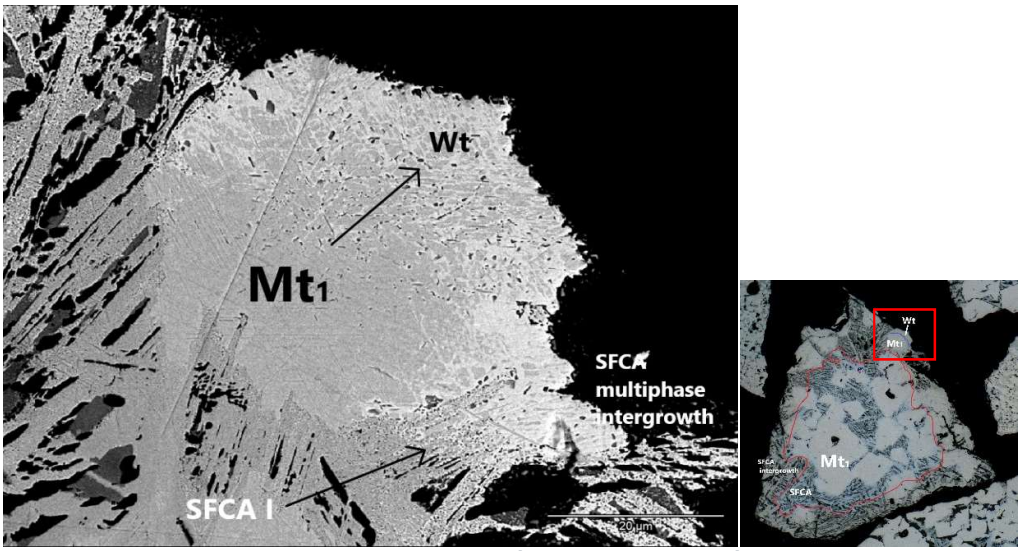

Figure 66. SEM image; Precipitated Magnetite → Wüstite and SFCA I → multiphase intergrowth

Table 18. Representative SEM chemical analyses, of the main minerals present in microstructure type 1 of sample WCS62 after 2-minute reduction under T=950°C/XCO=0,65/N_2=0.5 in the GERO furnace.

Mineral	**Magnetite**		**SFCA-I**			**C2S**			**wustite from Mt**		
Atom %											
C	0.00	0.00	0.00	0.00	0.00	0.00	0.00	0.00	0.00	0.00	0.00
O	50.30	50.25	50.72	50.78	50.75	56.79	57.05	57.19	50.31	50.21	50.39
Na	0.06	0.14	0.11	0.07	0.17	0.15	0.24	0.10	0.07	0.10	0.00
Mg	1.64	1.62	0.66	0.64	0.34	0.00	0.02	0.00	1.62	1.71	0.34
Al	0.87	0.78	1.45	1.31	1.34	0.46	0.11	0.02	0.77	0.60	0.34
Si	0.16	0.13	0.78	0.86	0.95	13.06	13.67	13.75	0.16	0.11	0.60
P	0.00	0.00	0.00	0.00	0.00	0.27	0.39	0.44	0.01	0.01	0.02
S	0.00	0.00	0.03	0.00	0.01	0.10	0.10	0.08	0.02	0.01	0.00
Cl	0.00	0.02	0.00	0.00	0.00	0.00	0.02	0.01	0.00	0.00	0.00
K	0.01	0.00	0.02	0.00	0.05	0.08	0.14	0.12	0.00	0.01	0.04
Ca	1.90	2.14	6.08	6.20	6.57	27.82	27.32	27.40	1.39	1.86	2.12
Ti	0.00	0.03	0.00	0.00	0.00	0.01	0.07	0.02	0.00	0.02	0.00
V	0.03	0.03	0.03	0.06	0.00	0.06	0.02	0.09	0.07	0.03	0.00
Mn	0.34	0.53	0.20	0.16	0.15	0.00	0.00	0.04	0.33	0.30	0.06
Fe	44.71	44.35	39.93	39.91	39.66	1.21	0.86	0.75	45.25	45.05	46.08
Oxide wt%											
Na2O	0.06	0.12	0.10	0.07	0.15	0.19	0.29	0.13	0.07	0.09	0.00
MgO	1.91	1.88	0.79	0.76	0.41	0.00	0.04	0.00	1.88	1.98	0.39
Al2O3	1.27	1.14	2.18	1.98	2.03	0.93	0.22	0.04	1.13	0.88	0.50
SiO2	0.27	0.23	1.38	1.53	1.70	31.48	33.19	33.41	0.27	0.18	1.02
P2O5	0.00	0.00	0.00	0.00	0.00	0.78	1.12	1.27	0.03	0.03	0.05
S	0.00	0.00	0.03	0.00	0.01	0.13	0.12	0.11	0.02	0.00	0.00
Cl	0.00	0.02	0.00	0.00	0.00	0.00	0.03	0.01	0.00	0.00	0.00
K2O	0.01	0.00	0.02	0.00	0.07	0.14	0.26	0.22	0.00	0.01	0.05
CaO	3.07	3.47	10.09	10.30	10.92	62.60	61.92	62.13	2.24	3.00	3.39
TiO2	0.00	0.07	0.00	0.00	0.00	0.01	0.23	0.08	0.00	0.04	0.00
V2O5	0.07	0.07	0.07	0.16	0.00	0.22	0.07	0.32	0.19	0.08	0.01
MnO	0.69	1.08	0.41	0.34	0.32	0.00	0.00	0.12	0.67	0.60	0.12
FeO	92.66	91.93	84.91	84.88	84.39	3.50	2.51	2.17	93.52	93.11	94.47
[Fe+Al]/[Ca+Mg]	12.88	12.00	6.14	6.03	5.93	0.06	0.04	0.03	15.29	12.79	18.87

The SFCA I reduces to the ***multiphase intergrowth*** comprised by three different phases (Figure 67). Again, these do not exactly fit any of the known stoichiometries (Figure 68).

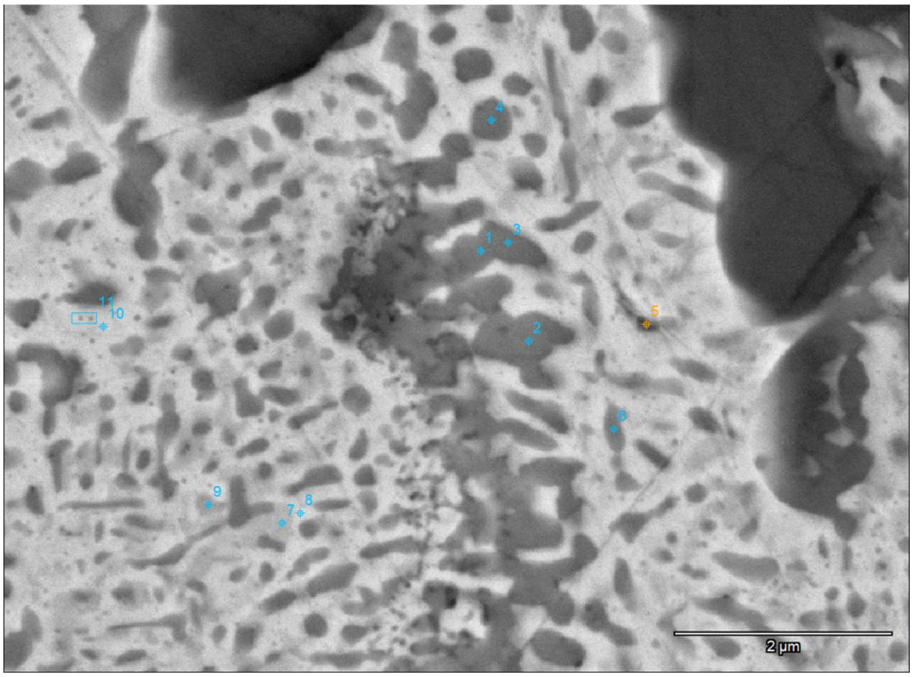

Figure 67. SEM image; WCS62 – Microstructure 1: multiphase intergrowth point analysis

Table 19. SEM point analysis on the SFCA multiphase intergrowth of the image in figure 63.

Point anal	**7**	**8**	**10**	**11**	**5**	**6**	**9**	**1**	**2**	**3**	**4**
Phase	White phase of the intergrowth				Grey phase of the intergrowth			Darkest phase of the intergrowth			
Atom %											
C	0.00	0.00	0.00	0.00	0.00	0.00	0.00	0.00	0.00	0.00	0.00
O	50.80	50.65	50.48	50.55	50.82	51.02	50.80	52.61	52.27	51.94	52.10
Na	0.00	0.03	0.00	0.06	0.00	0.03	0.00	0.10	0.00	0.12	0.08
Mg	0.21	0.35	0.42	0.35	0.18	0.12	0.29	0.15	0.15	0.03	0.07
Al	1.85	1.09	0.78	1.03	1.14	1.75	1.35	1.69	2.36	2.18	2.26
Si	0.62	0.60	0.51	0.65	0.88	0.99	0.75	3.58	2.53	2.35	2.99
P	0.00	0.01	0.00	0.00	0.00	0.00	0.06	0.01	0.01	0.00	0.03
S	0.00	0.05	0.00	0.05	0.02	0.00	0.00	0.03	0.00	0.00	0.00
Cl	0.03	0.00	0.07	0.01	0.00	0.00	0.00	0.03	0.00	0.03	0.00
K	0.00	0.04	0.02	0.00	0.09	0.00	0.00	0.02	0.01	0.00	0.02
Ca	3.77	3.63	3.91	4.59	8.67	13.10	6.49	18.55	19.76	19.29	19.96
Ti	0.09	0.00	0.02	0.03	0.06	0.12	0.07	0.82	0.78	0.43	0.09
V	0.00	0.15	0.09	0.00	0.13	0.05	0.02	0.04	0.03	0.07	0.00
Mn	0.34	0.03	0.00	0.00	0.05	0.28	0.33	0.00	0.21	0.00	0.00
Fe	42.30	43.37	43.71	42.68	37.95	32.55	39.84	22.38	21.89	23.55	22.40
Oxide wt%											
Na2O	0.00	0.03	0.00	0.06	0.00	0.03	0.00	0.10	0.00	0.12	0.09
MgO	0.24	0.41	0.49	0.41	0.22	0.15	0.34	0.20	0.19	0.04	0.10
Al2O3	2.75	1.61	1.14	1.53	1.74	2.73	2.03	2.84	3.95	3.61	3.79
SiO2	1.08	1.04	0.89	1.13	1.58	1.82	1.34	7.10	5.00	4.59	5.91
P2O5	0.00	0.02	0.00	0.00	0.00	0.00	0.11	0.02	0.02	0.01	0.07
S	0.00	0.04	0.00	0.05	0.02	0.00	0.00	0.03	0.00	0.00	0.00
Cl	0.03	0.00	0.08	0.01	0.00	0.00	0.00	0.03	0.00	0.03	0.00
K2O	0.00	0.05	0.03	0.00	0.12	0.00	0.01	0.03	0.02	0.00	0.03
CaO	6.17	5.91	6.33	7.49	14.48	22.53	10.76	34.31	36.44	35.20	36.83
TiO2	0.21	0.00	0.04	0.08	0.15	0.30	0.17	2.15	2.05	1.13	0.24
V2O5	0.00	0.40	0.23	0.00	0.34	0.13	0.05	0.14	0.11	0.20	0.00
MnO	0.71	0.06	0.01	0.00	0.11	0.61	0.68	0.00	0.50	0.00	0.00
FeO	88.81	90.43	90.78	89.25	81.24	71.70	84.52	53.05	51.72	55.06	52.96
[Fe+Al]/[C	11.09	11.17	10.27	8.85	4.42	2.59	6.08	1.29	1.22	1.33	1.23

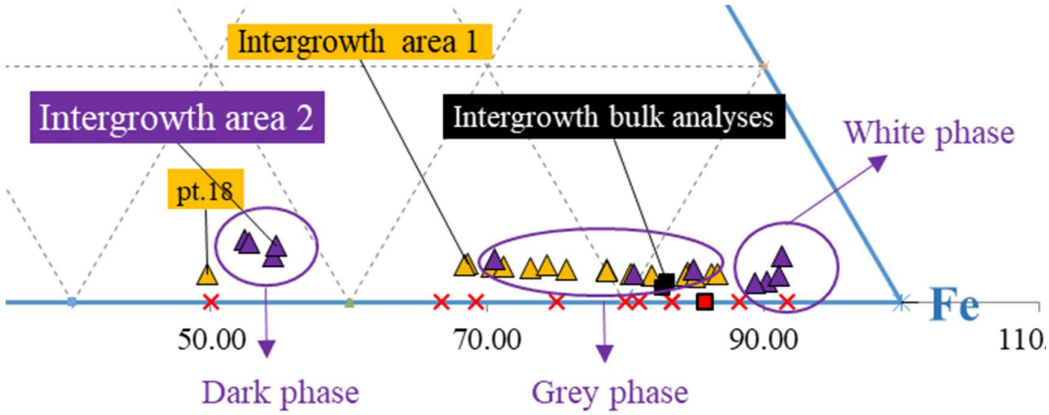

Figure 68. Left corner of triangular diagram. Additional SEM analyses of the multiphase intergrowth on a second position (purple). SEM point analyses of intergrown phases again plot between endmembers of calcium ferrites and reference SFCA compositions. The white phase of the intergrowth is getting even more enriched in Fe.

Based on the SEM spot analysis on the multiphase structure the *bright white phase* is the one hosting the highest Fe-content from the previous SFCA I phase, while becoming less calcic. Compared to the white phase in the intergrowth seen in WCS108, it is even more enriched in Fe and poorer in Ca. Its composition is in between a very high Fe - SFCA I and iron oxides Fe_xO_x, without fitting exactly in neither of the two.

The *grey phase* on the other hand, is slightly poorer in Fe, and richer in calcium. Its composition resembles to a lower-Fe SFCA I or high -Fe SFCA type II, with its stoichiometry not fitting precisely. Finally, the *darkest phase*, appearing in skeletal patterns in Figure 67 has a stoichiometry that more closely approaches Brownmillerite (C2F), but it is characterized by great fluctuations between Fe and Ca, due to higher Fe content. It is not believed to be the same phase as the dark phase (point 18) in the previous intergrowth position, since it does not include as high silica quantities as seen before.

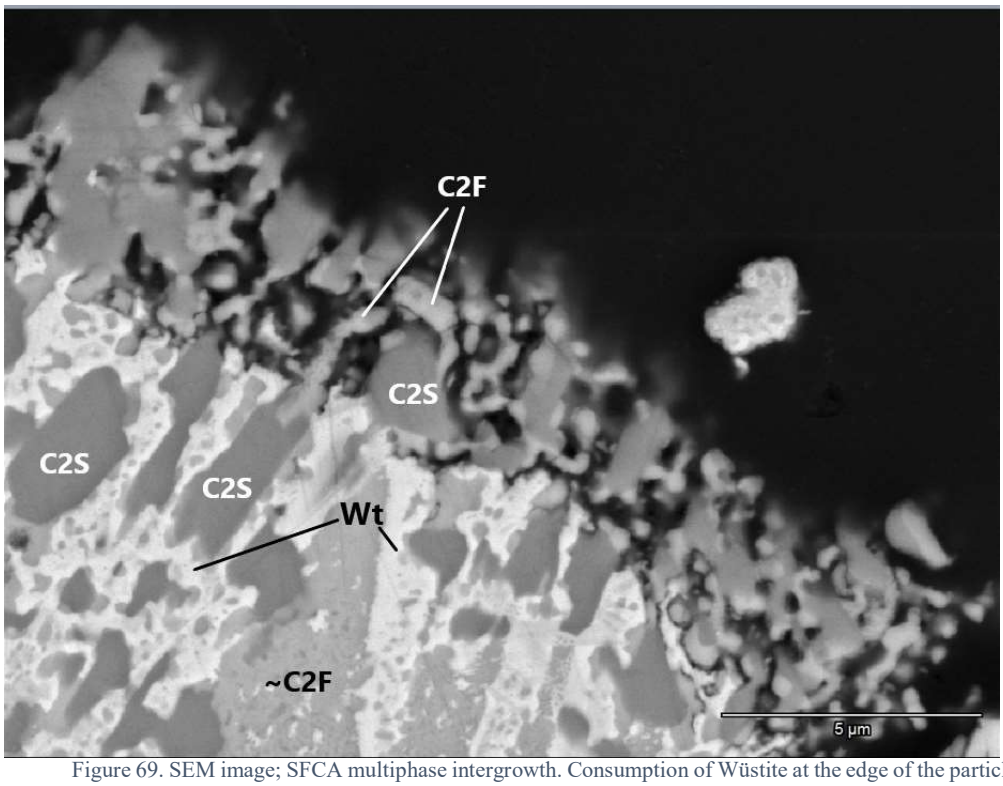

Figure 69. SEM image; SFCA multiphase intergrowth. Consumption of Wüstite at the edge of the particle.

Figure 69 shows this multiphase intergrowth at the very edge of the particle. The assemblage of the picture is comprised by the white phase, which has escalated to Wüstite, the grey phase that again holds an Fe-rich Brownmillerite C2F-like composition and the darkest one, which corresponds to C2S. It is worth noticing, that the Fe-rich white phase appears to be consumed at the very edge of the particle from between C2S and ~C2F, which can either be shrinkage or escapade evidence.

i. Microstructure Type 1 –T=750°C/XCO=0.55/N_2=0.5

The microstructure of type 1 was found present in all the reduced samples, also under the more moderate conditions. Samples with higher starting Hematite content and short reduction times, show the current microstructure in greater abundance. Examples from **microstructure-1** are presented in the following optical and scan electron microscope images taken from sinter samples. Again, sample **WCS108** was chosen to demonstrate a typical image of microstructure -1 after t=5minutes under **T=750°C** in the GERO furnace, since it is the sample mostly characterized by this microstructure.

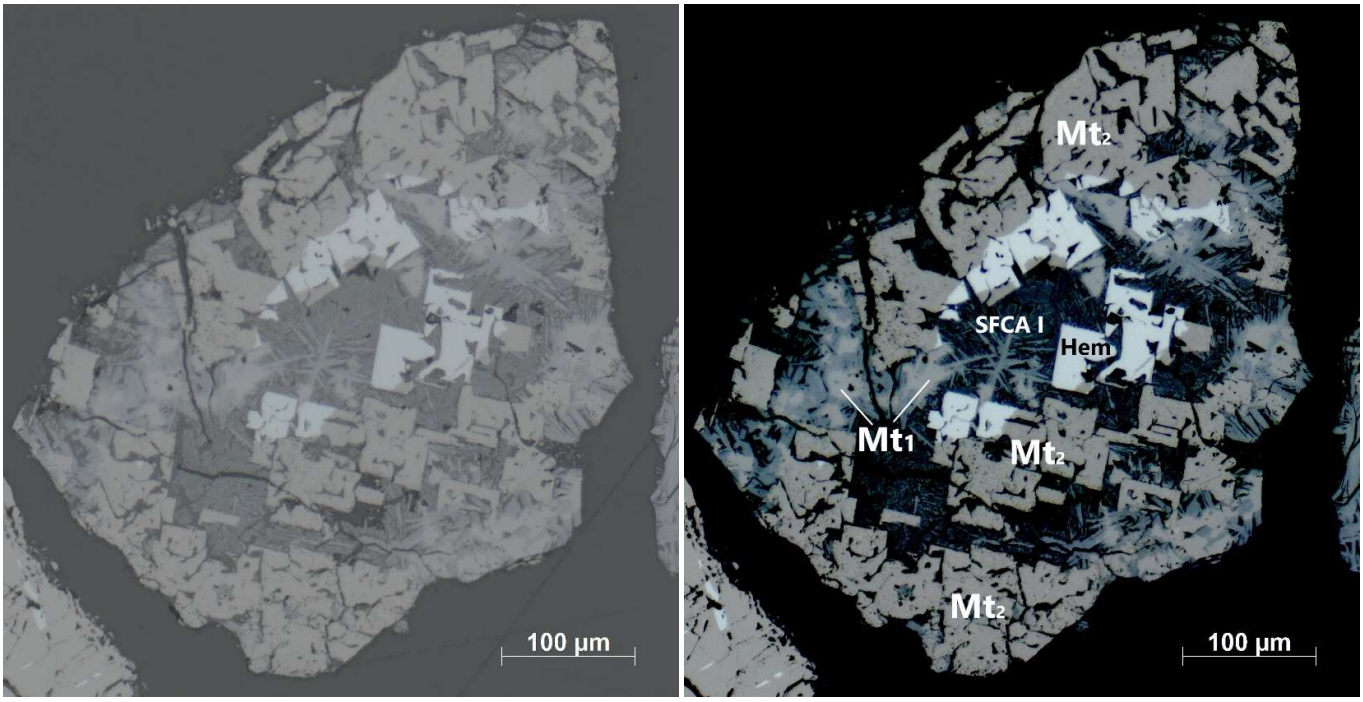

Figure 70. Polarised reflected light microscopy image (20x magnification). WCS108 Grain reduced for t=5minutes under T=750°C/XCO=0.65/N_2=0.50 in the GERO furnace. **Left**; Original picture from optical microscope. **Right**; Picture with changed contract to distinguish different phases. Phases are labelled on the grain.

Figure 70 presents all the phases existing on the WCS108 grain; As seen under 950°C, also in this instance, *Hematite* shows a clear reduction front transitioning to Magnetite. *Newly formed Magnetite (Mt_2)* is abundant in the structure, indicating the former positions of precipitated Hematite. Apart from its characteristic chemical composition, it is visually identified from its brittle-looking appearance when compared to precipitated Magnetite, which has a smoother surface. Again, the formation of Magnetite is accompanied by the formation of secondary porosity, which is closely captured in Figure 71 and Figure 72, where disintegration on the surface of Magnetite is shown. In addition, tiny traces of Wüstite were verified on secondary Magnetite by SEM.

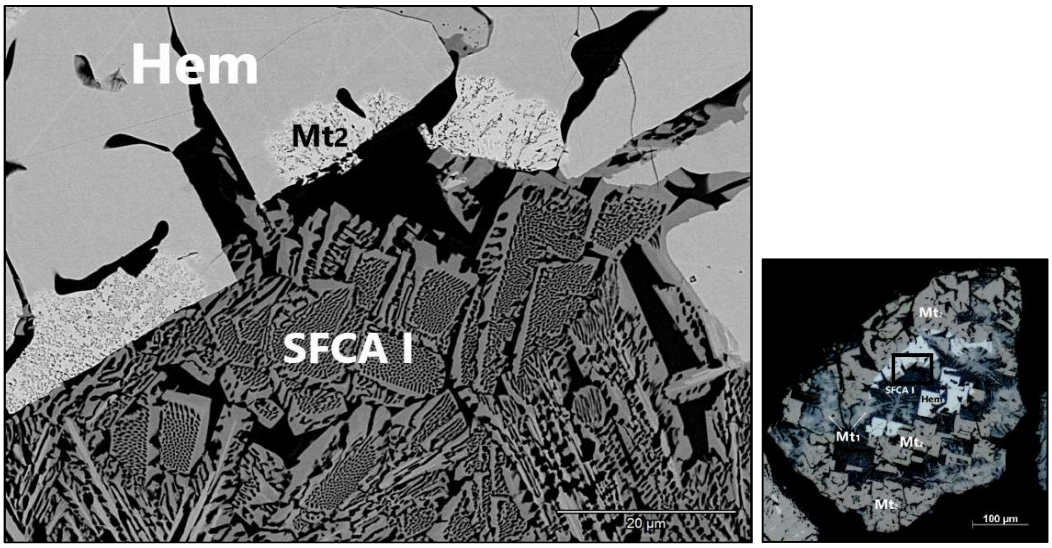

Figure 71. Optical microscope RL image; Hematite transition to Magnetite and SFCA.

Precipitated Magnetite is mainly observed in crystals positioned in between the SFCA I assemblage, while Magnetite formed from Hematite reduction is found in distinct idiomorphic crystals, following Hematite's crystal structure. *SFCA I* is the blue-colored mineral, with thin acicular crystals developed in dendritic forms. The SFCA minerals are characterized by their high Fe content also in this case, thus they are referred as SFCA type 1.

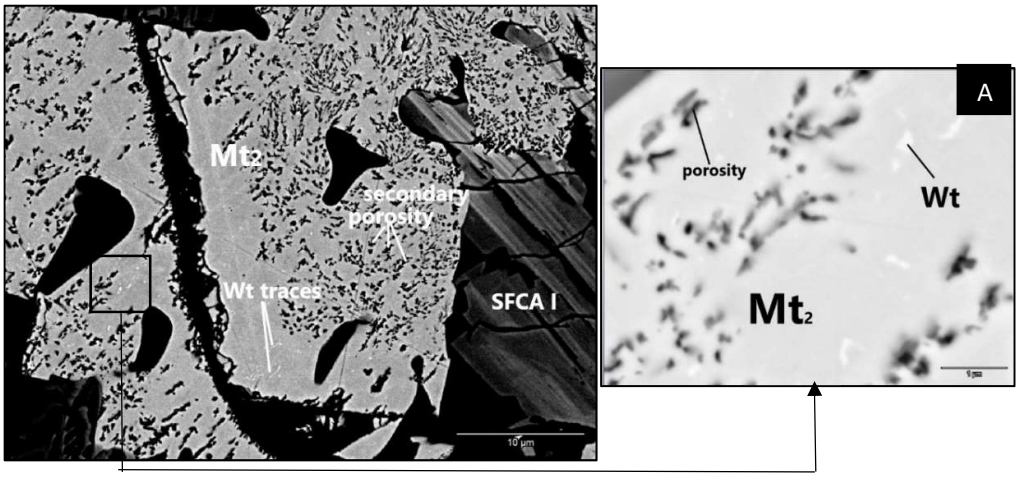

Figure 72. SEM image. Hematite → Magnetite + secondary porosity (+traces of Wüstite). A: BSE image

At 750ºC, in contrast with Hematite which shows a clear unreacted core, SFCA does not demonstrate a clear reduction front to the multiphase intergrowth that was seen under the intense reduction conditions of T=950ºC. In fact, it looks like it almost has not changed at all due to reduction.

The reduction of SFCA does not look much progressed on this grain, even under the SEM. However, there are evidence of alteration to the multiphase intergrowth, albeit limited; The SEM high magnification image of Figure 73 shows the existing reduction front of the original SFCA to the multiphase intergrowth that was observed before. The reduction is very limited only on an intrusive line at the outer part of the crystal, where the kinetics and circumstantial conditions must have favored the reaction of the SFCA I. SFCA I on its original form demonstrates a chemical zoning in this case, between the high Fe-SFCA I, and a more calcic, less iron-rich chemical phase, perhaps corresponding to SFCA II.

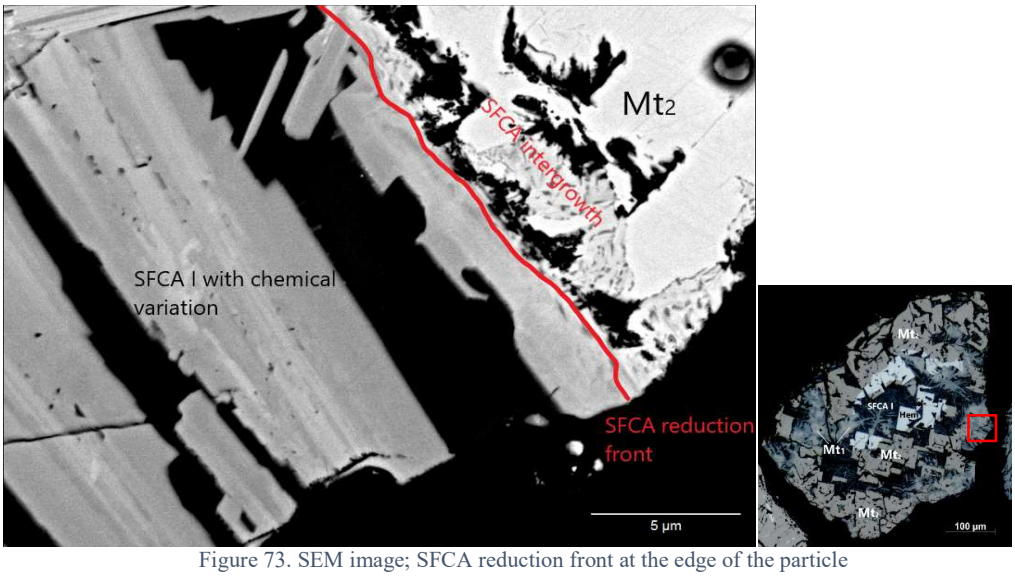

Figure 73. SEM image; SFCA reduction front at the edge of the particle

Hence, the SFCA 1 has reacted, but much less than Hematite, which displays a much more progressed reaction. This is also confirmed by the WCS108 grain under T=950°C, where the Hematite reduction front is deeper in the grain than the one of SFCA. However, at T=750°C the difference between the two respective reduction fronts is much greater, since the SFCA front is barely traceable. Therefore, it seems like under the more intense conditions the reduction fronts of the two phases converge, while under the moderate ones they become more distant to each other. This can be indicative of the SFCA behavior under different temperatures and gas atmospheres.

This discrepancy between the relative reduction progresses of the two minerals under different conditions is also confirmed by the XRD data; According to the graph of Figure 74, starting from the same point respectively, the difference in the reduction progress of the two minerals is less under the high temperature conditions, while it gets enhanced under low temperature. At early times of reduction, like in the cases examined under the microscope, at 750°C – t=5minutes, Hematite and SFCA have a difference in reduction of 40%, in comparison to 950°C – t=4minutes, where their difference in reduction is way less (Δ(wt%)=14%) even though the reduction duration was less.

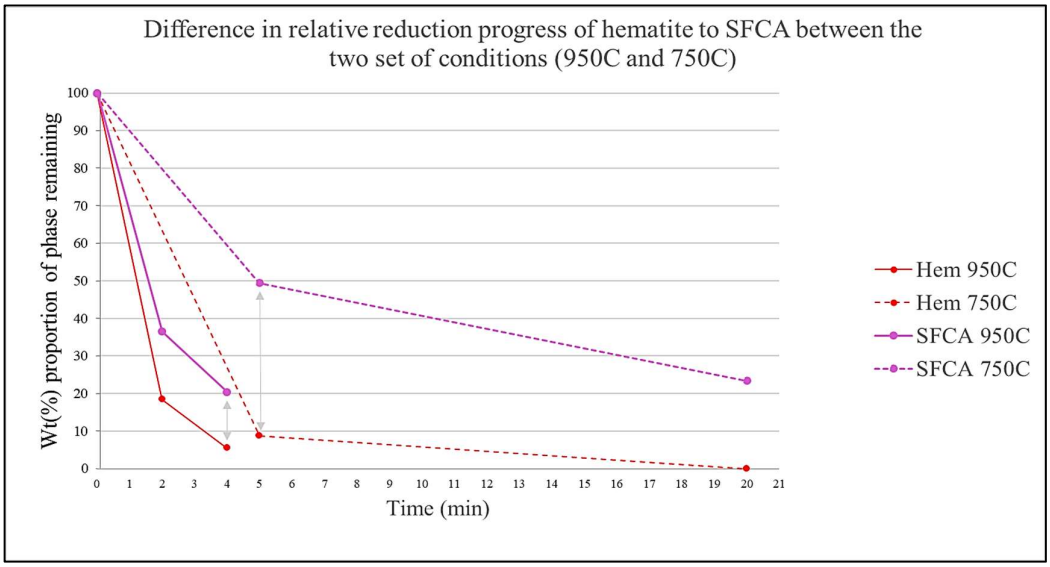

Figure 74 Hematite and SFCA I relative weight percent loss from t=0min to t=2min/t=5min under the T=950°C/T=750°C conditions, respectively.

Table 20. Representative SEM chemical analyses, of the main minerals present in microstructure type 1 of sample WCS108 after 5-minute reduction under T=750°C/XCO=0.55/N_2=0.5 in the GERO furnace. (bdl: below detection limit)

Mineral	Hematite			Secondary Magnetite			Precipitated Magnetite			SFCA I/II			C2S		
Atom %															
C	0.00	0.00	0.00	0.00	0.00	0.00	0.00	0.00	0.00	0.00	0.00	0.00	0.00	0.00	0.00
O	50.33	50.35	50.28	50.17	50.28	50.23	50.29	50.28	50.36	51.33	51.67	51.30	57.16	57.25	57.20
Na	0.09	0.11	0.13	0.11	0.17	0.18	0.04	0.09	0.04	0.08	0.10	0.11	0.22	0.17	0.26
Mg	0.09	0.10	0.05	1.76	3.38	4.24	0.09	0.03	0.06	0.86	0.72	1.32	0.01	0.03	0.03
Al	0.82	0.91	0.85	0.51	0.90	0.75	0.73	0.87	0.77	1.96	1.80	2.35	0.07	0.04	0.06
Si	0.10	0.14	0.15	0.13	0.13	0.13	0.13	0.14	0.11	1.66	2.46	1.47	14.02	14.04	13.98
P	0.01	0.03	0.00	0.02	0.03	0.04	0.03	0.00	0.02	0.04	0.00	0.01	0.29	0.32	0.38
S	0.00	0.02	0.01	0.00	0.01	0.00	0.00	0.00	0.01	0.00	0.01	0.00	0.04	0.04	0.04
Cl	0.02	0.00	0.02	0.01	0.01	0.01	0.00	0.02	0.01	0.00	0.00	0.01	0.00	0.00	0.01
K	0.02	0.00	0.02	0.01	0.00	0.00	0.04	0.00	0.01	0.00	0.00	0.01	0.11	0.07	0.15
Ca	0.17	0.11	0.13	1.09	1.47	1.15	0.15	0.19	0.12	5.90	7.29	6.21	27.14	27.14	27.17
Ti	0.13	0.12	0.03	0.00	0.03	0.00	0.08	0.04	0.09	0.00	0.01	0.00	0.03	0.04	0.02
V	0.05	0.00	0.04	0.00	0.00	0.00	0.00	0.00	0.09	0.00	0.01	0.00	0.01	0.00	0.04
Mn	0.16	0.09	0.02	0.29	0.85	1.06	0.05	0.00	0.05	0.15	0.11	0.63	0.02	0.00	0.00
Fe	48.03	48.01	48.27	45.91	42.74	42.22	48.37	48.34	48.25	38.01	35.82	36.59	0.88	0.79	0.66
Oxide wt%															
Na2O	0.08	0.09	0.11	0.10	0.16	0.17	0.03	0.08	0.03	0.08	0.09	0.10	0.28	0.22	0.33
MgO	0.10	0.11	0.06	2.03	3.99	5.03	0.10	0.03	0.07	1.05	0.89	1.62	0.01	0.05	0.05
Al2O3	1.18	1.31	1.23	0.74	1.34	1.13	1.05	1.25	1.11	3.02	2.81	3.64	0.14	0.09	0.13
SiO2	0.16	0.24	0.25	0.22	0.23	0.22	0.22	0.23	0.19	3.01	4.54	2.69	34.11	34.20	34.08
P2O5	0.02	0.07	0.00	0.04	0.06	0.08	0.06	0.01	0.04	0.09	0.01	0.03	0.84	0.93	1.08
S	0.00	0.02	0.01	0.00	0.01	0.00	0.00	0.00	0.01	0.00	0.01	0.00	0.05	0.05	0.06
Cl	0.02	0.00	0.02	0.01	0.01	0.01	0.00	0.02	0.01	0.00	0.00	0.01	0.00	0.00	0.01
K2O	0.03	0.00	0.02	0.01	0.00	0.00	0.06	0.00	0.01	0.00	0.00	0.01	0.21	0.13	0.28
CaO	0.26	0.18	0.21	1.75	2.42	1.90	0.23	0.30	0.19	9.99	12.53	10.59	61.63	61.71	61.84
TiO2	0.29	0.27	0.07	0.00	0.07	0.00	0.19	0.10	0.19	0.00	0.04	0.00	0.10	0.14	0.06
V2O5	0.14	0.00	0.10	0.00	0.01	0.00	0.00	0.00	0.24	0.00	0.03	0.00	0.03	0.19	0.16
MnO	0.32	0.18	0.04	0.58	1.76	2.21	0.09	0.00	0.10	0.32	0.23	1.35	0.05	0.01	0.00
FeO	97.41	97.52	97.88	94.52	89.94	89.27	97.97	97.98	97.80	82.45	78.84	79.96	2.55	2.29	1.93
[Fe+Al]/[C	187.88	232.95	272.89	16.29	9.00	7.97	204.58	223.68	272.33	5.91	4.70	5.17	0.03	0.03	0.03

ii. Microstructure Type 2

Microstructure type 2 is very similar to microstructure 1, however it differs regarding the type of SFCA and its reduced form. A typical image of microstructure 2 is presented in Figure 75. The grain belongs to the sample WCS86 after t=2minutes reduction under T=950ºC/XCO=0.65/N_2=0.5. The unreacted core of the particle is again comprised by precipitated Hematite and Magnetite, but in this case, combined with tabular (blue) SFCA/SFCA II and Larnite. The reacted front includes secondary Magnetite from former Hematite, secondary precipitated Magnetite, and reacted SFCA.

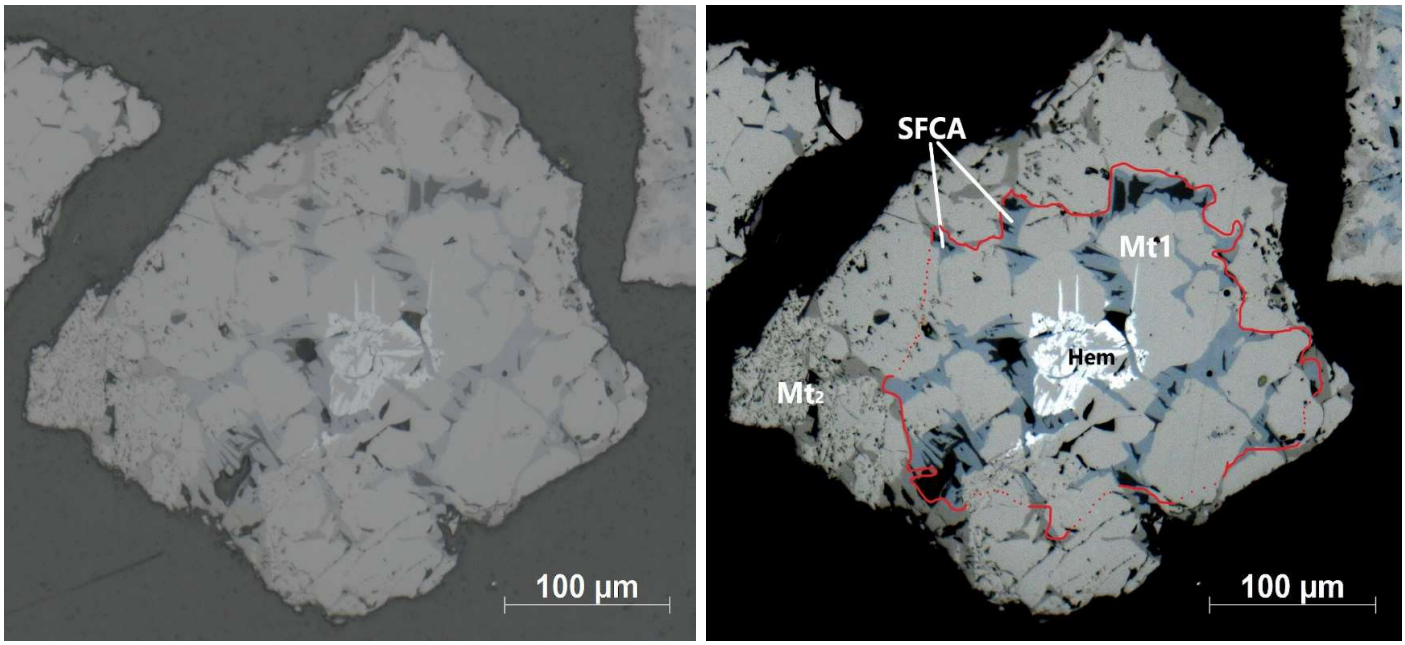

Figure 75. Polarised reflected light microscopy image (20x magnification). WCS86 Grain reduced for t=2minutes under T=950ºC/XCO=0.65/N_2=0.50 in the GERO furnace; **SFCA and Hematite reduction fronts.**

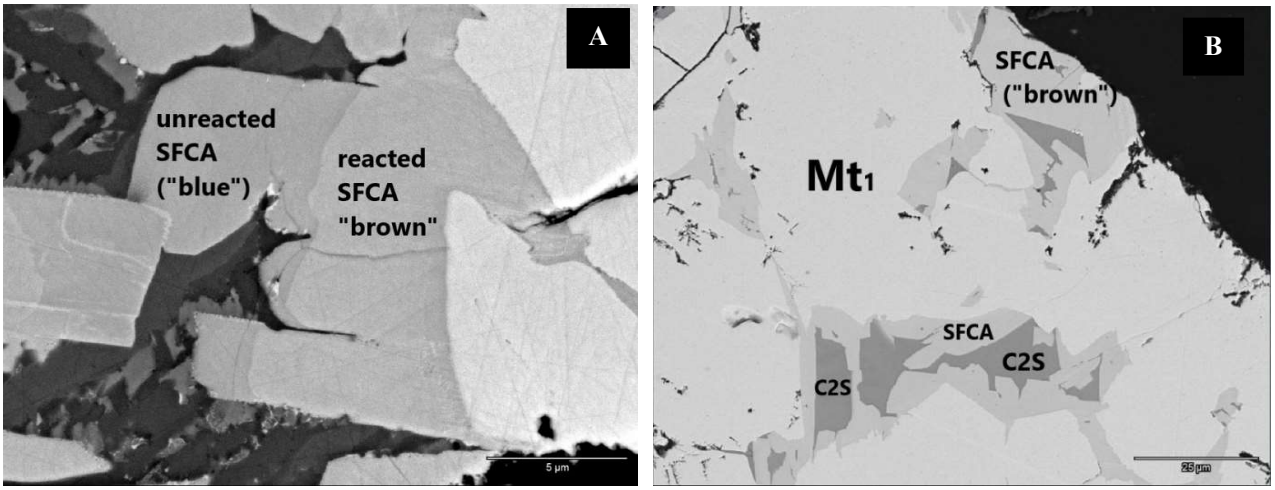

Figure 76. SEM images from different parts of the grain. Image A; SFCA reduction front of 1-to-1 phase transition. Image B; Precipitated Magnetite crystal, with reacted SFCA intergrown with Larnite C2S

As shown in Figure 76 and Figure 77, SFCA transitions only to 1 phase, visible by its different (brown) color. The unreacted SFCA in this case is characterized by its low Fe-content and its high calcium in comparison with the high Fe-SFCA I. Representative compositions of the mineral are shown in the SEM chemical analyses of Table 21.

Table 21. Representative SEM chemical analyses, of the main minerals present in microstructure type 2 of sample WCS108 after 2-minute reduction under T=950ºC/XCO=0,65/N_2=0.5 in the GERO furnace.

Mineral	Hematite			Secondary Magnetite			Secondary Magnetite			SFCA (blue)			SFCA (brown)			C2S		
Atom %																		
C	0.00	0.00	0.00	0.00	0.00	0.00	0.00	0.00	0.00	0.00	0.00	0.00	0.00	0.00	0.00	0.00	0.00	0.00
O	50.38	50.20	50.27	50.32	50.31	50.17	50.28	50.30	50.34	52.58	52.72	52.66	52.43	52.35	52.45	57.25	57.26	57.23
Na	0.01	0.07	0.06	0.00	0.08	0.22	0.09	0.08	0.15	0.07	0.10	0.10	0.08	0.11	0.13	0.18	0.20	0.16
Mg	0.09	0.05	0.12	0.15	0.22	0.25	2.14	2.38	2.44	0.29	0.62	0.28	0.27	1.24	0.37	0.02	0.01	0.00
Al	0.13	0.64	0.76	0.85	0.84	0.79	0.94	1.02	1.05	2.34	1.96	2.37	2.11	1.62	2.04	0.01	0.01	0.03
Si	0.14	0.12	0.14	0.08	0.29	0.12	0.11	0.13	0.14	3.97	4.39	4.02	3.68	3.90	3.69	13.82	13.87	13.92
P	0.03	0.00	0.01	0.00	0.00	0.02	0.00	0.00	0.02	0.00	0.00	0.00	0.01	0.03	0.03	0.53	0.46	0.36
S	0.02	0.00	0.00	0.00	0.01	0.01	0.03	0.02	0.00	0.00	0.00	0.00	0.04	0.04	0.01	0.04	0.00	0.03
Cl	0.02	0.00	0.00	0.00	0.02	0.10	0.03	0.00	0.04	0.00	0.02	0.00	0.00	0.00	0.00	0.01	0.00	0.01
K	0.03	0.00	0.00	0.00	0.00	0.00	0.00	0.03	0.02	0.01	0.00	0.02	0.00	0.00	0.00	0.14	0.08	0.06
Ca	0.00	0.14	0.18	0.34	0.19	0.08	0.90	1.13	1.16	8.23	7.85	8.40	8.02	7.17	7.86	27.30	27.37	27.33
Ti	0.24	0.00	0.00	0.04	0.00	0.00	0.00	0.04	0.06	0.06	0.14	0.12	0.10	0.04	0.13	0.10	0.03	0.00
V	0.22	0.00	0.03	0.06	0.00	0.01	0.06	0.00	0.04	0.00	0.00	0.04	0.07	0.00	0.06	0.00	0.05	0.10
Mn	0.00	0.19	0.00	0.36	0.39	0.06	0.28	0.43	0.36	0.11	0.15	0.00	0.05	0.36	0.00	0.00	0.00	0.02
Fe	48.68	48.61	48.44	47.80	47.64	48.19	45.13	44.44	44.18	32.35	32.05	31.98	33.15	33.16	33.24	0.59	0.66	0.74
Oxide wt%																		
Na2O	0.01	0.06	0.05	0.00	0.07	0.19	0.08	0.07	0.13	0.07	0.09	0.10	0.08	0.11	0.13	0.23	0.25	0.20
MgO	0.10	0.06	0.13	0.18	0.25	0.28	2.48	2.78	2.86	0.37	0.79	0.35	0.33	1.57	0.47	0.04	0.01	0.00
Al2O3	0.19	0.91	1.09	1.23	1.21	1.14	1.38	1.51	1.56	3.76	3.17	3.82	3.36	2.59	3.26	0.02	0.02	0.06
SiO2	0.23	0.20	0.23	0.14	0.48	0.20	0.19	0.23	0.24	7.52	8.36	7.64	6.93	7.36	6.94	33.68	33.80	33.88
P2O5	0.07	0.00	0.02	0.00	0.00	0.04	0.00	0.00	0.04	0.00	0.00	0.01	0.02	0.06	0.07	1.54	1.32	1.04
S	0.02	0.00	0.00	0.00	0.01	0.01	0.03	0.02	0.00	0.00	0.00	0.00	0.04	0.04	0.01	0.05	0.01	0.04
Cl	0.02	0.00	0.00	0.00	0.02	0.10	0.03	0.00	0.04	0.00	0.03	0.00	0.00	0.00	0.00	0.02	0.00	0.01
K2O	0.04	0.00	0.00	0.00	0.00	0.00	0.00	0.04	0.03	0.02	0.00	0.04	0.00	0.00	0.00	0.26	0.15	0.12
CaO	0.00	0.22	0.28	0.53	0.30	0.12	1.46	1.84	1.89	14.56	13.94	14.90	14.08	12.61	13.81	62.12	62.24	62.07
TiO2	0.54	0.00	0.00	0.08	0.00	0.00	0.00	0.10	0.14	0.14	0.34	0.30	0.24	0.10	0.32	0.31	0.09	0.01
V2O5	0.57	0.00	0.07	0.15	0.00	0.02	0.17	0.00	0.09	0.01	0.00	0.13	0.21	0.00	0.16	0.00	0.19	0.36
MnO	0.00	0.37	0.00	0.73	0.78	0.11	0.57	0.88	0.74	0.24	0.34	0.00	0.10	0.79	0.00	0.00	0.00	0.05
FeO	98.22	98.19	98.12	96.96	96.86	97.79	93.59	92.54	92.22	73.33	72.94	72.71	74.59	74.79	74.83	1.71	1.92	2.15
[Fe+Al]/[Ca+Mg]	542.33	259.21	164.00	99.29	118.24	148.42	15.15	12.95	12.56	4.07	4.02	3.96	4.25	4.14	4.29	0.02	0.02	0.03

In addition, the chemical composition of the newly formed SFCA phase is not very much different from the one of the original SFCA. In some cases, like in Figure 77, the new SFCA is locally more enriched in Fe, but in most cases the reduced SFCA preserves the same chemical composition as the original SFCA and only changes its color.

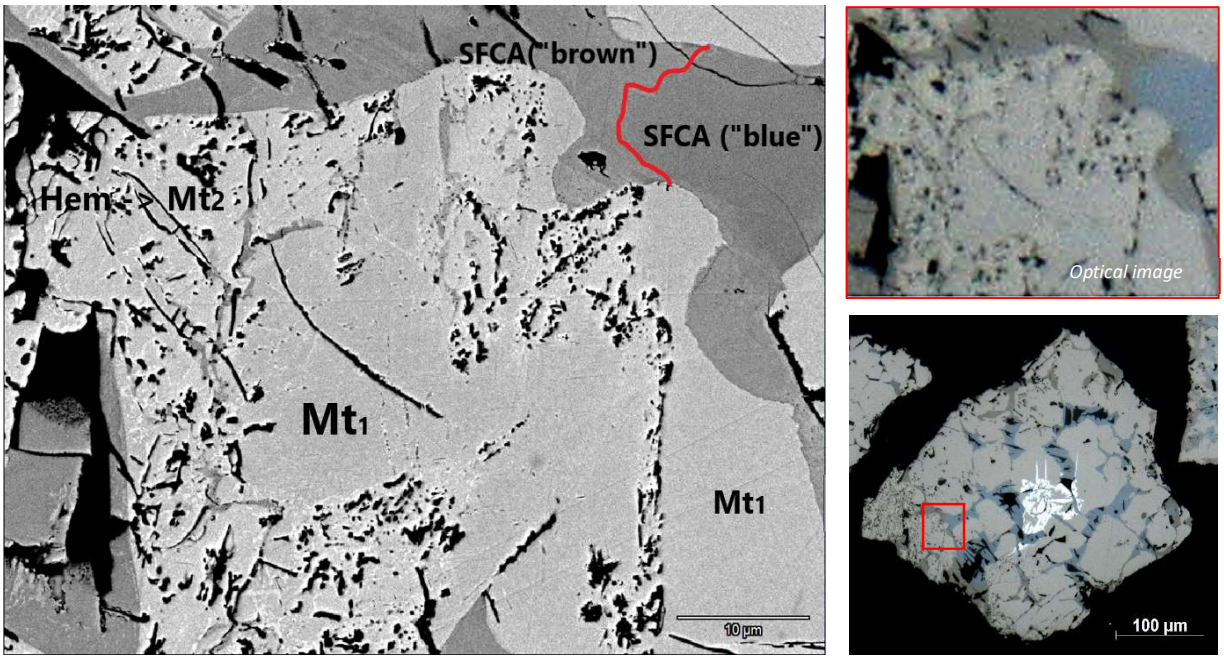

Figure 77. SEM image combined with respective optical image and map image; Secondary Magnetite from former Hematite and precipitated Magnetite. SFCA reduction front; 1-to-1 phase SFCA reduction.

iii. Microstructure Type 3

The third type of microstructure is characterized by ore-relict Hematite and ore-relict Magnetite. These can be present in the form of originally coarsely crystalline Hematite ore - core surrounded by coarse crystals of Magnetite. However, Magnetite and Hematite are also co-existing in exsolution structures, where secondary Hematite forms lamellas on primary Magnetite crystals. Examples of both structures are shown in the following pictures. The lamella structure is found in combination with other microstructure types, in this case1 and 4, where Hematite's transition to newly formed Magnetite, acicular or tabular SFCAs and precipitated Magnetite are also present.

Figure 78 A. shows a WCS108 grain from the sample reduced for t=2min under the conditions of T=950°C. The grain is comprised by a Hematite ore relict core and a surrounding Magnetite ore crown.

Figure 78 B. also displays the same structure under the more moderate conditions. This was taken from the sample WCS108 under T=750°C. The structure of the grain is very similar to the one of image A, demonstrating a Hematite bulk ore core with primary Magnetite. Representative analyses of the two minerals are given in Table 22, for both conditions.

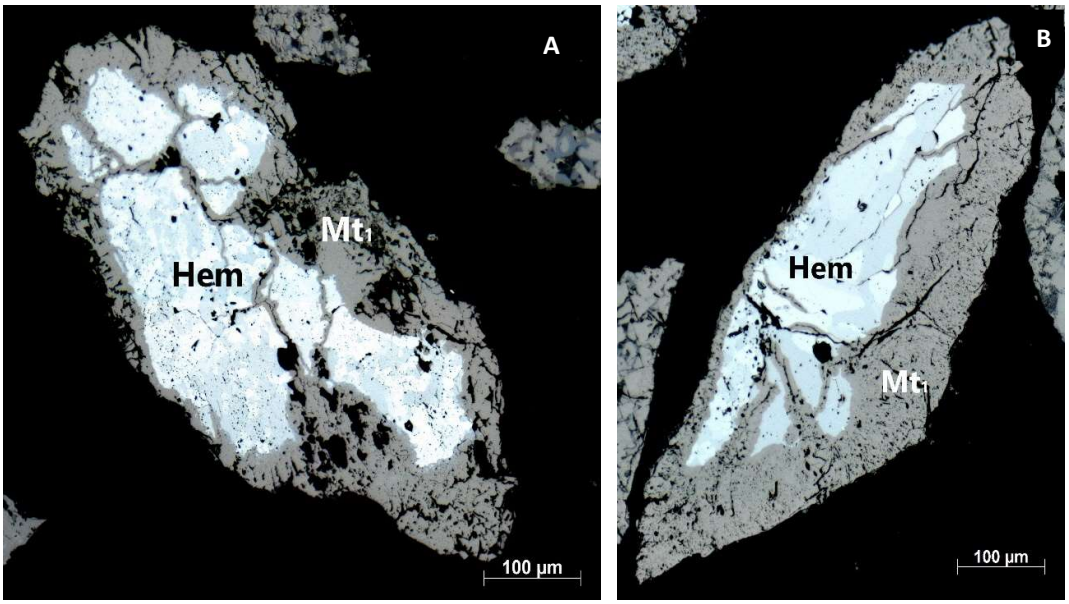

Figure 78. Polarised reflected light microscopy images (20x magnification). Microstructure type 3, under the two different conditions of temperature and gas composition; **A.** Microstructure 3 in **WCS108** grain after reduction for t=2minutes under **T=950°C/XCO=0.65/N_2=0.50**. **B.** Microstructure 3 in **WCS108** grain after reduction for t=5minutes under **T=750°C/XCO=0.55/N_2=0.50**.

Table 22 Representative SEM chemical analyses, of grains A and B of WCS108 under the two different reduction conditions.

	Grain A / T=950C				Grain B / T=750C			
Mineral	**Hematite**		**Magnetite**		**Hematite**		**Magnetite**	
Atom %								
C	0.00	0.00	0.00	0.00	0.00	0.00	0.00	0.00
O	50.21	50.36	50.29	50.18	50.04	50.11	50.09	50.13
Na	0.04	0.00	0.08	0.07	0.12	0.03	0.07	0.05
Mg	0.02	0.00	0.10	0.04	0.03	0.06	0.02	0.07
Al	0.02	0.04	0.02	0.12	0.01	0.03	0.02	0.05
Si	0.42	0.71	0.64	0.34	0.13	0.23	0.17	0.26
P	0.00	0.01	0.01	0.01	0.02	0.00	0.00	0.00
S	0.00	0.00	0.01	0.02	0.01	0.00	0.00	0.00
Cl	0.00	0.00	0.05	0.00	0.00	0.00	0.00	0.00
K	0.00	0.04	0.05	0.02	0.04	0.02	0.01	0.02
Ca	0.00	0.03	0.00	0.04	0.00	0.00	0.00	0.02
Ti	0.00	0.00	0.02	0.00	0.01	0.00	0.00	0.00
V	0.00	0.00	0.00	0.00	0.00	0.00	0.03	0.00
Mn	0.18	0.06	0.08	0.04	0.21	0.00	0.00	0.17
Fe	49.12	48.76	48.65	49.12	49.38	49.53	49.59	49.23
Oxide wt%								
Na2O	0.03	0.00	0.07	0.06	0.10	0.03	0.06	0.04
MgO	0.02	0.00	0.11	0.05	0.04	0.07	0.02	0.07
Al2O3	0.03	0.05	0.03	0.17	0.02	0.04	0.02	0.07
SiO2	0.71	1.20	1.09	0.57	0.21	0.38	0.29	0.44
P2O5	0.00	0.01	0.02	0.02	0.04	0.00	0.00	0.00
S	0.00	0.00	0.01	0.01	0.01	0.00	0.00	0.00
Cl	0.00	0.00	0.05	0.00	0.00	0.00	0.00	0.00
K2O	0.00	0.06	0.07	0.02	0.05	0.02	0.01	0.03
CaO	0.00	0.05	0.00	0.07	0.00	0.00	0.00	0.02
TiO2	0.00	0.00	0.05	0.00	0.02	0.00	0.00	0.00
V2O5	0.00	0.00	0.00	0.01	0.00	0.00	0.07	0.00
MnO	0.36	0.11	0.16	0.09	0.41	0.00	0.00	0.35
FeO	98.85	98.52	98.34	98.93	99.10	99.46	99.52	98.97
[Fe+Al]/[Ca+Mg]	2457.00	1626.67	486.70	615.50	1646.33	826.00	2480.50	547.56

The *lamella exsolution of Hematite* from primary Magnetite is shown in Figure 79, where it is found with combination with microstructure type 2. The grain is from sample

WCS86 (t=2min, T=950oC). Exsolution Microstructure 3 is also displayed on the grain of Figure 80, taken from WCS108 (t=2min, T=950oC), in combination with microstructure type 1.

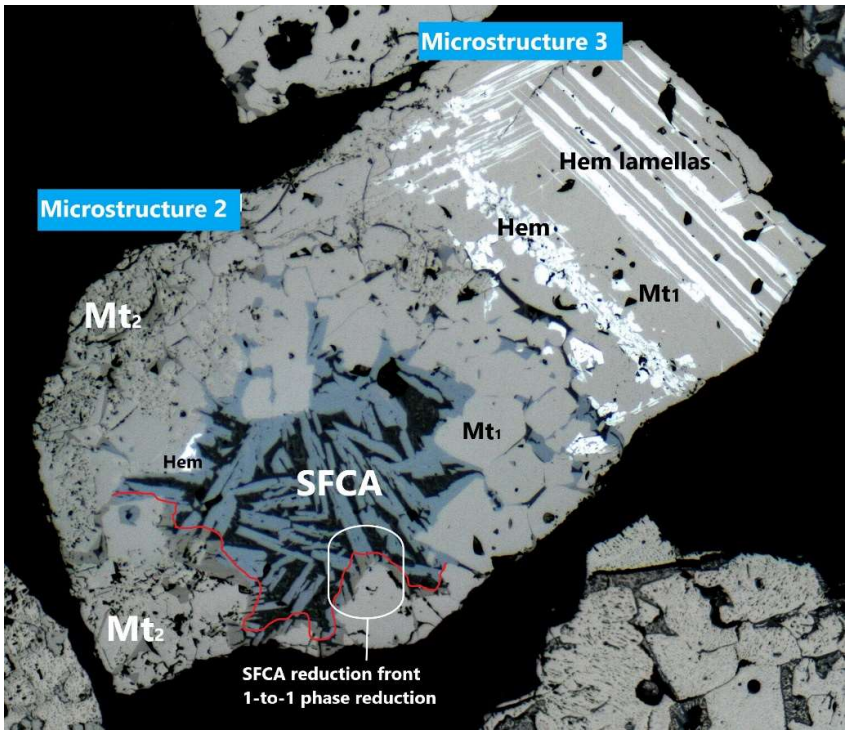

Figure 79. Polarised reflected light microscopy image (20x magnification). WCS86 Grain (t=2minutes under T=950ºC/XCO=0.65/N_2=0.50); **Combination of microstructure type 2 and microstructure type 3.**

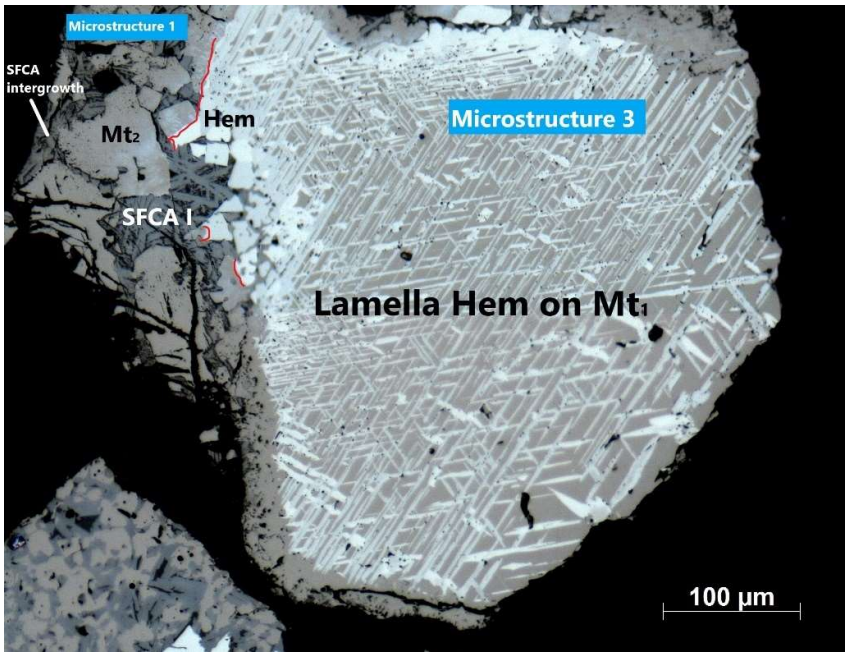

Figure 80. Polarised reflected light microscopy image (20x magnification). WCS108 Grain (t=2minutes under T=950ºC/XCO=0.65/N_2=0.50); **Combination of microstructure type 2 and microstructure type 3**.

iv. Microstructure Type 4

Another type of microstructure was identified, being most abundant in samples of higher basicity. This includes precipitated Magnetite crystals intergrown with various calcium ferrites. An example of microstructure type 4 is presented in Figure 81, taken from the highest basicity sample WCS62, after it was reduced for t=2minutes under T=950ºC.

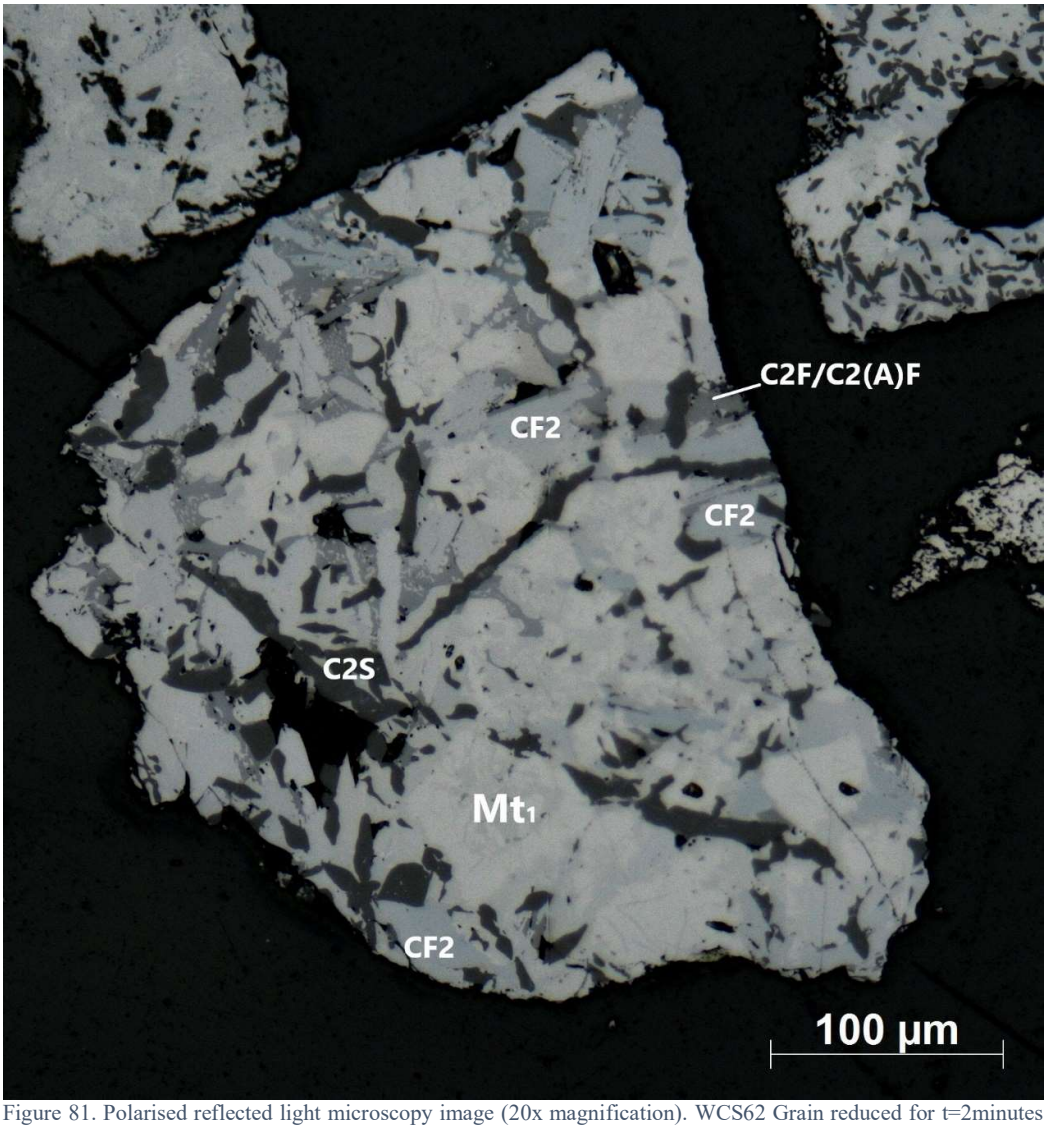

Figure 81. Polarised reflected light microscopy image (20x magnification). WCS62 Grain reduced for t=2minutes under T=950ºC/XCO=0.65/N_2=0.50; **Microstructure type 4.**

In this type of microstructure, there is no clear evidence of reduction on the grain, nor is a reduction front present. The microstructure includes a type of precipitated Magnetite, which is characterized by a form of chemical zoning that gives two different colours on its surface. Along with Magnetite, a great amount of C2S is identified all over the grain, being the dark phase developed in thick veins and bulk crystals. In addition, CF2 is also abundantly present in the structure, with pale blue colour. An intermediate grey phase is also identified, which has a close stoichiometry to Brownmillerite C2F/C2(A)F, but again does not always precisely fit it. The mineral phases are also displayed in the SEM pictures in Figure 82 and Figure 83.

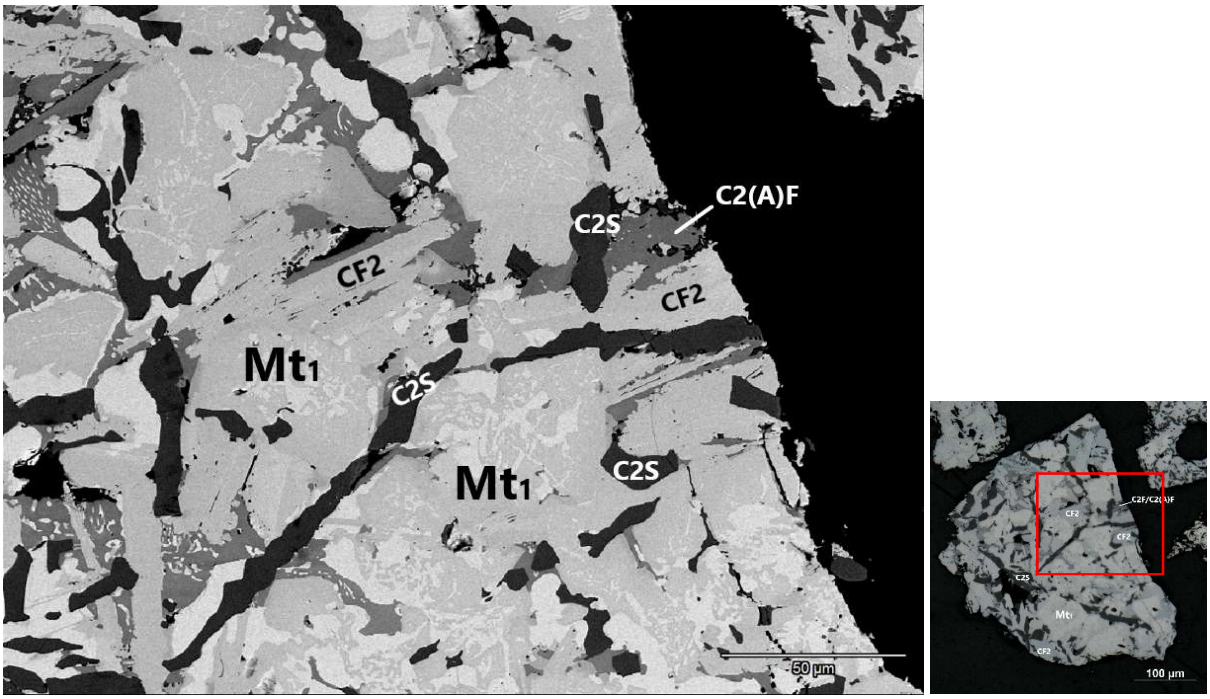

Figure 82. SEM image; Precipitated Magnetite with chemical zoning intergrown with SFCA I, Larnite C2S and Brownmillerite C2(A)F.

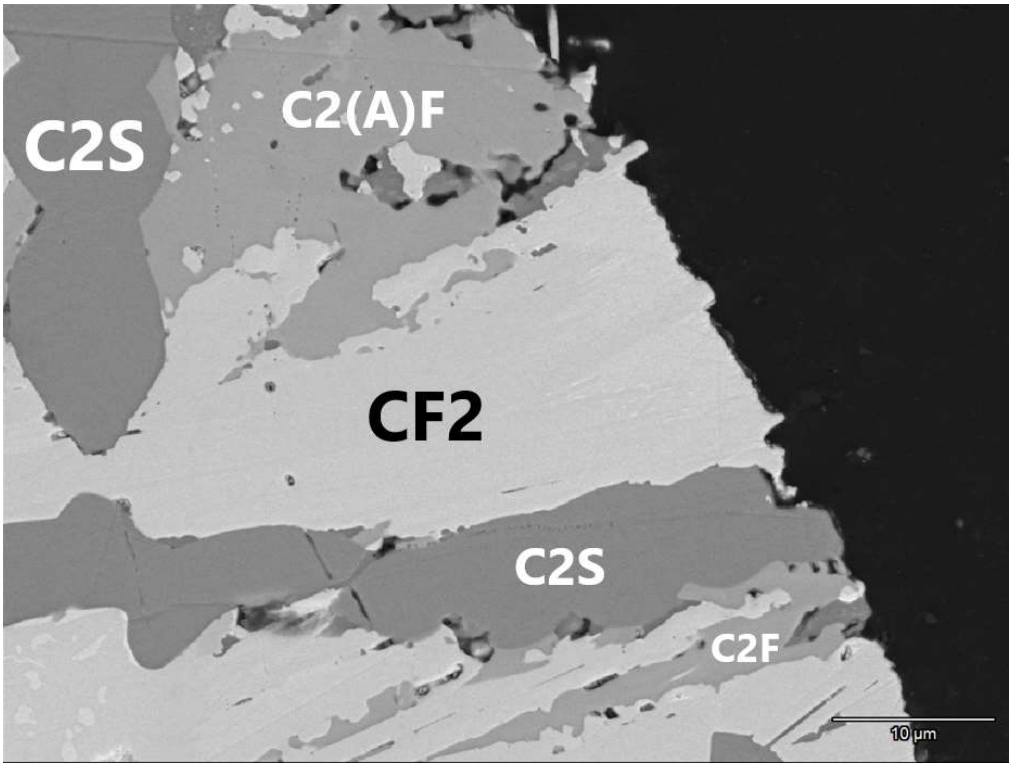

Figure 83. SEM image; Calcium ferrites of Microstructure 4: SFCA I, Larnite C2S and Brownmillerite C2(A)F.

Representative SEM chemical analyses of all the phases present in this grain are presented in Table 23.

Table 23. Representative SEM chemical analyses, of the main minerals present in microstructure type 4 of sample WCS62 after 2-minute reduction under T=950°C/XCO=0,65/N_2=0.5 in the GERO furnace.

Mineral	Precipitated Magnetite			CF2			C2S			C2F/C2(A)F		
Atom %												
C	0.00	0.00	0.00	0.00	0.00	0.00	0.00	0.00	0.00	0.00	0.00	0.00
O	50.12	50.11	50.20	50.25	50.28	50.26	57.28	57.16	57.13	51.45	51.21	52.43
Na	0.07	0.14	0.13	0.04	0.00	0.00	0.13	0.17	0.10	0.03	0.02	0.06
Mg	2.54	2.72	2.19	0.36	0.61	0.42	0.02	0.04	0.00	0.01	0.00	0.09
Al	0.21	0.21	0.28	0.47	0.33	0.45	0.01	0.03	0.05	1.62	1.49	7.17
Si	0.09	0.14	0.16	0.10	0.13	0.12	14.04	14.00	14.12	1.52	1.39	0.88
P	0.04	0.04	0.06	0.00	0.00	0.01	0.36	0.27	0.09	0.03	0.01	0.00
S	0.01	0.02	0.00	0.00	0.00	0.00	0.01	0.03	0.13	0.00	0.05	0.03
Cl	0.00	0.00	0.00	0.00	0.01	0.01	0.00	0.03	0.00	0.00	0.06	0.00
K	0.01	0.00	0.01	0.00	0.02	0.00	0.06	0.08	0.04	0.00	0.01	0.00
Ca	1.15	1.11	0.92	9.35	8.16	9.51	27.32	27.22	27.16	22.43	22.88	21.74
Ti	0.00	0.00	0.00	0.11	0.15	0.12	0.05	0.03	0.07	0.37	0.38	0.46
V	0.03	0.00	0.05	0.04	0.09	0.03	0.02	0.03	0.07	0.12	0.02	0.00
Mn	0.42	0.32	0.41	0.19	0.12	0.38	0.00	0.00	0.00	0.00	0.06	0.06
Fe	45.30	45.18	45.58	39.09	40.11	38.69	0.67	0.91	1.05	22.42	22.43	17.08
Oxide wt%												
Na2O	0.07	0.13	0.11	0.03	0.00	0.00	0.17	0.22	0.12	0.03	0.02	0.06
MgO	2.95	3.16	2.54	0.42	0.72	0.50	0.04	0.07	0.00	0.01	0.00	0.12
Al2O3	0.30	0.31	0.41	0.70	0.49	0.68	0.03	0.06	0.11	2.67	2.45	12.55
SiO2	0.16	0.25	0.28	0.18	0.23	0.22	34.23	34.02	34.25	2.97	2.70	1.82
P2O5	0.08	0.09	0.13	0.00	0.00	0.03	1.05	0.78	0.26	0.06	0.02	0.00
S	0.01	0.02	0.00	0.00	0.00	0.00	0.02	0.03	0.17	0.00	0.05	0.03
Cl	0.00	0.00	0.00	0.00	0.01	0.01	0.00	0.05	0.00	0.00	0.07	0.00
K2O	0.01	0.00	0.01	0.00	0.03	0.00	0.12	0.16	0.08	0.00	0.01	0.00
CaO	1.85	1.79	1.47	15.40	13.39	15.68	62.16	61.76	61.51	40.75	41.46	41.87
TiO2	0.00	0.00	0.00	0.26	0.34	0.28	0.16	0.09	0.21	0.95	0.97	1.26
V2O5	0.08	0.00	0.14	0.12	0.23	0.07	0.07	0.13	0.26	0.36	0.07	0.00
MnO	0.86	0.66	0.84	0.40	0.24	0.79	0.00	0.00	0.00	0.01	0.13	0.16
FeO	93.63	93.61	94.06	82.48	84.32	81.75	1.95	2.64	3.03	52.18	52.06	42.14
[Fe+Al]/[Ca+Mg]	12.33	11.85	14.75	4.07	4.61	3.94	0.02	0.03	0.04	1.07	1.05	1.11

6.4.2.1.Microstructures after longer experiments

i. 20 minutes reduction

Examples of grains exposed in reducing conditions for longer times are shown in the following images. Grains from samples WCS108 and WCS90 after 20 minutes reduction under the 750°C conditions are shown in Figure 84. Microstructure 1 is identified in both cases.

Reduction is clearly more progressed at this reduction time and Hematite crystals have almost entirely transitioned into newly formed Magnetite, which is characterized by its “dirty” looking surface for both grains.

SFCA is also further reduced, and it has reacted almost completely in the case of WCS90 grain, whereas in WCS108 it still preserves an unreacted core. The SFCA reacts into the multiphase intergrowth, which is observed with the SEM images in both cases. The multiphase intergrowth of WCS108 is shown in Figure 85. The intergrowth has a different development than before, since it is forming in small exsolution lines, rather than tiny spots. The three phases that are found intergrowing are also more distinct than before, and further separated.

Wüstite is also more intensively separating from Magnetite forming numerous small bright lines on its surface, as shown in SEM image Figure 86.

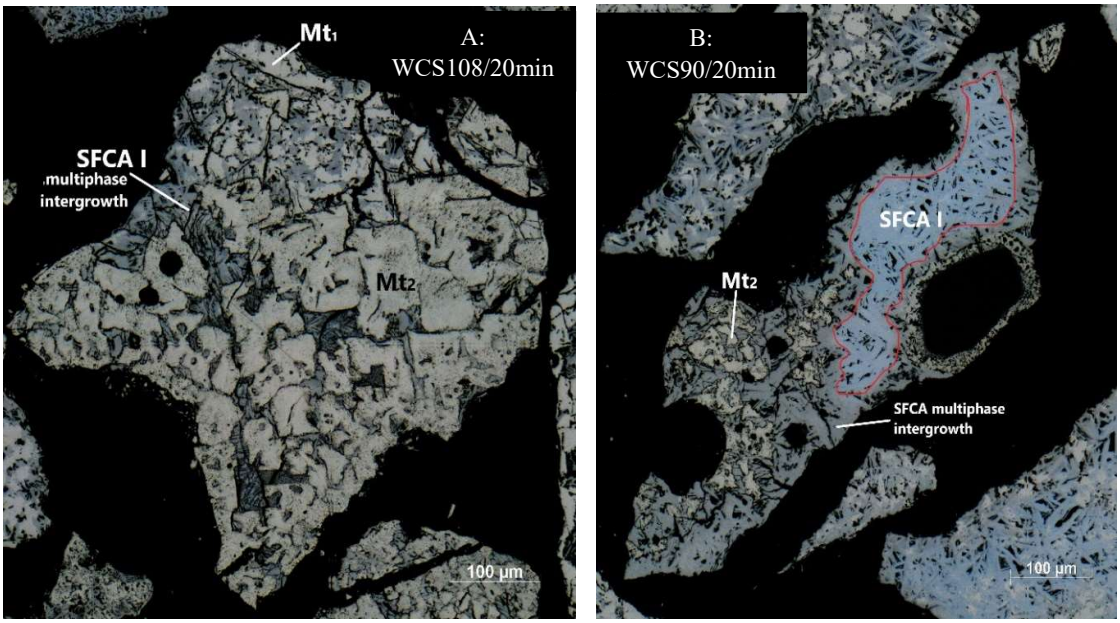

Figure 84. Polarised reflected light microscopy image (20x magnification). **Microstructure 1 after 20 minutes reduction (750°C/XCO=0.55/N_2=0.5); A.** Grain from sample WCS108 after t=20min **B.** Grain from sample WCS90 after t=20min

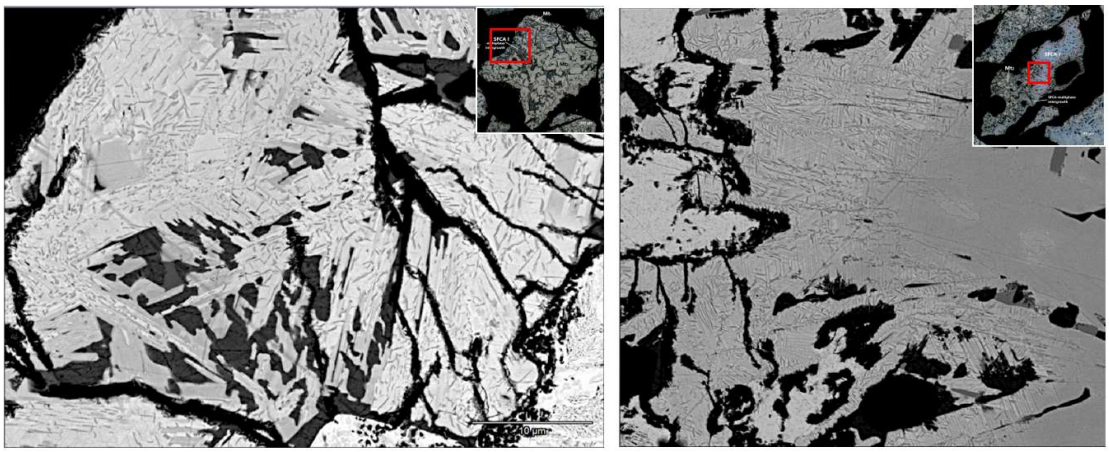

Figure 85. SEM images showing the multiphase intergrowth of WCS108 and WC90 grains after reduction for 20 minutes under T=950°C.

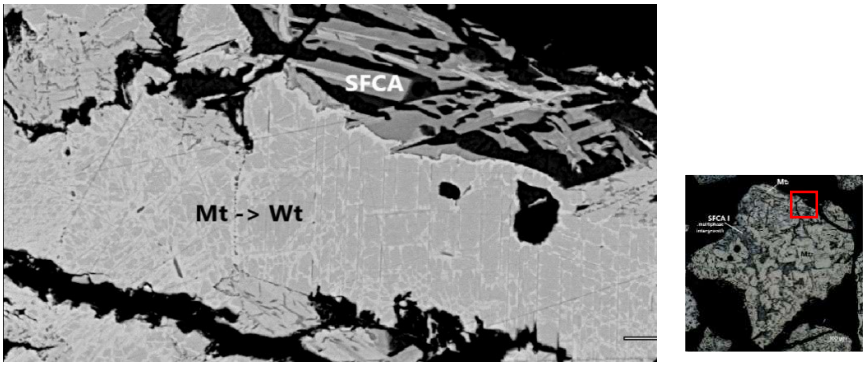

Figure 86. SEM image; Magnetite □Wüstite (WCS108, t=20min, T=950°C)

ii. Longest duration reduction (t=5hours/t=4.5days)

After long-time experiments for t=5hours under T=950ºC/XCO=0.65/N_2=0.5 and t=4.5days under T=750ºC/XCO=0.55/N^2=0.5, the sinter samples look much different in comparison to the ones produced from shorter experiment runs. This is because they contain fewer phases than the starting and short-run materials. As shown before, the initial sinter samples start reducing with a variety of different phases, which all tend to transition to a few, more stable phases under the ever-changing reducing conditions. In accordance, after longer times, these reactions have further escalated and the system approaches equilibrium. This results to the formation of the final end-destination minerals. Examples of the long-time experiment - phase assemblage is shown in Figure 87 and Figure 88.

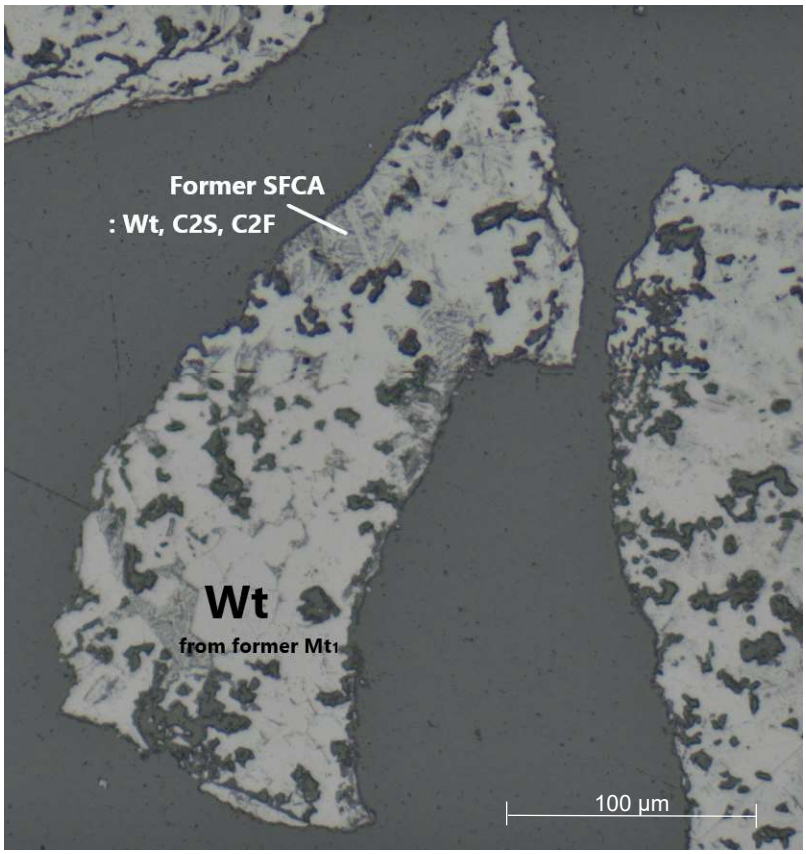

Figure 87. Polarised reflected light microscopy image (20x magnification). Microstructure of a WCS108 grain after reduction for 5hours under T=950ºC/XCO=0.65/N_2=0.5.

The assemblage is optically comprised by Wüstite, Larnite, Brownmillerite and silicate phases. In addition, the newly formed microstructure does not contain any Hematite or Magnetite, since both minerals had been consumed towards the formation of other, more stable phases like Wüstite. The same goes for SFCA and calcium ferrites that have been so abundant in previous cases, have now been displaced by Wüstite, Larnite and Brownmillerite in the structures. The origin of the newly formed phases can be observed by the shape of the crystal they are found in. This is because some crystals preserve the shape of the previous phase, hence the new phases can be placed on the typical elongated acicular or columnar crystal forms of SFCA or the quadrangle crystals of Magnetite.

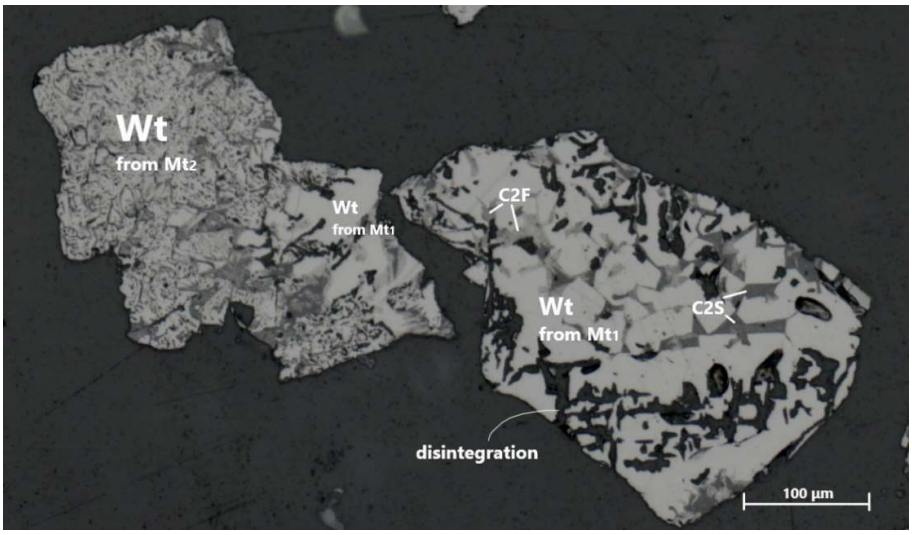

Figure 88. Polarised reflected light microscopy image (20x magnification). Microstructures of WCS86 grains after reduction for 4.5 days under T=750ºC/XCO=0.55/N_2=0.5.

1.4.2.1.Microstructures of industrial sinter

The microscopical study also focused on the microstructures present in the industrial sinter, in order to investigate whether there is any difference between the types found in the pilot-pot sinters. All microstructure types previously observed were also found in the MH1785/21 sample, except for the exsolution structures of microstructure type 3 which were not observed in any sample. The sample demonstrates abundance in microstructures 1 and 1a, as well as microstructures 3 and 4. Microstructure 2 is also present, however the limitation of lack of SEM point analysis on the sample does not allow to clearly distinguish between microstructure type 1 and 2. Moreover, the industrial sample often demonstrates different particle shapes, since a number of them appears to be quite elongated, indicating a breakage tendency during grinding, on the particles' y-axis.

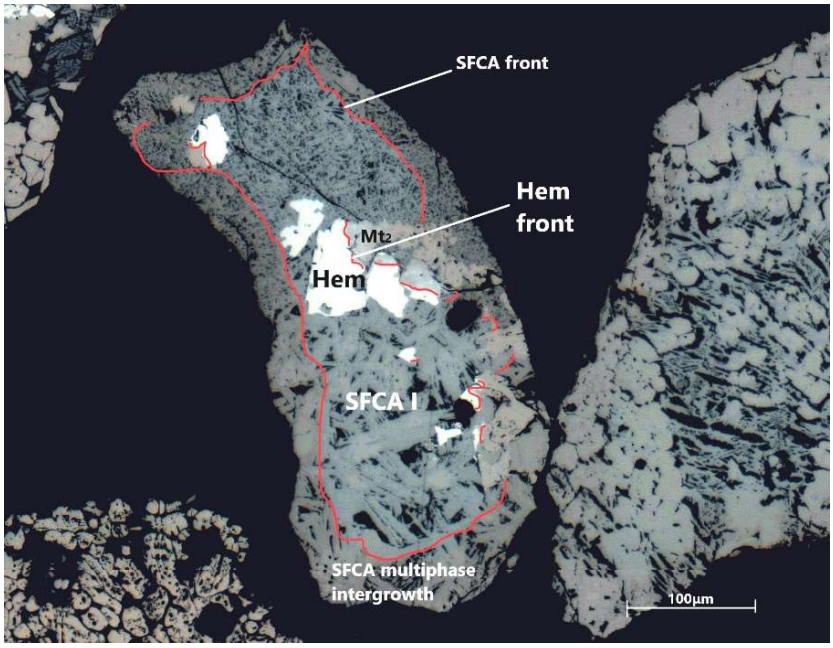

Figure 89. Polarised reflected light microscopy image (20x magnification). **Microstructure 1** in industrial sinter grain (MH1785/21) after reduction for 2 minutes under T=950ºC/XCO=0.65/N_2=0.5.

Example grains showing each microstructural type detected in the industrial sinter are presented in the following images. In addition, examples of the same microstructures included in elongated grains are also provided.

Figure 89 shows an example of MH1785/21 **microstructure type 1**. It has the typical assemblage of the microstructure, with the unreacted core to be comprised by precipitated Hematite, SFCA I and precipitated Magnetite (Mt_1) (and potential Larnite C2S and other calcium ferrites which are not optically visible in the image). The reacted front includes newly formed Magnetite (Mt_2), resulting from the transition of former Hematite, and the SFCA multiphase intergrowth which has a brown/grey color in contrast with the unreacted blue SFCA. The reaction boundaries of SFCA and Hematite are marked with red lines. The industrial sinter also demonstrates Hematite's reduction front to be deeper in the particle, in comparison to the respective reaction front of SFCA.

The alternative version of microstructure 1, was also found present in the industrial sample. This is the same with the previous structure, but without involving precipitated Hematite and his transition products. Figure 90 shows a characteristic example of microstructure 1a found in the industrial sample. The existing assemblage is comprised by SFCA I and precipitated Magnetite (±C2S, ±other Ca-ferrites) in the unreacted part, and reacted SFCA/SFCA multiphase intergrowth with precipitated Magnetite (±C2S, ±other Ca-ferrites) in the reduced areas.

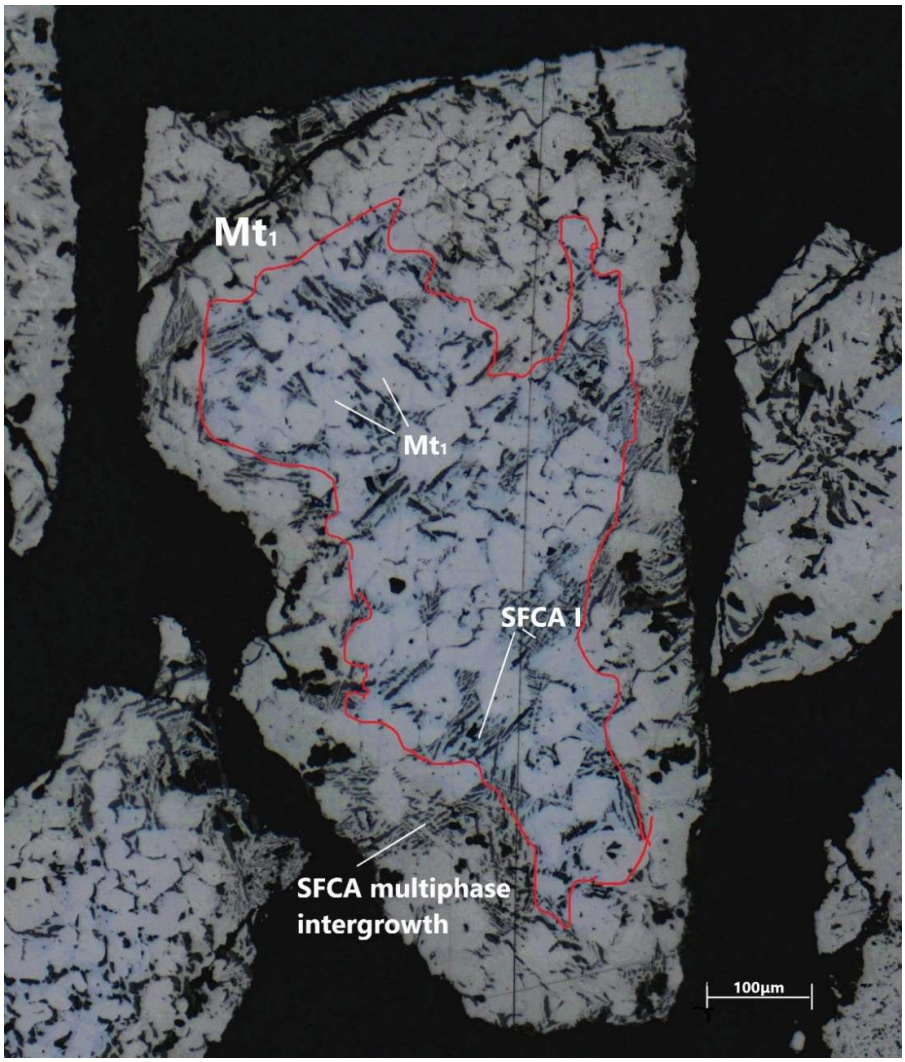

Figure 90. Polarised reflected light microscopy image (20x magnification). **Microstructure 1a** in industrial sinter grain (MH1785/21) after reduction for 4 minutes under T=950°C/XCO=0.65/N_2=0.5.

An example of the same microstructure, but existing on a characteristic elongated grain is shown in Figure 91.

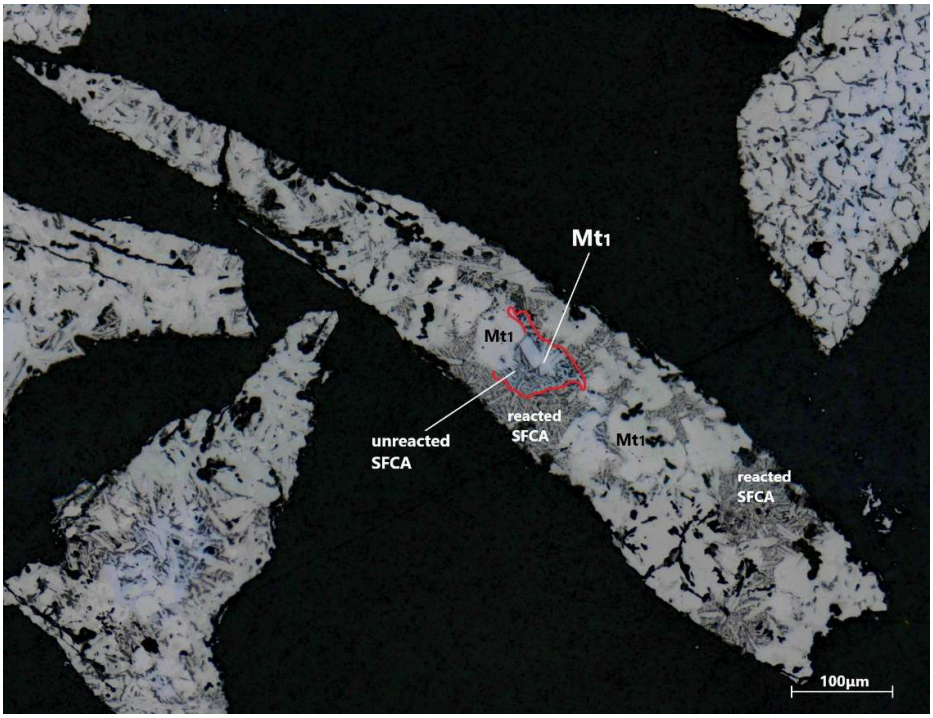

Figure 91. Polarised reflected light microscopy image (20x magnification). **Microstructure 1a** in an elongated grain from the industrial sinter sample (MH1785/21) after reduction for 4 minutes under T=950°C/XCO=0.65/N_2=0.5.

Microstructure type 2 can potentially also be present in the industrial sample. However, it cannot easily be optically distinguishable by Microstructure 1, since they only differ based on the different composition of their unreacted and reacted SFCAs. The only optical feature that can maybe be a categorizing evidence is the shape of SFCA, taken that the high Ca-Al-SFCA type was observed to have more tabular forms. Hence, Figure 92 shows a potential example of **Microstructure type 2 in MH1785/21**.

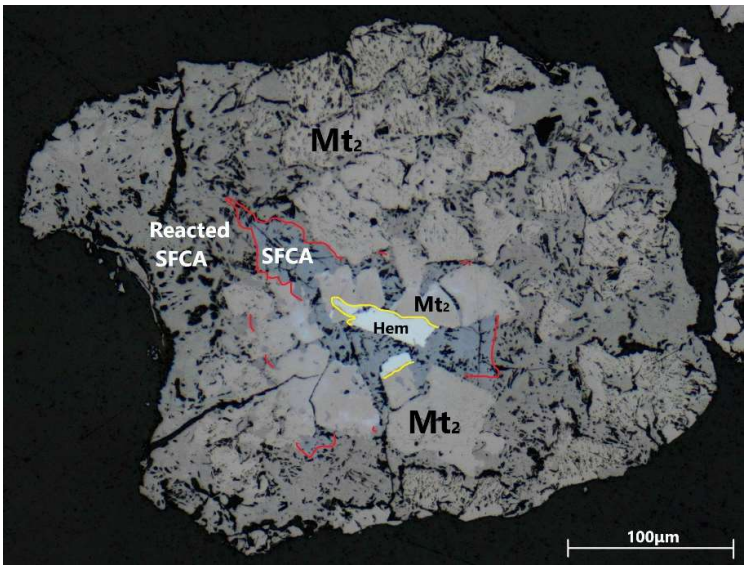

Figure 92 Polarised reflected light microscopy image (20x magnification). **Microstructure 2** in industrial sinter grain (MH1785/21) after reduction for 4 minutes under T=950°C/XCO=0.65/N_2=0.5.

The ore relict microstructure (type 3) was also present in the starting and reduced industrial samples. It is not as abundant as microstructures 1/2 and 4 are, but it is clearly existing in several grains. However, the second type of microstructure type 3, being the exsolution lamellas of Hematite on Magnetite ore, is completely absent from the structures of the industrial sinter. An example of microstructure 3a from MH1785 is shown in Figure 93. Figure 94 shows the ore relict microstructure on a typical elongated particle.

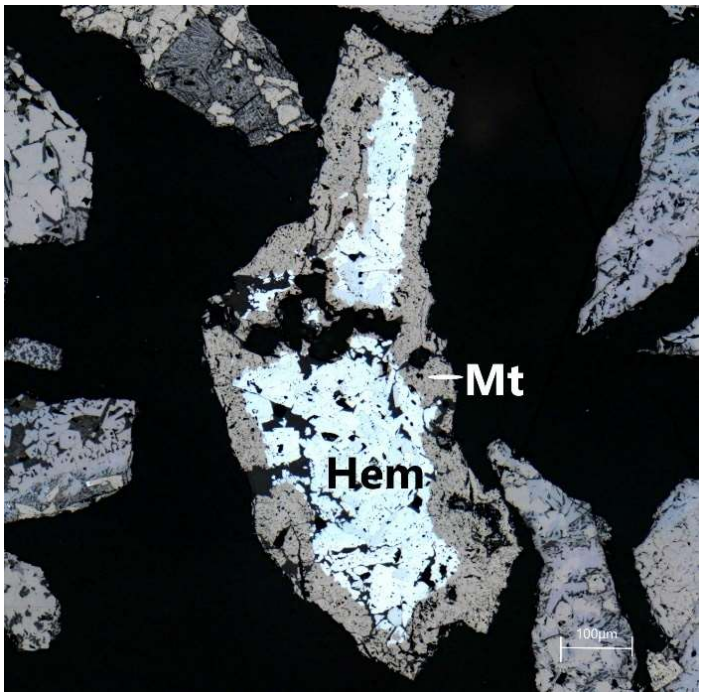

Figure 93 Polarised reflected light microscopy image (20x magnification). **Microstructure 3a** in industrial sinter grain (MH1785/21) after reduction for 5 minutes under T=750°C/XCO=0.65/N_2=0.5.

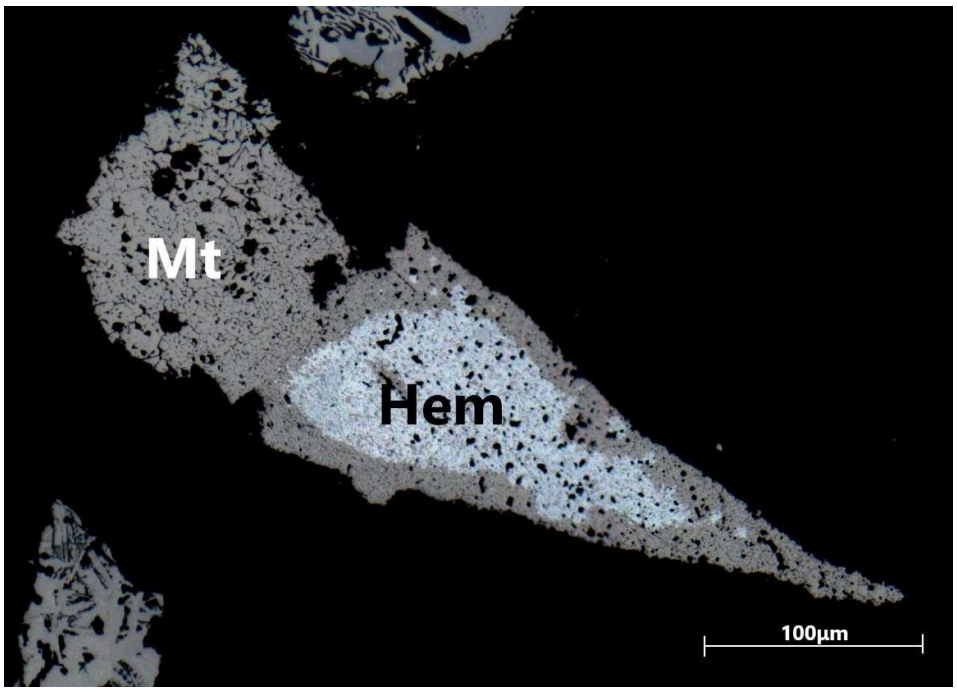

Figure 94. Polarised reflected light microscopy image (20x magnification). **Microstructure 3a** in an elongated industrial sinter grain (MH1785/21) after reduction for 5 minutes under T=750°C/XCO=0.65/N_2=0.5.

Finally, microstructure 4 is found in great proportional abundance in the sample. A representative image of the microstructure taken from the industrial sinter is presented in Figure 95. The structure is comprised by precipitated Magnetite, along with calcium ferrites and well-developed calcium silicate crystals, like those of Larnite C2S.

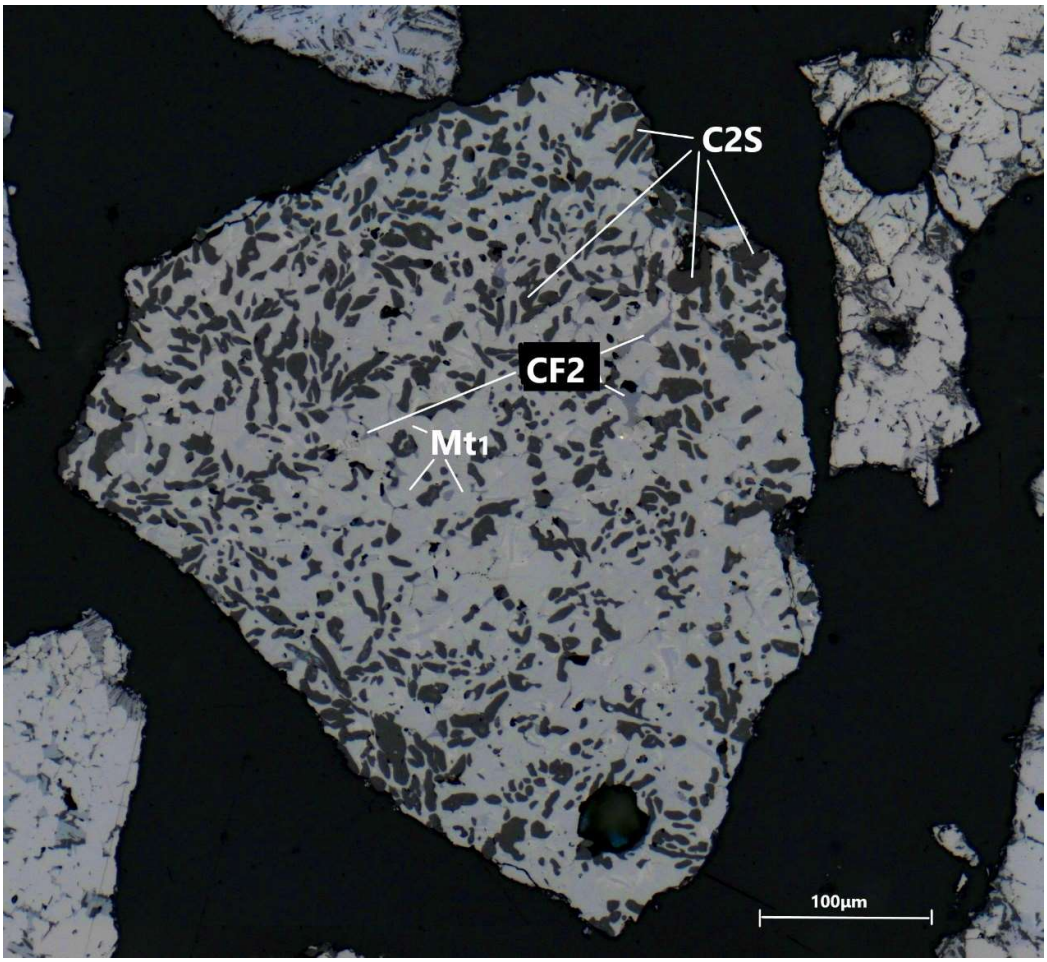

Figure 95 Polarised reflected light microscopy image (20x magnification). **Microstructure 4** in industrial sinter grain (MH1785/21) after reduction for 5 minutes under T=750°C/XCO=0.65/N_2=0.5.

Therefore, the industrial sinter MH1785/21 demonstrates the same microstructural types as the rest of the sinters, even though the latter were produced in a small sinter pot. The main difference is the lack of exsolution structures, but in general no odd new structures are introduced by the sample.

6. Discussion

The current chapter addresses the research hypothesis and research questions, by using the findings from the experimental and analytical work that was presented in the previous chapters. The objective of the study is to verify the influence of mineralogy and microstructure on sinter's direct reducibility. Most of the existing studies do not separate the influence of porosity features from the impact of the compositional/mineralogy characteristics of sinter. Thus, it remains unanswered whether the observed difference in sinter reduction behaviour is due to the one characteristic factor or the other. This section attempts to give answers to the individual research questions, in order to confirm or deny the research hypothesis, which solely focuses on the factor of sinter mineralogy and microstructure concerning sinter reduction, when deliberately excluding meso-structure and macro-porosity.

Sinter reducibility is governed by thermodynamics and metallurgical kinetics; therefore, it is currently studied in these terms. The main research question of this study is whether different starting sinter composition and mineralogy influences reducibility kinetics and how. More specifically, whether sinters of different basicity and FeO contents have a different reduction behaviour under certain conditions. Multiple reduction experiments were performed in order to answer the current enquiry, by using the TGA and GERO in order to provide the relative reaction state of sinters at different reduction times. The relative reduction state of the six sinters governed only by micro-scale effects, at certain times of the reaction process under a certain temperature and gas composition, provides relative reducibility kinetics. This addresses whether different mineralogy and chemical composition do influence the speed rate that the samples get reduced. Evidence from the previous chapters provide the following explanations;

1. *Do different starting composition and mineralogy influence reducibility kinetics?*

As observed in the TGA and GERO experiments, the initial composition and mineralogy do impact sinter reducibility kinetics. Sinters with different composition-mineralogy demonstrate different reaction progress curves under identical experimental conditions. The differences in the shape of the reduction progress curves are clearly related to differences in mineralogical composition. Sample reduction progress varies in the TGA, showing different relative reduction degrees versus time, in correlation to different starting composition. The same goes for the resulting O/Fe TGA curves, where the redox state of the samples is included. Again, sinters give different reduction curves, and reduction rates compared to each other, as well as different reaction speed patterns.

The mineralogy of the samples is clearly reflected by the samples' different TGA O/Fe reduction rates. According to the patterns, most reactions happen during the very first minutes of the reduction experiments, indicated by the samples' speed rate peaks. The sample WCS108 presents the highest initial reduction rate peak, followed by WCS90, WCS86 and finally WCS62 (Figure 96).

The different rate patterns of the samples are linked to the reduction of main sinter minerals. What is indicative of the mineralogy effects is the characteristic kink in the rate signal of WCS108 and WCS86. Both samples show a high starting peak that slows down only to from a second-rate peak. This indicates that there is a certain kinetic barrier for the two samples, which causes their reduction rates to abruptly slowdown and reach a low peak, before rising back up again. This kinetic barrier is attributed to their similar mineralogy, and more specifically to their greater Hematite content in comparison to the other two samples. However, that alone does not distinguish them from WCS90 specifically, since the latter also displays relatively high Hematite amounts, similar to WCS86. Their difference is that they also demonstrate higher Magnetite and lower SFCA quantities.

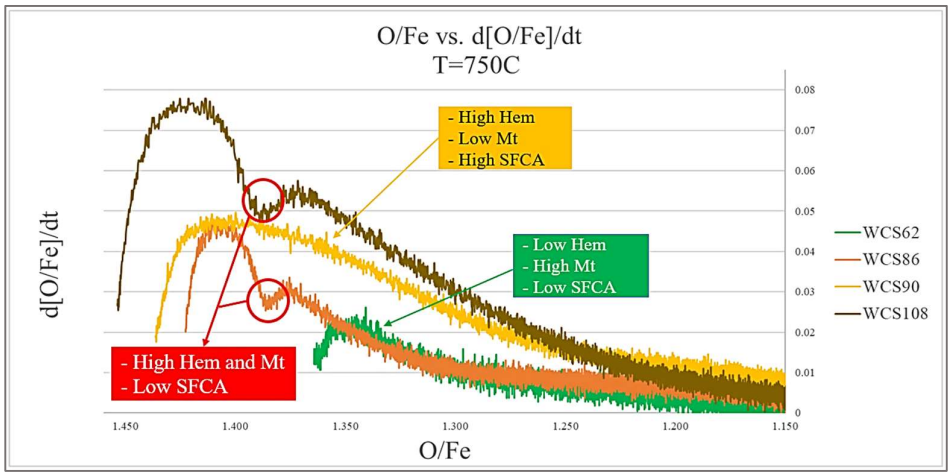

Figure 96. O/Fe reduction rates of samples tested in TGA vs. O/Fe for T=750°C/XCO=0.55/N_2=0.5, linked to sample mineralogy.

Most specifically, WCS108 which has the greatest Hematite content presents the earliest and highest peak from the mineral's reduction to secondary Magnetite. Then its rate slows down possibly due to Hematite consumption and rises back up when the reduction of Magnetite starts to dominate the reduction peak. WCS86 follows the same pattern, albeit its initial peak is much smaller in comparison to WCS108, since it has less content in Hematite. They both present the kink at the same point of reduction progress and rise accordingly after. Very similar levels of Hematite compared to WCS86, has the sample WCS90, and this is also shown in their initial peaks' altitudes. However, in contrast with WCS86, WCS90 does not demonstrate any falling kink, and its reduction rate remains high until it smoothly reduces later. This pattern can be attributed to its less Magnetite and higher SFCA contents. Evidence from the microscopy work verify that the first mineral to reduce is Hematite, followed by the reduction of SFCA, while Magnetite remains stable for longer. This provided, Hematite's reduction in WCS90 is succeeded by SFCA reduction, which does not let the rate to reduce, nor form a kink.

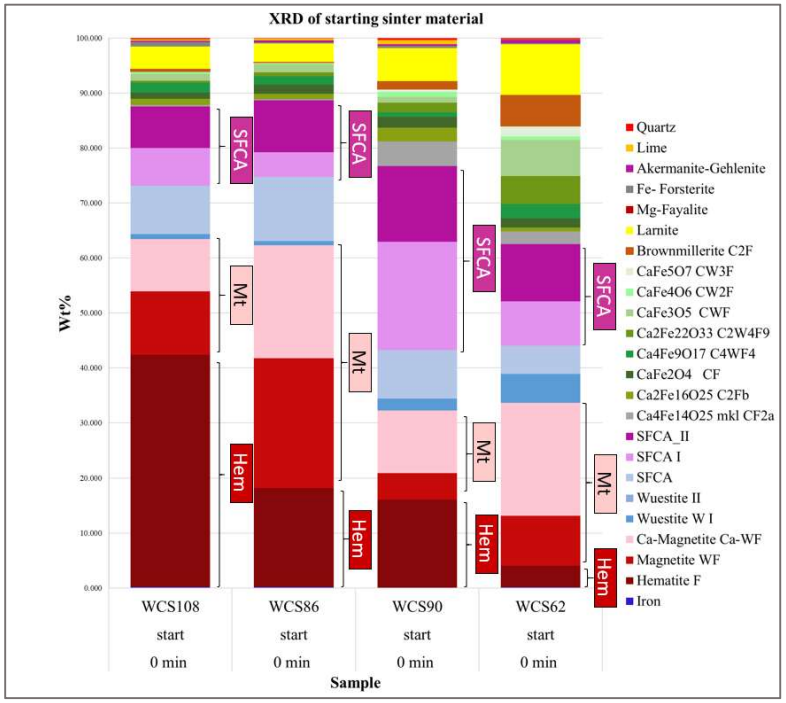

Figure 97. Starting mineralogy of samples tested in TGA for T=750°C/XCO=0.55/N_2=0.5

Finally, WCS62 starts reducing last of all the samples based on relative reduction progress, and it starts with a very small peak followed by a tiny kink, to then rise on a second much higher peak. The initial peak is so small that it is not clearly visible in the graph of Figure 96. The starting little peak of WCS62 corresponds to the reduction of the limited Hematite amounts. This is then followed by the reduction of mostly precipitated and ore relict Magnetite, which is much more abundant in the sample. Magnetite in WCS86 and WCS108 starts to dominate the reduction signal at the same point of the reaction progress, and since both samples are Hematite-rich, most of this Magnetite is considered to be newly formed. This is probably the reason why WCS108 has a larger second peak than WCS86, albeit WCS86 is initially much more enriched in precipitated and ore-relict Magnetite based on the XRD analysis. This is also supported by evidence from microscopy, which show the respective samples being rich in primary Hematite in the unreacted cores, and in secondary Magnetite in the reacted fronts.

Hence, it is implied that the reduction rate signal results from the coinciding effect of signals of mineral phases. However, based on the point in the reduction progress, the signal is mostly dominated by the reduction of one certain mineral that is getting reduced more massively, as illustrated in Figure 98. The figure schematically illustrates the reduction of minerals linked to the TGA rate curves.

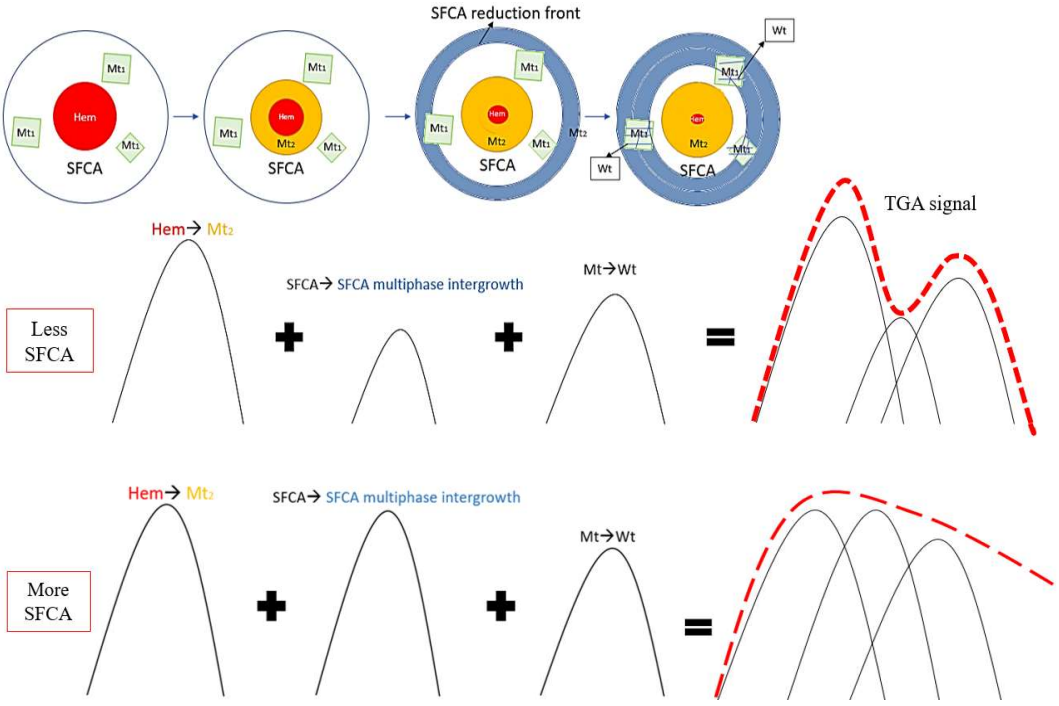

Figure 98. TGA reduction rates linked to reduction of certain minerals.

The first mineral to dominate the rate appears to be Hematite, which is the first phase to get consumed. Based on the XRD analysis, Hematite, is almost completely absent when Wüstite starts to form. In addition, based on microscopy, Hematite reduction fronts are much deeper in the grain than SFCA's reduction. This indicates that SFCA can stay stable for longer under certain conditions, whereas Hematite gets displaced by Magnetite. This provided, the reduction rate is secondarily dominated by SFCA's reduction; Hence, this is why the SFCA-rich sample WCS90 does not illustrate a slowing kink after its initial Hematite-dominated reduction peak. Samples with less SFCA amounts will follow the first signal illustration, forming a slowing kink after Hematite's reduction signal, while samples with higher SFCA contents will follow the second illustration. Magnetite on the other hand remains stable longer

than both Hematite and SFCA, therefore it starts to reduce more intensely later in the reduction progress. Accordingly, the SFCA dominated signal of WCS90 does not slow down, due to Magnetite's increasing reduction signal.

The O/Fe reduction rates of the two extreme samples under the T=950°C conditions, show additional patterns that can be associated with the samples' different mineralogy. These patterns indicate that the higher temperature conditions cause minerals to reduce differently in relation.

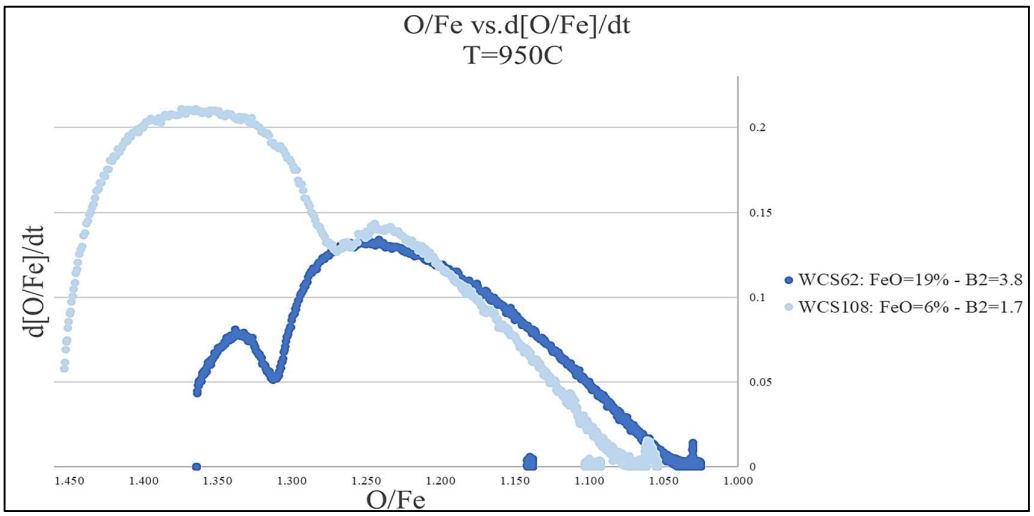

Figure 99. O/Fe reduction rates of two samples of extreme composition tested in TGA vs. O/Fe for T=950°C/XCO=065/N_2=0.5, linked to sample mineralogy.

At T=950°C, WCS 108 again starts with a very high peak due to Hematite's reduction, which this time is reducing in much greater amounts than in T=750°C, but also lasts for a greater range of the reduction progress (Figure 99). The excessive reduction amount of Hematite that gives this extensive first peak, stalls Magnetite's dominance on the reduction signal, that succeeds it. Under 750°C, the second peak occurs much earlier in O/Fe reaction progress, but also, does not last for a great reduction progress rate as it does under T=950°C. In the meantime, WCS62 starts reducing more Hematite amounts than the minimum observed under 750°C, and proceeds with Magnetite-dominated reduction, earlier even than WCS108, which is still governed by its first peak. In addition, the amount of Magnetite reduced, referring to the second peak of WCS62, is much greater in proportion than the one consumed under the low temperature conditions. Hence, the T=950°C conditions appear to be more favourable for the reduction of samples with more (primary and/or precipitated) Magnetite, as they boost the mineral's relative reaction.

The observation that more Magnetite is generated, thus is getting further reduced relative to Hematite is also supported by XRD results. WCS62 after 2-minutes reduction has generated much more Wüstite in its assemblage, even though its Hematite is not entirely consumed. On the other hand, after 5 minutes under 950°C, all Hematite contents are gone but relatively to other samples, less Wüstite is present.

GERO experiments also confirm the reduction differences between the sinter materials of various starting compositions. The reduction states of the sinter differ at different experiment interruption times, indicating that some are more progressively reacted than others. This means that at certain times under the two specified conditions, samples demonstrate different weight losses due to the subtraction of oxygen from their phases, showing that the presence of different mineral phases can facilitate or undermine oxygen escape.

This is coupled with quantitative analysis from the XRD that verifies that mineralogy of samples does change during reduction, and that it is a dynamic system, which starts from a certain starting point, that influences reduction patterns and sinter behaviour. Qualitative mineralogical changes during reduction are also captured from microscopy, providing evidence

that sinters which show certain reduction patterns are characterized by greater abundance of specific dynamic microstructures.

Therefore, certain mineralogical features have an advancing impact to sinter reduction behavior. In addition, the way minerals influence reducibility is clearly depended on the imposed conditions. Low temperature conditions seem to favor samples that have greater Hematite and SFCA amounts, boosting their reduction progress in comparison to samples with less amounts in the minerals and more Magnetite content. Whereas, high temperature conditions merge the reduction differences of low and high basicity samples, due to the relative reduction progress of minerals, like primary/precipitated Magnetite.

2. *Can the effect of mineralogy and composition on reducibility kinetics be separated from the effect of open porosity?*

Different internal porosity is important, since it can be a contributing factor on sample reduction behaviour on top of mineralogical and compositional effects. The BET measurements performed on sinter samples have demonstrated some variability. These differences in measured BET specific surface don't appear to be dominated by the contribution from any variation in particle size distribution. Based on the assumption that all the particles are dense spherical balls, the specific surface areas of the sample, and their size distribution do not fluctuate much in accordance, since this variation is much more limited than the one observed in the BET measurements. Therefore, this variation observed in the BET specific surface area must be due to either one or both of;

1) Differences in external morphology of the particles. The particles are not plane dense spheres, but they have more complex shapes with potential for systematic differences in the surface area of the particles between samples.

and/or

2) Differences in the open porosity internally within the particles.

However, even this distinction can be quite subjective, as it should first be defined what is considered part of the exterior of the particle, and what is considered an open pore.

By plotting the BET values on the sample composition matrix, it is observed that there is a correlation with respective changes in sinter composition (Figure 100). It appears that samples with greater FeO content tend to have smaller specific surface areas, while samples of lower FeO demonstrate the opposite.

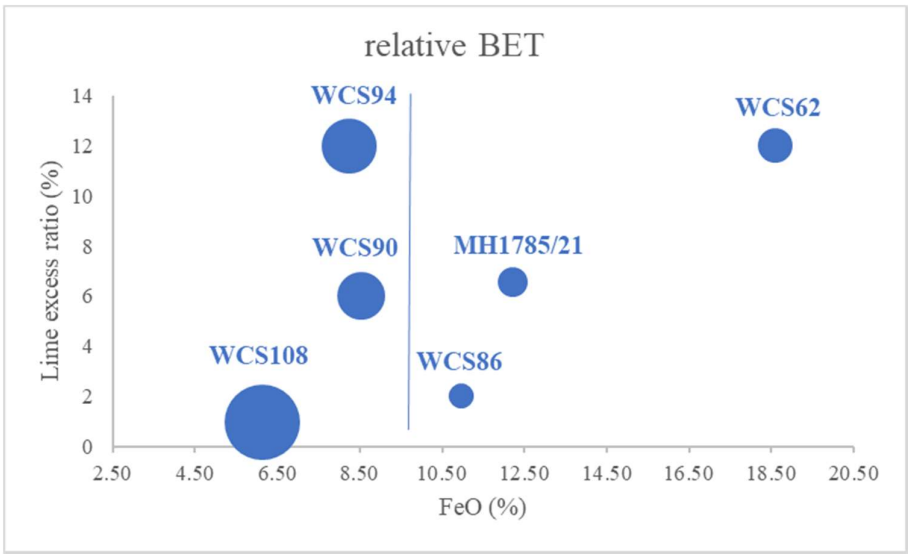

Figure 100. Specific surface area (BET) is linked to sintering composition.

Therefore, differences in the relative specific area appear to have some kind of relation with differences in sample composition and therefore mineralogy. Provided that these differences are attributed to different internal porosity, this indicates that micro-porosity is interrelated with composition and mineralogy, since the presence and formation of difference minerals and their relative structure tailors the existing microstructure; hence, influences open porosity. Hereafter, it is firmly arguable that changing one of these characteristics inevitably alters the other.

Based on the above, even though open porosity can show some substantial variations, mineralogy and microstructure can directly influence sinter reducibility, even when these other variables are kept as constant as practically possible.

3. *How do different staring composition and mineralogy influence kinetics (reduction rate and reduction degree)?*

Evidence obtained via optical and scanning electron microscopy reveal the relative reducibility of certain minerals and the meta-stable reduction paths of others. The reduction fronts of the minerals differ in relative grain depth. In a dense grain, reduction starts from the edges progressing gradually to the core. Therefore, the conditions of gas atmosphere and temperature vary within one grain and they locally interact with the different phases. At the same depth where conditions allegedly are the same, certain minerals were observed to react, whereas others stayed intact. More specifically, Hematite demonstrates deeper reduction fronts in comparison to other phases, and it is the first mineral to get reduced under a certain set of conditions imposed at a specific depth in the grain. Its reduction to Magnetite is more rapid than SFCA and CF2 transition to their respective phase intergrowths (Figure 101). Even within the same microstructure, Hematite is clearly reduced to a greater distance from the particle exterior than the Ca-ferrites surrounding it, and in the XRD analyses the normalized decrease in Hematite from its initial concentration is clearly faster than that for any of the Ca-ferrites (SFCA, CF2). SFCA follows with a reaction front that consistently forms a corona on the outer parts of the grains keeping a clear distance from the front of Hematite's transition. This implies that SFCA is a mineral that can remain stable for longer under the same imposed conditions, compared to Hematite. Magnetite on the other hand, precipitated and secondarily formed shows no to little evidence of alternation in the same context. It can be found within the reduced area of SFCA with no apparent reaction occurrence. In accordance, precipitated Magnetite appears to be even harder to reduce than the other two minerals, as it can take more reducing conditions without altering its appearance, whereas secondary Magnetite is still forming.

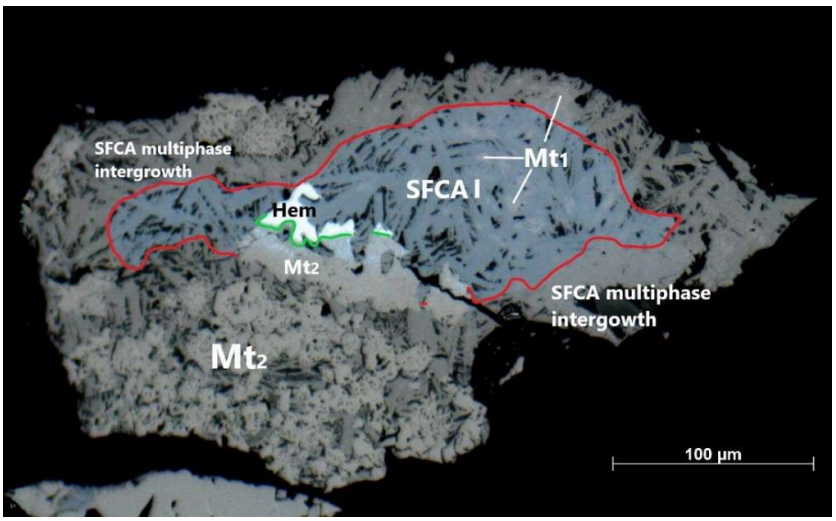

Figure 101. Hematite reduction front deeper in the particle than SFCA front. Magnetite is present in the unreacted core and in the reduced areas.

The relative positioning of the reduction fronts can also vary based on the reduction experiment conditions. Under the more moderate conditions of T=750°C/XCO=0.55/N_2=0.5, the difference between the two relative reduction fronts of Hematite and SFCA is much greater, than the respective fronts of the two minerals under T=950°C/XCO=0.65/N_2=0.5. It seems like under the more intense conditions the reduction fronts of the two phases converge, while under the moderate ones they become more distant to each other. This can be indicative of the SFCA behavior under different temperatures and gas atmospheres. This discrepancy is also confirmed by the XRD data; According to the graph of Figure 102, starting from the same point respectively, the difference in the reduction progress of the two minerals is less under more reducing conditions, while it gets enhanced under the moderate ones. At early times of reduction, like in the cases examined under the microscope, at 750 – t=5minutes, Hematite and SFCA have a difference in reduction of 40%, in comparison to 950 – t=4minutes, where their difference in reduction is way less (Δ(wt%)=14%) even though the reduction duration was less.

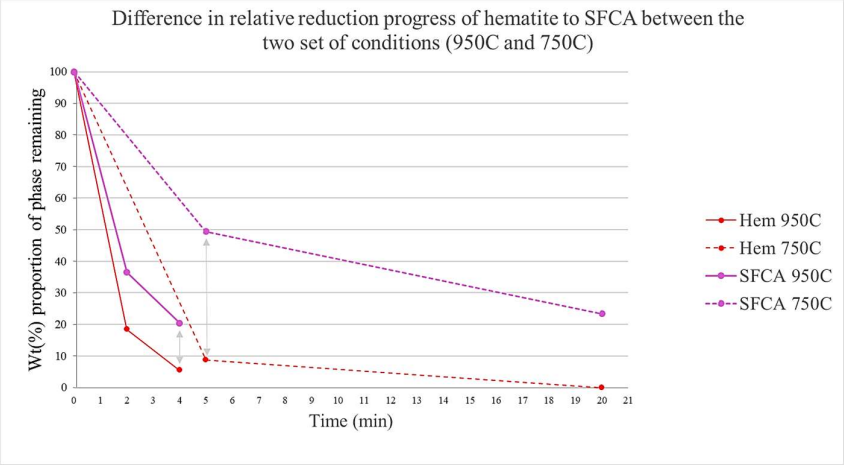

Figure 102. Relative reduction progress of Hematite and SFCA between the two sets of conditions (950°C and 750°C)

SFCA transition was also captured under the microscope, revealing information on phase transformation according to its initial chemical type. Two types of precipitated SFCA were found in this study, one very high in Fe content, referred to as SFCA-1 and one low in Fe and high in Ca and Si. The calcic type SFCA would only transition to 1 apparent phase, which was not much different in chemistry, but clearly displayed a different color. On the other hand, SFCA 1 would transition to a very fine multiphase intergrowth, in which clear stoichiometric phases are hardly distinguished. At short reduction times, it was verified that this intergrowth is comprised by 3 different phases, one Fe-rich white phase with more Fe than the SFCA-I bulk composition, a high-Ca grey phase relatively poorer in Fe and richer in Ca, and a darker phase with a stoichiometry more closely approaching the one of Brownmillerite (C2F, C2(A)F), but with higher contents in alumina and/or silica (Figure 103).

All three phases from the intergrowth plot between the nominal compositions of SFCA types and the endmembers of known Ca-ferrites like CF2, CF3, CWF, CW3F and others. At more reduced positions, the bright white phase of the intergrowth becomes more ferrous and less calcic, distancing from SFCA 1 composition, while approaching the composition of iron oxides Fe_xO_y, without fitting neither of the two. The grey phase on the other hand, becomes poorer in Fe, and richer in calcium approaching more the composition of calcium ferrites, while the darkest phase, is even richer in calcium and silica while more closely approaching Brownmillerite's composition (C2F, C2(A)F), without quite fitting the phase stoichiometry due to its higher Si and Fe contents.

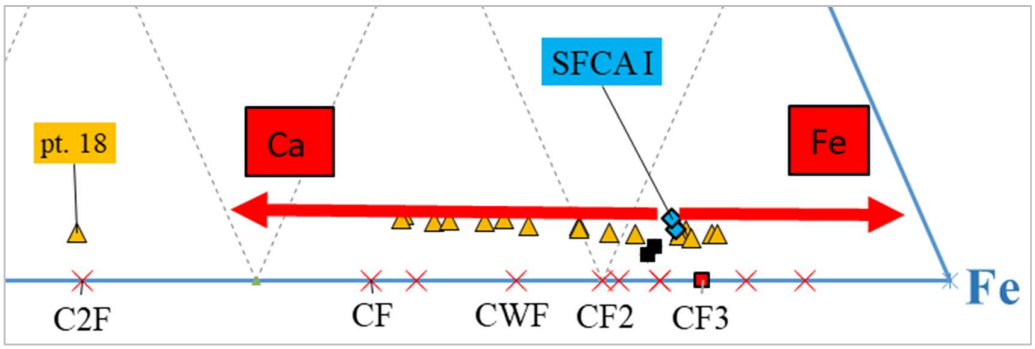

Figure 103. Phase separation and chemical distribution starting from SFCA I.

These findings show the start of SFCA reduction towards Wüstite, ±Brownmillerite C2F, ±Larnite C2S and ±Melilite. It is apparent that there are two main transformation paths forming, one accumulating Fe and one becoming enriched in Ca. The paths of the intergrowth development are illustrated in Figure 104.

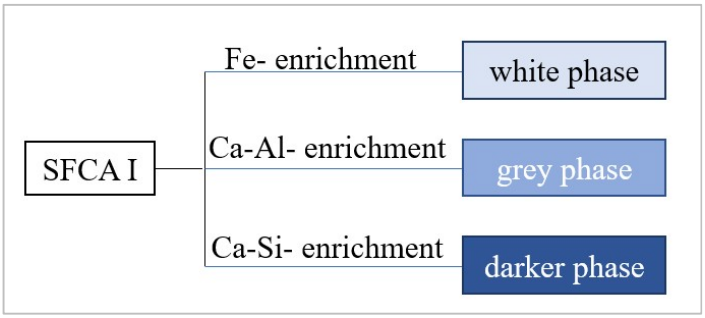

Figure 104. Multiphase intergrowth chemical paths illustration.

The images of shorter-time experiments are only relevant to the initial part of the reduction, when Magnetite is still forming from other phases. However, the subsequent reduction of Magnetite to Wüstite and the formation of intermediate 'transient' Ca-ferrites such as CWF to [Wüstite + C2F] is also important. Some samples might experience an initially faster reduction followed by slower reduction once Wüstite starts to form, and vice versa. It's clear that even with an external gas atmosphere which should be in equilibrium with Wüstite, the particles experience a clear sequence of intermediate reactions on the way to the equilibrium with the gas phase; first Magnetite forms, then it turns into Wüstite, while throughout this, C2F and Larnite increase in abundance. Based on XRD, CWF and CW3F show a similar transient behavior to Magnetite, by forming and then disappearing again. This implies that are also a reflection of a path through the phase diagram, from Hematite and SFCA stability, through to the final destination stability field (Wüstite, ± C2F, ± C2S, ± Melilite).

These intermediate reactions all have an influence on the developing microstructure which has consequences for the kinetics of the reactions that follow. This will become especially important at the bottom of the reserve zone where metal starts to form. The phase intergrowths that form in the volumes of former SFCA or other Ca-ferrite crystals will behave differently during metallization than a grain which started out as an ore-relict Hematite, precipitated Hematite, ore-relict Magnetite or as precipitated Magnetite. Therefore, specific grains undergo important complex alterations in their microstructure on their way to the reserve zone and within it, before the first formation of metal in the BRASS test (also in the real BF process), while other grains do not. Most of the differences in reduction behavior further down the line are already influenced by what happens in the temperature ranges of 600 – 950°C; Hence, under conditions nominally within the Wüstite stability field.

4. Which sample composition is more prone to reduction?

According to the TGA results, and the relative sample reduction degree versus time in Figure 105, the moderate basicity- moderate FeO sample WCS90 has the optimum starting composition and mineralogy to get the most reduced under the conditions of T=750°C/XCO=0.55/N_2=0.5, after t=50 minutes of reduction. The rest of sample-curves follow with small, but solid differences.

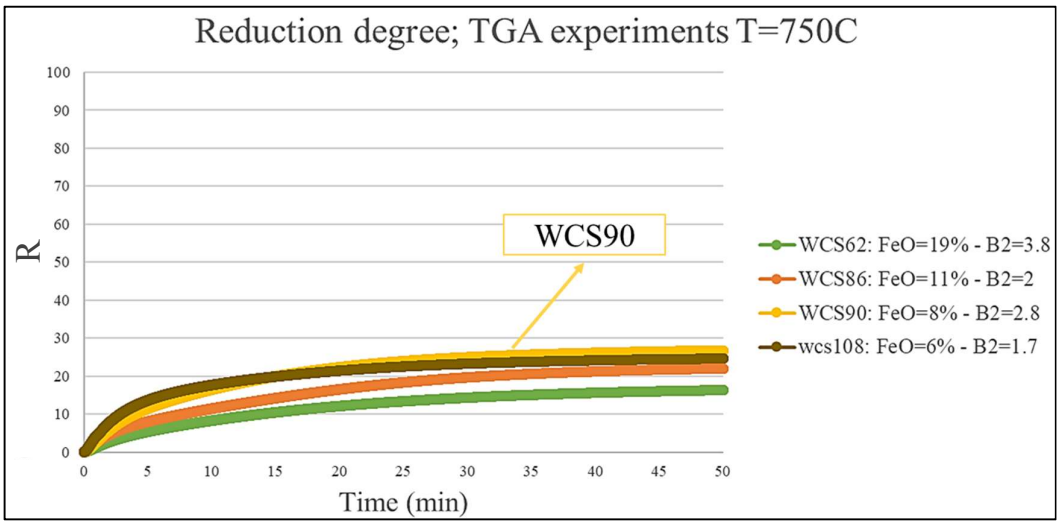

Figure 105. WCS90 it the most reduced sample after t=50 min in the TGA under the conditions of T=750°C.

At the most reducing conditions of T=950°C/XCO=0.65/N_2=0.5, and for t=35minutes in the TGA, WCS108 demonstrates the greatest weight percent oxygen loss, in comparison with the other sample of extreme composition, being WCS62. However, the two curves plot even closer to each other than in 750°C (Figure 106), showing that the most reducing conditions merge curves close together, mostly due to the proportional reduction boost of WCS62. This may indicate that the effect of mineralogy is weaker under more intense conditions, or rather that samples of high basicity are mostly favored when condition are more reducing.

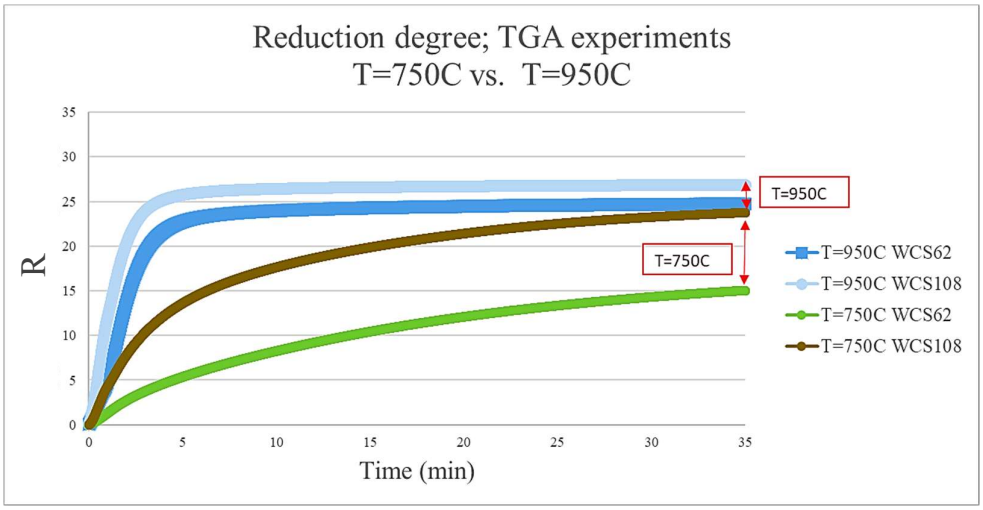

Figure 106. Reduction degree curves of WCS62 and WCS108 merge together under the more reducing conditions of T=950°C.

WCS90, not only reduces further in absolute terms of reduction degree, but it also ends up being the most reduced in the case where the initial O/Fe of the samples is considered. Therefore, even when its initial reduced redox state is not taken into account, it still appears to be the sample presenting the greatest mass loss in the TGA. Based on current knowledge the lowest basicity samples like WCS108 or WCS86 were expected to show greater reduction, rather than WCS90, which is of higher basicity. However, its progressed reduction can be attributed to the sample's different mineralogy.

As mentioned before, WCS90 has quite different Magnetite levels to WCS86, albeit they have similar high amounts of Hematite. WCS86 has much more Magnetite and Ca-Magnetite than WCS90, which in turn displays much greater amounts of SFCA and calcium ferrites. The presence of Magnetite in WCS86 makes it harder to reduce, while WCS90 demonstrates less amount of the mineral. In comparison to WCS108, WCS90 has less Hematite, and similar amounts of Magnetite. However, what differentiates it is the highest amount of SFCA amongst the 4 samples tested under T=750ºC in the TGA, indicating that these mineralogy characteristics may be the most favorable for greater reduction.

Under the conditions of T=950ºC in the TGA, the O/Fe curves of WCS62 and WCS108 not only merge together, but WCS62 surpasses WCS108 in reduction (Figure 107). This is because it already starts from a much more reduced state, and their absolute relative reduction coincides under the more reducing conditions. Therefore, when the absolute weight loss of WCS62 in the TGA approaches the weight loss of WCS108, and then their redox states are added, WCS62 ends up being more reduced. The fact that their relative reduction progress of the two extreme samples merges together is shown by the respective reduction rates. Their patterns indicate that the more reducing conditions cause minerals to reduce in differently in relation.

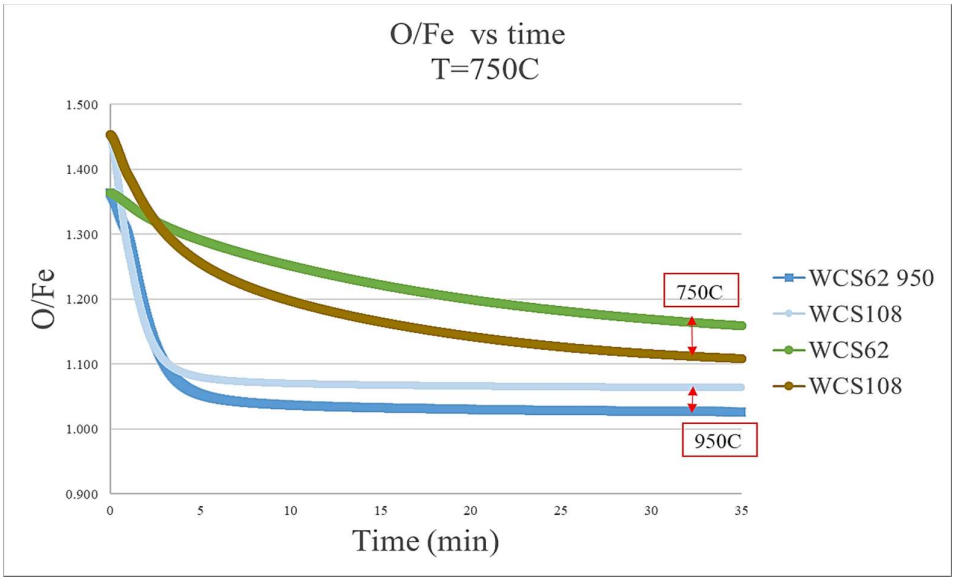

Figure 107. O/Fe curves of WCS62 and WCS108 merge together under the more reducing conditions of T=950ºC.

Reduction experiments were also performed in the GERO, using the total of the samples. The GERO results are in upright agreement with TGA, even though the two methods show clear discrepancies, with TGA being more reducing in general. WCS90 is again consistently more reduced than expected in the GERO, plotting after WCS108, even after long-time experiments. When reduction weight losses in the GERO are normalized to the initial redox state of the samples, the latter are positioned according to their starting sequence based on initial reduction state, and it is only after long experiments that their positions get reversed. The order of the samples based on reduction is always the same after long exposure; WCS108 is the most reduced, followed by WCS90, WCS86, the industrial sinter MH1785, WCS62 and

WCS94. This sequence is close to the one resulting from the TGA experiments under the moderate conditions, where most of the samples were tested.

However, the reduction results of the GERO experiments were not so systematically considered due to limitations of the weight loss measurement method. The process of measuring mass loss includes weighting the different crucibles that contain the reduced sample grains. The precision scale that was used would have an accuracy of 3 digits, leaving space for minor errors. In addition, the method is more prone to sample losses. Given that, the TGA was considered a more reliable technique for monitoring sinter reduction, since it includes real-time weight loss measurements. On the other hand, the reduction in the GERO was essential for other parts of the project, as it enabled sample generation for the performance of analytical techniques like XRD, or microscopy.

5. What microstructural changes are observed under the microscope due to reduction?

All four main microstructures were identified in each sinter sample, with varying abundance based on sample composition. Microstructure types 1 and 2 were mostly present in samples of lower basicity like WCS108 and WCS86. More specifically, Microstructure 1 is often present in samples with less Hematite content and higher basicity like WCS62, WCS94 and MH1785/21, in the form of its alternative version, being microstructure 1a, where Hematite is absent in the grains. Microstructure 3 is again more prominent in samples with more Hematite contents, but it is clearly present in all the samples, remaining from the sintering process. Finally, microstructure 4 is characteristic for higher basicity samples like WCS62, WCS94 and MH1784 since they are sinters rich in precipitated Magnetite and calcium ferrites, especially in Larnite C2S.

The most important microstructure themes observed are;

1) Multiphase intergrowths forming from the low-Si-Al, high-Fe SFCA types ('SFCA I') as oppose to the apparent single-phase or sub-microscopic intergrowths forming from the high-Si-Al SFCA.
2) The formation of secondary porosity in more coarsely crystalline Hematite grains (either precipitated secondary Hematite or originally coarsely crystalline Hematite ore) during its reduction to Magnetite.
3) Apparent lack of porosity forming in Magnetite during its reduction to Wüstite
4) Formation of distinctive void structures at the exteriors of the particles, and along apparent cracks extending into the particles, at the phase intergrowth positions. These show the consumption of the iron-rich phase (Wüstite) of the intergrowth.
5) The phases comprising the fine intergrowths formed within the former SFCA and other Ca-ferrites are not precisely identified but they are plotted to the closest relevant phase.

The dynamic reduction progress is captured in microstructures in grains of samples after different reduction times. With greater residence time under more reducing conditions, Hematite (if any initially) is the first mineral to be transitioned. Its product is the porous -newly formed Magnetite. This transitioned is followed by SFCA I and high Ca-Al SFCA, optically turn to a brown phase which is either indeed one phase, or a multiphase intergrowth. Then, as reaction continues precipitated Magnetite and newly formed Magnetite turn into Wüstite, which starts to form veins on their structures. Wüstite also starts to from the intergrowth, along with calcium ferrites, Larnite and potentially Melilite. Finally, the major phases observed in the assemblage are mostly Wüstite, Brownmillerite, Larnite and ±Melilite. Grains from different reduction times are shown in Figure 108. They all correspond to microstructure 1. They present its escalation with greater reduction and residence time. Image A contains the starting microstructure and its initial alternation after 2 minutes of reduction under the conditions of T=950^{o}C; this all together gives microstructure type 1 in its original form. Image B shows the same microstructure after 20 minutes reduction under the conditions of T=750^{o}C. Both Hematite and SFCA are completely reacted in the structure, and microstructure 1 mineralogy is changed. Finally, image C shows microstructure after 5 hours of reduction under the conditions of T=950^{o}C, showing all the phases from the previous assemblage to have transitioned into Wüstite, Brownmillerite and Larnite (and potentially Melilite).

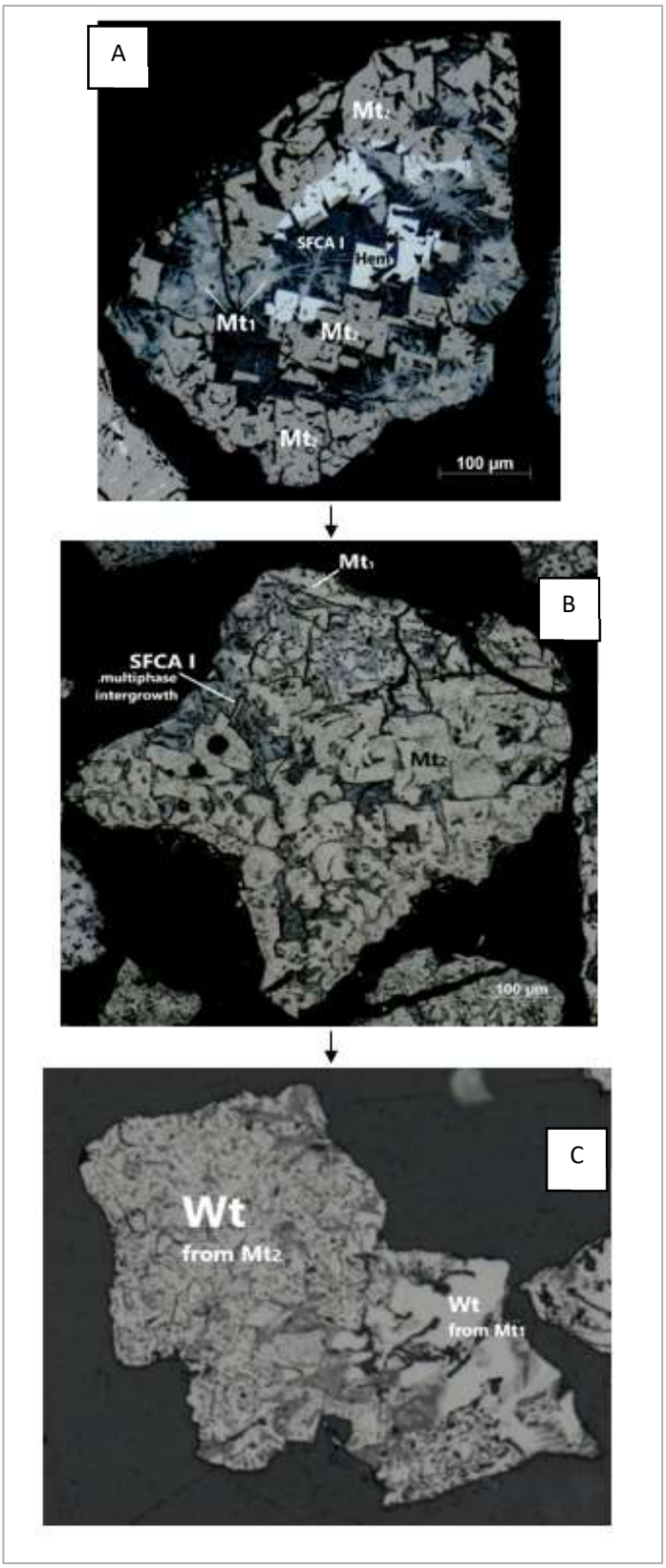

Figure 108. Polarised reflected light microscopy images (20x magnification) of Microstructure 1 and its escalation with longer residence time under the reducing conditions of T=750°C/XCO=0.55/N_2=0.5: A. Microstructure 1 after reduction for 5 minutes; B. Microstructure 1 after reduction for 20 minutes; Microstructure 1 after reduction for 4.5 days.

6. *Do the production sinter and controlled sinter with similar composition reduce differently in practice?*

Focus was also given on the reduction behaviour of the industrial sinter in comparison to the pilot-pot sinters. The BRASS test analysis had shown that industrial sinters tend to be less reducible than sinters of controlled sinter pots referred to as the pilot-pot cluster. In the current study, no particular differences emerged regarding the MH1785/21 sample and the pilot-pot samples of adjacent composition. Mostly, it has been WCS90 that stood out of the bunch as being more reduced than expected, but the rest do not demonstrate peculiar reduction behaviours.

MH1785 was reduced in the GERO furnace, along with the rest of the samples under the conditions of T=750°C and T=950°C. After short-run experiments it does not stand out from the rest of the bunch, and it is reasonably positioned close to WCS86 and WCS94. After longer times in the furnace, its weight loss is slightly less than the one of WCS94, which is one of the samples of highest basicity and should in principle be less reduced in relation. On the other hand, the industrial sinter MH1785 has higher FeO than WCS86 and WCS90, which can arguably make it harder to reduce. In addition, it starts reducing with slightly greater amounts of Hematite, but also greater amounts of Magnetite in comparison to WCS94. On the other hand, WCS94 may have fewer Hematite and Magnetite amounts to some extent, but it precedes in SFCA contents.

In addition, research on the industrial sample under the microscope, has shown no irregularities regarding the sample's microstructures. All 4 microstructural categories were also present in this sample, with microstructures 1 and 4 being the most abundant. The only differences observed compared to the pilot plot sinters is that no Hematite exsolution structures were found on any on the grains, while several grains would have wide looking- elongated shapes.

All outcomes considered, the comparison between the industrial sample and the pot sinters is uneven, since it is governed by the limitation of having only one industrial sample available for the relative assessment.

7. *How does different initial composition and mineralogy impact phase equilibria in practice? Is there agreement with the thermodynamic predictions about the expected O/Fe and mineral phase assemblage at equilibrium?*

The comparison between the resulting O/Fe from the reduction experiments in the GERO/TGA, and the O/Fe predicted by FactSage software at equilibrium, shows that GERO results are in closer agreement with software predictions than the TGA results, for both conditions of different temperature and gas atmosphere. However, there are still some small deviations between what is expected by the software and GERO outcomes. For the most reducing conditions of T=950°C, FactSage underestimates the reduction of most of the samples, while it is in high agreement with the O/Fe values of samples WCS86 and WCS94. TGA final O/Fe values are not in line with FactSage under the most intense conditions for the two samples of extreme composition. TGA more closely approaches the predictions under the moderate conditions of 750°C, with the O/Fe of most samples being overestimated except for WCS108, which is in great alignment with the expected values. In addition, most GERO results under the moderate conditions are also slightly underestimated by the software, with only WCS90 standing out as more reduced in comparison to the prediction.

The results from FactSage software also include the final equilibrium phase assemblage, at the relevant range of temperature and imposed gas composition. The phases expected at equilibrium were compared with the XRD results to examine whether the thermodynamic predictions are in consent with what was revealed in practice. From the comparison, there is more qualitative agreement between the results, than there is quantitative.

The sinter assemblages are comprised by much more phases than the main four phases predicted on FactSage. The difference in the phases, is mostly attributed to limitations in the XRD analysis. This means that, except for Wüstite, Larnite, Brownmillerite and Melilite, the

presence of most of the remaining minerals corresponds to XRD fitting artefacts. Hence, the current graph includes only the 4 main phases expected at equilibrium, which were obtained from the XRD analysis assemblages and were normalized to the respective GERO weight losses for each sample. In addition, the fact that FactSage calculates a bulk equilibrium for the starting composition used as input, contributing to this phase quantity difference. This is because the real samples on the other hand, are a collection of heterogeneous particles, characterized by their individual composition, and effectively, their own FactSage calculation.

However, the relative results have shown that the main mineral phases qualitatively tend to follow FactSage predictions and often fluctuate in alignment with thermodynamic calculations per sample. Generally, better correspondence is observed with the XRD phases under the most reducing conditions of 950ºC.

Nevertheless, the actual amounts of the minerals differ in some cases. Therefore, even when including only the 4 main phases expected at equilibrium, the quantitate differences between the XRD phases and FactSage are substantial. FactSage underestimates the Wüstite contents of samples under both reduction conditions. In addition, it eliminates the presence of Brownmillerite in any of the two samples of lowest basicity, while XRD clearly demonstrates that they do contain some quantities of the mineral. In contrast to Wüstite, the absolute quantities of Brownmillerite and Larnite are underestimated by the predictions. Finally, Melilite's quantities are broadly lower than the ones predicted by the software.

Given the above, it seems likely that the differences lie in calcium distribution between different phases. Moreover, the thermodynamic calculations overestimate Wüstite and Melilite amounts in all the samples, in expense of C2S and C2F, implying that FactSage assumes the formation of more calcic Wüstite and Melilite. Hence, the predicted solubility of Ca in the Wüstite phase is higher than in the Wüstite of the actual XRD results, resulting to greater formation of Brownmillerite C2(A,F) and Larnite C2S to take up the Ca, which would otherwise be contained within the Wüstite solution phase.

That taken, the FactSage calculations show discrepancies with the actual XRD results regarding the calcium distribution to different phases, leading to the formation of greater quantities of certain minerals in expense of others. In general, there is a solid alignment between the phases percentages trends per sample, with the XRD results. Finally, there is a firm limitation to the comparison, since sinter samples are comprised of heterogeneous grains, as it was thoroughly demonstrated by the activities under the microscope, contradicting the software homogeneity assumptions.

7. Conclusions and recommendations

7.1. Conclusions

The objective of the present MSc research was to study on a more fundamental level the phase equilibria, microstructural transformations and ultimately reaction kinetics as relevant for sinter material being reduced in the upper shaft down to the reserve zone of the blast furnace. The project was inspired by an initial statistical analysis on historical BRASS test data collected from tests performed during the past 10 years at Tata Steel Europe (Ijmuiden, the Netherlands). This analysis showed that sinters of various composition and mineralogy behave differently when reduced under conditions simulating the upper shaft zone of the blast furnace.

In order to isolate the effect of mineralogy and microstructure from sinter macro-structural characteristics, 6 samples with strongly variable bulk mineralogical and chemical composition were sized down to fractions of 250-500μm, being a grain range adequately fine to isolate microstructural effects, while excluding the impact of meso-porosity and mechanical fractures (>1 mm). A industrial sinter sample of similar composition was included in order to verify potential differences in reduction. The starting materials were analysed with XRD, XRF, size distribution and BET measurements.

Several isothermal reduction experiments were performed in the TGA and GERO furnaces under two set of conditions; i) T=750°C/XCO=0.55/N_2=0.5, ii) T=950°C/XCO=0.65/N_2=0.5, simulating point-conditions of the BRASS test. The reduced samples were analysed with XRD, reflected light optical microscopy and SEM. The results were compared with thermodynamic calculations conducted with FactSage software.

Hereby, based on the mentioned research work the research hypothesis can be confirmed; Sinter reduction experiments coupled with thermodynamic modelling and quantitative and qualitative analytical techniques of the reduced mineral phase reveal that *sinter microstructure and mineralogy influences sinter reducibility.*

This is a finding not addressed in the existing literature regarding sinter reducibility. Most studies do not distinguish the effects of micro-scale and meso-scale sinter features. As such, they either investigate the behaviour of single phases more fundamentally, or research much less controlled sinter materials under complex testing conditions where the interpretation of results is severely hampered. The current study fills the gap in between.

The confirmation of the research hypothesis, that *sinter microstructure and mineralogy do influence sinter reducibility* is supported by the following research outcomes:

- Starting composition and mineralogy influences reducibility kinetics.
- The way minerals influence reducibility is dependent on the imposed conditions.
- Higher temperature conditions converge the differences between the reduction rates of low and high basicity samples, due to enhancement of the relative reduction progress of minerals like precipitated Magnetite. The rate at which the transition of Magnetite to Wüstite occurs differs more at samples at low temperature. Based on the TGA and GERO results, the second reduction pick is dominated by the reduction of Magnetite to Wüstite.
- Mineralogy and microstructure are interrelated to open particle porosity. They can directly influence sinter reducibility, even when particle size distribution is kept as constant as practically as possible.
- Hematite is the most prone mineral to reduction followed by silico-ferrite of calcium and alumina (SFCA), while Magnetite stays stable for longer. Even within the same microstructure, Hematite is clearly reduced to a greater distance from the particle exterior than the Ca-ferrites surrounding it, and its

normalized decrease in the XRD analyses from its initial concentration is clearly faster than that for any of the Ca-ferrites (SFCA, CF2).

- The relative reduction of Hematite and silico-ferrites of calcium and alumina (SFCA) differs between the two sets of conditions; more reducing conditions converge the reduction progress of the two phases, due to SFCA's greater reduction. The reduction fronts of Hematite and SFCA converge in a single sinter particle with higher temperature conditions.
- SFCA 1 starts reducing into a multiphase intergrowth, comprised by a Fe-rich path and a Ca-Si-Al -rich path, which are the start of reduction towards Wüstite, ±Brownmillerite C2F, ±Larnite C2S and ±Melilite. Even with an external gas atmosphere which should be in equilibrium with Wüstite, the particles experience a clear sequence of intermediate reactions on the way to the equilibrium with the gas phase.
- Longer-time experiments always give the same sample sequence based on reduction progress; WCS108 is the most reduced, followed by WCS90, WCS86, the industrial sinter MH1785, WCS62 and WCS94.
- No particular differences were observed in reduction behavior of the industrial sinter MH1785/21 compared to Pilot-pot Sinter samples.
- The O/Fe values of the sinter samples after the longest reduction times in the GERO and TGA show marginal differences compared to the respective O/Fe values predicted by FactSage software at equilibrium. The GERO results are in greater agreement with FactSage predictions for both conditions of different temperature and gas atmosphere, than the TGA results.
- The thermodynamic predictions from FactSage are in qualitative agreement with XRD results, but they differ quantitatively.

7.2. Recommendations

In the following section important recommendations are provided for the suggested best course of action to be taken towards expanding on the results obtained in the current project:

- The contribution of differences in external morphology of the particles could also be estimated by image analysis on the polarised light optical microscopy mosaic and individual tile images. If no correlation with BET is found, then it should be clear that the actual intrinsic micro porosity of the particles dominates the BET differences, instead of size distribution or particle shape.
- In order to reproduce the exact atmosphere conditions of the BRASS metallurgical test, corresponding to an atmosphere of CO-CO_2-H_2-H_2O-N_2, TGA and GERO furnace should be equipped with a heating system that resolves the problem of condensation issues in the lower part of the tube of the furnaces related to the usage of hydrogen.
- To ensure the differences between the industrial and the pilot-pot sinters an additional study should be focused on examining greater variety of industrial sinters. More specifically, at least three pilot pot sinters can be generated based on the composition of at least three individual industrial samples in order to compare their relative reduction.
- Due to technical difficulties and shortage of gas supplies, duplicates of the TGA measurements could not be conducted during this research. It is recommended that repetition of the TGA experiments should be carried out in order to verify data validity and result confidence.
- The polarized optical microscopy images (396) and SEM images (~100) can be used for further research on the fundamentals of mineralogical changes during sinter reduction.

- Higher spatial-resolution chemical and crystallographic analyses would be necessary to resolve the identity and characteristics of the phases in the SFCA intergrowths formed after short run experiment times

Acknowledgments

I would like to express my sincerest gratitude to my research mentor Dr. James Small (TATA Steel Europe, Ceramic Center - CRC), who has provided his continuous guidance, advice, support, and time throughout this project. I am very grateful for his creative suggestions, broad vision, and passion for research.

I would also like to thank deeply my main supervisor Dr. Yanping Xiao (TATA Steel Europe, R&D) for her support, contributing suggestions and valuable feedback. Moreover, I am grateful to Dr. Xiao for giving me the opportunity to perform internship work for Tata Steel and gain experience in the industry.

In addition, I would like to offer my special thanks to the rest of my committee, Dr. Yongxiang Yang (TU Delft, Department of Materials Science and Engineering - MSE) and Dr. Mike Buxton (TU Delft, Department of Geoscience and Engineering) for their support and efforts into examining my study.

Finally, I would like to sincerely thank all the people at the Ceramic Research Centre of TATA Steel Europe in Ijmuiden (Holland), whose contribution has been critical in the realization of this project; Special thanks to Mary van Wijngaarden for her assistance and provided training with the GERO furnace and XRD sample preparation, as well as for her pleasant company. I am also grateful to Dr. Stefan Melzer for his support with the XRD Rietveld analysis and valuable expertise and advice. Many thanks to Frank van der Does for preparing the total of thick sections enabling the microscopy work. Also, special thanks to Chris Kooij for demonstrating the TGA equipment and for providing the TGA measurements. Finally, I would like to warmly thank Marcel Schilder for providing the results of material size distribution and BET measurements, especially in such short notice.

References

Bale, C. W., Bélisle, E., Chartrand, P., Decterov, S. A., Eriksson, G., Gheribi, A. E., Hack, K., Jung, I., Kang, Y., Melançon, J., Pelton, A. D., Petersen, S., Robelin, C., Sangster, J., Spencer, P. & Van Ende, M., 2016. FactSage Thermochemical Software and Databases, 2010-2016. Calphad, Volume 54, pp. 35-53.

Ball, D. F. Dartnell, J., Davison, J., Grieve, A. & Wild, R., 1973. Agglomeration of Iron Ores. In: London: Heinemann Educational Books Limited, pp. 136-139.

Bhagat, R. P., Chattoraj, U. S. & Sil, S. K., 2006. Porosity of Sinter and Its Relation with the Sintering Indices. ISIJ International, 46(11), pp. 1728-1730.

Biswas, A. K., 1981. Principles of blast furnace Ironmaking – theory and practice. Brisbane, Australia.: Cootha Publishing House.

Bölükbaşi, O. S., Tufan, B., Batar, T. & Altun, A., 2013. The Influence of Raw Material Composition on the Quality of Sinter. Life Science Journal, 10(4), pp. 584-594.

Bristow, N. J. & Waters, A. G., 1991. Role of SFCA in promoting high-temperature reduction properties of iron ore sinters. Mineral Processing & Extractive Metallurgy, 100(C), pp. C1-C10.

Brunauer, S., Emmett, P. H. & Teller, E., 1938. Adsorption of Gases in Multimolecular Layers. Journal of the American Chemical Society, 60(2), pp. 309-319.

Buytendijk, C., 2019. Separating the roles of mineralogy and microstructure in influencing gaseous reduction of iron ore sinter in the blast furnace process, Amsterdam: Master Thesis, VU Amsterdam.

Cameron, I., Sukhram, M., K, L. & Davenport, W., 2019. Blast Furnace Ironmaking Analysis, Control, and Optimiztion. 1st ed. United States: Elsevier Science Publishing Co Inc.

Clout, J. M. F. & Manuel, J. R., 2003. Fundamental investigations of difference in bonding mechanisms in iron ore sinter formed from magnetite concentrates and hematite ores. Powder Technology, 130(1-3), pp. 393-399.

Cores, A., Babich, A., Muñiz, M., Ferreira, S. G. & Mochon, J., 2010. The influence of different iron ores mixtures composition on the quality of sinter. ISIJ International , 50(8), pp. 1089-1098.

Costa, E., Coheur, J. P., Vanderheyden, B. & Munnix, R., 1995. Slag Formation in the Adhering Layer of Granules and Its Reaction with Nuclei in Iron Ore Sintering. ISIJ International, 35(2), pp. 138-147.

Dawson, P. R., 1993. Recent developments in iron ore sintering. Ironmaking and Steelmaking(UK) , 20(2), pp. 135-136.

Dwarapudi, S., Ghosh, T. K., Shankar, A., Tathavadkar, V., Bhattacharjee, D. & Venugopal, R., 2011. Effect of pellet basicity and MgO content on the quality and microstructure of hematite pellets. International Journal of Mineral Processing, 99(1), pp. 43-53.

Fernandez-González, D., Ruiz-Bustinza, I., Mochón, J., González-Gasca, C. & Verdeja, L. F., 2017. Iron Ore Sintering: Process. Mineral Processing and Extractive Metallurgy , 38(4), pp. 215-227.

Geerdes, M., Toxopeus, H. & Van Der Vliet, V., 2015. Modern Blast Furnace Ironmaking: An Introduction.. 2 ed. Delft: Delft University Press.

Ghost, A. & Chatterjee, A., 2008. Ironmaking and Steelmaking: Theory and Practice. 1 ed. Delhi, India: Prentice-Hall of India Pvt. Ltd.

Hida, Y., Ito, K., Okazaki, J., Sasaki, M. & Umezu, Y., 1982. Evaluation of coarse ores for sintering on the basis of their mineralogical properties. Tetsu-to-Hagane/Journal of the Iron and Steel Institute of Japan, 68(6), pp. 2166-2173.

Higuch, K., Naito, M., Nakano, M. & Takamoto, Y., 2004. Optimization of Chemical Composition and Microstructure of Iron Ore Sinter for Low-temperature Drip of Molten Iron with High Permeability. ISIJ International, 44(12), pp. 2057-2066.

Janeček, M., Krajňák, T., Stráská, J., Čížek, J., Lee, D. J., Kim, H. S. & Gubicza, J., 2014. Microstructure evolution in ultrafine-grained interstitial free steel processed by high pressure torsion. IOP Conference Series: Materials Science and Engineering, 63(1).

Jursova, S. & Honus, S., 2016. Study on disintegration of metallurgical sinter. MM Science Journal, Issue 05, pp. 1440-1444.

Jursová, S., Pustejovska, P. & Brozova, S., 2017. Study on reducibility and porosity of metallurgical sinter. Alexandria Engineering Journal, 57(3).

Jursova, S., Pustejovska, P. & Brozova, S., 2018. Study on reducibility and porosity of metallurgical sinter. Alexandria Engineering Journal, 57(3), pp. 1657-1664.

Knepper, W. A., 1962. Agglomeration. New York: Interscience Publishers (John Wiley and Sons).

Konstanciak, A., 2012. The Effect of Coke Quality on Blast Furnace Working. Material Science Forum, Volume 706-709, pp. 2164-2169.

Krajňák, T., Máthis, K., Janeček, M. & Gubicza, J., 2014. Comparison of the microstructure and the mechanical properties of AX41 magnesium alloy processed by EX-ECAP via three different routes A, Bc and C. IOP Conference Series Materials Science and Engineering, 63(1).

Loo, C. E., Matthews, L. T. & O'dea, D., 2011. Lump ore and sinter behavior during sofeting and melting. ISIJ intenrational 51(6), 51(6), pp. 930-938.

Maeda, T. & Ono, Y., 1985. Behavior of Constituent Minerals in the Carbon Monoxide Reduction of Sinter at 900°C. ISIJ International, 25(12), pp. 1191-1193.

Maeda, T. & Ono, Y., 1986. Experimental study on the relation between microstructures of cinsistuent minerals and pores and reducibility of sinter. Tetsu-To-Hagane/Journal of the Iron and Steel Institute of Japan, 72(7), pp. 775-782.

Moffat, K.-U. K. a. G., 2008. Annual Report, Brussels, Belgium.: EUROFER.

Mumme, W. G., 2003. The crystal structure of SFCA-II, Ca5.1Al9.3Fe3+ 18.7Fe2+ 0.9O48 a new homologue of the aenigmatite structure-type, and structure refinement of SFCA-type, Ca2Al5Fe7O20. Implications for the nature of the "ternary-phase solid-solution" previously reported. Neues Jahrbuch für Mineralogie - Abhandlungen: Journal of Mineralogy and Geochemistry, 178(29), pp. 307-335.

Odenthal, H.-J., 2017. An insight into steelmaking processes by Computational Fluid Dynamics. Hannover, XVIII International UIE-Congress - Electrotechnologies for Material Processing.

Oluwadare, G. O., 2007. Microstructures of Sinters Produced from Some Nigerian Ores. Trends in Applied Science Research, 2(6), pp. 508-514.

Ono, H., Dohi, Y., Arikata, Y. & Usui, T., 2009. Effect of Mineral Composition and Pore Structure on Reducibility of Composite Iron Ore Sinter. ISIJ International, 49(5), pp. 722-728.

Panigrahy, S. C., Verstraeten, P. & Dilewijns, J., 1984. Influence of MgO addition on mineralogy of iron ore sinte. Metallurgical Transactions B, 15(1), pp. 23-32.

Phillips, B. & Muan, A., 2006. Phase Equilibria in the System CaO-iron Oxide-SiO2 in Air. Journal of American Ceramic Society, 42(9), pp. 413-423.

Pimenta, H. P. & Seshadri, V., 2002. Influence of Al2O3 and TiO2 degradation behaviour of sinter and hematite at low temperatures on reduction. Ironmaking & Steelmaking: Processes, Products and Applications, 29(3), pp. 175-179.

Rajisha, K. R., Deepa, B., Pothan, L. A. & Thomas, S., 2011. Thermomechanical and spectroscopic characterization of natural fibre composites. In: N. E. Zafeiropoulos, ed. Interface Engineering of Natural Fibre Composites for Maximum Performance. s.l.:Woodhead Publishing Series in Composites Science and Engineering, pp. 241-274.

Sakamoto, N., Fukuyo, H., Iwata, Y. & Miyashita, T., 1984. Kinetics of Reducibility of Sinter. Tetsu-to-Hagane/Journal of the Iron and Steel Institute of Japan, 70(6), pp. 504-511.

Sato, Y., 1982. R&D laboratories notes, s.l.: Nippon Steel Corporation; R&D laboratories.

Shi, B. Zhu, D., Pan, J., Liu, X. & Li, S., 2019. Combined effect of MgO and basicity varied by different dolomite and burnt lime addition on sintering performance of magnetite concentrates. Ironmaking & Steelmaking: Processes, Products and Applications, pp. 1743-2812.

Small, J., 2010. Tata Steel Europe IJmuiden B.V. Unpublished in-house report

Small, J., Crama, M., Kooij, C., Melzer, N. & Bouwens, P. 2017. Tata Steel Europe IJmuiden B.V. Unpublished in-house report.

Song, Q., 2013. Effect of nut coke on the performance of the ironmaking blast furnace. Delft, NL: PhD thesis, Delft University of Technology.

Strassburger, J. H., 1969. Blast Furnace Theory and Practice. 1st ed. Netherlands: Gordon and Breach Science Publishers.

Taichi, M., Takeyuki, K. & Eiki, E., 2015. Reduction and Disintegration Behavior of Sinter under N2–CO–CO2–H2–H2O Gas at 773 K. ISIJ International, 55(6), pp. 1181-1187.

Torre de Palacios, L. D. L., 2011. Natural resources sustainability: iron ore mining. Dyna 78(170), Volume 78, pp. 227-234.

Umadevi, T., Brahmacharyulu, A., Roy, A. K., Mahapatra, P. C., Prabhu, M. & Ranjan, M., 2011. Influence of Iron Ore Fines Feed Size on Microstructure, Productivity and Quality of Iron Ore Sinter. ISIJ International, 51(6), pp. 922-929.

Umadevi, T., Brahmacharyulu, A., Sah, R., Mahapatra, PB. & Prabhu, M., 2014. Optimisation of MgO addition in low and high silica iron ore sinter to improve sinter reducibility. Ironmaking & Steelmaking, 41(4), pp. 270-278.

Umadevi, T., Karthik, P., Mahapatra, PB., Prabhu, M. & Ranjan, M., 2012. Optimisation of FeO in iron ore sinter at JSW Steel Limited. Ironmaking & Steelmaking, 39(3), pp. 180-189.

Umadevi, T., Nelson, K., Mahapatra, P. C., Prabhu, M. & Ranjan, M., 2009. Influence of magnesia on iron ore sinter properties and productivity. Ironmaking & Steelmaking, 36(7), pp. 515-520.

Wang, Y. C., Zhang, J. L., F.Zhang, F. & Luo, G. P., 2011. Formation Characteristics of Calcium Ferrite in Low Silicon Sinter. Journal of Iron and Steel Research International, 18(10), pp. 1-7.

Webster, N. A. S., Pownceby, M. I., Madsen, I. C. & Kimpton, J. A., 2012. Silico-ferrite of Calciumand Aluminum (SFCA) Iron Ore Sinter Bonding Phases: New Insights into Their Formation during Heating and Cooling, Metallurgical and Materials Transactions. Metallurgical and Materials Transactions B, 43(6).

Woollacott, L. C. & Eric, R. H., 1994. Mineral and metal extraction : an overview. s.l.:Johannesburg, South African Intitute of Mining and Metallurgy.

Xiao, Y., 2018. Tata Steel Europe IJmuiden B.V. Unpublished in-house report., s.l.: s.n.

Yamaguchi, K., Ueno, H., Kawaguchi, T., Matsunaga, S., Oda, H. & Amano, S., 1994. Influence of Al2O3 on Reduction-Meltdown Behavior of Sinter in Blast Furnace. Isij International, 34(12), pp. 964-972.

Zhang, M. & Andrade, M. W., 2016. Effect of MgO and basicity on microstructure and metallurgical properties of iron ore sinter. In: S. J. Ikhmayies, et al. eds. Characterization of Minerals, Metals and Materials 2016. Tennessee: TMS 2016 145th annual meeting & excibition, pp. 167-174.

Zhang, M. & Andrade, M. W., 2017. Effect of Alumina and Magnesia on Microstructure and Mineralogy of Iron Ore Sinter. In: Characterization of Minerals, Metals, and Materials 2017. s.l.:Springer International Publishing, pp. 291-309.

Zhang, M., Coe, M. S. & Andrade, M. W., 2015. Effect of Sinter Basicity on Sinter Productivity and Quality with High Rate of Recycled Materials. In: T. P. BattleJerome, et al. eds. Drying, Roasting, and Calcining of Minerals. East Chicago, USA: Springer, Cham, pp. 259-267.

Zhou, M., Yang, S. T., Jiang, T. & Xue, X. X., 2015. Influence of MgO in form of magnesite on properties and mineralogy of high chromium, vanadium, titanium magnetite sinters. Ironmaking & Steelmaking: Process, Products and Applications, 42(3), pp. 217-225.

Zhu, D., Chou, J., Shi, B. & Pan, J., 2019. Influence of MgO on Low Temperature Reduction and Mineralogical Changes of Sinter in Simulated COREX Shaft Furnace Reducing Conditions. Minerals, 9(5).